January 2020

Time-Dependent Plastic Deformation Of Mg Nanocomposites: Ambient And Elevated Temperature Assessments

Jiselle Thornby

TIME-DEPENDENT PLASTIC DEFORMATION OF Mg NANOCOMPOSITES: AMBIENT AND ELEVATED TEMPERATURE ASSESSMENTS

by

Jiselle Lee Thornby

Bachelor of Science, University of North Dakota, 2019

A Thesis

Submitted to the Graduate Faculty

of the

University of North Dakota

in partial fulfillment of the requirements

for the degree of

Master of Science

Grand Forks, North Dakota

May

2020

This thesis, submitted by Jiselle Thornby in partial fulfillment of the requirements for the Degree of Master of Science in Chemical Engineering from the University of North Dakota, has been read by the Faculty Advisory Committee under whom the work has been done and is hereby approved.

Wayne Seames 04-21-2020

Dr. Wayne Seames, Chairperson

Meysam Haghshenas 04-22-2020

Dr. Meysam Haghshenas, Co-Chair

Edward Kolodka 04-22-2020

Dr. Edward Kolodka, Committee Member

This thesis is being submitted by the appointed advisory committee as having met all of the requirements of the School of Graduate Studies at the University of North Dakota and is hereby approved.

DocuSigned by:
Chris Nelson
13D0157109424B1...

Dr. Chris Nelson, Associate Dean
School of Graduate Studies

4/22/2020

Date

PERMISSION

Title	Time-Dependent Plastic Deformation of Mg Nanocomposites: Ambient and Elevated Temperature Assessments
Department	Chemical Engineering
Degree	Master of Science

In presenting this thesis in partial fulfillment of the requirements for a graduate degree from the University of North Dakota, I agree that the library of this University shall make it freely available for inspection. I further agree that permission for extensive copying for scholarly purposes may be granted by the professor who supervised my thesis work or, in his absence, by the Chairperson of the department or the dean of the School of Graduate Studies. It is understood that any copying or publication or other use of this thesis or part thereof for financial gain shall not be allowed without my written permission. It is also understood that due recognition shall be given to me and to the University of North Dakota in any scholarly use which may be made of any material in my thesis.

Jiselle Thornby

7 February 2020

Signature: Wayne S Seames 4-21-2020
Wayne S Seames 4-21-2020 (Apr 21, 2020)
Email: wayne.seames@und.edu

Signature: Edward Kolodka (Apr 22, 2020)
Email: edward.kolodka@und.edu

Signature: Meysam Haghshenas
Meysam Haghshenas (Apr 22, 2020)
Email: meysam.haghshenas@utoledo.edu

TABLE OF CONTENTS

LIST OF FIGURES ..... **viii**

LIST OF TABLES ..... **xiii**

NOMENCLATURE ..... **xiii**

GREEK NOMENCLATURE ..... **xiv**

ACKNOWLEDGEMENTS ..... **xv**

ABSTRACT ..... **xviii**

CHAPTER I - INTRODUCTION **1**

1.1. Motivation **1**

1.2. Objectives **3**

1.3. Thesis Organization **3**

REFERENCES **5**

CHAPTER II - LITERATURE REVIEW **12**

2.1. Introduction to Magnesium **12**

2.1.1. Selected Properties of Magnesium 12

2.1.2. Magnesium Alloys 14

2.2. Applications of Mg, Mg Alloys, and Mg Composites **18**

2.2.1. Automotive Industry 18

2.2.2. Aerospace Industry 20

2.2.3. Biomedical Applications 21

2.2.4. Other Noteworthy Applications 22

2.2.4.1. Military 22

2.2.4.2. Nuclear 23

2.2.4.3. Consumer Electronics 23

2.2.4.4. Sports Equipment 23

2.3. Metal Matrix Composites (MMCs) **24**

2.3.1. What is a Metal Matrix Composite? 24

2.3.2. Types of Reinforcements 25

2.3.2.1. Carbon Nanotubes (CNTs) 25

2.3.3. Why “nano” and not “micro” reinforcement particles? Why nanocomposites? 28
2.3.4. Strengthening Mechanisms in Nanocomposites 30
2.3.4.1. Effective Load Transfer 30
2.3.4.2. Hall-Petch Strengthening 30
2.3.4.3. Orowan Strengthening 31
2.3.4.4. Increased Dislocation Density Caused by Thermal Expansion and Elastic Modulus Mismatch 32
2.4. The Promise of Magnesium-CNT Nanocomposites 35
2.4.1. CNTs in Magnesium: What properties have already been improved and why? 36
2.5. What is creep? 39
2.5.1. Dislocation Creep – Glide (Slip) and Climb 40
2.5.2. Diffusional Creep Mechanisms – Nabarro-Herring Creep and Coble Creep 41
2.6. Conventional Creep Testing 42
2.6.1. Compressive/Tensile Uniaxial Creep Testing 42
2.6.2. Impression Testing 43
2.7. Indentation Creep Testing (Non-conventional method) 45
2.7.1. Room Temperature Creep Studies on Mg-nanocomposites 48
2.7.2. High-Temperature Creep Studies on Mg-nanocomposites 50
2.7.2.1. Uniaxial Creep Tests 50
2.7.2.2. Impression Creep Tests 52
2.7.2.3. Nanoindentation Creep of Mg-nanocomposites 54
2.8. Project Outlook 55
2.8.1. Project Objectives 55
2.8.2. Project Novelty 55
2.8.3. Project Contributions to the Scientific Community 56
REFERENCES 58
CHAPTER III - EXPERIMENTAL PROCEDURE 74
3.1. Mg-CNT Nanocomposite Fabrication 74
3.2. Experimental Procedure for Room Temperature Creep Tests 76
3.3. Experimental Procedure for Elevated Temperature Creep Tests 80

3.4. From *P-h* curves to Useful Mechanical Properties: Hardness, Young's Modulus, and Steady-State Creep Theory for Nanoindentation 83
REFERENCES 88

CHAPTER IV - RESULTS AND DISCUSSION OF INDENTATION CREEP TESTS PERFORMED AT ROOM AND ELEVATED TEMPERATURE 91
4.1. Microstructure and Grain Morphology 91
4.2. Ambient (Room) Temperature Results 96
4.2.1. Load-Displacement Curves 96
4.2.2. Indentation Stress versus Depth Behavior 98
4.2.3. Indentation Hardness as a Function of CNT Loading 101
4.2.4. Creep Rate and Displacement as a Function of Time 103
4.2.5. Creep Power Exponent for Dominant Creep Mechanism at 298 K 107
4.3. Elevated-Temperature Results 109
4.3.1. Berkovich Indentation Morphologies 109
4.3.2. Load-Displacement (*P-h*) Curves 113
4.3.2.1. *P-h* Curves as a Function of Temperature 113
4.3.2.2. *P-h* Curves as a Function of Load Rate 114
4.3.3. Indentation Stress vs. Depth Behavior: Indentation Size Effect 117
4.3.3.1. Indentation Size Effect (ISE) Curves as a Function of Temperature 117
4.3.3.2. ISE Curves as a Function of Load Rate 120
4.3.3.3. ISE Curves as a Function of CNT Content 122
4.3.4. Indentation Hardness Behavior 124
4.3.4.1. Hardness Behavior as a Function of Temperature and Load Rate 124
4.3.5. Young's (Elastic) Modulus Response 126
4.3.6. Creep Rate Curves 128
4.3.6.1. Creep Rate Curves as a Function of Temperature 128
4.3.6.2. Creep Rate Curves as a Function of Load Rate 130
4.3.6.3. Creep Rate Curves as a Function of CNT Loading 131
4.3.7. Creep Displacement Behavior 133

4.3.7.1. Creep Displacement Behavior as a Function of Temperature 133
4.3.7.2. Creep Displacement Behavior as a Function of Load Rate 135
4.3.7.3. Creep Displacement Behavior as a Function of CNT Loading 136
4.3.8. Creep Power Exponent for Dominant Creep Mechanism Determination 138
REFERENCES 141
CHAPTER V - CONCLUSIONS AND FUTURE WORK 146
5.1. Project Conclusions 146
5.1.1. Ambient-Temperature Conclusions 146
5.1.2. Elevated-Temperature Conclusions 147
5.1.2.1. Conclusions Drawn from SEM Observations 147
5.1.2.2. Conclusions Drawn from Nanoindentation Tests 148
5.2. Recommendations for Future Work 150
REFERENCES 153
Appendix A: Intermediate Results Supporting Magnesium Trend Price ... A-1
Appendix B: Supplementary *P-h* curves B-1
Appendix C: Supplementary Indentation Size Effect (ISE) Curves C-1
Appendix D: Supplementary Creep Rate Curves D-1
Appendix E: Supplementary Creep Displacement Curves E-1

LIST OF FIGURES

Figure 2.1. Creep strength of commercial Mg die-cast alloys to produce 0.1% creep strain in 100 hrs, at 175°C [27]. Note that AXJ530 has similar creep strength to A380 (an aluminum alloy) and Mg-RE alloy AM-HP2+ has surpassed the creep strength of A380..... 17
Figure 2.2. Examples of commercial vehicle parts which have incorporated magnesium into their design: **(a)** magnesium steering wheel core for Toyota Camry weighing 0.75 kg, **(b)** seat support for Jaguar and Fiat models weighing 2.6 kg, **(c)** rear transfer case made from Mg alloy AZ91D weighing 2.7 kg [32]. 19
Figure 2.3. X-ray images in Lee et al. study [37] of: **(i)** distal radius fracture and the scaphoid nonunion before surgical intervention, **(ii)** implantation site image taken immediately after the surgical procedures to fix the distal radius fracture, **(iii)** 6-month follow-up X-ray, and **(iv)** complete degradation and bone healing after 1-year post-operation. The red arrow shows distal radius fracture, white arrow points at the scaphoid nonunion, and the yellow arrow indicates the Mg alloy implant. 22
Figure 2.4. A single-walled carbon nanotube (SWCNT) is pictured on the left. A multi-walled carbon nanotube (MWCNT) is pictured on the right. Image credit goes to Choudhary et al. [50]..... 26
Figure 2.5. Common issues with micro-particulate reinforcements: broken particles (a), particulate aggregations (b), and voids at the particle-matrix interface. All SEM image credit goes to El-Saeid Essa et al. [76]. 29
Figure 2.6. Steps taken to form Orowan loops (left) [82] and dislocation rings upon bow-out of Ni_3Si particles in a Ni-Si alloy (right) [83]. 32
Figure 2.7. Effect of various strengthening contributions and total resulting strengthening increment calculated for an aluminum matrix composite reinforced with 2 wt.% Al_2O_3 [81]..... 35
Figure 2.8. SEM image of Mg-1 vol.% CNT (d on left), and XRD pattern of this nanocomposite revealing the presence of MgO in the sample (heart-shaped markers) (c on right) [86]. 37
Figure 2.9. Representative stress-strain curves obtained in Goh et al. [87] study. Mg-1.3 wt.% CNT exhibits the best mechanical behavior of all CNT contents tested in Mg..... 38
Figure 2.10. Two common diffusional creep mechanisms: (a) Nabarro-Herring creep and (b) Coble creep [92]..... 41
Figure 2.11. Typical setup of a uniaxial creep test [93]..... 43

Figure 2.12. Schematic illustrating the deformation zone formed around a punch during impression creep testing [94]. 44
Figure 2.13. A typical load-displacement curve obtained during an indentation creep test (a), and a schematic of the interaction between the indenter tip and sample (b) [95]. 46
Figure 3.1. Schematic of the Mg-CNT nanocomposite fabrication method. Note that step 2 (blending step) is omitted for pure Mg only. Figure credit goes to Uchino [1] for sintering process and Gupta et. al [2] for hybrid microwave setup graphic. 75
Figure 3.2. Four samples (pictured after nanoindentation) used for room-temperature tests: (a) Pure Mg, (b) Mg-0.25 CNT, (c) Mg-0.5 CNT, and (d) Mg-0.75 CNT. 77
Figure 3.3. KLA-Tencor iNano nanoindenter (left) and indentation platform (right). 78
Figure 3.4. Geometry of a Berkovich indenter (left) where "a" is the angle defined as the angle between the centerline axis and any of the faces (also called "half angle" and "face angle"). SEM image of a diamond Berkovich indenter tip (right) [3]. 79
Figure 3.5. Typical load-displacement curves (also called *P-h* curves) generated during a dual-stage indentation test. Schematic (a) is the cross-sectional view of an indentation. Diagram (b) is a typical load-displacement curve obtained during an indentation creep test and key parameters for analysis are identified [4]. The curve on the right also illustrates stiffness (dP/dh) and creep, but additionally indicates where thermal drift corrections occur [5]. 80
Figure 3.6. Four samples (pictured after nanoindentation) used for elevated-temperature tests: **(a)** Pure Mg, **(b)** Mg-0.25 CNT, **(c)** Mg-0.5 CNT, and **(d)** Mg-0.75 CNT. 81
Figure 3.7. The NanoTest Xtreme nanoindenter (Micro Materials, UK) situated inside the vacuum chamber [6]. 82
Figure 3.8. Schematic depiction of how load-displacement information from a creep test (strictly under the holding/dwell period) can be used to determine the values of the stress exponent and the activation energy taken from Goodall and Clyne [15]. 87
Figure 4.1. Optical micrographs revealing the cross-sectional grain morphologies and microstructures (those parallel to the extrusion direction) of **(a)** Pure Mg, **(b)** Mg-0.25 CNT, **(c)** Mg-0.5 CNT, and **(d)** Mg-0.75 CNT. Arrows are added to **(a)** to indicate the presence of mechanical twins in Pure Mg. 92

Figure 4.2. Scanning electron microscopy (SEM) images of Mg-0.5 vol.% CNT. A single CNT fiber is pointed out in the higher-magnification SEM inset, indicated with an arrow. 93
Figure 4.3. Energy Dispersive X-ray Spectroscopy (EDS) performed on Mg-0.5 vol.% CNT sample to verify the sample composition. 95
Figure 4.4. Load-displacement (or *P-h*) curves displaying loading, holding, and unloading measurements at all four strain rates tested (0.01–10 s^{-1}) for: **(a)** Pure Mg, **(b)** Mg-0.25 vol.% CNT, **(c)** Mg-0.5 vol.% CNT, and **(d)** Mg-0.75 vol.% CNT. 97
Figure 4.5. Indentation stress (σ_{ind}) versus displacement (h) curves for all materials over strain rates of: **(a)** 0.01 /s, **(b)** 0.1 /s, **(c)** 1.0 /s, and **(d)** 10 /s. The indentation size effect (ISE) is observed in all tests. 99
Figure 4.6. Indentation hardness (H_{ind}) as a function of CNT loading for all materials over four strain rates: **(a)** 0.01 /s, **(b)** 0.1 /s, **(c)** 1.0 /s, and **(d)** 10 /s..... 103
Figure 4.7. Creep rate (/s) as a function of time for all materials over the four strain rates of: **(a)** 0.01 /s, **(b)** 0.1 /s, **(c)** 1.0 /s, and **(d)** 10 /s..... 105
Figure 4.8. Creep displacement (nm) versus dwell time (500 s) for all materials over the four strain rates of: **(a)** 0.01 /s, **(b)** 0.1 /s, **(c)** 1.0 /s, and **(d)** 10 /s. The transition from transient to steady-state creep is observed in all tests (demarcated with a red dashed line). 106
Figure 4.9. Power law exponent (*n*) values for all strain rates tested. 108
Figure 4.10. Scanning electron microscopy (SEM) image of Berkovich indentations made on pure Mg at 500x magnification and a close-up of a single indentation made at 3,000x magnification (inset). Red arrows point out microcracks near indentations. 110
Figure 4.11. SEM image of indentations made on Mg-0.75 v/v% CNT at 300x magnification and a close-up of a single indentation made at 3,000x magnification (inset). 111
Figure 4.12. SEM image of Mg-0.75 v/v% CNT with distinct groups of indentations (circled). Largest indentations are made at 300°C, the smallest indentations at room temperature (25°C), etc. Indents in the dashed orange grouping were re-runs. Surfaces of pure Mg, Mg-0.25, and Mg-0.5 v/v% CNT are visually similar. 112
Figure 4.13. Load-displacement (*P-h*) curves as a function of temperature for a fixed load rate of 0.5 mN/s for: **(a)** Pure Mg, **(b)** Mg-0.25 vol.% CNT, **(c)** Mg-0.5 vol.% CNT, and **(d)** Mg-0.75 vol.% CNT. **RT**: room temperature (298 K). 114

Figure 4.14. Load-displacement (*P*-*h*) curves as a function of load rate for a fixed temperature of 300°C for: **(a)** Pure Mg, **(b)** Mg-0.25 vol.% CNT, **(c)** Mg-0.5 vol.% CNT, and **(d)** Mg-0.75 vol.% CNT. 116
Figure 4.15. Indentation stress versus loading depth behavior (ISE behavior) as a function of temperature for a fixed load rate of 0.5 mN/s for: **(a)** Pure Mg, **(b)** Mg-0.25 vol.% CNT, **(c)** Mg-0.5 vol.% CNT, and **(d)** Mg-0.75 vol.% CNT. **RT**: room temperature (298 K). 119
Figure 4.16. Schematic on the temperature dependence of ISE and GND storage volume [27]. 119
Figure 4.17. Indentation stress versus loading depth behavior (ISE behavior) as a function of load rate for a fixed temperature of 300°C for: **(a)** Pure Mg, **(b)** Mg-0.25 vol.% CNT, **(c)** Mg-0.5 vol.% CNT, and **(d)** Mg-0.75 vol.% CNT. **RT**: room temperature (298 K). 121
Figure 4.18. Indentation stress versus loading depth behavior (ISE behavior) as a function of CNT content at a fixed temperature of 300°C over all load rates tested: **(a)** 0.5 mN/s, **(b)** 5 mN/s, and **(c)** 50 mN/s. 123
Figure 4.19. Variation of indentation hardness as a function of CNT loading and temperature over three load rates: **(a)** 0.5 mN/s, **(b)** 5 mN/s, and **(c)** 50 mN/s. 125
Figure 4.20. Variation of Young's modulus as a function of CNT loading and temperature over three load rates: **(a)** 0.5 mN/s, **(b)** 5 mN/s, and **(c)** 50 mN/s. 127
Figure 4.21. Creep rate versus holding time behavior as a function of temperature for a fixed load rate of 5 mN/s for: **(a)** Pure Mg, **(b)** Mg-0.25 vol.% CNT, **(c)** Mg-0.5 vol.% CNT, and **(d)** Mg-0.75 vol.% CNT. **RT**: room temperature (298 K). 129
Figure 4.22. Creep rate versus holding time behavior as a function of load rate for a fixed temperature of 300°C for: **(a)** Pure Mg, **(b)** Mg-0.25 vol.% CNT, **(c)** Mg-0.5 vol.% CNT, and **(d)** Mg-0.75 vol.% CNT. **RT**: room temperature (298 K). 130
Figure 4.23. Creep rate versus holding time behavior as a function of material tested (CNT loading) at a fixed load rate of 50 mN/s, over all temperatures tested: **(a)** RT, **(b)** 100°C, **(c)** 200°C, and **(d)** 300°C. **RT**: room temperature (298 K). 132
Figure 4.24. Creep displacement versus holding time behavior as a function of temperature for a fixed load rate of 50 mN/s for: **(a)** Pure Mg, **(b)** Mg-0.25 vol.% CNT, **(c)** Mg-0.5 vol.% CNT, and **(d)** Mg-0.75 vol.% CNT. **RT**: room temperature (298 K). 134

Figure 4.25. Creep displacement versus holding time behavior as a function of load rate at a fixed temperature of 200°C for: **(a)** Pure Mg, **(b)** Mg-0.25 vol.% CNT, **(c)** Mg-0.5 vol.% CNT, and **(d)** Mg-0.75 vol.% CNT. **RT**: room temperature (298 K). 135
Figure 4.26. Creep displacement versus holding time behavior as a function of material tested (CNT loading) at a fixed load rate of 50 mN/s, over all temperatures tested: **(a)** RT, **(b)** 100°C, **(c)** 200°C, and **(d)** 300°C. **RT**: room temperature (298 K). 137
Figure 4.27. Creep power exponents (*n*-values) for all materials over all temperatures and for all load rates tested: **(a)** 0.5 mN/s, **(b)** 5 mN/s, and **(c)** 50 mN/s.. 140

LIST OF TABLES

Table 2.1. Advantages and challenges of pure magnesium. 13

Table 2.2. Advantages and disadvantages of four major alloying agents for improving magnesium alloy performance at high temperatures [26]..... 16

Table 2.3. Summary of some remarkable properties of carbon nanotubes. 27

NOMENCLATURE

Al_2O_3	aluminum oxide, or alumina
b	Burgers vector
BNNC	boron nitride nanocomposite
CNT	carbon nanotube
CO_2	carbon dioxide
DSP	dislocation starved plasticity
E	elastic modulus, also Young's modulus (in GPa)
E_i	elastic modulus of indenter
E_r	reduced modulus
E_s	elastic modulus of the specimen
EDS	energy dispersive spectroscopy
FE SEM	field emission scanning electron microscopy
GHG	greenhouse gas
G_m	shear modulus of the matrix
GND	geometrically necessary dislocation
h	indentation displacement, or depth (in nm)
HCP	hexagonally close-packed
$H_{ind.}$	indentation hardness (in GPa)

ISE	indentation size effect
M	Taylor factor
Mg	magnesium
MgO	magnesium oxide
MMC	metal matrix composite
MWCNT	multi-walled carbon nanotube
n	creep rate exponent, or power law exponent (dimensionless)
OM	optical microscopy
P	indentation load (in mN)
RT	room temperature (25°C, or 298 K)
SiC	silicon carbide
SEM	scanning electron microscopy
SGP	strain gradient plasticity
SWCNT	single-walled carbon nanotube
v/v%	volume percentage (also vol.%)
Y_2O_3	yttrium oxide, or yttria

GREEK NOMENCLATURE

$\Delta\sigma_{Orowan}$	Orowan strengthening effect
$\varepsilon_{ind.}$	indentation strain rate, also creep rate (in reciprocal seconds)
ν_i	Poisson's ratio of the indenter
ν_s	Poisson's ratio of the specimen
ρ	density (commonly in kg/m^3 or g/cm^3)
$\sigma_{ind.}$	indentation stress (in GPa)

ACKNOWLEDGEMENTS

Not a single word, figure, or table in this thesis would have been possible without the help of my mentors, friends, and family. I cannot possibly begin to thank everyone who helped me get to this point, but I'd like to try. The following paragraphs are my attempts to wholeheartedly express my gratitude to those who have played an indispensable role in my journey.

Endless thanks go to my graduate research advisor, Dr. Meysam Haghshenas. We met at approximately 2:00 pm on December 18, 2017, and I cannot thank him enough for taking a chance on a chemical engineering student, who at that time, knew nothing about creep, to take on this mechanical engineering project. Meysam, you epitomize the qualities of an ideal research advisor, all in your patience, scientific expertise, and your vivacious personality. Thank you for helping me realize it was time to expand an undergraduate research project into a Master's thesis. It has been an honor to work alongside you and any future student to work with you is immensely lucky to do so.

I must also thank my academic advisor of five years, Dr. Wayne Seames. The seeds of this thesis were sown in his International Research Experiences for Students (IRES) program at UND and the University of Leeds in my undergraduate junior year. I am privileged to have been a participant in the 2019 cohort. Thank you for your guidance throughout my time at UND, for constantly pushing me to be excellent in all I do, and for convincing me to join the world of academia (or "academentia" as he jokingly calls it).

Additionally, many thanks go to my family and friends for their love and support through everything. Special thanks go to Matthew Kraft, a friend who has been loyal to me since kindergarten, for being the best companion I could ask for in gradeschool and now the first person I'll call to put my mind at ease after a long day. I would also like to

thank Kelsey Young and Lance Johnson for the gift of their support, humor, and nearly seven years of continued friendship since Governor's School 2013. Also, a personal thanks to Eli Vettel for his love, support, and bringing happiness into my life in ways I never thought possible. Eli, you are an absolute gem.

I experienced the tough demographic process of mortality during the writing of this thesis. My paternal grandmother, Janet Gallagher, passed during this journey and unfortunately could not see this piece of writing to its completion. Jan loved writing and was a reporter for the Minot Daily News in the 1960s. She achieved her life-long dream of becoming a college graduate at the age of 64. She would be so thrilled to know I've authored this thesis as a first-generation student in the Thornby family. This thesis is dedicated to my family, and in the loving memory of Jan.

Importantly, none of this work would have been possible without the generosity of several funding sources, including, but not limited to, the University of North Dakota departments of Mechanical Engineering and Chemical Engineering, and the National Science Foundation (NSF) under Grant #1458962. The nanoindentation creep tests performed in this project would not have been conducted without the help of Devendra Verma at NanoScience Instruments Laboratory (room temperature) and Adrian Harris, Andy Bird, and Ben Beake at Micro Materials Ltd., in Wrexham, England (elevated temperature). I am also largely indebted to Dr. Manoj Gupta and his student, Vyasaraj Manakari, for synthesizing the nanocomposites for this project.

Finally, complete conversion of my thoughts to the written words comprising this thesis would not have taken place without the help of caffeine, whether it be in the form of coffee, the many flavors of Mountain Dew, or otherwise. Thank you.

This thesis is dedicated to the Thornby family and

in loving memory of my grandmother Janet.

I hope I make you proud.

ABSTRACT

Magnesium (Mg) nanocomposites are promising materials for many lightweight engineering applications. By adding a nanoparticle phase, like carbon nanotubes (CNTs) to a Mg matrix phase, new strengthening mechanisms are activated and enable the resulting nanocomposite to have better mechanical properties, e.g., strength and ductility, than unreinforced Mg. The viability of using Mg-CNT nanocomposites in lieu of heavier structural metals in industrial dimensions, especially those at high temperatures, cannot be assessed until these materials have been comprehensively characterized.

In the present project, the nanoindentation technique was used to assess the creep and hardness response of pure Mg and Mg reinforced with 0.25, 0.5, and 0.75 vol.% CNTs at room and elevated (373, 473, and 573 K) temperatures. This work has shown that CNTs improve strength and creep resistance of Mg matrices. It was found that the dominant creep mechanisms at room and elevated temperatures are not necessarily the same mechanism.

CHAPTER I
INTRODUCTION

1.1. Motivation

Global average atmospheric carbon dioxide (CO_2) levels are higher today than they were at any point 800,000 years ago [1]. High concentrations of CO_2 in the atmosphere trap thermal radiation emitted from the earth's surface and prevent these emissions from traveling back into space, which in turn causes temperature on the earth to rise. Globally, approximately 35 billion metric tons of energy-related CO_2 emissions were recorded for the year 2019, and it is projected that there will be 43 billion metric tons of energy-related CO_2 emissions by the year 2050 [2]. If no action is taken to mitigate CO_2 and other greenhouse gas (GHG) emissions, the future on this globe may be one ridden with extreme weather events, massive species extinctions, food deprivation, and many other grave, possibly irreversible consequences [3]. To this end, reducing GHG emissions is one of the most pressing and relevant issues of our time.

The transportation sector was the fourth largest contributor to GHG emissions globally in 2010 [4], and was the biggest contributor to GHG emissions in the U.S. in 2017 [5]. While many efforts to reduce transportation-related emissions are in place, e.g., carpooling, development of sustainable transportation fuels, electric vehicles, public transportation, improving fuel economy, and many more, these methods alone are insufficient to keep up with the projected increase in world population, continued global industrialization, and mankind's wanderlust [6,7]. The pursuit of lighter, more fuel-

efficient, higher-performance vehicles for transportation is ongoing and has attracted the attention of many researchers. In recent years, many studies on magnesium matrix composites indicate that these materials are promising replacements for heavy vehicle components made of Al, Ti, and steels [8, 9]. Making this material switch could save considerable weight in vehicles, thereby reducing emissions, and in turn, potentially play an appreciable role in mitigating global climate change. However, widespread industrial application of magnesium matrix composites is not a reality currently because of an outstanding gap in knowledge which this thesis seeks to address.

Magnesium matrix composites refer to materials which consist of one or more reinforcing phases, typically ceramic- or carbon-based, and usually micron- or nano-sized, dispersed throughout a magnesium matrix. Several studies report improved strength, ductility, and other mechanical properties upon adding small nano-sized volume fractions of carbon nanotubes (CNTs) [10-17], Al_2O_3 [18-24], SiC [25-29], Y_2O_3 [30-35], and numerous other reinforcing phases [36-44] to pure Mg and Mg alloys. Despite so much mechanical characterization of Mg matrix composites, several fail to address the creep response behavior.

In many industrial applications, the maximum operating temperature is commonly limited by the creep resistance of the material [45]. Magnesium is notorious for its low creep resistance (HCP crystal structure). In fact, this is the number one drawback of magnesium which limits its wider industrial application [46]. In order to fully assess the

viability of implementing Mg matrix composites in vehicles at higher-than-room temperatures, expansion of our current understanding of the creep behavior of these materials is required. Therefore, the project undertaken in this thesis examines the creep performance of magnesium with three different volume fractions of CNTs against pure Mg. This assessment is performed via depth-sensing indentation creep tests, a nonconventional method which is to be discussed in greater detail in Chapter II.

1.2. Objectives

The objective of this work is to assess the effect of temperature, strain rate, and dwell time on the rate-dependent plastic response (creep) of Mg-CNT nanocomposites with 0.25, 0.5, and 0.75 vol.% of CNTs through nanoindentation at ambient (298 K) and elevated (373, 473, and 573 K) temperatures.

1.3. Thesis Organization

In this thesis, one research paper on room-temperature nanoindentation and one research paper on high-temperature nanoindentation are included. The first paper is published according to the below citation. The second paper was, or will be submitted for peer review according to the second citation shown below.

(1) Thornby, J., Verma, D., Cochrane, R., Westwood, A., Manakari, V.B., Gupta, M., and Haghshenas, M. “Indentation-based characterization of creep and hardness behavior of magnesium carbon nanotube nanocomposites at room temperature.”

Springer Nature Applied Sciences, vol. 1, June 2019. doi:10.1007/s42452-019-0696-9.

(2) Thornby, J., Harris, A., Bird, A., Beake, B., Manakari, V.B., Gupta, M., Haghshenas, M. (2020) Investigation of Creep and Hardness Behavior of Mg-CNT Nanocomposites from 25 to 300°C through Nanoindentation. Manuscript in preparation.

This thesis is organized into a total of five chapters. Below is the breakdown:

- **Chapter I** delivers a brief summary of the motivations and objectives of the project, and the thesis layout.
- **Chapter II** gives up-to-date background information on magnesium, carbon nanotubes, nanocomposites, creep, and indentation testing in the form of a literature review. A project outlook is at the end of the chapter, to review project goals, project novelty, and significant contributions of the thesis to the scientific community.
- **Chapter III** provides the experimental procedure necessary if this project were to be repeated.
- **Chapter IV** presents the results and discussion for both the room-temperature and the elevated-temperature tests conducted in the project.
- **Chapter V** summarizes all findings from the project, drawing all project conclusions. Future directions of the work and recommendations are also stated.

REFERENCES

CHAPTER I – INTRODUCTION

[1] Lüthi, D., et al. "High-Resolution Carbon Dioxide Concentration Record 650,000–800,000 Years before Present." *Nature*, vol. 453, no. 7193, May 2008, pp. 379–82. doi:10.1038/nature06949.

[2] International Energy Outlook 2019 with projections to 2050; September 2019.

[3] Heim Jr., R.R. "An Overview of Weather and Climate Extremes – Products and Trends." *Weather and Climate Extremes*, vol. 10, Dec. 2015, pp. 1-9. doi:10.1016/j.wace.2015.11.001.

[4] "Global Greenhouse Gas Emissions Data." *EPA*, Environmental Protection Agency, 13 September 2019, www.epa.gov/ghgemissions/global-greenhouse-gas-emissions-data#Sector. Accessed 19 February 2020.

[5] "Carbon Pollution from Transportation." *EPA*, Environmental Protection Agency, 10 June 2019, www.epa.gov/transportation-air-pollution-and-climate-change/carbon-pollution-transportation. Accessed 19 February 2020.

[6] Kay, A., Noland, R.B., Rodier, C.J. "Achieving reductions in greenhouse gases in the US road transportation sector." *Energy Policy*, vol. 69, June 2014, pp. 536-545. doi:10.1016/j.enpol.2014.02.012.

[7] Zhao, X., Ke, Y., Zuo, J., Xiong, W., and Wu, P. "Evaluation of sustainable transport research in 2000-2019." *Journal of Cleaner Production*, vol. 256, May 2020. doi:10.1016/j.jclepro.2020.120404.

[8] Gupta, M., and Wong, W.L.E. "Magnesium-Based Nanocomposites: Lightweight Materials of the Future." *Materials Characterization*, vol. 105, July 2015, pp. 30-46. doi:10.1016/j.matchar.2015.04.015.

[9] Gupta, M., and Sharon, N.M.L. *Magnesium, Magnesium Alloys, and Magnesium Composites*. Jon Wiley & Sons, Inc., 2010, pp. 5-11. doi:10.1002/9780470905098.fmatter.

[10] Liang, J., Li, H., Qi, L., Tian, W., Li, X., Chao, X., and Wei, J. "Fabrication and mechanical properties of CNTs/Mg composites prepared by combining friction stir processing and ultrasonic assisted extrusion." *Journal of Alloys and Compounds*, vol. 728, December 2017, pp. 282-288.

[11] Paramsothy, M., Tan, X.H., Chan, J., Kwok, R., and Gupta, M. "Carbon nanotube addition to concentrated magnesium alloy AZ81: Enhanced ductility with occasional significant increase in strength." *Materials & Design*, vol. 45, March 2013, pp. 15-23.

[12] Zhou, X., Su, D., Wu, C., and Liu, L. "Tensile mechanical properties and strengthening mechanism of hybrid carbon nanotube and silicon carbide nanoparticle-reinforced magnesium alloy composites." *Journal of Nanomaterials*, vol. 2012, August 2012, pp. 1-7. doi:10.1155/2012/851862.

[13] Paramsothy, M., Hassan, S.F., Srikanth, N., and Gupta, M. "Simultaneous enhancement of tensile/compressive strength and ductility of magnesium alloy AZ31 using carbon nanotubes." *Journal of Nanoscience and Technology*, vol. 10, no. 2, February 2010, pp. 956-964.

[14] Goh, C.S., Wei, J., Lee, L.C., Gupta, M. "Ductility improvement and fatigue studies in Mg-CNT nanocomposites" *Composites Science and Technology*, vol. 68, no. 6, May 2008, pp. 1432-1439. doi:10.1016/j.compscitech.2007.10.057.

[15] Shimizu, Y., et al., "Multi-walled carbon nanotube-reinforced magnesium alloy composites." *Scripta Materialia*, vol. 58, no. 4, February 2008, pp. 267-270. doi:10.1016/j.scriptamat.2007.10.014

[16] Goh, C.S., Wei, J., Lee, L.C., Gupta, M. "Simultaneous enhancement in strength and ductility by reinforcing magnesium with carbon nanotubes." *Materials Science and Engineering A*, vol. 423, May 2006, pp. 153-156. doi:10.1016/j.msea.2005.10.071

[17] Goh, C.S., Wei, J., Lee, L.C., Gupta, M. "Development of novel carbon nanotube reinforced magnesium nanocomposites using the powder metallurgy technique." *Nanotechnology*, vol. 17, no. 1, January 2006, pp. 7-12.

[18] Ghasali, E., et al. "Porous and non-porous alumina reinforced magnesium matrix composite through microwave and spark plasma sintering process." *Materials Chemistry and Physics*, vol. 212, June 2018, pp. 252-259.

[19] Li, H., Fan, J., Geng, X., et al. "Alumina powder assisted carbon nanotubes reinforced Mg matrix composites." *Materials & Design*, vol. 60, August 2014, pp. 637-642.

[20] Sankaranarayanan, S., Jayalakshmi, S., Gupta, M. "Effect of ball milling the hybrid reinforcements on the microstructure and mechanical properties of Mg-(Ti + *n*-Al_2O_3) composites." *Journal of Alloys and Compounds*, vol. 509, no. 26, June 2011, pp. 7229-7237. doi:10.1016/j.jallcom.2011.04.083

[21] Jayaramanavar, P, Paramsothy, M., Balaji, A., Gupta, M. "Tailoring the tensile/compressive response of magnesium alloy ZK60A using Al2O3 nanoparticles." *Journal of Materials Science*, vol 45, no. 5, February 2010, pp. 1170-1178. doi:10.1007/s10853-009-4059-6

[22] Nguyen, Q.B., and Gupta, M. "Increasing significantly the failure strain and work of fracture of solidification processed AZ31B using nano-Al_2O_3 particulates." *Journal of Alloys and Compounds*, vol. 459, no. 1-2, July 2008, pp. 244-250.

[23] Thakur, S.K., Srivatsan, T.S., Gupta, M. "Synthesis and mechanical behavior of carbon nanotube-magnesium composites hybridized with nanoparticles of alumina." *Materials Science and Engineering A*, vol. 466, no. 1-2, September 2007, pp. 32-37.

[24] Hassan, S.F., and Gupta, M. "Enhancing physical and mechanical properties of Mg using nanosized Al2O3 particulate as reinforcement." *Metallurgical and Materials Transactions A*, vol. 36, no. 8, July 2005, pp. 2253-2258.

[25] Chen, L.Y., Xu, J.Q., Choi, H., Pozuelo, M., Ma, X., Bhowmick, S., et al. "Processing and properties of magnesium containing a dense uniform dispersion of nanoparticles." *Nature*, vol. 528, December 2015, pp. 539-543.

[26] Rzychoń, T., Dybowski, B., Gryc, A., and Dudek, M. "Mechanical properties and microstructure of WE43 magnesium matrix composite reinforced SiC particles." *Archives of Foundry Engineering*, vol. 15, January 2015, pp. 99-102.

[27] Erman, A., Groza, J., Li, X., Choi, H., Cao, G. "Nanoparticle effects in cast Mg-1 wt% SiC nanocomposites." *Materials Science and Engineering A*, vol. 558, December 2012, pp. 39-43.

[28] Sun, K., Shi, Q.Y., Sun, Y.J., and Chen, G.Q. "Microstructure and mechanical property of nano-SiCp reinforced high strength Mg bulk composites produced by friction stir processing." *Materials Science and Engineering A*, vol. 547, June 2012, pp. 32-37.

[29] Cao, G., Konishi, H., and Li, X. "Mechanical properties and microstructure of SiC-reinforced Mg-(2,4)Al-1Si nanocomposites fabricated by ultrasonic cavitation based solidification processing." *Materials Science and Engineering A*, vol. 486, no. 1-2, July 2008, pp. 357-362.

[29] Ferkel, H., and Mordike, B.L. "Magnesium strengthened by SiC nanoparticles." *Materials Science and Engineering A*, vol. 298, no. 1-2, January 2001, pp. 193-199.

[30] Mallick, A., Tun, K.S., and Gupta, M. "Deformation behavior of Mg/Y_2O_3 nanocomposite at elevated temperatures." *Materials Science and Engineering A*, vol. 551, August 2012, pp. 222-230.

[31] Tun, K.S., and Gupta, M. "Compressive deformation behavior of Mg and Mg/(Y_2O_3 + Ni) nanocomposites." *Materials Science and Engineering A*, vol. 527, August 2010, pp. 5550-5556.

[32] Tun, K.S., and Gupta, M. "Improving mechanical properties of magnesium using nano-yttria reinforcement and microwave assisted powder metallurgy method." *Composites Science and Technology*, vol. 67, no. 13, October 2007, pp. 2657-2664.

[33] Goh, C.S., Wei, J., Lee, L.C., and Gupta, M. "Properties and deformation behavior of Mg-Y_2O_3 nanocomposites." *Acta Materialia*, vol. 55, no. 15, September 2007, pp. 5115-5121.

[34] Hassan, S.F., and Gupta, M. "Development of nano-Y_2O_3 containing magnesium nanocomposites using solidification processing." *Journal of Alloys and Compounds*, vol. 429, no. 1-2, February 2007, pp. 176-183.

[35] Han, B.Q., and Dunand, D.C. "Microstructure and mechanical properties of magnesium containing high volume fractions of yttria dispersoids." *Materials Science and Engineering A*, vol. 277, no. 1-2, January 2000, pp. 297-304.

[36] Turan, M.E., et al. "Effects of carbonaceous reinforcements on microstructure and corrosion properties of magnesium matrix composites." *Materials Chemistry and Physics*, vol. 218, October 2018, pp. 182-188.

[37] Kujur, M., et al. "Enhancement of thermal, mechanical, ignition, and damping response of magnesium using nano-ceria particles." *Ceramics International*, vol. 44, no. 13, September 2018, pp. 15035-15043.

[38] Turan, M.E., Sun, Y, and Akgul, Y. "Mechanical, tribological, and corrosion properties of fullerene reinforced magnesium matrix composites fabricated by semi powder metallurgy." *Journal of Alloys and Compounds*, vol. 740, April 2018, pp. 1149-1158.

[39] Gobara, M., Shamekh, M., and Akid, R. "Improving the corrosion resistance of AZ91D magnesium alloy through reinforcement with titanium carbides and borides." *Journal of Magnesium and Alloys*, vol. 3, no. 2, June 2015, pp. 112-120.

[40] Sankaranarayanan, S., Sabat, R.K., Jayalakshmi, S., Suwas, S., and Gupta, M. "Microstructural evolution and mechanical properties of Mg composites containing nano-B_4C hybridized micro-Ti particulates." *Materials Chemistry and Physics*, vol. 143, no. 3, February 2014, pp. 1178-1190.

[41] Sankaranarayanan, S., et al. "Nano-ZnO particle addition to monolithic magnesium for enhanced tensile and compressive response." *Journal of Alloys and Compounds*, vol. 615, December 2014, pp. 211-219.

[42] Cao, G., Choi, H., Oportus, J., Konishi, H, and Li, X. "Study on tensile properties and microstructure of cast AZ91/AlN nanocomposites." *Materials Science and Engineering A*, vol. 494, no. 1-2, pp. 127-131.

[43] Hassan, S.F., and Gupta, M. "Effect of nano-ZrO_2 particulates reinforcement on microstructure and mechanical behavior of solidification processed elemental Mg." *Journal of Composite Materials*, vol. 41, no. 21, November 2007, pp. 2533-2543.

[44] Wong, W.L.E., and Gupta, M. "Development of Mg/Cu nanocomposites using microwave assisted rapid sintering." *Composites Science and Technology*, vol. 67, no. 7-8, June 2007, pp. 1541-1552.

[45] Larsson, J. *Evaluation of current methods for creep analysis and impression creep testing of power plant steels.* 2012. KTH Royal Institute of Technology, Master's Thesis. *DiVa Portal*, diva2:605630.

[46] Mo, N., et al. "Current development of creep-resistant magnesium cast alloys: A review." *Materials & Design*, vol. 155, October 2018, pp. 422-442.

CHAPTER II
LITERATURE REVIEW

2.1. Introduction to Magnesium

2.1.1. Selected Properties of Magnesium

Magnesium (Mg) is the lightest structural metal. Mg has a density of 1.74 g/cm^3, which is roughly two-thirds that of aluminum (Al), nearly half that of titanium (Ti), and one-fourth that of steel [1-4]. The potential weight savings from using Mg in place of heavy metallic materials like Al, Ti, and steels, especially in weight-critical components, are considerable. This makes Mg a tempting material to use in automotive and aerospace applications, however pure Mg alone cannot be used in service applications due to some noteworthy and unavoidable challenges. The advantages and challenges of pure Mg are summarized in Table 2.1.

The selected properties categorized as advantages or challenges in Table 2.1 give rise to certain applications for magnesium. This is a topic that is discussed more thoroughly in the next section. Nonetheless, it is worth highlighting that magnesium's lightness, high specific properties, and good machinability are the features that draw the automotive industry toward using Mg in broader applications. For now, it is crucial to recognize that pure, unreinforced magnesium cannot be used in wider automotive (and other industrial) applications because of the challenges of Mg listed in Table 2.1.

Specifically, an issue with magnesium which fundamentally impedes its wider application in the automotive sector is how the metal loses strength at elevated

temperatures. Magnesium is not unique in this regard as many metals also experience poorer mechanical and thermal properties at elevated temperatures. However, many automotive applications (e.g., crucial powertrain components such as automatic transmission casings, engine blocks, and engine pistons) require creep resistance at and above 125°C [23].

Table 2.1. Advantages and challenges of pure magnesium.

Advantages	**Challenges**
The lowest density of all the structural metals [1-5]	Low creep resistance. This is due to magnesium's HCP lattice (brittle) [13-15]
Most easily machined metal of all the structural metals, e.g., good castability [5]	Poor corrosion resistance due to its position on the EMF series at -2.36 V [16-17]
Biocompatible and biodegradable [6]	Poor formability and ductility at room temperature because of magnesium's HCP lattice structure [18]
Eighth most abundant element in the earth's crust and the third most abundant element dissolved in seawater [7]	Low strength. Elastic modulus of Mg is only 45 GPa [19]
High damping capacity [8]	Relatively expensive unit price (1.41 USD/lb Mg at a basis date of 2020*) mostly due to energy-intensive extraction processes [20]
Excellent electromagnetic shielding [9]	Flammable and fairly easy to ignite [21]
High specific mechanical properties, i.e., stiffness, strength [10]	Some alloys and composites are not easily recyclable [22]
Fair thermal conductivity and specific heat capacity appropriate for the high thermal performance required for higher speeds and good heat dissipation in consumer electronics [11-12]	

* Please see Appendix A for intermediate results supporting this trend price.

2.1.2. Magnesium Alloys

Traditional approaches to improve pure magnesium's high-temperature performance are to alloy magnesium or perform thermomechanical treatments on magnesium [24]. Several different elements have been alloyed with magnesium, so a standard four-part ASTM system is in place to keep the alloys organized [25]. The ASTM nomenclature for magnesium alloys can be further investigated in Reference 25 for the curious reader.

There are many alloying options available for magnesium and it is possible to tailor the properties of magnesium for specific applications using these alloying agents and combinations of these alloying agents. For this project, creep resistance is of particular interest, especially at high temperatures. Several alloys have been tailored to be creep resilient at higher operating temperatures, like the temperatures in automobile engines. To name a few, some commercial Mg alloys developed for high-temperature applications include AZ91D, ZE41, and WE43. There are also some Mg alloys developed in R&D for high-temperature use in automobile powertrains. Some of these Mg alloys include MRI 230D, MRI 153M, MRI 201S, and MRI 202S.

There is a wide array of magnesium alloys available when it comes to material selection for high-temperature performance. It is a challenge for alloy developers to find the optimum amounts of each alloying element to meet service requirements and affordability. The most promising alloying ingredients for high-temperature Mg alloys which are creep-resistant are: Al, Ca, Sr, and rare earth (RE). Each alloying additive has

its advantages and disadvantages. Table 2.2 summarizes these advantages and disadvantages.

Tailoring a magnesium alloy for high-temperature performance is a tradeoff among many factors. However, in principle, creep resistance, cost, and castability are to be considered more heavily for high-temperature applications. It is easy to see that much work has already been done in the area of crafting these alloys. Mo et al. [27] report a visual summary of how Mg-Al alloys compare to Al-alloys in terms of creep strength. As seen in Figure 2.1, it is possible to design a magnesium alloy with equivalent, or greater creep strength than aluminum alloys, at least at 175°C.

Table 2.2. Advantages and disadvantages of four major alloying agents for improving magnesium alloy performance at high temperatures [26].

Mg Alloy Additive	Advantages	Disadvantages
Aluminum (Al)	• Castability and corrosion resistance increases • Ambient tensile, compressive, and fatigue strength improves • Alloying with Al negligibly affects alloy cost	• Creep properties, ductility, and impact strength decrease • Does not significantly contribute to creep resistance improvement
Calcium (Ca)	• The maximum increase in ambient tensile and compressive strength • Relatively inexpensive • The atomic weight of Ca is less than half that of Sr and is less than a third of those of REs. (Best increase in properties per dollar compared to Sr and REs)	• Lowers castability, ductility, and impact strength
Strontium (Sr)	• Improves creep strength • Improves ambient strength	• Increases alloy cost • Lowers castability, ductility, and impact strength
Rare earth (RE)	• Significant improvement in creep properties • The moderate increase in ambient strength	• Increases alloy cost • Lowers castability, ductility, and impact strength

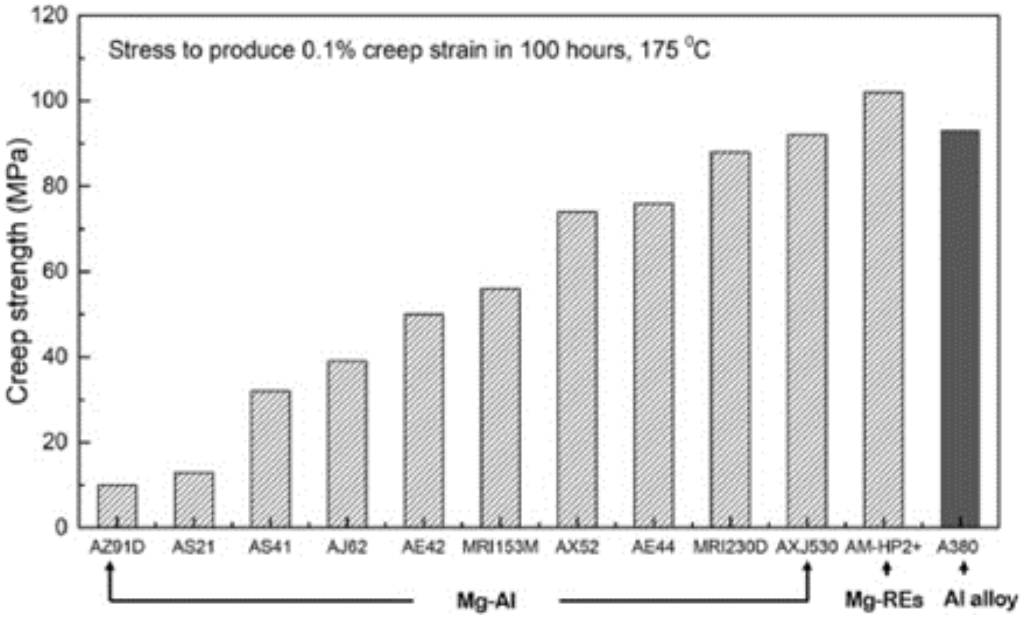

Figure 2.1. Creep strength of commercial Mg die-cast alloys to produce 0.1% creep strain in 100 hrs, at 175°C [27]. Note that AXJ530 has similar creep strength to A380 (an aluminum alloy) and Mg-RE alloy AM-HP2+ has surpassed the creep strength of A380.

Although Mg alloys have come a long way to meet and surpass aluminum alloys in creep resistance just below 200°C (a relatively low temperature), these Mg alloys still have room for improvement at higher temperatures, especially if they are to be used in critical components (e.g., engines) in automotive and aerospace sectors. The issue is that alloying can only do so much, and Mo et al. [27] and Nie et al. [28] report that alloying has reached a limit in terms of contributing toward Mg property enhancement.

The modern way to overcome the temperature barrier of magnesium is to use nano-reinforcements, i.e., explore metal matrix composites (MMCs), namely, magnesium matrix composites. Gupta et al. [29] spearheaded the exploration into the world of magnesium

nanocomposites, and they report that magnesium-based nanocomposites are the lightweight materials of the future. Applications of magnesium, its alloys, and its composites are discussed in the next section.

2.2. Applications of Mg, Mg Alloys, and Mg Composites

2.2.1. Automotive Industry

In recent times, saving weight in vehicles is critical to reduce emissions, improve fuel economy, and meet legislative pressures. Incorporating magnesium into vehicle components can drastically save weight since magnesium is the lightest structural metal. An MIT study [30] estimates that for every 100 kg reduction in vehicle weight, cars can save 0.4 L fuel/ 100 km traveled and light trucks (weighing 1000- 3800 kg) can save 0.5 L fuel/ 100 km traveled. Currently, magnesium still only represents a measly 0.3% of the total weight in a typical 3,360 lb (1520 kg) vehicle [31]. There is room for improvement for Mg to be better represented in everyday consumer vehicles.

Magnesium is most commonly incorporated into the following parts of an automobile: instrument panel beams, transfer cases, manual transmission cases, valve/cam covers, steering components, and various housings and brackets [23]. Magnesium automobile components are considerably lighter than those normally made of aluminum, titanium, or stainless steel. Examples of automobile parts made of magnesium that have been incorporated into commercial vehicles are shown in Figure 2.2.

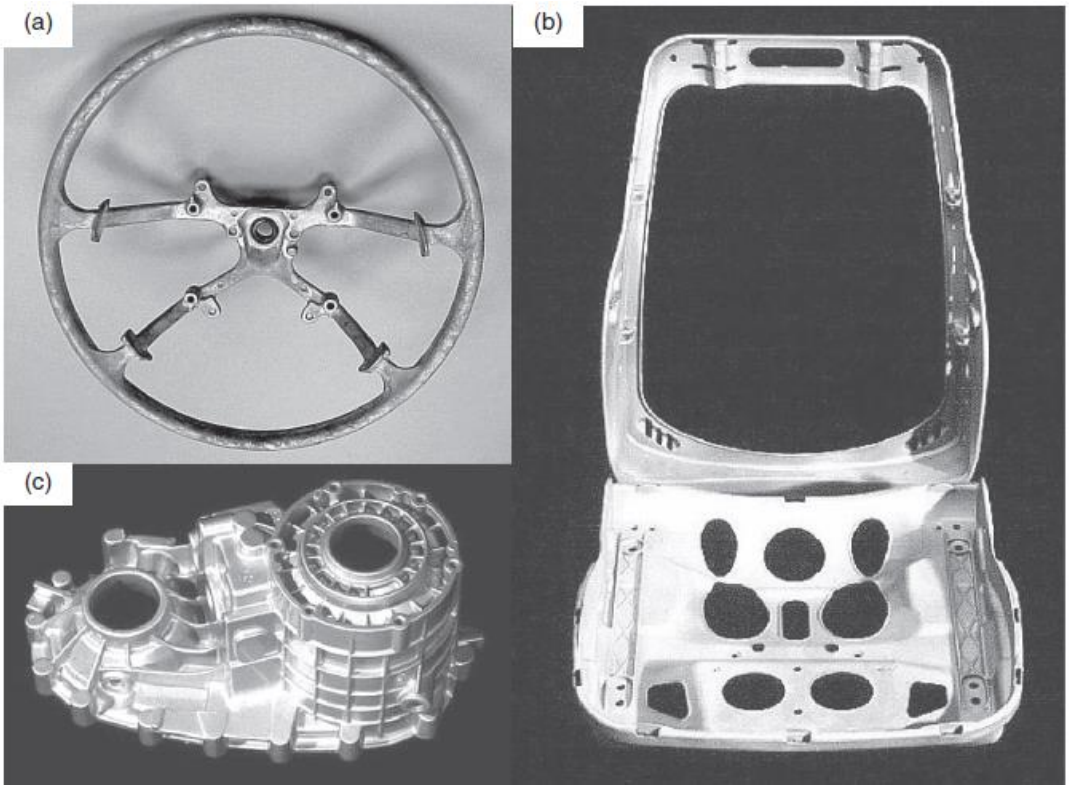

Figure 2.2. Examples of commercial vehicle parts which have incorporated magnesium into their design: **(a)** magnesium steering wheel core for Toyota Camry weighing 0.75 kg, **(b)** seat support for Jaguar and Fiat models weighing 2.6 kg, **(c)** rear transfer case made from Mg alloy AZ91D weighing 2.7 kg [32].

Note that most automobile applications with magnesium are not directly in automobile engines. Automobile engine components are exposed to higher thermal and physical stresses than a majority of the other components in the vehicle. Most major powertrain components operate at temperatures above 125°C, which is a temperature where most commercial magnesium alloys suffer from poor creep resistance. This is why most magnesium alloys are inadequate for powertrain applications. Automatic transmission cases can operate at up to 175°C, engine blocks up to 200°C and engine

pistons up to 300°C [23]. Most powertrain components are currently made of aluminum or cast iron. Magnesium can drastically lighten automobile engines, but a certain required amount of creep resistance must be met first.

2.2.2. Aerospace Industry

Weight reduction is also critical in the aerospace industry. Small weight reductions in aircraft translate to large savings in overall operational costs. The lightness of magnesium draws aircraft manufacturers to the metal and Mg has been successfully incorporated into both civil and military aircraft throughout history.

A few examples of magnesium's application in aircraft include thrust reversers (Boeing 737, 747, 757, 767), gearboxes (Rolls-Royce), engines, and helicopter transmission casings [32]. These aircraft were from an era when there was not a limit on how much magnesium could be used in aircraft interiors. However, until recently there are new restrictions set and enforced by the Society of Automotive Engineers (SAE) and the Federal Aviation Administration (FAA) regarding how much magnesium can be in aircraft interiors as of 2015 [33]. As weight restrictions tighten and the cost of aviation fuel rises, a push to update current commercial aircraft is necessary and each pound of aircraft weight is crucial. On a basis date of 2006, it is estimated that 3, 300, 3,000, and 30,000 USD are the respective values of money saved per pound in automobile, commercial/transport, fighter, and space aerospace segments [34].

2.2.3. Biomedical Applications

On account of magnesium's biocompatibility and biodegradability, Mg is suitable for several uses in the biomedical field. One notable example is using magnesium in biodegradable implants for surgeries. Biodegradable implants have a huge advantage over "bio-inert" implants because biodegradable implants will corrode *in vivo* (they dissolve in the patient completely upon fulfilling their medical healing purpose), whereas bio-inert implants may require a secondary operation to remove from a patient, which is undesirable as it increases the risk for infection and complications, not to mention more recovery time and medical costs [35].

Further, magnesium occurs naturally in the human body and the metal has an elastic modulus and compressive yield strength more comparable to that of natural bone than of any other commonly used metallic implant material [36]. All of these promising properties of magnesium make the metal of special attraction. Lee et al. [37] performed a long-term clinical study to investigate the biodegradability of Mg implants in humans with a distal radius fracture. Figure 2.3 illustrates how the Mg implant dissolved over 1 year, so the patient did not need any secondary surgery or any complications that may have come from this.

Figure 2.3. X-ray images in Lee et al. study [37] of: **(i)** distal radius fracture and the scaphoid nonunion before surgical intervention, **(ii)** implantation site image taken immediately after the surgical procedures to fix the distal radius fracture, **(iii)** 6-month follow-up X-ray, and **(iv)** complete degradation and bone healing after 1-year post-operation. The red arrow shows distal radius fracture, white arrow points at the scaphoid nonunion, and the yellow arrow indicates the Mg alloy implant.

Magnesium is a promising implant material, and studies are being conducted currently with different Mg alloying elements to tailor the in the vivo corrosion rate of Mg implants to ensure sufficient healing time is provided for patients [32].

2.2.4. Other Noteworthy Applications

2.2.4.1. Military

Jet bombers, spacecraft, military armor (both for soldiers and vehicles), and even a few intercontinental ballistic missiles (namely, Titan, Agena, and Atlas) reaped in weight reduction benefits from magnesium [32,38-44].

2.2.4.2. Nuclear

Contrary to popular belief, initial research on creep properties of Mg were not driven by the automotive industry, but instead stemmed from its use in nuclear canning applications [45-47]. Magnesium has certain advantages over competing materials which make Mg ideal for some nuclear reactors. Magnesium has: (a) a low tendency to absorb neutrons, (b) it does not alloy with uranium, and (c) adequate CO_2 resistance up to most of the highest service temperatures envisioned, and (d) fair thermal conductivity [48].

2.2.4.3. Consumer Electronics

Many consumer electronics require small and highly intricate components (e.g., housings for cameras, cell phones, laptops, and other portable media devices), a requirement which Mg satisfies. Magnesium also has advantages over certain plastics, aluminum, and zinc in this particular field. When it comes to weight, magnesium, and plastic are nearly a tie. However, magnesium outperforms plastics when it comes to strength, heat transfer, and the ability to shield electromagnetic interference and radio frequency interference [32]. Over aluminum, magnesium has much better die filling behavior and is lighter. Zinc alloys have superior die casting compared to magnesium, but zinc is usually too heavy for most consumer electronics components [12].

2.2.4.4. Sports Equipment

Magnesium's ability to be formed into intricate pieces is a property that the sports equipment industry has also noted. Magnesium alloys and composites are perfect for creating sports equipment with high strength which is not overly heavy. Magnesium can

be incorporated into bicycle frames, archery bow handles, tennis racquets, golf club heads, skates, fishing reels, and many others [32].

2.3. Metal Matrix Composites (MMCs)

2.3.1. What is a Metal Matrix Composite?

The concept of reinforcing homogeneous materials with supportive phases to make composites with better properties is not a new one. Egyptian mudbricks incorporated straw and sometimes animal droppings into the bricks for enhanced strength over four thousand years ago. Modern examples include steel-reinforced concrete, nylon and rayon cord-reinforced tires, and fiberglass-reinforced plastics. Composite structures are a part of everyday life and in recent years, considerable progress has been made in the area of metal matrix composites, a special kind of composite.

A metal matrix composite (MMC) is a blend of at least two constituents. One constituent must be metal, and this metal is considered to be the matrix material. The other constituents may be one or more reinforcement phases that are dispersed throughout this matrix, typically in relatively small volume or weight percentages. Reinforcement phases can take on many morphologies (e.g., whiskers, particles, fibers) and compositions (e.g., ceramic, carbonaceous, organic).

It is worth reinforcing that MMCs are distinctly different than alloys. A large difference lies in the strengthening mechanisms of the materials, a topic that is explored deeper in Section 2.3.4. For now, keep in mind that dispersion hardening and precipitation strengthening are two separate mechanisms. One mode of strengthening that occurs in an

MMC is load transfer, i.e., when reinforcements are the primary load-bearing components. Reinforcement particles remain stable and strong at high temperatures, unlike reinforcement phases in an alloy which might dissolve at higher temperatures. In alloys, there are small, hard phases in the material which restrict, or impede the motion of dislocations, and this is called dispersion strengthening. Now that this strengthening mechanism distinction is made, a deeper connection can be made with the reinforcement phases discussed in the next section of this chapter.

2.3.2. Types of Reinforcements

Many reinforcement phases are available to strengthen metal matrices. For example, common reinforcement phases to Mg include ceramics (e.g., borides, nitrides, carbides, oxides) and carbonaceous reinforcements (e.g., carbon nanotubes, fullerenes, graphene nanoplatelets) This section discusses carbon nanotubes (CNTs), the reinforcement added to Mg in this study.

2.3.2.1. Carbon Nanotubes (CNTs)

Carbon nanotubes were discovered in 1991 by Iijima [49] and ever since their discovery, CNTs have beguiled scientists on account of their excellent electrical, mechanical, and thermal properties. As the name suggests, a carbon nanotube is simply a rolled-up sheet of graphene in the form of a cylinder which is one carbon atom thick. The CNT is a member of the fullerene family, and CNTs can be single-walled (SWCNTs) or multi-walled (MWCNTs). Figure 2.4 illustrates the difference between a SWCNT and a MWCNT.

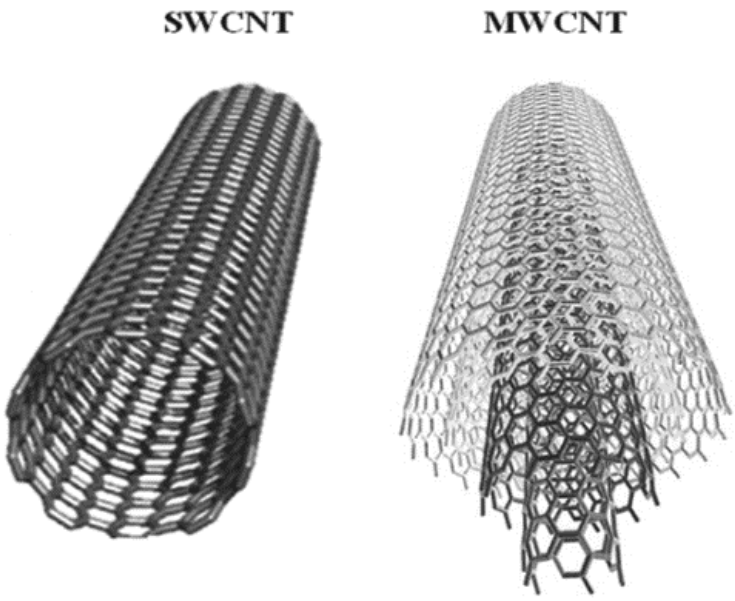

Figure 2.4. A single-walled carbon nanotube (SWCNT) is pictured on the left. A multi-walled carbon nanotube (MWCNT) is pictured on the right. Image credit goes to Choudhary et al. [50].

Typical diameters of SWCNTs and MWCNTs range from 0.4 to 10 nm and from 4 to 100 nm, respectively, and their lengths tend to reach micrometer range, but some CNTs on the order of centimeters have been synthesized [51]. In terms of mechanical properties, CNTs are the strongest and stiffest materials discovered in terms of tensile strength and elastic modulus, respectively. It is worth noting that diamond nanothreads (DNTs) may be giving CNTs a run for their money in terms of stiffness and elastic modulus [52], but DNTs are not fully characterized and to the best of the author's knowledge have not been used as reinforcements in MMCs, yet. A few of the most remarkable properties of CNTs are tabulated in Table 2.3.

Table 2.3. Summary of some remarkable properties of carbon nanotubes.

Property	**Measured Value**
Elastic Modulus (E)	**270 – 950 GPa** [53]
Tensile Strength	**11-63 GPa.** This is roughly 100 times greater than that of steel [69]. Pitroda et al. report **150 GPa** for SWCNTs and MWCNTs [51]
Electrical Conductivity	It can reach as high as **10^6-10^7 S/m** for pure CNTs (similar to copper!) [54] but in practice are usually around **10^4-10^5 S/m** [55-56].
Thermal Conductivity (k)	**3000 W*m^{-1}*K^{-1}** for a MWCNT of 14 nm diameter [57]
Aspect Ratio (ratio of length to diameter)	Varies from tube-to-tube. Typical aspect ratios are around **10,000** (this is for the case of a SWCNT 10 μm in length and 1 nm in diameter. However, it is possible to achieve aspect ratios >100,000,000 when SWCNTs reach cm-lengths [58].
Surface Area	**1315 m^2/g** for SWCNTs, and progressively less for MWCNTs (e.g., **680-850 m^2/g** for 2WCNTs, **295-430 m^2/g** for 5WCNTs, etc.) [59].

Several characterization studies [60-75] have been conducted on MMCs with CNTs in attempt to better understand how the composite properties compare to those of the individual constituents of the MMCs. Typically, CNTs enhance the mechanical properties of the composite material. However, caution should be taken to not overload the matrix with too many CNTs or else the CNTs can agglomerate due to strong van der Waals forces, resulting in weakened mechanical properties. Tailoring CNT-composites is almost always an optimization problem, and many characterization studies are helping to identify which properties are enhanced or reduced upon the addition of CNTs.

For example, Selvamani et al. [60] studied the mechanical, tribological, and metallurgical behavior of magnesium alloy AZ91D reinforced with 2, 3, and 4 wt.% CNTs. The nanocomposites were fabricated through the stir casting method. Composites with 4 wt.% CNTs showed the best hardness, however composites with 3 wt.% CNTs showed better tensile strength, yield strength, and wear resistance. Selvamani et al. conclude that 4 wt.% CNTs did not give the best strength properties or wear resistance because the CNTs agglomerated and had poor particle-matrix interfacial integrity, causing these mechanical properties to decline.

2.3.3. Why "nano" and not "micro" reinforcement particles? Why nanocomposites?

Great emphasis was placed on the volume or weight percent of reinforcement in the prior section when it came to reinforcing metal matrix composites. This section seeks to emphasize how critical the size of reinforcement phases is in MMCs for ideal mechanical property enhancement. El-Saeid Essa et al. [76] notes some common issues which occur with micro-particulate reinforcements, e.g., broken particles, voids at particle-matrix interface, and agglomerations. Some of these issues are illustrated in Figure 2.5.

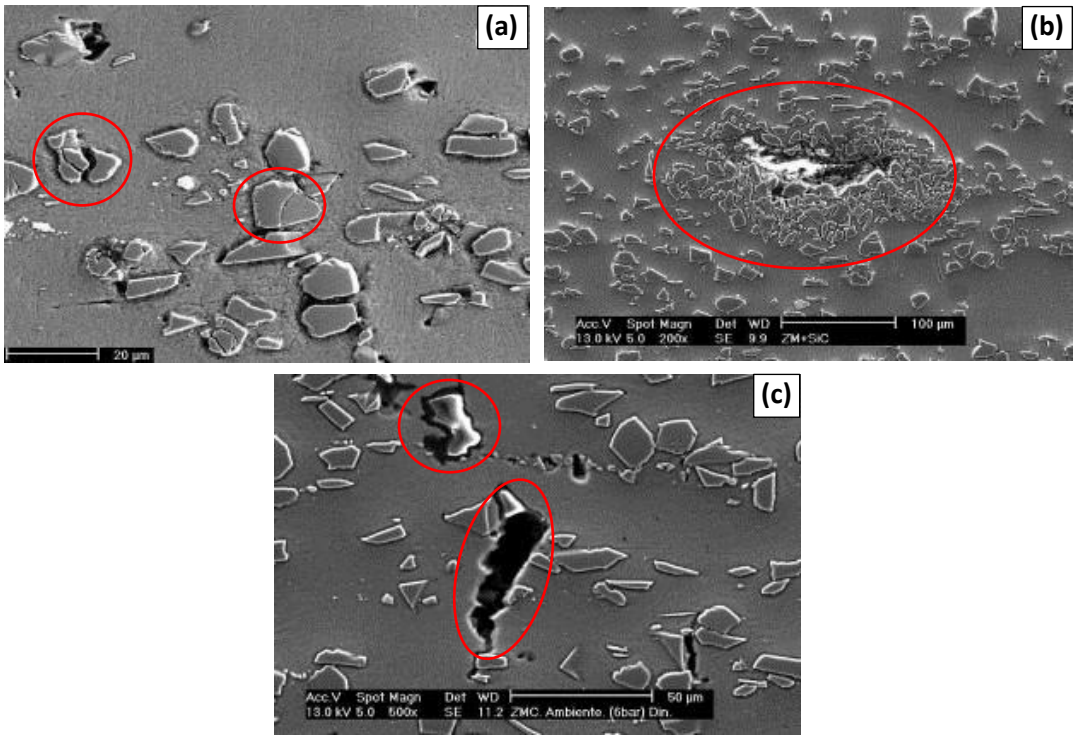

Figure 2.5. Common issues with micro-particulate reinforcements: broken particles (a), particulate aggregations (b), and voids at the particle-matrix interface. All SEM image credit goes to El-Saeid Essa et al. [76].

Micron-sized nanoparticles are known to strengthen the metal matrix. However, ductility is usually reduced in the MMC, and it may be reduced as much as 80% [29, 77]. Nanoparticles have much greater surface area than micron-sized particles do, so they have much more area for particle-matrix interactions to occur. One major advantage of using nanoparticles include gaining matrix strength without this significant reduction in ductility. This is one reason why nanoparticulate reinforcements, namely carbon nanotubes were used in this study. Some strengthening mechanisms for nanoparticles responsible for enhanced material properties are discussed in greater detail in the next section.

2.3.4. Strengthening Mechanisms in Nanocomposites

2.3.4.1. Effective Load Transfer

Metal matrix composites may be strengthened by the load transfer effect. This strengthening occurs when a load placed on an MMC is transferred from the soft matrix to the hard and stiff reinforcement particles, called the load-bearing effect. This kind of strengthening only occurs when the cohesion between the particles and the matrix is strong at the atomic level, i.e., the nanoparticles are directly bonded to the matrix [78]. The improvement factor for load transfer in a MMC can be quantified with Equation 2.1.

$$f_1 = \frac{1}{2}V_p - P \qquad \text{(Equation 2.1)}$$

Where f_1 is an improvement factor associated with the load-bearing effect, P is the volume fraction of porosity in the MMC, and V_p is the volume fraction of nanoparticles added in the metal matrix [79].

2.3.4.2. Hall-Petch Strengthening

Hall-Petch strengthening is another strengthening mechanism that can occur in MMCs as a result of grain refinement. Grain size plays a large role in the strength of composites since grain boundaries can hinder the dislocation movement. This is due to the different orientation of adjacent grains and high lattice disorder of these regions, which prevents the dislocations from moving in a continuous slip plane [80].

The strength contribution attributed to Hall-Petch strengthening is given by Equation 2.2.

$$\Delta\sigma_{Hall-Petch} = \frac{k_y}{\sqrt{d}} \qquad \text{(Equation 2.2)}$$

Where k_y is the strengthening coefficient, which is a characteristic constant for each material, and d is the average grain size (or grain diameter) [81]. Finer grains result in more grain boundaries, and these grain boundaries can act as obstacles to dislocation motion. This means higher stress is needed to cause plastic deformation (higher strength materials have finer grains).

2.3.4.3. Orowan Strengthening

Orowan strengthening (also Orowan bowing) is another mechanism by which metal matrix composites may be strengthened. When closely spaced hard particles are subject to the passing of dislocations, Orowan loops can form. Imagine a dislocation line traveling through the material being sheared by the hard, closely spaced nanoparticles. The dislocation line bows and leaves dislocation rings around the bypassed particle, which greatly strengthens the overall composite. Figure 2.6 illustrates the steps of Orowan loop formation and dislocation ring formation in a Ni-Si alloy.

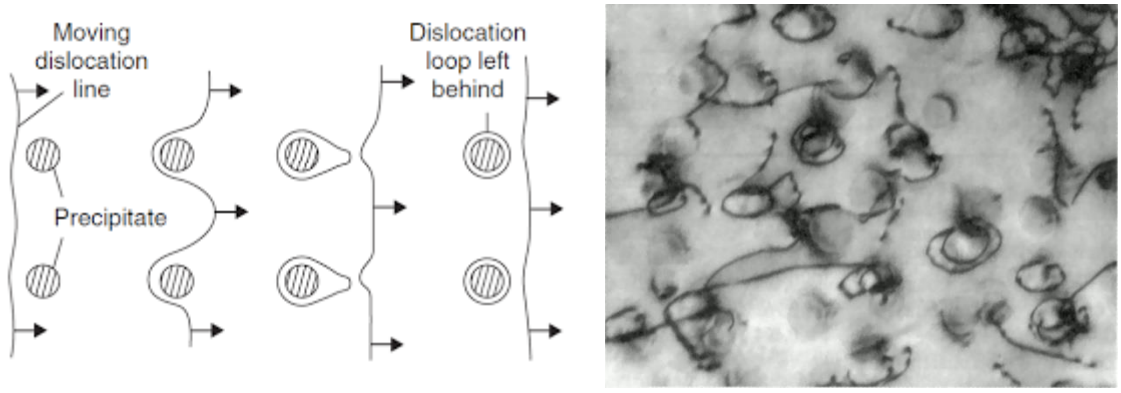

Figure 2.6. Steps taken to form Orowan loops (left) [82] and dislocation rings upon bow-out of Ni_3Si particles in a Ni-Si alloy (right) [83].

An estimate of the improvement factor of strengthening occurring through dislocation bowing, or Orowan looping, is given by Equation 2.3 [79].

$$f_{Orowan} = \frac{0.13 G_m b}{\lambda Y_m} \ln\left(\frac{d_p}{2b}\right) \qquad \text{(Equation 2.2)}$$

Where G_m is the shear modulus, b is the Burgers vector, λ is the interparticle spacing, Y_m is the yield strength of the matrix, and d_p is the particle diameter.

2.3.4.4. Increased Dislocation Density Caused by Thermal Expansion and Elastic Modulus Mismatch

It is common for a metal matrix and the reinforcement phase in a metal matrix composite to have different coefficients of thermal expansion (CTE) and elastic moduli. This difference in CTE and elastic modulus causes geometrically necessary dislocations (GNDs) near the particle-matrix interface to generate during any thermal processing or imposed strain on the material during its fabrication. The formation of GNDs due to CTE

and elastic modulus mismatch are simply the metal matrix composite's way of accommodating thermal and physical strains imposed during the material during processing, and these GNDs strengthen the material. GND density due to CTE mismatch can be estimated by Equation 2.3 [81,84]:

$$\rho^{\mathrm{CTE}} = \frac{\mathrm{A}\Delta\alpha\Delta\mathrm{T}\upsilon_{\mathrm{p}}}{\mathrm{bd_p}\left(1\text{-}\upsilon_{\mathrm{p}}\right)} \qquad \text{(Equation 2.3)}$$

Where A is a geometric constant, $\Delta\alpha$ is the difference in CTE, ΔT is the difference between test processing or heat treatment temperatures, and υ_p is the volume fraction of reinforcement particles. GND density due to elastic modulus (EM) mismatch can be estimated by Equation 2.4 [81,84]. The term ε represents uniform deformation.

$$\rho^{\mathrm{EM}} = \frac{6\upsilon_{\mathrm{p}}}{\pi \mathrm{d}_{\mathrm{p}}^{3}}\varepsilon \qquad \text{(Equation 2.4)}$$

Equations 2.3 and 2.4 can be combined to estimate the combined strengthening due to both CTE and EM mismatch by the Taylor equation [84], presented as Equation 2.5.

$$\Delta\sigma_{\mathrm{CTE+EM}} = \sqrt{3}\beta \mathrm{Gb}\left(\sqrt{\rho^{\mathrm{CTE}}} + \sqrt{\rho^{\mathrm{EM}}}\right) \qquad \text{(Equation 2.5)}$$

The load-transfer effect, Hall-Petch strengthening, Orowan strengthening, and the formation of GNDs are just a few of the strengthening mechanisms to consider when trying to understand the strength of MMCs. The topic is fairly complex and the curious reader interested in mechanisms that influence MMC strength should also investigate those which

influence MMC ductility, as they are related. A few other factors to consider include grain refinement, the activation of non-basal slip systems, texture modification, reduction in size and sharpness of the second phase, and a stress state change from plane strain to plane stress [85].

A limited number of studies actually breakdown the strengthening mechanisms to see how much strengthening is coming from which strengthening mechanism [81]. Casati and Verdani [81] did this for an Al matrix composite reinforced with 2 wt.% Al_2O_3. Figure 2.7 shows which strengthening mechanisms had the greatest strength contribution as a function of alumina particle size. CTE mismatch was the mechanism that contributed the most to this composite's strength for all alumina diameter sizes. Another important observation to see in Fig. 2.7 is that all of the strengthening mechanisms discussed are amplified at lower particle diameters, especially those less than 50 nm. This is a result that again emphasizes the advantage nanoparticles have over micron-sized particles in metal matrices.

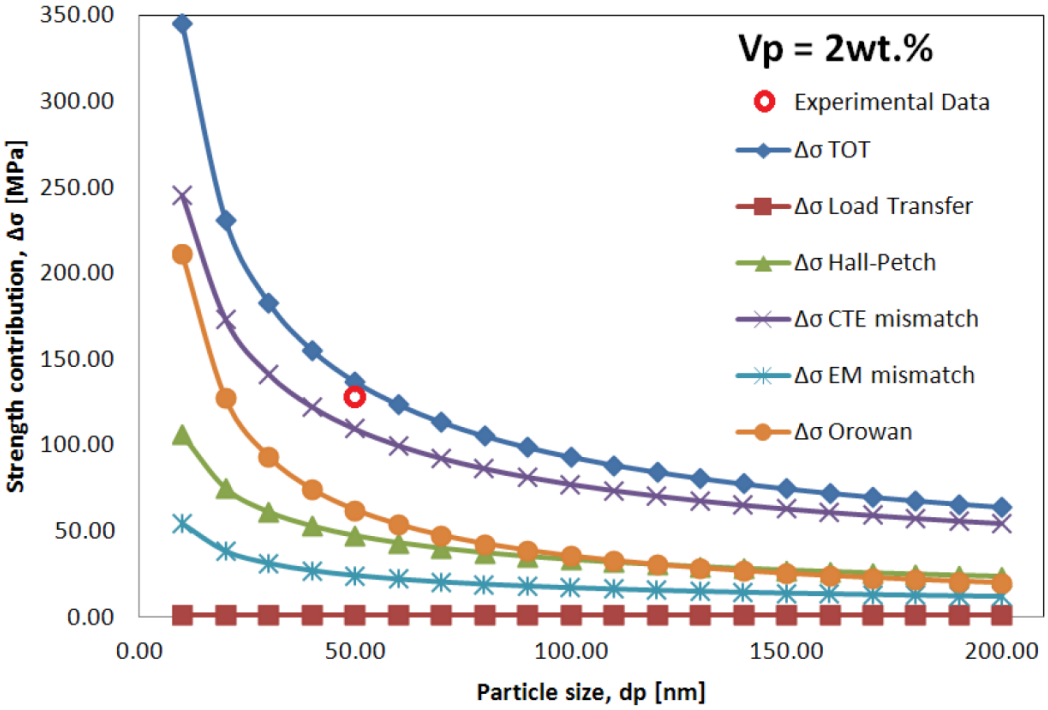

Figure 2.7. Effect of various strengthening contributions and total resulting strengthening increment calculated for an aluminum matrix composite reinforced with 2 wt.% Al_2O_3 [81].

2.4. The Promise of Magnesium-CNT Nanocomposites

Now that the strengthening mechanisms at play in metal matrix composites have been introduced, the role of CNTs in magnesium can be more deeply understood. This section is dedicated to further development of magnesium matrix composites, their material property enhancement with nanoparticles, namely CNTs, understanding what studies have already been done in this area, and why they are a promising material for future industrial applications.

2.4.1. CNTs in Magnesium: What properties have already been improved and why?

Only a few studies [75, 86, 87-89] successfully synthesized and characterized magnesium carbon nanotube nanocomposites. A majority of the studies were conducted at room temperature, and the one study [89] done at a higher temperature (25-500°C) failed to obtain creep behavior of Mg-CNT nanocomposites.

Ding et al. [86] fabricated a Mg-1 vol.% CNT nanocomposite by ball milling, note that the CNTs were nickel-coated. Mechanical testing revealed the yield strength and compressive strength of the nanocomposite to be 454 MPa and 505 MPa, respectively. These values are both over 200% greater than those for pure Mg. The yield strength of the nanocomposite was also much higher than that of pure Mg. Ding et al. attribute these mechanical property enhancements to load transfer, dislocation obstruction, and the fairly uniform dispersion of CNTs throughout the CNT matrix.

Ding et al. also note that MgO was present in their nanocomposite. This was also an observation made in our group's study [75] on Mg-CNT nanocomposites. The formation of MgO is nearly inevitable in any kind of powder metallurgy processing by its nature. Figure 2.8 shows an SEM micrograph of the Mg-1 vol.% CNT nanocomposite and its X-ray powder diffraction (XRD) pattern used in the Ding et al. [86] study. The MgO particles may influence material properties, i.e., hardness and strength, since MgO is a hard reinforcement phase itself. Our group's room temperature study [75] on Mg-CNT nanocomposites is discussed in greater detail in Chapter IV.

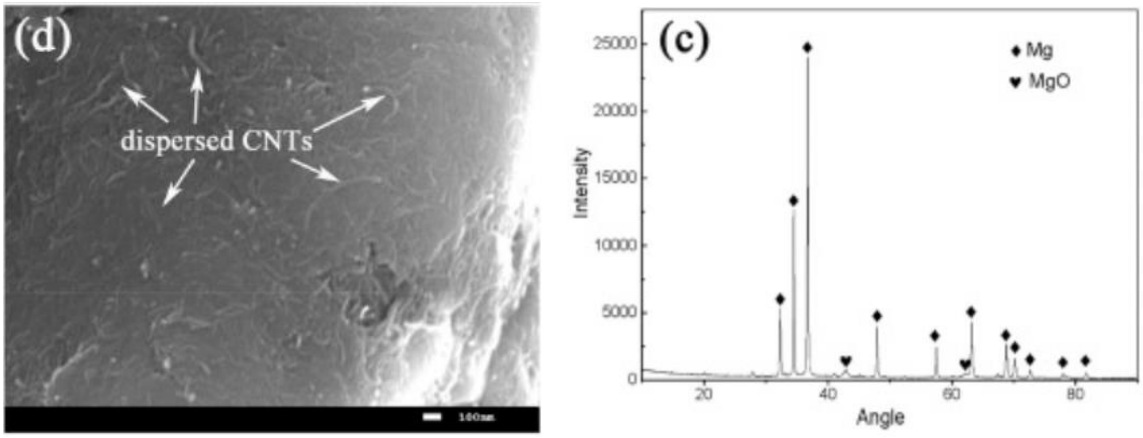

Figure 2.8. SEM image of Mg-1 vol.% CNT (d on left), and XRD pattern of this nanocomposite revealing the presence of MgO in the sample (heart-shaped markers) (c on right) [86].

Goh et al. [87] used disintegrated melt deposition (DMD) to fabricate Mg nanocomposites reinforced with 0.3, 1.3, 1.6, and 2 wt.% CNTs. They report improved yield strength, ultimate tensile strength, and ductility in the nanocomposites until a threshold of 1.3 wt.% CNTs was reached. They attribute these mechanical enhancements in ductility to the potential activation of the cross slip in non-basal planes in Mg by the presence of CNTs. Increases in tensile and ultimate tensile strength are attributed to dislocation generation and CNTs being able to impede dislocation motion.

Figure 2.9 shows the representative stress-strain curves obtained in the Goh et al. [87] study. They report that nanocomposites with volume fractions higher than 1.3 wt.% CNTs showed worsening mechanical properties because CNTs agglomerated (and are a source of porosity in Mg), and thereby caused strength to deteriorate.

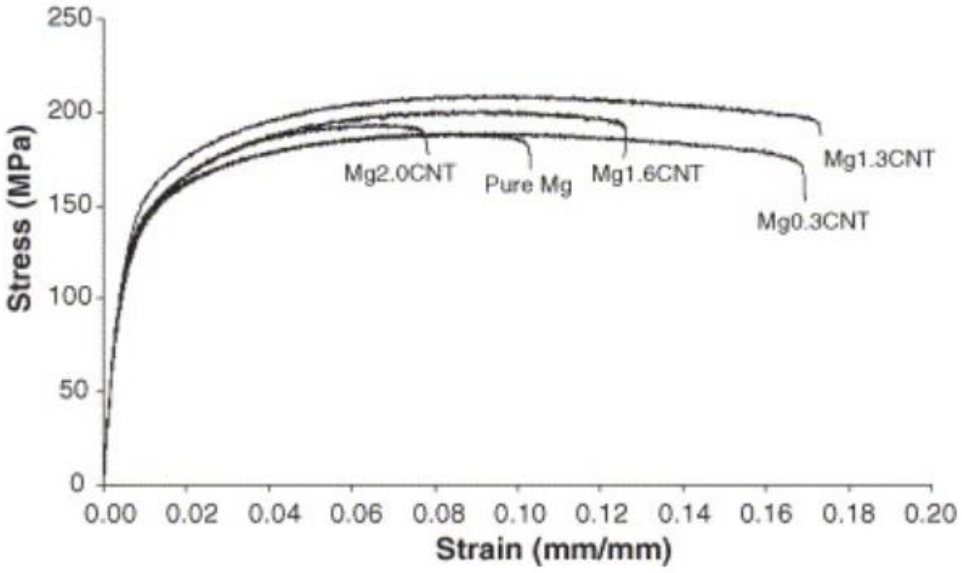

Figure 2.9. Representative stress-strain curves obtained in Goh et al. [87] study. Mg-1.3 wt.% CNT exhibits the best mechanical behavior of all CNT contents tested in Mg.

Goh et al. [88] performed another Mg-CNT nanocomposite study two years after the study [87] mentioned just before this one. In this study, ductility and fatigue studies were performed on only Mg-1.3 wt.% CNT against pure Mg. This study confirmed that prismatic slip and basal system slip are activated with CNTs, which explains why the nanocomposite has improved ductility. Fatigue tests reveal that the nanocomposite also has fewer cycles to failure than pure Mg, attributed to the formation of sessile forest dislocations.

Finally, Iqbal et al. [89] investigated the thermal properties of magnesium nanocomposites reinforced with 0.5 and 1.0 wt.% MWCNTs, fabricated by powder metallurgy by cold pressing followed by sintering. A laser flash method was used to

measure thermal diffusivity, and a NETZSCH DIL-402C method was used for obtaining CTE and heat capacity. Thermal capacity and thermal diffusivity were highest in Mg reinforced with the highest weight percent of MWCNTs, 1 wt.%. The lowest CTE was exhibited in Mg-1 vol.% MWCNT.

Iqbal et al. [89] points out that Mg reinforced with 1 wt.% MWCNTs has the best thermal properties over pure Mg and Mg-0.5 vol.% MWCNT. However, for many current and potential high-temperature applications for magnesium, especially those in the automotive and aerospace industries, creep resistance is a requirement. The room-temperature and high-temperature work conducted in this project aim to close this gap of knowledge in the area of creep response behavior of Mg-CNT nanocomposites.

2.5. What is creep?

Creep is defined as the time-dependent plastic deformation that results when a material is subject to a constant load over a given period of time. Creep can also be thought of as the steady application of a force which results in an invisible, internal structural rearrangement. Creep occurs as a result of long-term exposure to high levels of stress that may be below the yield strength of the material. In general, creep is a complex function of stress, temperature, time, grain size and shape, microstructure, volume fraction and viscosity of glassy phases at the grain boundaries, dislocation mobility, and many other factors [90].

Creep deformation is generally undesirable and is irreversible. Creep failure is often used as a criterion to estimate the expected service life of some structural components [91]. To this end, understanding creep, its mechanisms, and how to measure this deformation is critical for accurate material assessment.

2.5.1. Dislocation Creep – Glide (Slip) and Climb

Dislocation creep is a mechanism of creep that can be conceptualized as a group of atoms moving from regions of compression or tension occurring by the coordinated movement of "blocks" of material via gliding or climbing, giving rise to the concepts of dislocation glide and dislocation climb. Vacancies in a material assist dislocation motion, helping them to overcome obstacles on a material's slip planes. For a dislocation line to climb, the combined effect of a group of vacancies is required. It is worth noting that at elevated temperatures, the probability of dislocation climb is higher because of the high equilibrium vacancy concentration [92]. The climbing movement of dislocations can be thought of as a non-conservative movement away from the slip plane.

Dislocation glide (or slip) is different than climb because the dislocations are now moving by applied shear stress on a slip plane. This movement of dislocations can be thought of as a conservative movement within the slip plane.

2.5.2. Diffusional Creep Mechanisms – Nabarro-Herring Creep and Coble Creep

Diffusional creep mechanisms play larger roles at higher temperatures in materials. Creep tends to occur by the transport of atoms by diffusion as opposed to the motion of dislocations at elevated temperatures. Whether the atomic diffusion is occurring along the grain boundaries or through the bulk material will determine if the mechanism is considered Nabarro-Herring or Coble creep.

Nabarro-Herring creep is the transport of atoms through the bulk (or volume diffusion), whereas Coble creep is the transport of atoms along grain boundaries. A simple schematic illustrating the difference between the two mechanisms is shown in Figure 2.10.

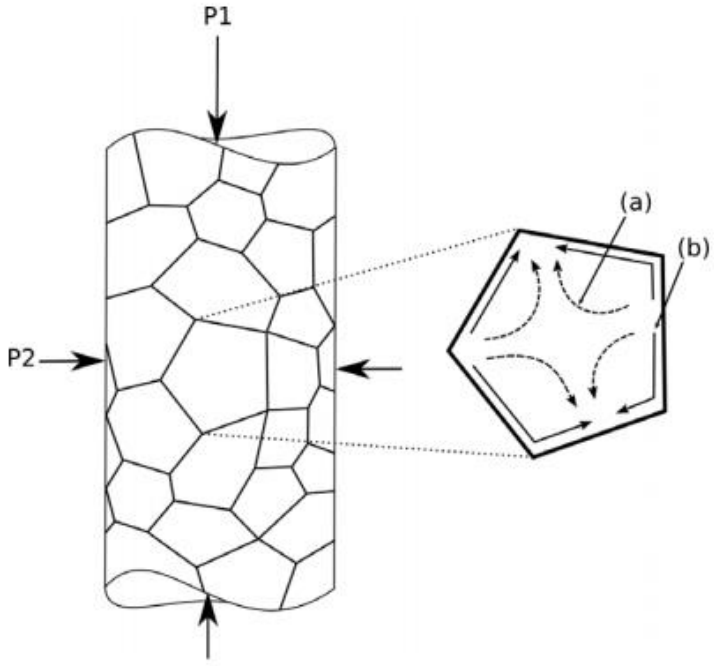

Figure 2.10. Two common diffusional creep mechanisms: (a) Nabarro-Herring creep and (b) Coble creep [92].

2.6. Conventional Creep Testing

This section discusses two of the most common traditional methods used to assess creep behavior in materials, namely uniaxial creep testing and impression creep testing. Conceptually, a creep test is quite straightforward. Simply apply a constant force to the material to measure its dimensional change over time. Each creep test aims to gather the same information in a slightly different way.

2.6.1. Compressive/Tensile Uniaxial Creep Testing

The most common way to obtain the creep behavior of a material is with a standardized Uniaxial Creep Test (UCT). For this test, a test coupon is required, and one end of the sample is fixed. To the unfixed end, a force is applied (compressive or tensile), but this time in terms of constant weight and thereby, constant loading. This constant loading is necessary to ensure the same uniaxial force is applied to the material throughout the test. Also, the material is usually held at a constant temperature throughout one of these creep tests. This test is considered destructive to the sample. A schematic of a uniaxial creep test is shown in Figure 2.11.

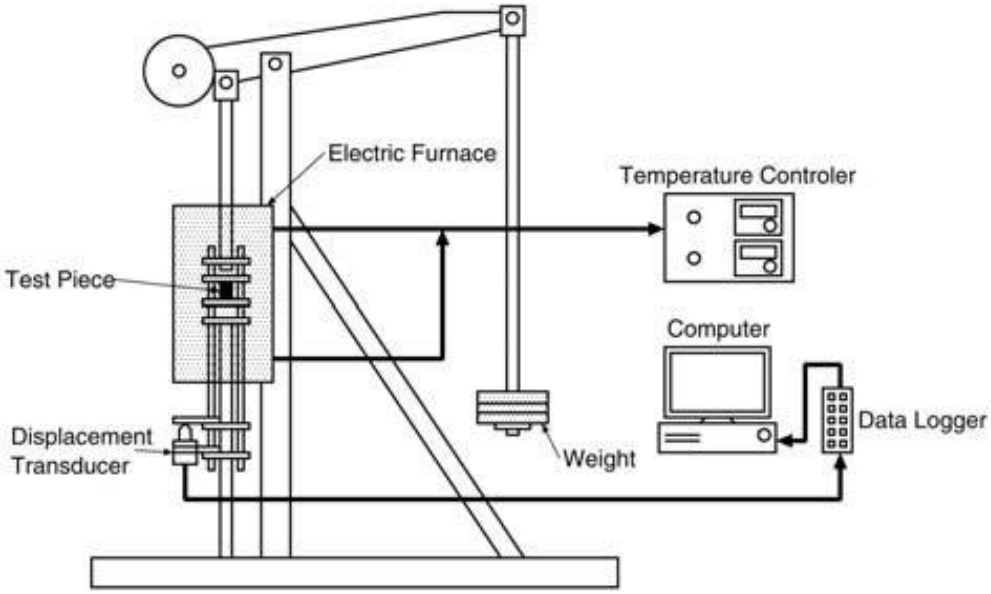

Figure 2.11. Typical setup of a uniaxial creep test [93].

2.6.2. Impression Testing

Impression testing is another common and conventional way to assess creep behavior. For creep assessment of materials of in-service power plant parts, impression testing is a preferable method. This is because impression creep testing only requires a small amount of metal and the test is considered a non-destructive sampling technique. This test can shed light on creep properties of materials where perhaps variation in creep properties exist (e.g., in the base metal, on a weld joint, or an area that has experienced thermal treatment). Impression testing involves the application of a constant load to a flat-ended indenter (typically cylindrical or rectangular) placed on the material surface, usually at a fixed temperature. A schematic of an impression creep test is shown in Figure 2.12.

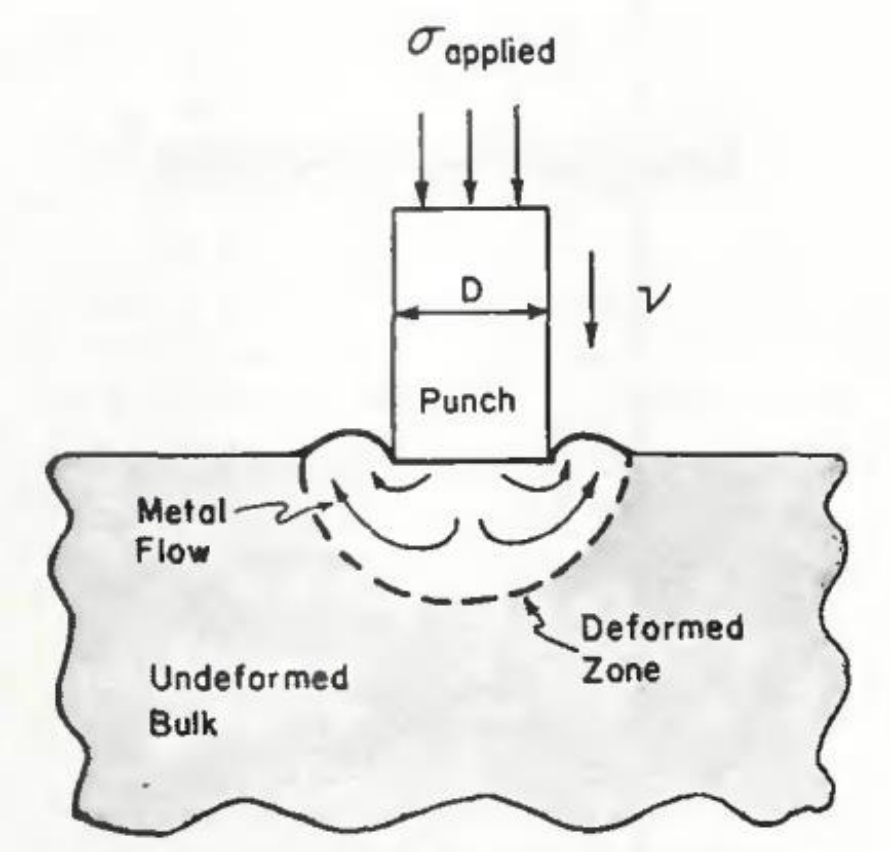

Figure 2.12. Schematic illustrating the deformation zone formed around a punch during impression creep testing [94].

2.7. Indentation Creep Testing (Non-conventional method)

Indentation creep testing is a nontraditional, non-conventional means of assessing creep properties of a material. However, the technique is a reliable, robust, and non-destructive means of assessing creep behavior. Indentation creep tests are useful for measuring properties at remarkably high resolution and can be used to measure properties of individual phases, films, or single crystals of a material.

Indentation tests can be done in a prescribed depth or load mode. Meaning, in such a test, a geometrically self-similar tip is to be pressed into the sample, either at a predetermined load or depth. Once pressed to this prescribed condition, the tip is held into the sample for a given period of time, i.e., the dwell (or holding) time. Creep occurs during this dwell period, and finally, the tip is retracted from the sample. Throughout the entire duration of the test, load and displacement measurements are taken for property determination.

The loading, holding, and unloading stages during an indentation test can be done over a wide array of forces (few μN to several hundreds of mN) and displacements (few nm to tens of μm). This makes the testing technique powerful in terms of versatility as well. A schematic of an indenter setup and typical load-displacement curve generated from an indentation creep test is shown in Figure 2.13.

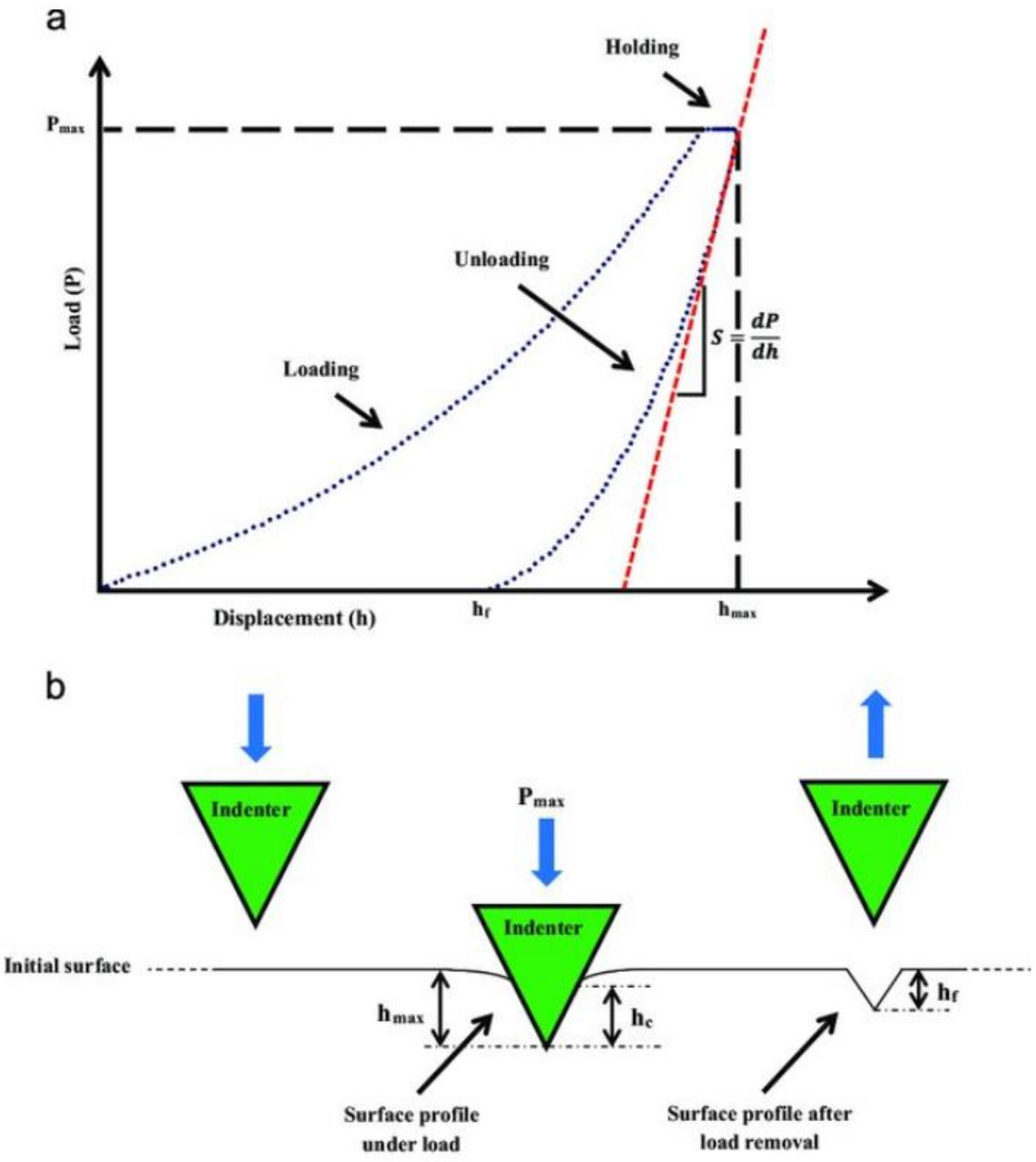

Figure 2.13. A typical load-displacement curve obtained during an indentation creep test (a), and a schematic of the interaction between the indenter tip and sample (b) [95].

There are a few intrinsic differences in the deformation mechanics of instrumented creep testing and those of uniaxial creep worth noting [85]:

1. The stress state beneath the indenter tip is relatively localized and is far more complicated than that in uniaxial tests.
2. The loading rate during indentation creep tests is 2-3 magnitudes larger (much faster) than conventional creep tests. Also, the recovery process for the deformation can be retarded.
3. Creep duration and thermal stability of indentation apparatuses are limited, so dwell times may not be as long as those conducted in uniaxial tests, and isothermal conditions are harder to maintain in indentation tests versus uniaxial ones.

Indentation creep testing also has several advantages over the uniaxial creep testing method which cannot be overstated:

1. Indentation tests are non-destructive. Uniaxial tests are destructive.
2. Indentation creep tests take much less time than uniaxial creep tests, and indentation tests can obtain creep behavior just as useful in far less time.
3. Indentation tests can reveal the creep behavior of single crystals, thin films, and isolated phases in a material. Uniaxial creep tests are very microstructure sensitive, i.e., many specimens need testing to verify results since microstructure varies from sample to sample, and these tests cannot give the same creep information about fine, isolated phases or films like indentation tests can.
4. Traditional uniaxial tests are challenging to analyze. Indentation creep testing is a well-established method that is comparatively easier to analyze and interpret.
5. Uniaxial tests require a relatively large material coupon/bone for testing. Indentation tests can produce reliable creep data from one sample, a fraction of the size of the material that would be needed in uniaxial tests. Much less material is needed for testing in indentation tests.

Overall, indentation creep tests are a unique, accepted, and convenient means to obtain creep properties of a material. For nanocomposites, i.e., MMCs with nanoparticle reinforcement phases, indentation a few nanometers into the sample can shed light on creep, among other properties of the composite and this kind of indentation test is called nanoindentation. Some nanoindentation creep studies performed on magnesium nanocomposites are discussed in the next section.

2.7.1. Room Temperature Creep Studies on Mg-nanocomposites

A limited number of researchers have investigated room-temperature creep deformation behavior of magnesium composites through conventional uniaxial creep testing and impression creep testing at room temperature. Much more research attention and efforts are focused on high-temperature, industrially relevant conditions for Mg-composites. However, there are a few notable studies that investigate the room temperature creep deformation of magnesium and its nanocomposites through nanoindentation.

It is first worth noting that Somekawa et al. [96] studied the room temperature creep response of *pure* magnesium with nanoindentation. They report that dislocation slip is the dominant creep mechanism at room temperature, but grain boundary sliding (GBS) is also present and can contribute about 10% of total strains. Sambhava et al. [97] also studied the room temperature creep response of pure Mg and also concluded that dislocation glide (slip) was the dominant creep mechanism at room temperature.

Room-temperature nanoindentation creep studies on Mg-nanocomposites are also quite limited. Haghshenas et al. [98] studied the room-temperature (~$0.32T_m$ of magnesium) creep response of magnesium reinforced with 0.5, 1.5, and 2.5 vol.% BN particulates through depth-sensing indentation tests. Every combination of the four materials (Pure Mg and three Mg-BN nanocomposites) and three load rates (0.05, 0.5, 5, and 50 mN/s) were tested. The peak load and dwell time were 50 mN and 400s, respectively. They report dislocation motion as the dominant creep deformation mechanism for all samples. This study also experimentally demonstrates that BN particles do enhance the creep resistance of magnesium, attributed to the ability of BN particles to hinder dislocation motion.

In a more recent study, Haghshenas et al [99] investigated the room temperature creep response of magnesium reinforced with a rare earth oxide, samarium oxide (Sm_2O_3), through nanoindentation. Magnesium reinforced with 0.5, 1.0, and 1.5 vol.% samarium oxide was tested against pure Mg. The peak load was 10 mN and one of three different loading rates (0.05, 0.5, and 5 mN/s) with a dwell time of 120 s were the testing conditions for each sample. The sample with 1.0 vol.% Sm_2O_3 particles displayed the best hardness properties, and samarium oxide was proven to enhance the creep resistance of Mg through grain boundary pinning and hindering dislocation motion. Dislocation glide was also the dominant creep mechanism for all materials tested.

2.7.2. High-Temperature Creep Studies on Mg-nanocomposites

Comparatively more high-temperature creep studies on Mg-nanocomposites have been conducted than those at room temperature. This is mostly due to the nature of industrial operating conditions, and researchers trying to mimic industrially relevant conditions as opposed to room-temperature conditions for completeness. This section will briefly address some of the high-temperature creep behavior on Mg-nanocomposites which has been obtained through uniaxial creep tests (2.7.2.1), impression creep tests (2.7.2.2), and indentation creep tests (2.7.2.3).

2.7.2.1. Uniaxial Creep Tests

Ferkel and Mordike [100] investigated the creep response of Mg reinforced with 3 vol.% SiC produced by a powder metallurgy technique. Uniaxial tensile testing was used with a strain rate of 3.3×10^{-4} s^{-1} at 200 and 300°C in air. They prepared one set of samples which were simply mixed (magnesium powder and nanoparticles) and a separate set of samples were milled. In the mixed powders, the nanoparticles coarsened the Mg grain boundaries after extrusion. In the case of the milled powders, a submicron-grained Mg structure was developed with the nano SiC particles decorating the shear band with the heavily deformed Mg and was partly dispersed into the matrix grains after extrusion. The milled composite showed the best creep resistance out of all samples tested.

Katsarou et al. [101] investigated the creep behavior of magnesium alloy Elektron21. They used compression creep testing at 240ºC between 70 and 200 MPa to

determine if the addition of 1 wt.% AlN into Elektron21 would improve the creep resistance of pure Elektron21. Katsarou et al. conclude that adding the AlN does improve the creep resistance of Elektron21.

Han and Dunand [102] conducted compressive creep tests on magnesium reinforced with 30 vol.% yttria (Y_2O_3) particles of 0.33 μm diameter. The tests were performed between 573 and 723 K at compressive stresses between 7 and 125 MPa. They report that the dominant creep mechanism at low stresses (those less than 30 MPa) is grain boundary sliding and the high-stress regime has dislocation creep as the dominant creep mechanism. The yttria reinforcements were also proven to enhance the creep behavior of pure magnesium over all temperatures tested.

Garcés et al. [103] also studied the high-temperature creep response of a Mg-Y_2O_3 nanocomposite. Tensile creep tests were performed on Mg reinforced with 6 vol.% yttria (of 6 μm diameter) against pure magnesium in the 100-500°C temperature range at an initial strain rate of 10^{-4} s^{-1}. They report that the yttria additions do provide pure magnesium with creep resistance. However, the reinforcement effect due to the texture is only effective up to 300°C.

Another successful Mg-nanocomposite creep characterization study was performed by Park et al. [104]. Three samples, magnesium alloy AS52, AS52 + 20 vol.% aluminum borate whiskers (AB_w) + 5 vol.% CNTs (hybrid MMC), and AS52 + 25 vol.% AB_w (single MMCs) were tested with a uniaxial tensile tester at 150-250°C. A strain rate of 0.001 s^{-1}

was used for all tests. The creep rates were lowest for the hybrid MMC and were the highest for the pure AS52 alloy.

2.7.2.2. Impression Creep Tests

Several studies have been performed on Mg-nanocomposites at elevated temperatures with impression creep testing. Therefore, only a few are presented here so the general idea and typical outcomes of these kinds of tests for Mg-nanocomposites are clear.

Talari et al. [105] studied the impression creep response of unmilled AlMg5 powders, milled AlMg5, and AlMg5 powders milled with 0.5 vol.% of Al_2O_3 nanoparticles. Impression tests were carried out over the temperatures 448-598 K and impression stresses 210-365 MPa. The AlMg5 powder reinforced with alumina showed the best creep resistance over all the elevated temperatures tested. However, the alumina-AlMg5 sample exhibits a higher creep rate and tensile elongation at 473 K due to the activation of grain boundary sliding.

Safari et al. [106] used impression creep testing to study the creep behavior of Mg reinforced with 1 vol.% TiO_2 against that of pure magnesium. The impression creep tests were carried out at 150°C and 225 MPa. The titania particles were shown to improve the creep resistance of magnesium at 150°C due to titania being in the grains and the grain boundaries, thereby hindering dislocation motion.

Ganguly and Mondal [107] investigated the microstructure and creep behavior of an AZ91-2.0Ca-0.3Sb alloy and its three nanocomposites, AZ91- 2.0Ca-0.3Sb-xSiC (x =

0.5, 1.0, and 2.0 wt.%) at the stress and temperature range of 300-480 MPa and 448-523 K for two hours. SiC nanoparticles were an average of 50 nm in size. Optimum creep resistance was recorded for the AZ91 alloy with the highest weight fraction of SiC nanoparticles at 2.0 wt.%. They also report the dominant creep deformation mechanism at these elevated temperatures to be dislocation climb controlled by pipe diffusion.

Kumar et al. [108] investigated the creep response of magnesium alloy AS41 and two nanocomposites of AS41 reinforced with 2 and 5 wt.% Al_2O_3. Impression creep tests were performed at 448, 473, 498, and 523 K at three different stresses of 109.2, 124.8, and 140.4 MPa. The results of their tests indicate that AS41 reinforced with 5 wt.% alumina has the highest creep resistance. Stress exponents from this study also indicate that dislocation creep is the dominant creep deformation mechanism operative over this temperature range.

2.7.2.3. Nanoindentation Creep of Mg-nanocomposites

The number of researchers who have studied the elevated-temperature creep response of Mg-composites with indentation testing is quite limited. This gap in Mg-composite knowledge is one which this thesis seeks to help close.

Khan et al. [109] used indentation creep testing to assess the creep behavior of Al-5% Mg matrix composites reinforced with 10 and 20 vol.% B_4C particles. Tests were conducted from room temperature to 500°C. They report that the apparent activation energy for creep increases as B_4C is added into the matrix, and this increase is attributed to the hard B_4C particles hindering the dislocation motion in the magnesium matrix.

Recently, Haghshenas et al. [110] studied the ambient and elevated-temperature creep response of Mg reinforced with Sm_2O_3 nanoparticles. A depth-sensing indentation creep testing approach was used. Pure Mg and Mg reinforced with 0.5, 1.0, and 1.5 vol.% Sm_2O_3 was studied at ambient (298 K) temperature up to 473 K. They report that pure Mg has the least creep resistance and Mg reinforced with 1.0 vol.% Sm_2O_3 has the greatest creep resistance. The samarium oxide nanoparticles effectively produce dislocation pile-ups and dislocation tangling. Creep exponents are also reported in the study and indicate that creep is glide-controlled at ambient conditions and at elevated temperatures the creep is glide-assisted with the dislocation climb mechanism.

2.8. Project Outlook

2.8.1. Project Objectives

The objectives of this project are outlined as follows:

1. Assess the effect of temperature, strain rate, and dwell time on the rate-dependent plastic response (creep response) of Mg-CNT nanocomposites reinforced with 0.25, 0.5, and 0.75 vol.% CNTs through nanoindentation and to compare the results with a pure Mg base metal (0% CNT). Volume fraction of CNTs is varied so optimum loading of CNTs can be identified for best material creep properties.
2. Determine if CNTs offer magnesium any creep resistance.
3. Identify the dominant creep mechanism operative at room (298 K) and at elevated (373, 473, and 573 K) temperatures. We would like to shed light on different mechanisms operating at ambient and non-ambient conditions.

2.8.2. Project Novelty

The materials used in this study, Mg nanocomposites reinforced with different volume fractions of the CNTs, along with the nanoindentation creep tests used to obtain creep properties of these materials are what make the project particularly novel. Mg-CNT nanocomposites have been synthesized before, but never in an identical processing technique (i.e., powder metallurgy). Though the static mechanical properties and microstructural evolution of Mg-CNT nanocomposites have been studied before, indentation-induced, time-dependent plastic deformation (creep) at ambient and non-ambient conditions to the best of the author's knowledge, has never been characterized.

2.8.3. Project Contributions to the Scientific Community

This project makes significant contributions to the fields of synthesizing and characterizing Mg-CNT nanocomposites, as well as gaining a better understanding of how CNTs influence the creep and hardness properties of magnesium matrices at room and elevated temperatures. The results of this project can be used for materials selection processes in the automobile sector, the aerospace sector, and altogether as a stepping stone for more Mg-nanocomposite characterizations to follow this one.

Indeed, as potential structural materials for vehicles, aircraft, and military armor, the creep and fatigue response of Mg alloys (and also Mg matrix nanocomposites) require in-depth investigations to understand their time- and rate-dependent characteristics. Conventional Mg alloys soften at about 120 –150 °C [111, 112]. Meaning, an increase in temperature in Mg and its alloys result in a quick loss of strength and limited creep resistance [113-116]. Improving the elevated temperature mechanical properties (i.e., creep) has become a critical issue to enable applications of Mg alloys at higher temperatures. Therefore, the primary focus currently is to develop a new generation of magnesium nanocomposites, capable of exhibiting a good combination of thermal and mechanical properties. To this end, researchers are attempting to manufacture Mg–matrix nanocomposites, employing different types and volume fractions of the nanoparticles, to obtain lightweight materials with acceptable strength and ductility at elevated temperatures.

Additionally, creep mechanisms for Mg nanocomposite materials, as emerging high-strength lightweight materials are not well-documented. This is the current gap in knowledge limiting the material's broader application. This project aims at providing an overview of creep-resistant Mg alloys and investigating the creep response of Mg-CNT nanocomposites.

The next chapter lays out the specific nanoindentation creep test protocol taken for Mg-CNT nanocomposites at ambient and elevated temperatures for this project.

REFERENCES

CHAPTER II– LITERATURE REVIEW

[1] Powell, B.R., Luo, A.A., et al. "Magnesium alloys for lightweight powertrains and automotive bodies." *Advanced Materials in Automotive Engineering*, edited by Jason Rowe. Woodhead Publishing Limited. 2012, p. 150.

[2] Simms, S., and Kowach, G. "General Properties of Materials." *Marks' Standard Handbook for Mechanical Engineers, 12th ed,* edited by Ali M. Sadegh and William M. Worek. McGraw-Hill Education. 2018, Table 4.1.5.

[3] Wilding, W. V., et al. "Chapter 2, Section 2.2: Physical Properties of Pure Substances." *Perry's Chemical Engineers' Handbook, 9th ed*, edited by Don W. Green and Marylee Z. Southard. McGraw-Hill Education. 2019. Table 2-1.

[4] Hammond, C.R., "Section 4: Properties of the Elements and Inorganic Compounds." *CRC Handbook of Chemistry and Physics, 86th ed*, edited by Lide, D.R. CRC Press LLC. 2005, pp. 4-1 through 4-36.

[5] Gupta, M., and Wong, W.L. "Section 4.3.4: Aluminum and Composites." *Microwaves and Metals*. Singapore. Markono Print Media Pte Ltd., 2007, pp. 116-117.

[6] Banerjee, P.C., Al-Saadi, S., Choudhary, L., Harandi, S.E., and Singh, R. "Magnesium Implants: Prospects and Challenges." *Materials (Basel, Switzerland),* vol. 12, no. 1, January 2019, pp. 1-21. doi:10.3390/ma12010136.

[7] Kramer, D.A. "Introduction and History." *Magnesium, its Alloys and Compounds*. U.S. Geological Survey Open-File Report 01-341. 2001, version 1.0, p.3. Retrieved from: https://pubs.usgs.gov/of/2001/of01-341/. Accessed 4 March 2020.

[8] Hu, X.S., Zhang, Y.K., Zheng, M.Y., and Wu, K. "A study of damping capacities in pure Mg and Mg-Ni alloys." *Scripta Materialia*, vol. 52, no. 11, June 2005, pp. 1141-1145. https://doi.org/10.1016/j.scriptamat.2005.01.048.

[9] Zhang, Z.H., Pan, F.S., Chen, X.H., and Liu, J. "Electromagnetic shielding properties of magnesium and magnesium alloys." *Journal of Materials Engineering*, 2013, pp. 52-57. DOI: 10.3969/j.issn.1001-4381.2013.01.011.

[10] Powell, B.R., Luo, A.A., et al. "Magnesium alloys for lightweight powertrains and automotive bodies." *Advanced Materials in Automotive Engineering*, edited by Jason Rowe. Woodhead Publishing Limited. 2012, p. 154.

[11] Lee, S., Ham, H.J., Kwon, S.Y., Kim, S.W., and Suh, C.M. "Thermal conductivity of magnesium alloys in the temperature range from -125°C to 400°C." *International Journal of Thermophysics*, vol. 34, January 2012, pp. 2343-2350. DOI 10.1007/s10765-011-1145-1.

[12] Abbott, T.B. "Why Choose Magnesium?" *Materials Science Forum*, vol. 618-619, Trans Tech Publications, Ltd., April 2009, pp. 3-6. doi:10.4028/www.scientific.net/msf.618-619.3.

[13] Sim, G.D., Kim, G., Lavenstein, S., Hamza, M.H., F, H., El-Awady, J.A. "Anomalous hardening in magnesium driven by a size-dependent transition in deformation modes." *Acta Materialia*, vol. 144, February 2018, pp. 11-20. https://doi.org/10.1016/j.actamat.2017.10.033.

[14] Ali, Y., Qiu, D., Jiang, B., Pan, F., Zhang, M.X. "Current research progress in grain refinement of cast magnesium alloys: A review article." *Journal of Alloys and Compounds*, vol. 619, January 2015, pp. 639-651. https://doi.org/10.1016/j.jallcom.2014.09.061.

[15] Milička, K, et al. "Anisotropy of creep resistance in extruded magnesium." *Scripta Materialia*, vol. 61, no. 12, December 2009, pp. 1109-1112. https://doi.org/10.1016/j.scriptamat.2009.08.033.

[16] Jones, D.A. “Chapter 15: Materials Selection and Design.” *Principles and Prevention of Corrosion, 2nd ed.*, edited by Patricia Daly. Prentice Hall, Inc., New Jersey. 1996, p. 528.

[17] Fontana, M.G. “Table 3-1 Standard emf series of metals” in Chapter 3: Eight Forms of Corrosion. *Corrosion Engineering, 3rd ed.*, edited by Sanjeev Rao. McGraw-Hill. 1986, p. 42.

[18] Yoo, M.H. “Slip, twinning, and fracture in hexagonal close-packed metals.” *Metallurgical Transactions A*, vol. 12, no. 3, 1981, pp. 409-418.

[19] Avedesian, M.M., Baker, H. *ASM Specialty Handbook: Magnesium and Magnesium Alloys*. ASM International, Materials Park, OH, 1999.

[20] Li, L., Grandfield, J., Sun, S., and Wang, C. Global Primary Magnesium Supply and Demand Balance 2016. IMA International Conference, May 2017.

[21] Czerwinski, F. “Controlling the ignition and flammability of magnesium for aerospace applications.” *Corrosion Science*, vol. 86, September 2014, pp. 1-16. https://doi.org/10.1016/j.corsci.2014.04.047.

[22] Mendis, C.L., Singh, A. “Magnesium recycling: To the grave and beyond.” *Journal of the Minerals, Metals & Materials Society*, vol. 65, no. 10, August 2013, pp. 1283-1284. DOI: 10.1007/s11837-013-0701-5.

[23] Luo, A.A. “Recent magnesium alloy developments for elevated temperature applications.” *International Material Reviews*, vol. 49, no. 1, 2004, pp. 13-30. https://doi.org/10.1179/095066004225010497.

[24] Lu, K., Lu, L., Suresh, S. “Strengthening materials by engineering coherent internal boundaries at the nanoscale.” *Science*, vol. 324, no. 5925, April 2009, pp. 349-352. DOI: 10.1126/science.1159610.

[25] "Introduction to Magnesium Alloys." *Engineering Properties of Magnesium Alloys*, edited by Charles Moosbrugger. ASM International. 2017, p. 3.

[26] Aghion, E., Bronfin, B., Von Buch, F., Schumann, S., and Friedrich, H. "Newly developed magnesium alloys for powertrain applications." *JOM*, vol. 55, November 2003, pp. 30-33.

[27] Mo., N. et al. "Current development of creep-resistant magnesium cast alloys: A review." *Materials & Design*, vol. 155, October 2018, pp. 422-442. https://doi.org/10.1016/j.matdes.2018.06.032.

[28] Nie., J.F. "Precipitation and hardening in magnesium alloys." *Metallurgical and Materials Transactions A*, vol. 43, no. 11, July 2012, pp. 3891-3939. DOI: 10.1007/s11661-012-1217-2.

[29] Gupta, M., Wong, W.L.E. "Magnesium-based nanocomposites: Lightweight materials of the future." *Materials Characterization*, vol. 105, April 2015, pp. 30-46. DOI: 10.1016/j.matchar.2015.04.015.

[30] Bandivadekar, A., Bodek, K., Cheah, L., Evans, C., et al. "On the road in 2035: Reducing transportation's petroleum consumption and GHG emissions." MIT Report, Laboratory for Energy and the Environment, July 2008.

[31] "Magnesium Vision 2020: A North American Automotive Strategic Vision for Magnesium." United States Automotive Materials Partnership, A consortium of the US Council for Automotive Research. December 2004, p. 3.

[32] Gupta, M., Sharon, N.M.L. "1.3. Applications." *Magnesium, Magnesium Alloys, and Magnesium Composites*, John Wiley & Sons, Inc., Hoboken, New Jersey, 2011, p. 5-12.

[33] Davis, B. “The application of magnesium alloys in aircraft interiors – Changing the rules.” *Magnesium Technology 2015,* edited by Manuel M.V., Singh, A., Alderman, V., Neelameggham, N.R., Springer, Cham, 2015, pp. 5-5.

[34] Friedrich, H.E., Mordike, B.L. (eds.) “Engineering Requirements, Strategies and Examples.” *Magnesium Technology – Metallurgy, Design Data, Applications*. Springer. 2006, p. 604.

[35] Haghshenas, M. “Mechanical characteristics of biodegradable magnesium matrix composites: A review.” *Journal of Magnesium and Alloys,* vol. 5, no. 2, June 2017, pp. 189-201. https://doi.org/10.1016/j.jma.2017.05.001.

[36] Staiger, M.P., Pietak, A.M., Haudmai, J., Dias, G. “Magnesium and its alloys as orthopedic biomaterials: A review.” *Biomaterials,* vol. 27, no. 9, March 2006, pp. 1728-1734. https://doi.org/10.1016/j.biomaterials.2005.10.003.

[37] Lee, J-W., Han, H-S., Han, K-J., Park, J., Jeon, H., et al. “Long-term clinical study and multiscale analysis of in vivo biodegradation mechanism of Mg alloy.” *Proceedings of the National Academy of Sciences (PNAS),* vol. 113, no. 3, January 2016, pp. 716-721. https://doi.org/10.1073/pnas.1518238113.

[38] Mathaudhu, S.N., Nyberg, E.A. “Magnesium alloys in US military applications: Past, current, and future solutions.” Pacific Northwest National Laboratory (PNNL), Richland, WA, 2010. http://www.osti.gov/scitech/biblio/ 1012885.

[39] Friedrich, H.E., Mordike, B.L. (eds.) “8.3.2 Past Aerospace Use.” *Magnesium Technology – Metallurgy, Design Data, Applications*. Springer. 2006, pp. 607-617.

[40] Landkof, B. “Development of high-strength magnesium based MMC reinforced with SiC particles for satellite structure applications.” *Materialwissenschaft und Werkstofftechnik,* vol. 34, no. 4, April 2003, pp. 395-399. DOI: 10.1002/mawe.200390082.

[41] Walsh, S.M., Scott, B.R., Jones, T.L., Cho, K., Wolbert, J. "A materials approach in the development of multi-threat warfighter head protection." *Proceedings of the 2008 Army Science Conference*, Orlando, FL, December 2008.

[42] Jones, T.L., Labukas, J.P., Placzankis, B.E. "Ballistic and corrosion analysis of new military-grade magnesium alloys AMX602 and ZAXE1711 for armor applications." *Army Research Laboratory,* Aberdeen, MD, February 2012, pp. 1-44.

[43] Abdullah, M.F., Abdullah, S., Omar, M.Z., et al. "Failure observation of the AZ31B magnesium alloy and the effect of lead addition content under ballistic impact." *Advances in Mechanical Engineering*, vol. 7, no. 5, March 2015, pp. 1-13. https://doi.org/10.1177/1687814015585428.

[44] Jones, T.L., Kondoh, K. "Ballistic analysis of new military grade magnesium alloys for armor applications." *Magnesium Technology 2011*, edited by Sillekens, W.H., Agnew, S.R., Neelameggham, N.R., and Mathaudhu, S.N. 2011, Springer, Cham, pp. 425-430.

[45] Kaya, A.A. "2.6.1. Creep behaviour of magnesium." *Fundamentals of Magnesium Alloy Metallurgy*, edited by Mihriban O. Pekguleryuz, Karl U. Kainer, and A. Arslan Kaya. Woodhead Publishing, 2013, p. 54.

[46] Brown, C. "The creep behaviour of a magnesium/ 0.3 wt% zirconium alloy at 400 and 450°C in carbon dioxide." *Journal of Nuclear Materials*, vol. 12, no. 2, July 1964, pp. 243-247. https://doi.org/10.1016/0022-3115(64)90147-3.

[47] Vagarali, S.S., Langdon, T.G. "Deformation mechanisms in h.c.p. metals at elevated temperatures-I. Creep behavior of magnesium." *Acta Metallurgica*, vol. 29, no. 12, December 1981, pp. 1969-1982. https://doi.org/10.1016/0001-6160(81)90034-1.

[48] Sahu, G., and Brijesh, P. "A Brief Review on Mg Alloys: Their Properties and Application." *International Journal of Advance Research in Science and Engineering (IJARSE)*, vol.4, Special Issue no. 1, May 2015, p. 70.

[49] Iijima, S. “Helical microtubules of graphitic carbon.” *Nature*, vol. 354, November 1991, pp. 56-58.

[50] Choudhary, V., Gupta. A. “Polymer/carbon nanotube nanocomposites.” *Carbon Nanotubes: Polymer Nanocomposites* edited by Siva Yellampalli, Chapter 4. IntechOpen, August 2011, p. 66. Retrieved from: https://www.intechopen.com Accessed 23 March 2020.

[51] Pitroda, J., Jethwa, B., Dave, S.K. “A critical review on carbon nanotubes.” *International Journal of Constructive Research in Civil Engineering*, vol. 2, no. 5, 2016, pp. 36-42. DOI: http://dx.doi.org/10.20431/2454-8693.0205007.

[52] Roman, R.E., Kwan, K., Cranford, S.W. “Mechanical properties and defect sensitivity of diamond nanothreads.” *Nano Letters by the American Chemical Society*, vol. 15, no. 3, February 2015, pp. 1585-1590. DOI: 10.1021/nl5041012.

[53] Saeed, K., Ibrahim. “Carbon nanotubes-properties and applications: A review.” *Carbon Letters*, vol. 14, no. 3, 2013, pp. 131-144. DOI: http://dx.doi.org/ DOI:10.5714/CL.2013.14.3.131.

[54] Wang, Y., Weng, G.J. “Electrical conductivity of carbon nanotube- and graphene-based nanocomposites.” *Micromechanics and Nanomechanics of Composite Solids*, edited by Meguid S. and Weng, G. Springer International Publishing AG. July 2017, pp. 123-156.

[55] Ebbesen, T.W., Lezec, H.J., Hiura, H., Bennett, J.W., Ghaemi, H.F., Thio, T. “Electrical conductivity of individual carbon nanotubes.” *Nature*, vol. 382, no. 54, July 1996, pp. 54-56. http://dx.doi.org/10.1038/382054a0.

[56] Wang, P., et al. “Gas infiltration of bromine to enhance the electrical conductivity of carbon nanotube fibers.” *Materials & Design*, vol. 159, December 2019, pp. 138-144. https://doi.org/10.1016/j.matdes.2018.08.030.

[57] Kim, P., Shi, L., Majumdar, A., Mceuen, P. "Thermal transport measurements of individual multiwalled nano-tubes." *Physical Review Letters*, vol. 87, no. 21, November 2001, p. 215502. DOI: 10.1103/PhysRevLett.87.215502.

[58] Wang, X., et al. "Fabrication of ultralong and electrically uniform single-walled carbon nanotubes on clean substrates." *Nano Letters*, vol. 9, no. 9, June 2009, pp. 3137-3141. DOI: 10.1021/nl901260b.

[59] Peigney, A., Laurent, Ch., Flahaut, E., Bacsa, R.R., Rousset, A. "Specific surface area of carbon nanotubes and bundles of carbon nanotubes." *Carbon*, vol. 39, no. 4, April 2001, pp. 507-514. https://doi.org/10.1016/S0008-6223(00)00155-X.

[60] Selvamani, S.T., Premkumar, S., Vigneshwar, M., Hariprasath, P., Palanikumar, K. "Influence of carbon nano tubes on mechanical, metallurgical and tribological behavior of magnesium nanocomposites." *Journal of Magnesium and Alloys*, vol. 5, no. 3, September 2017, pp. 326-335. https://doi.org/10.1016/j.jma.2017.08.006.

[61] Okoro, A.M., Machaka, R., Lephuthing, S.S., Oke, S.R., Awotunde, M.A., Olubambi, P.A. "Nanoindentation studies of the mechanical behaviours of spark plasma sintered multiwall carbon nanotubes reinforced Ti6Al4V nanocomposites." *Materials Science and Engineering A*, vol. 765, September 2019, p. 138320. https://doi.org/10.1016/j.msea.2019.138320.

[62] Chen, B., Shen, J., Ye, X., Jia, L., Li, S., Umeda, J., Takahashi, M., Kondoh, K. "Length effect of carbon nanotubes on the strengthening mechanisms in metal matrix composites." *Acta Materialia*, vol. 140, November 2017, pp. 317-325. https://doi.org/10.1016/j.actamat.2017.08.048.

[63] Chen, B., Li, S., Imai, H., Jia, L., et al. "Carbon nanotube induced microstructural characteristics in powder metallurgy Al matrix composites and their effects on mechanical and conductive properties." *Journal of Alloys and Compounds*, vol. 651, December 2015, pp. 608-615. https://doi.org/10.1016/j.jallcom.2015.08.178.

[64] Akbarpour, M.R., Mirabad, H.M., Alipour, S., Kim, H.S. “Enhanced tensile properties and electrical conductivity of Cu-CNT nanocomposites processed via the combination of flake powder metallurgy and high pressure torsion methods.” *Materials Science and Engineering A*, vol. 773, January 2020, p. 138888. https://doi.org/10.1016/j.msea.2019.138888.

[65] Shimizu, Y., Miki, S., Soga, T., Itoh, I., et al. “Multi-walled carbon nanotube-reinforced magnesium alloy composites.” *Scripta Materialia*, vol. 58, no. 4, February 2008, pp. 267-270. https://doi.org/10.1016/j.scriptamat.2007.10.014.

[66] Subramaniam, C., Yamada, T., Kobashi, K., Sekiguchi, A., Futaba, D.N., Yumura, M., Hata, K. “One hundred fold increase in current carrying capacity in a carbon nanotube-copper composite.” *Nature Communications*, vol. 4, no. 2202, July 2013, pp. 1-7. DOI: 10.1038/ncomms3202.

[67] Park, S.H., Cho, D.H., Cho, K.M., Park, I.M. “Creep properties of squeeze-infiltrated carbon nanotube and aluminum borate whisker reinforced AS52 Mg metal matrix composites.” *Metals and Materials International*, vol. 24, June 2018, pp. 1162-1171. https://doi.org/10.1007/s12540-018-0149-9.

[68] Cho, S., Kikuchi, K., Lee, E., Choi, M., Jo, I., et al. “Chromium carbide/carbon nanotube hybrid structure assisted copper composites with low temperature coefficient of resistance.” *Scientific Reports*, vol. 7, no. 14943, November 2017, pp. 1-8. DOI:10.1038/s41598-017-14915-7.

[69] Reddy, B.M., Anand, P. “Exploration of properties of Al 5056/CNT metal matrix nano composites.” *Materials Today: Proceedings*, vol. 18, part 7, 2019, pp. 4360-4365. https://doi.org/10.1016/j.matpr.2019.07.399.

[70] Smart, D.S.R, Pradeep Kumar, J., Sanjit Cyrus, R. “Development and investigations of Al5083/CNT/Ni/MoS_2 metal matrix composite for offshore applications.”

Materials Today: Proceedings, vol. 19, part 2, 2019, pp. 682-685. https://doi.org/10.1016/j.matpr.2019.07.753.

[71] Tjong, S.C., "Recent progress in the development and properties of novel metal matrix nanocomposites reinforced with carbon nanotubes and graphene nanosheets." *Materials Science and Engineering: R: Reports*, vol. 74, no. 10, October 2013, pp. 281-350. https://doi.org/10.1016/j.mser.2013.08.001.

[72] Goh, C.S., Wei, J., Lee, L.C., Gupta, M. "Simultaneous enhancement in strength and ductility by reinforcing magnesium with carbon nanotubes." *Materials Science and Engineering:A*, vol. 423, no, 1-2, May 2006, pp. 153-156. https://doi.org/10.1016/j.msea.2005.10.071.

[73] Goh, C.S., Wei, J., Lee, L.C., Gupta, M. "Ductility improvement and fatigue studies in Mg-CNT nanocomposites." *Composites Science and Technology*, vol. 68, no. 6, May 2008, pp. 1432-1439. https://doi.org/10.1016/j.compscitech.2007.10.057.

[74] Iqbal, S.S., Mustafa, A., Talapatra, S., Filipl, P. "Thermal properties of carbon nano tubes reinforced MG-Matrix nanocomposites." *TMS 2012 – 141st Annual Meeting and Exhibition, Supplemental Readings*, vol. 1, 2012, pp. 395-402.

[75] Thornby, J., Verma, D., Cochrane, R., Westwood, A., Manakari, V.B., Gupta, M., Haghshenas, M. "Indentation-based characterization of creep and hardness behavior of magnesium carbon nanotube nanocomposites at room temperature." *Springer Nature Applied Sciences*, vol. 1, no. 695, June 2019. https://doi.org/10.1007/s42452-019-0696-9.

[76] El-Saeid Essa, Y., Fernández-Sáez, J., Pérez-Castellanos, J.L. "Some aspects of damage and failure mechanisms at high strain-rate and elevated temperatures of particulate magnesium matrix composites." *Composites Part B: Engineering*, vol. 34, no. 6, September 2003, pp. 551-560. https://doi.org/10.1016/S1359-8368(03)00046-5.

[77] Lloyd, D.J., "Particle reinforced aluminum and magnesium matrix composites." *International Materials Reviews*, vol. 39, no. 1, July 2013, pp. 1-23.

[78] Ceschini, L., Dahle, A., Gupta, M., Jarfors, A.E.W., Jayalakshmi, S., Morri, A., Rotundo, F., Toschi, S., Singh, R.A. "1.2 Strengthening Mechanisms." *Aluminum and Magnesium Matrix Composites*, Springer Nature Singapore, 2017, pp. 1-4. DOI 10.1007/978-981-10-2681-2.

[79] Mizra, F.A., Chen, D.L. "A unified model for the prediction of yield strength in particulate-reinforced metal matrix nanocomposites." *Materials*, vol. 8, no. 8, 2015, pp. 5138-5153. https://doi.org/10.3390/ma8085138.

[80] Hull, D., Bacon, D.J. *Introduction to Dislocations, 5th ed.*, Butterworth Einemann, Oxford, UK, 2011.

[81] Casati, R., Vedani, M. "Metal matrix composites: Composites reinforced by nano-particles: A review." *Metals*, vol. 4, no. 1, March 2014, pp. 65-83. doi:10.3390/met4010065.

[82] Smallman, R.E., Ngan, A.H.W. "7.2.3. Mechanisms of Precipitation Hardening." *Physical Metallurgy and Advanced Materials, 7th ed.*, Butterworth-Heinemann, 2007, p. 396.

[83] "Orowan Mechanism." Foundry Lexicon. 2020. Web reference. Retrieved from: giessereilexikon.com. Accessed 29 March 2020.

[84] Santy-Zadeh, A. "Comparison between current models for the strength of particulate-reinforced metal matrix nanocomposites with emphasis on consideration of Hall-Petch effect." *Materials Science and Engineering: A*, vol. 531, January 2012, pp. 112-118. https://doi.org/10.1016/j.msea.2011.10.043.

[85] Haghshenas, M., Gupta, M. "Magnesium nanocomposites: An overview on time-dependent plastic (creep) deformation." *Defence Technology*, vol. 15, no. 2, April 2019, pp. 123-131. https://doi.org/10.1016/j.dt.2018.08.008.

[86] Ding, Y., Xu, J., Hu, J., Gao, Q., et al. "High performance carbon nanotube-reinforced magnesium nanocomposite." *Materials Science and Engineering A*, vol. 771, January 2020, article no. 138575.

[87] Goh, C.S., Wei, J., Lee, L.C., Gupta, M. "Simultaneous enhancement in strength and ductility by reinforcing magnesium with carbon nanotubes." *Materials Science and Engineering:A*, vol. 423, no, 1-2, May 2006, pp. 153-156. https://doi.org/10.1016/j.msea.2005.10.071.

[88] Goh, C.S., Wei, J., Lee, L.C., Gupta, M. "Ductility improvement and fatigue studies in Mg-CNT nanocomposites." *Composites Science and Technology*, vol. 68, no. 6, May 2008, pp. 1432-1439. https://doi.org/10.1016/j.compscitech.2007.10.057.

[89] Iqbal, S.S., Mustafa, A., Talapatra, S., Filipl, P. "Thermal properties of carbon nano tubes reinforced MG-Matrix nanocomposites." *TMS 2012 – 141st Annual Meeting and Exhibition, Supplemental Readings*, vol. 1, 2012, pp. 395-402.

[90] Barsoum, M.W. "12.2 Creep." *Fundamentals of Ceramics*, edited by B. Cantor and M.J. Goringe. Taylor & Francis Group, 2003, p. 401.

[91] Castillo, R., Koul, A.K., Toscano, E.H. "Lifetime prediction under constant load creep conditions for a cast Ni-base superalloy." *The International Gas Turbine Conference and Exhibit*, Dusseldorf, West Germany, June 1966.

[92] Babu, B. "Physically based model for plasticity and creep of Ti-6Al-4V." *Licentiate Thesis*. Luleå University of Technology, Sweden, 2008, p. 10-11.

[93] Arai, M., Tanaka, H., Matsushita, K., Sugimoto, K. "Characterization of thermo-viscoelastic property of thermoplastic resin reinforced by carbon nanofiber."

Journal of the Society of Materials Science Japan, vol. 57, no. 2., January 2008, pp. 167-173. DOI: 10.2472/jsms.57.167.

[94] Gibbs, W.S., Wang, S.H., Matlock, D.K., Olson, D.L. "High temperature impression creep testing of weldments." *Supplement to the Welding Journal*, June 1985, pp. 153s-158s.

[95] Ayatollahi, M.R., Yahya, M.Y., Shirazi, H., Hassan, S.A. "Mechanical and tribological properties of hydroxyapatite nanoparticles extracted from natural bovine bone and the bone cement developed by nano-sized bovine hydroxyapatite filler." *Ceramics International*, vol. 41, no. 9, April 2015, pp. 10818-10827. https://doi.org/10.1016/j.ceramint.2015.05.021.

[96] Somekawa, H., Mukai, T. "Nanoindentation creep behavior of grain boundary in pure magnesium." *Philosophical Magazine Letters*, vol. 90, no. 12, December 2010, pp. 883-890. DOI: 10.1080/09500839.2010.514577.

[97] Sambhava, K., Nautiyal, P., Jain, J. "Model based phenomenological and experimental investigation of nanoindentation creep in pure Mg and AZ61 alloy." *Materials and Design*, vol. 105, September 2016, pp. 152-151. https://doi.org/10.1016/j.matdes.2016.05.036.

[98] Haghshenas, M., Islam, R., Wang, Y., Cheng, Y-T., Gupta, M. "Depth sensing indentation of magnesium/ boron nitride nanocomposites." *Journal of Composite Materials*, November 2018, pp. 1-13. DOI: 10.1177/0021998318808358.

[99] Haghshenas, M., Song, X., Hasannaeimi, V., Mukherjee, S., Gupta, M. "Magnesium-samarium oxide nanocomposites: Room-temperature depth-sensing nanoindentation response." *International Journal of Lightweight Materials and Manufacture*, December 2019. https://doi.org/10.1016/j.ijlmm.2019.12.003.

[100] Ferkel, H., Mordike, B.L. “Magnesium strengthened by SiC nanoparticles.” *Materials Science and Engineering: A*, vol. 298, no. 1-2, January 2001, pp. 193-199. https://doi.org/10.1016/S0921-5093(00)01283-1.

[101] Katsarou, L., et al. “Microstructure, mechanical properties and creep of magnesium alloy Elektron21 reinforced with AlN nanoparticles by ultrasound-assisted stirring.” *Materials Science and Engineering: A*, vol. 659, April 2016, pp. 84-92. https://doi.org/10.1016/j.msea.2016.02.042.

[102] Han, B.Q., Dunand, D.C. “Creep of magnesium strengthened with high volume fractions of yttria dispersoids.” *Materials Science and Engineering: A*, vol. 300, no. 1-2, February 2001, pp. 235-244. https://doi.org/10.1016/S0921-5093(00)01781-0.

[103] Garcés, G., Rodríguez, M., Pérez, P., Adeva, P. “High temperature mechanical properties of Mg-Y2O3 composite: Competition between texture and reinforcement contributions.” *Composites Science and Technology*, vol. 67, no. 3-4, March 2007, pp. 632-637. https://doi.org/10.1016/j.compscitech.2006.07.021.

[104] Park, S.H., Cho, D.H., Cho, K.M., Park, I.M. “Creep properties of squeeze-infiltrated carbon nanotube and aluminum borate whisker reinforced AS52 Mg metal matrix composites.” *Metals and Materials International*, vol. 24, June 2018, pp. 1162-1171. https://doi.org/10.1007/s12540-018-0149-9.

[105] Talari, M.K., Babu, N.K., Kallip, K., Leparoux, M., Koller, R.E., et. al. “Microstructure, mechanical, and impression creep properties of AlMg5-0.5 vol% Al_2O_3 nanocomposites.” *Advanced Engineering Materials*, vol. 18, no. 11, 2016, pp. 1958-1966. DOI: 10.1002/adem.201600301.

[106] Safari, A., Mahmudi, R. “High temperature mechanical properties of an extruded Mg-TiO_2 nano-composite.” *Advanced Engineering Materials*, vol. 17, no. 11, 2015, pp. 1639-1644. DOI: 10.1002/adem.201500132.

[107] Ganguly, S., Mondal, A.K. “Influence of SiC nanoparticles addition on microstructure and creep behavior of squeeze-cast AZ91-Ca-Sb magnesium alloy.” *Materials Science and Engineering: A*, vol. 718, March 2018, pp. 377-389. https://doi.org/10.1016/j.msea.2018.01.131.

[108] Kumar, H., Chaudhari, G.P. “Creep behavior of AS41 alloy matrix nano-composites.” *Materials Science and Engineering: A*, vol. 607, June 2014, pp. 434-444. https://doi.org/10.1016/j.msea.2014.04.020.

[109] Khan, K.B., Kutty, T.R.G., Surappa, M.K. ”Hot hardness and indentation creep study on Al-5% Mg alloy matrix-B_4C particle reinforced composites.” *Materials Science and Engineering A*, vol. 427, 2006, pp. 76-82. doi:10.1016/j.msea.2006.04.015.

[110] Haghshenas, M., Muhammad, M., Hasannaeimi, V., Mukherjee, S., Gupta, M. “Ambient and non-ambient Mg-Sm_2O_3 nanocomposites.” *The International Journal of Advanced Manufacturing Technology*, vol. 105, no. 7-8, November 2019, pp. 2947-2956. DOI: 10.1007/s00170-019-04583-4.

[111] Abaspour, S., Cáceres, C.H. “Thermodynamics-based selection and design of creep-resistant cast Mg alloys.” *Metallurgical and Materials Transactions A*, vol. 46, 2015, pp. 5972-5988. DOI: 10.1007/s11661-015-3128-5.

[112] Mendis, C.L., Kainer, K.U., Hort, N. “High strength magnesium alloys through precipitation hardening and micro alloying: Considerations for alloy design.” *JOM*, vol. 67, no. 10, August 2015, pp. 2427-2432. DOI: 10.1007/s11837-015-1561-y.

[113] Moll, F., Kainer, K.U. “Chapter 12: Particle-Reinforced Magnesium Alloys.” *Magnesium – Alloys and Technology*. Weinheim: Wiley-VCH. February 2003, pp. 197-217. DOI:10.1002/3527602046.

[114] Nguyen, Q.B., Gupta, M. “Increasing significantly the failure strain and work of fracture of solidification processed AZ31B using nano-Al_2O_3 particulates.” *Journal*

of Alloys and Composites, vol. 459, no. 1-2, pp. 244-250. https://doi.org/10.1016/j.jallcom.2007.05.038.

[115] Martín, A., Llorca, J. "Mechanical behaviour and failure mechanisms of a binary Mg 6%Zn alloy reinforced with SiC particulates." *Materials Science and Engineering: A*, vol. 201, no. 1-2, October 1995, pp. 77-87. https://doi.org/10.1016/0921-5093(95)09777-5.

[116] Alam, M.E., Han, S., Nguyen, Q.B., Hamouda, A.M.S., Gupta, M. "Development of new magnesium based alloys and their nanocomposites." *Journal of Alloys and Compounds*, vol. 509, no. 34, August 2011, pp. 8522-8529. https://doi.org/10.1016/j.jallcom.2011.06.020.

CHAPTER III
EXPERIMENTAL PROCEDURE

3.1. Mg-CNT Nanocomposite Fabrication

Magnesium powder is the matrix material, and high-purity (>95%), single-walled carbon nanotubes (SWCNTs) from US Research Nanomaterials Inc., 15-50 μm in length, with an average diameter of 1.1 nm are the reinforcement phase in this project. A powder metallurgy technique was used to fabricate both monolithic magnesium and magnesium reinforced with 0.25, 0.5, and 0.75 vol.% CNTs at the National University of Singapore (NUS) by Dr. Manoj Gupta, and his student, Vyasaraj Manakari. This project would not be possible without their help fabricating these nanocomposites.

Magnesium powders and their appropriate, carefully weighed amounts of carbon nanotubes were blended in the absence of balls using a RETSCH PM-400 (Retsch, GmbH, Haan, Germany) mechanical alloying machine at 200 rpm for two hours. These blended powders were compacted using a 100-ton uniaxial compaction machine to obtain a green compact. This green compact was then sintered using a hybrid microwave setup (640°C for the total duration of approximately 15 minutes) to obtain a near-dense billet. The as-sintered billet was then soaked at 400°C for one hour in an isothermal furnace before extrusion at 350°C at an extrusion ratio of 20.25:1 using a 150 T hydraulic press. Cylindrical rods of 8 mm diameter were obtained. This process is shown in Figure 3.1.

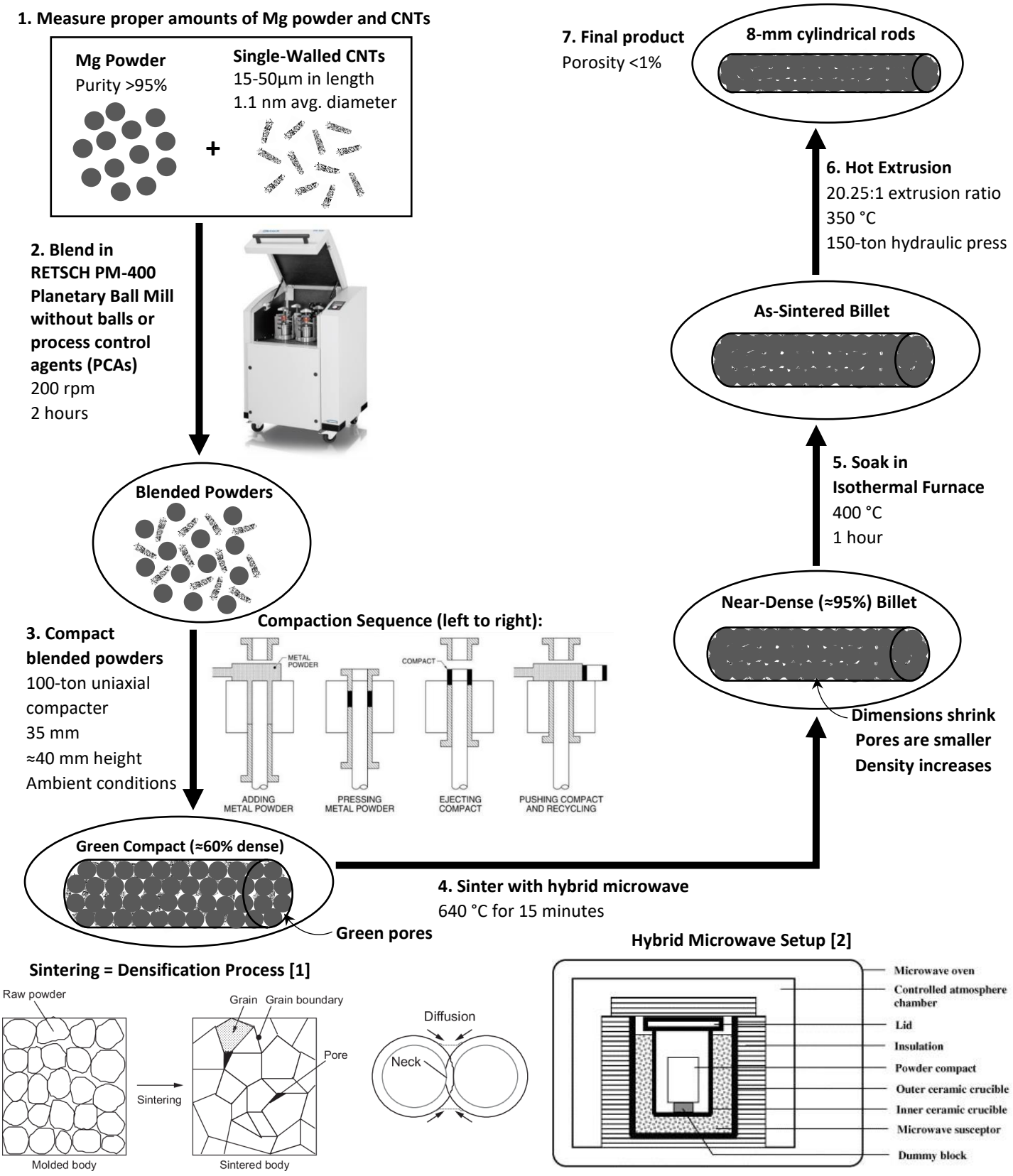

Figure 3.1. Schematic of the Mg-CNT nanocomposite fabrication method. Note that step 2 (blending step) is omitted for pure Mg only. Figure credit goes to Uchino [1] for sintering process and Gupta et. al [2] for hybrid microwave setup graphic.

Samples from these extruded rods were characterized for microstructure, hardness, and creep characterization at ambient (i.e., room) and elevated temperatures. High-magnification field emission scanning electron microscope (FE SEM) observations were used to ensure the CNTs were evenly distributed throughout the Mg matrix for homogeneous microstructure and that minimal clusters were present at NUS. Dr. Manoj Gupta and his research group selected an optimized extrusion ratio of 20.25:1 because this ratio has porosity levels of less than 1% in most cases. For clarification, all properties assessed in this project, everything from hardness to creep response, refer to those taken with measurements parallel to the extrusion direction. Further studies must be performed to quantify the dependence of measurement direction on Mg-CNT nanocomposite properties.

3.2. Experimental Procedure for Room Temperature Creep Tests

Before characterizing the samples with optical microscopy and scanning electron microscopy (SEM), the samples were first mounted in black phenolic mounting powder, as shown in Figure 3.2. Then, the surface of each sample was mechanically polished with a series of progressively finer SiC sandpapers until each sample surface was scratch-free and mirror-like. To finish the polishing process, the samples were treated with a suspension of 0.1 μm alumina polishing powder, followed by final polishing with a bare cloth under water for approximately ten minutes to remove any residual strains. Lastly, all samples were placed in an acidic acetic-picral etchant (100 mL ethanol, 2.5 g picric

acid, 25 mL acetic acid, and 25 mL distilled water) for around 10 seconds to reveal the microstructure of the sample.

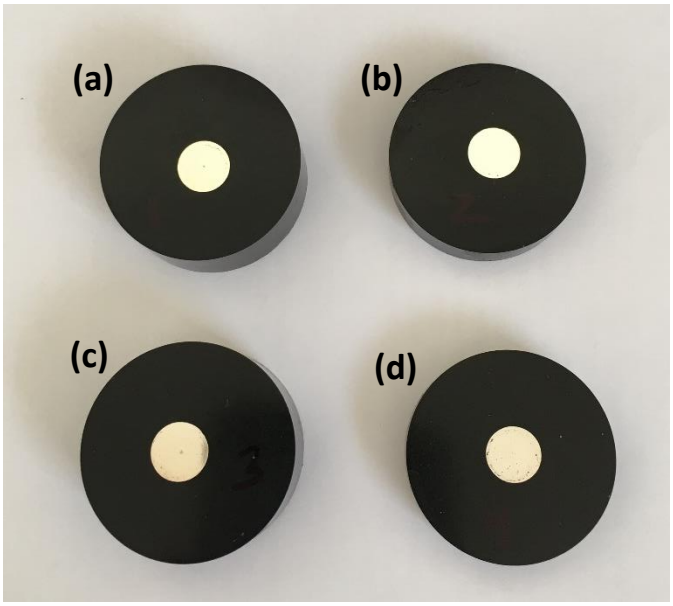

Figure 3.2. Four samples (pictured after nanoindentation) used for room-temperature tests: (a) Pure Mg, (b) Mg-0.25 CNT, (c) Mg-0.5 CNT, and (d) Mg-0.75 CNT.

Room temperature indentation creep tests were performed with an iNano Nanoindenter (KLA-Tencor Corporation), pictured in Figure 3.3, equipped with a diamond Berkovich indenter with a tip roundness of about 100 nm. The geometry of a Berkovich indenter is shown in Figure 3.4. All tests were dual-stage in nature and each test generates a load-displacement curve, as shown in Figure 3.5. The first test stage involves loading the materials at one of four strain rates (0.01, 0.1, 1, or 10 s^{-1}) until a peak load of 50 mN is reached, at which point the second stage, holding, occurs. At this second stage, the peak load is held constant for 500 seconds (dwell period), and at this

time the plastic deformation (creep) data are recorded at fixed intervals. Finally, the indenter is unloaded by 10% of the maximum load and held for another 120 seconds to correct for thermal drift (keeping this error below 0.05 nm/s). The effect of thermal drift is negligible in the room temperature portion of the project because: (i) the tests are done at room temperature, and (ii) the dwell time is relatively short, 120 seconds. For every combination of material and load rate, five indentation creep tests were performed, for a total of 80 room temperature creep tests.

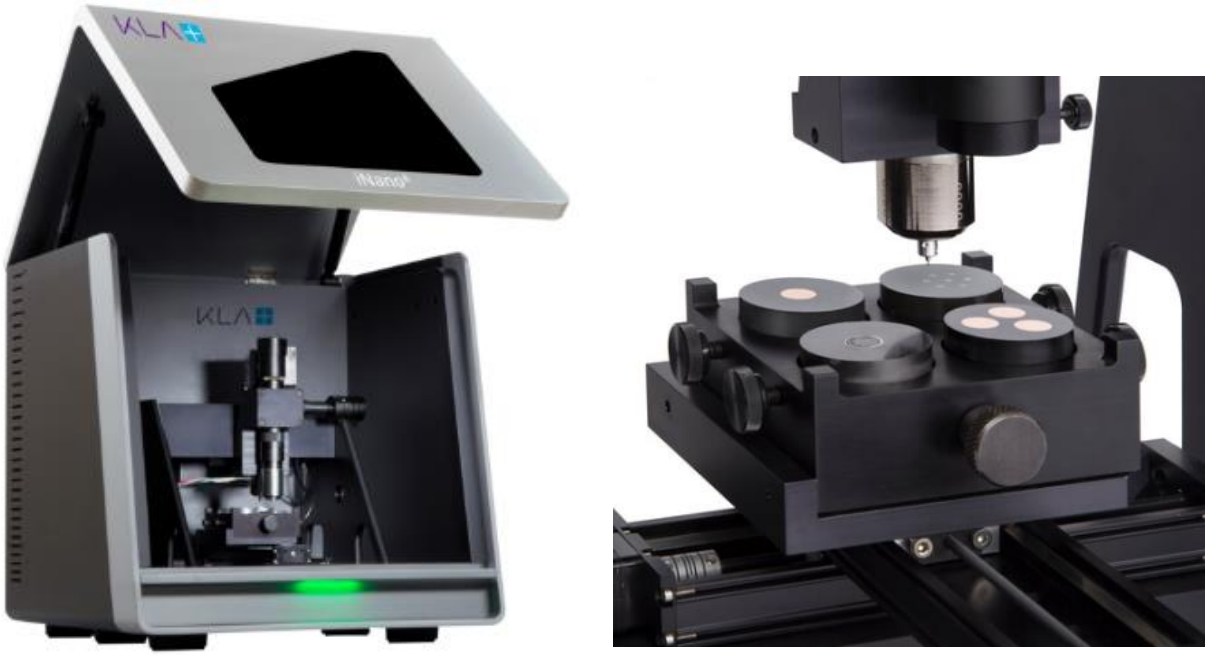

Figure 3.3. KLA-Tencor iNano nanoindenter (left) and indentation platform (right).

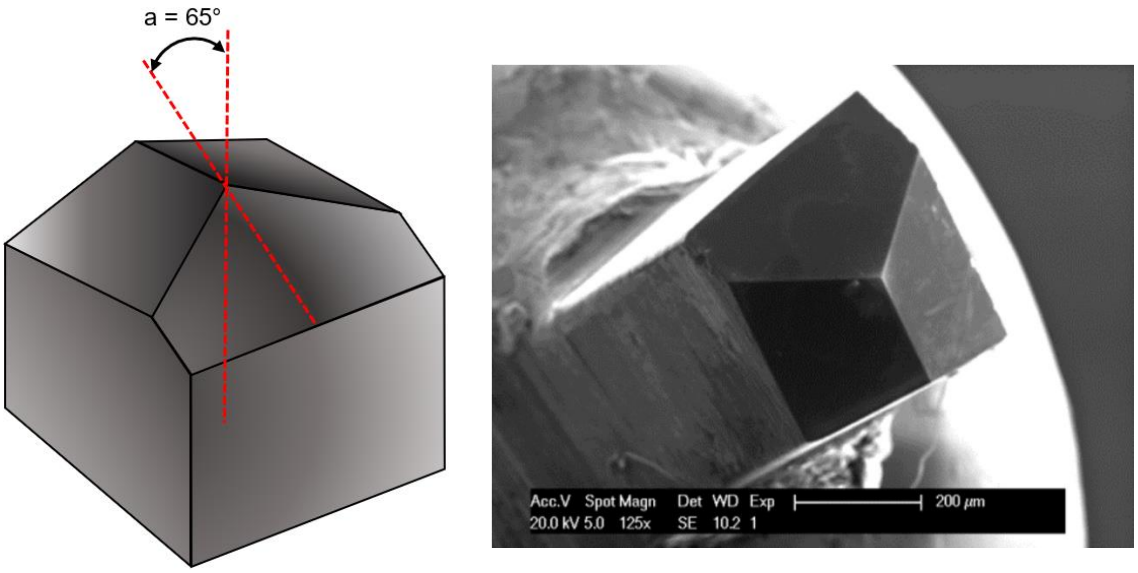

Figure 3.4. Geometry of a Berkovich indenter (left) where "a" is the angle defined as the angle between the centerline axis and any of the faces (also called "half angle" and "face angle"). SEM image of a diamond Berkovich indenter tip (right) [3].

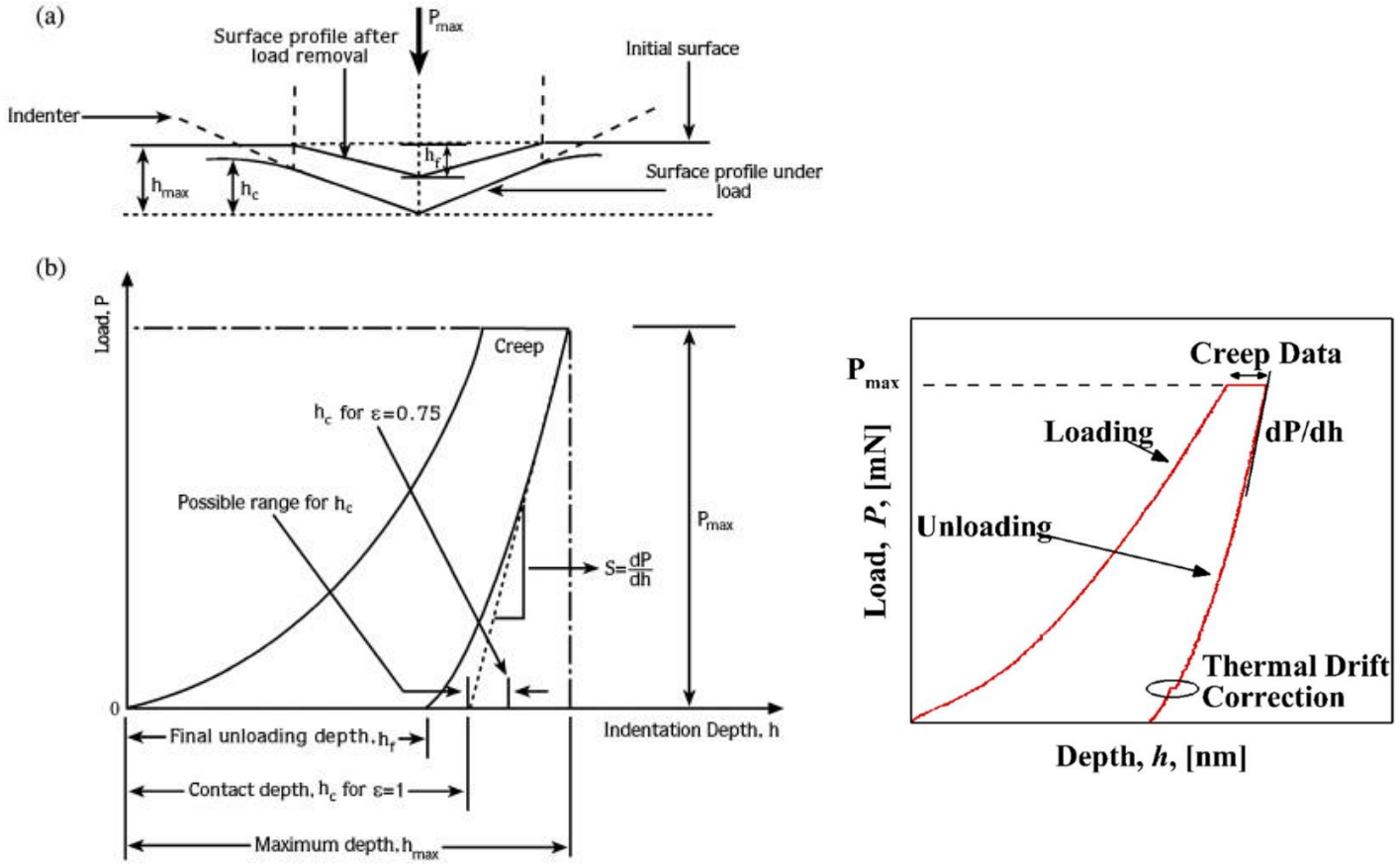

Figure 3.5. Typical load-displacement curves (also called *P-h* curves) generated during a dual-stage indentation test. Schematic (a) is the cross-sectional view of an indentation. Diagram (b) is a typical load-displacement curve obtained during an indentation creep test and key parameters for analysis are identified [4]. The curve on the right also illustrates stiffness (dP/dh) and creep, but additionally indicates where thermal drift corrections occur [5].

3.3. Experimental Procedure for Elevated Temperature Creep Tests

The preparation procedure for high-temperature creep tests is similar to that for room temperature, only these samples are not mounted, testing parameters are slightly different, and a different nanoindenter was used for these tests.

The samples for high-temperature indentation creep tests were cut from the same billets as the samples for room temperature study. These samples are not mounted in the black phenolic powder because this powder would soften under the high-temperature testing conditions, thereby ruining the creep tests. Instead, small, unmounted sections of the billet were carefully polished to the mirror-like and scratch-free condition described in the room temperature procedure and were then ready for elevated-temperature nanoindentation testing. Figure 3.6 shows the small, unmounted samples used in this project after the nanoindentation tests were performed.

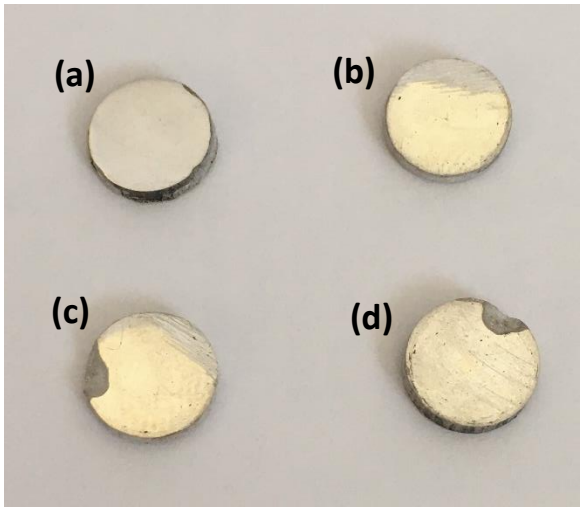

Figure 3.6. Four samples (pictured after nanoindentation) used for elevated-temperature tests: **(a)** Pure Mg, **(b)** Mg-0.25 CNT, **(c)** Mg-0.5 CNT, and **(d)** Mg-0.75 CNT.

Elevated-temperature indentation creep tests were performed using a high-temperature vacuum nanoindentation system (NanoTest Xtreme, Micro Materials, UK) equipped with a cubic boron nitride nanocomposite (BNNC) Berkovich indenter (tip roundness ≈ 470 nm). The NanoTest Xtreme is pictured in Fig. 3.7. Again, the dual-stage testing protocol was followed (illustrated in Figure 3.5).

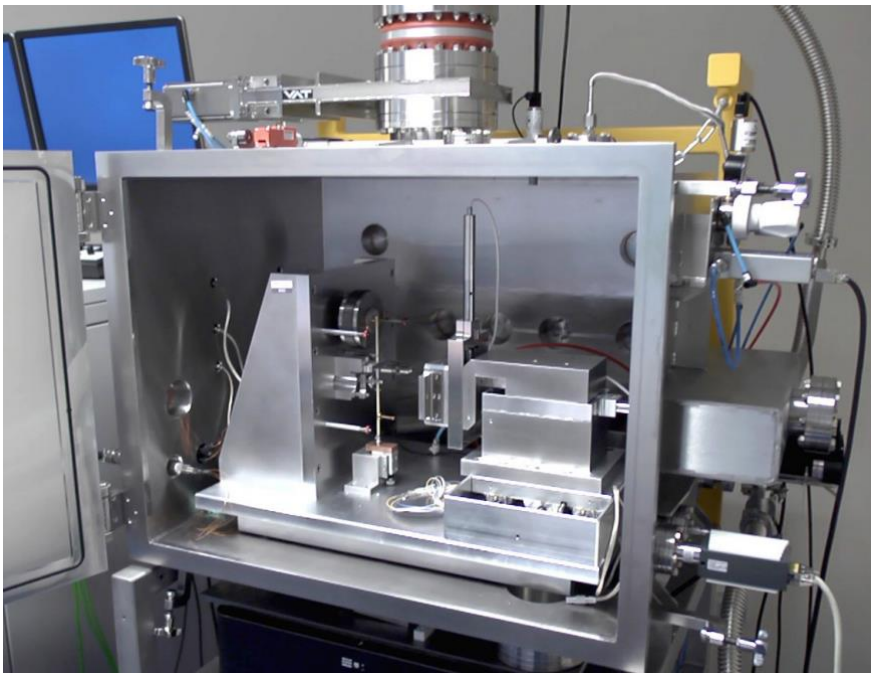

Figure 3.7. The NanoTest Xtreme nanoindenter (Micro Materials, UK) situated inside the vacuum chamber [6].

This time, each of the four samples was loaded according to one of three loading rates (0.5, 5, or 50 mN/s) until a peak load of 50 mN was reached. This peak load was held constant for a dwell period of 120 seconds. These testing combinations were all carried out at 298 K, 373, 473, and 573 K. Five creep tests were performed for every combination of material, load rate, and temperature for a total of 240 tests, not including 5 reruns on one parameter combination.

3.4. From *P-h* curves to Useful Mechanical Properties: Hardness, Young's Modulus, and Steady-State Creep Theory for Nanoindentation

In an indentation test, the two most common and readily available mechanical properties that can be extracted from the load-displacement curves (Fig. 3.5) are indentation hardness and elastic modulus. Oliver and Pharr [7] are to thank for spearheading the extraction of these mechanical properties from indentation tests by devising the Oliver-Pharr method in 1992, which is used to this day to readily obtain these properties. The indentation hardness during an indentation test can be obtained with the following equation:

$$H_{ind} = \frac{P_{max}}{A_c} \qquad \text{(Equation 3.1)}$$

Where H_{ind} is the indentation hardness (in GPa in this project), P_{max} is the maximum indentation load, i.e., 50 mN across all tests here, and A_c is the projected area of the hardness impression.

Nanoindentation tests readily provide reduced elastic moduli (E_r), but to be more relevant these results must be converted from reduced moduli to elastic moduli. The following equation illustrates how this conversion is made mathematically.

$$\frac{1}{E_r} = \frac{(1-\nu_s^2)}{E_s} + \frac{(1-\nu_i^2)}{E_i} \qquad \text{(Equation 3.2)}$$

Where ν is Poisson's ratio, E is elastic (Young's) modulus, and *i* corresponds to indenter, and *s* corresponds to sample. For diamond indenters, E_i = 1140 GPa and ν_i = 0.07. For a boron nitride nanocomposite (BNNC) indenter, E_i = 800 GPa and ν_i = 0.12. Other useful properties that can be obtained from hardness and reduced elastic modulus results are elastic strain resistance $\left(\frac{H}{E_r}\right)$ and elastic pressure $\left(\frac{H^3}{E_r^2}\right)$.

Extracting creep information from load-displacement data is not quite as straightforward as the extraction of hardness and Young's modulus, but the procedure is doable so long as a careful analysis is conducted. It is important to keep in mind that all creep information is extracted from the holding/dwell part of the load-displacement curve (the flat portion of Fig. 3.5), because this is where creep occurs in the material.

Mayo and Nix [8] generalized the minimum indentation creep (or equivalently, strain) rate of Pollock et. al [9] to pyramidal indenters (e.g., Berkovich indenters) as follows:

$$\dot{\varepsilon}_{ind} = \frac{1}{h} * \frac{dh}{dt} \qquad \text{(Equation 3.3)}$$

where $\dot{\varepsilon}_{ind}$ is the minimum indentation creep rate (or indentation strain rate), h is indentation depth, and $\frac{dh}{dt}$ is the depth rate. This equation can be further narrowed down to represent the steady-state creep rate of crystalline materials as shown by the well-established Mukherjee-Bird-Dorn equation (also a close variant of the Norton-Arrhenius equation) [10-14]:

$$\dot{\varepsilon}_{\text{ind}} = \frac{AD_0Gb}{k_BT}\left(\frac{b}{d}\right)^p\left(\frac{\sigma_{ind}}{G}\right)^n \exp\left(-\frac{\Delta Q}{k_BT}\right) \qquad \text{(Equation 3.4)}$$

where A is the material constant, D_0 is the frequency factor, G is the shear modulus, b is the Burgers vector, p is the inverse grain size exponent, n is the stress exponent (also called the power law exponent), Q (sometimes written Q_c or Q_{ind}) is the apparent activation energy for creep, k_B is the Boltzmann constant, T is absolute temperature, d is the grain size, and σ_{ind} is the applied indentation stress. Specific to Berkovich indenters, σ_{ind} is expressed in Eqn. 3.5, where C is a constant, h is indentation depth, and R is tip radius.

$$\sigma_{\text{ind}} = \frac{P}{24.56 * C(h + 0.06R)^2} \qquad \text{(Equation 3.5)}$$

Additionally, the steady-state creep rate can be further narrowed to that of a polycrystalline material as shown [12]:

$$\dot{\varepsilon}_{ind} = \frac{A\sigma_{\text{ind}}^n}{d^qT}\exp\left(-\frac{Q_{\text{ind}}}{RT}\right) \qquad \text{(Equation 3.6)}$$

with all of the equation variables defined the same as in Eqn. 3.4. A key variable of interest to this project is n, the stress exponent, because it gives information regarding the rate-controlling deformation mechanism during creep. Lumping the constant terms, $\frac{A}{d^q T}$, in Eqn. 3.6 together and calling this new term, *B*, the equation is reduced to Eqn. 3.7 shown below, and the stress exponent is more readily determinable.

$$\dot{\varepsilon}_{ind} = B\sigma_{ind}^{n} \exp\left(-\frac{Q_{\text{ind}}}{RT}\right) \qquad \text{(Equation 3.7)}$$

Applying elementary algebra and the laws of logarithms to this equation, we arrive at an intermediate step to isolating the stress exponent, shown below:

$$\ln \dot{\varepsilon}_{\text{ind}} = \ln \text{B} + n \ln \sigma_{\text{ind}} - \frac{Q_{\text{ind}}}{RT} \qquad \text{(Equation 3.8)}$$

At isothermal and steady-state creep conditions, the stress exponent, *n*, can be determined from the slope of a plot graphing $\ln \dot{\varepsilon}_{ind}$ versus $\ln \sigma_{ind}$, in accordance with this creep power law equation:

$$n = \frac{d \ln \dot{\varepsilon}_{ind}}{d \ln \sigma_{ind}} \qquad \text{(Equation 3.9)}$$

Additionally, Q can be calculated from the slop of the plot of a graph of $\ln \dot{\varepsilon}_{ind}$ versus $\frac{1}{T}$ (for a constant stress). A schematic depiction of the logarithmic plots and calculations necessary to obtain *n* and Q are shown in Figure 3.8.

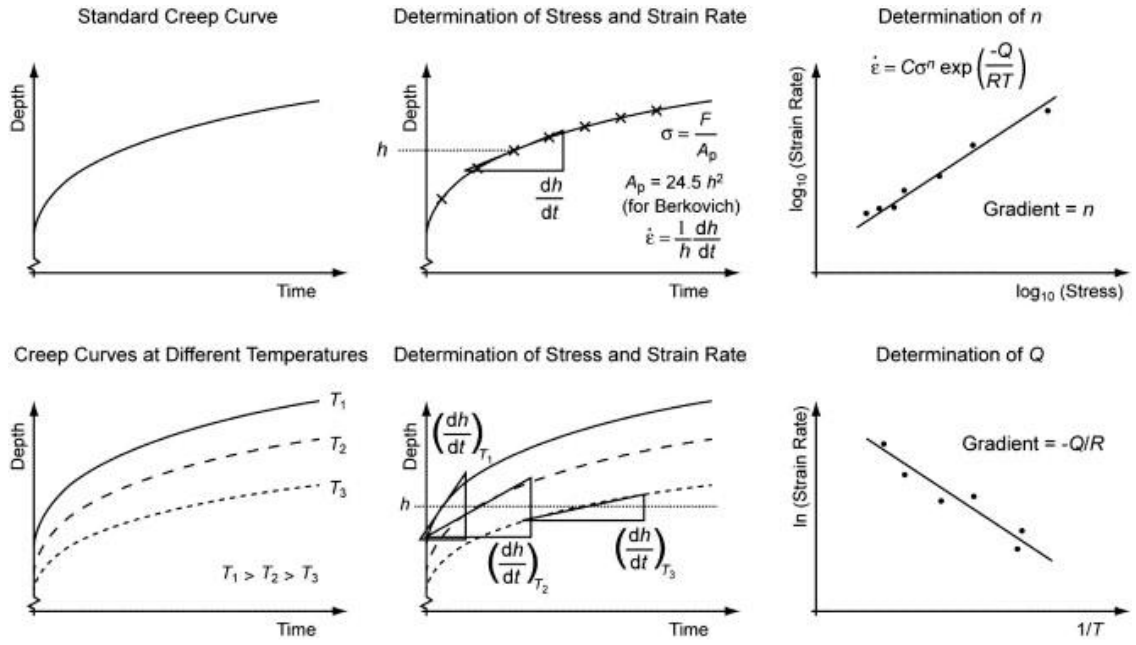

Figure 3.8. Schematic depiction of how load-displacement information from a creep test (strictly under the holding/dwell period) can be used to determine the values of the stress exponent and the activation energy taken from Goodall and Clyne [15].

REFERENCES

CHAPTER III – EXPERIMENTAL PROCEDURE

[1] Uchino, K., "Manufacturing Methods for Piezoelectric Ceramic Materials." *Advanced Piezoelectric Materials*. December 2017, p. 398. DOI: 10.1016/B978-0-08-102135-4.00010-2

[2] Gupta, M., and Wong, W.L.E. "Enhancing overall mechanical performance of metallic materials using two-directional microwave assisted rapid sintering." *Scripta Materialia*, vol. 52, no. 6, March 2005, pp. 479-483. doi:10.1016/j.scriptamat.2004.11.006

[3] Zhang, H. *Experimentally validated multi-scale fracture modelling scheme of cementitious materials.* October 2019, p. 42. Delft University of Technology, Dissertation.

[4] Şahin, O., Uzun, O., Kölemen, U., and Uçar, N. "Mecahnical characterization for β-Sn single crystals using nanoindentation tests." *Materials Characterization*, vol. 59, no. 4, April 2008, pp. 427-434. doi:10.1016/j.matchar.2007.02.016

[5] Verma, D., Qu, T., and Tomar, V. "Scale Dependence of the Mechanical Properties and Microstructure of Crustaceans Thin Films as Biomimetic Materials." *Journal of The Minerals, Metals & Materials Society (TMS)*, vol. 67, no. 4, March 2015, pp. 858-866. DOI: 10.1007/s11837-015-1337-4.

[6] "NanoTest Xtreme Advantages." NanoTest Xtreme datasheet. Micro Materials Ltd. Retrieved from: www.micromaterials.co.uk. Accessed 12 March 2020.

[7] Oliver, W.C., Pharr, G.M. "An improved technique for determining hardness and elastic modulus using load and displacement sensing indentation experiments." *Journal of Materials Research*, vol. 7, no. 6, June 1992, pp. 1564-1583. https://doi.org/10.1557/JMR.1992.1564.

[8] Goodall, R., and Clyne, T.W. “A critical appraisal of the extraction of creep parameters from nanoindentation data obtained at room temperature.” *Acta Materialia*, vol. 54, no. 20, December 2006, pp. 5849-5499. doi:10.1016/j.actamat.2006.07.020

[9] Pollock, H.M., Maugis, D., and Barquins, M. “Characterisation of submicrometre surface layers by indentation.” In: Blau, P.J., Lawn, B.R., editors. Microindentation techniques in materials science and engineering. Philadelphia (PA): ASTM; 1986, p. 47-71.

[10] Katsarou, L., et al. “Microstructure, mechanical properties and creep of magnesium alloy Elektron21 reinforced with AlN nanoparticles by ultrasound-assisted stirring.” *Materials Science & Engineering A*, vol. 659, April 2016, pp. 84-92. http://dx.doi.org/10.1016/j.msea.2016.02.042

[11] Ganguly, S., and Mondal, A.K. “Influence of SiC nanoparticles addition on microstructure and creep behavior of squeeze-cast AZ91-Ca-Sb magnesium alloy.” *Materials Science and Engineering A*, vol. 718, March 2018, pp. 377-389. https://doi.org/10.1016/j.msea.2018.01.131

[12] Mukherjee, A.K., Bird, J.E., Dorn, J.E. “Experimental correlations for high-temperature creep.” *Trans. ASM*, vol. 62, 1969, pp. 155-179.

[13] Fernández, R., and González-Doncel, G. “Threshold stress and load partitioning during creep of metal matrix composites.” *Acta Materialia*, vol. 56, no. 11, June 2008, pp. 2549-2562. doi:10.1016/j.actamat.2008.01.037.

[14] Ma, Z.Y., Mishra, R.S., Tjong, S.C. “High-temperature creep behavior of TiC particulate reinforced Ti-6Al-4V alloy composite.” *Acta Materialia*, vol. 50, no. 17, October 2002, pp. 4293-4302. https://doi.org/10.1016/S1359-6454(02)00261-6.

[15] Goodall, R., and Clyne, T.W. “A critical appraisal of the extraction of creep parameters from nanoindentation data obtained at room temperature.” *Acta Materialia*, vol. 54, no. 20, December 2006, pp. 5849-5499. doi:10.1016/j.actamat.2006.07.020

CHAPTER IV
RESULTS AND DISCUSSION OF INDENTATION CREEP TESTS PERFORMED AT ROOM AND ELEVATED TEMPERATURE

4.1. Microstructure and Grain Morphology

Optical microscopy (OM) was used to characterize the microstructure and grain morphology of the Mg-CNT nanocomposites. The optical micrographs taken to investigate the size, condition, and orientation of the grains are shown in Figure 4.1. Most readily noticeable are the severely deformed grains visible in all four samples, due to the hot extrusion step in the manufacturing process. Mechanical twins are also evident in Pure Mg (a) in Figure 4.1. Kumar et al. report that twinning adversely impacts the strength and formability of magnesium [1]. Twinning in pure Mg is a feature that can also help explain other mechanical properties, i.e., creep and hardness, discussed later.

Some marginal grain refinement is also visible in Fig. 4.1, when comparing the evolving microstructure behavior from pure Mg to higher CNT loadings of CNTs. From the OM images taken, the grain sizes of these samples fell in the 75-100 μm range.

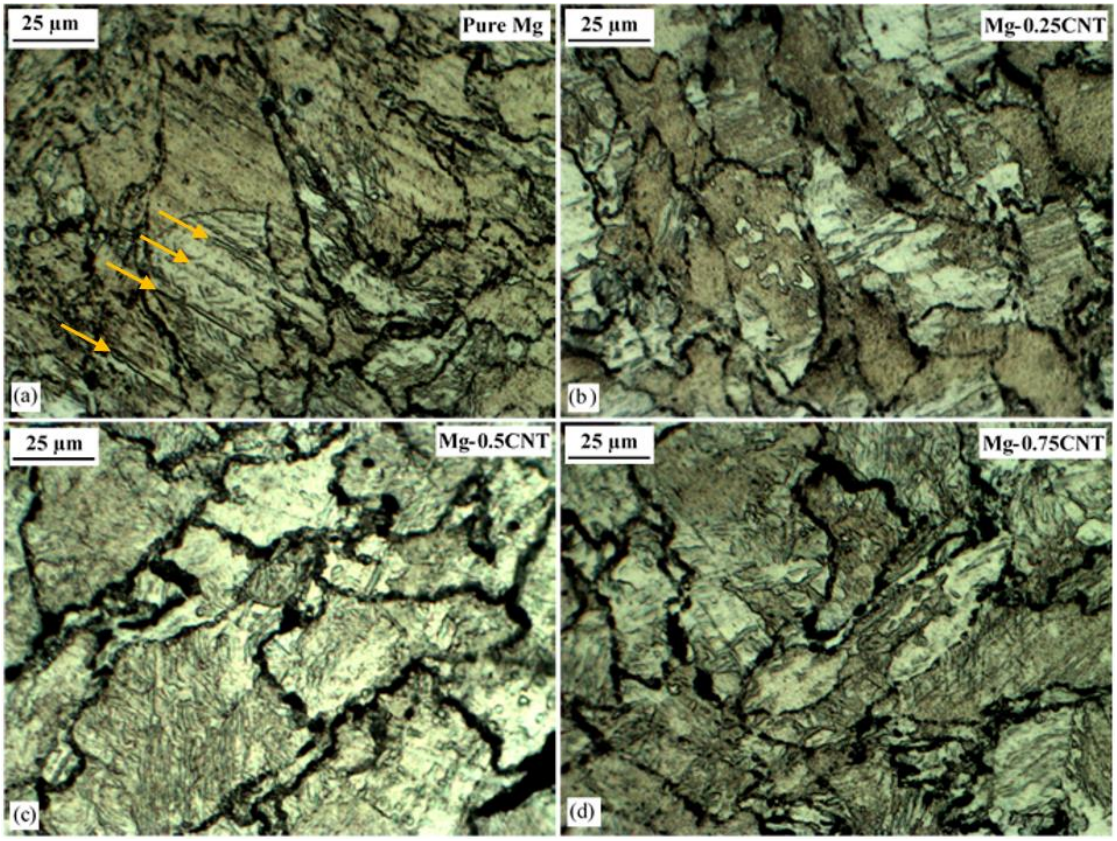

Figure 4.1. Optical micrographs revealing the cross-sectional grain morphologies and microstructures (those parallel to the extrusion direction) of **(a)** Pure Mg, **(b)** Mg-0.25 CNT, **(c)** Mg-0.5 CNT, and **(d)** Mg-0.75 CNT. Arrows are added to **(a)** to indicate the presence of mechanical twins in Pure Mg.

Scanning electron microscopy (SEM) imaging was used to assess the integrity of the particle-matrix interface to assure the CNTs were in fair condition and were well-dispersed throughout the matrix. Figure 4.2 presents magnesium reinforced with 0.5 vol.% CNTs, and the inset at higher magnification reveals the fibrous nature of the CNTs in the Mg matrix.

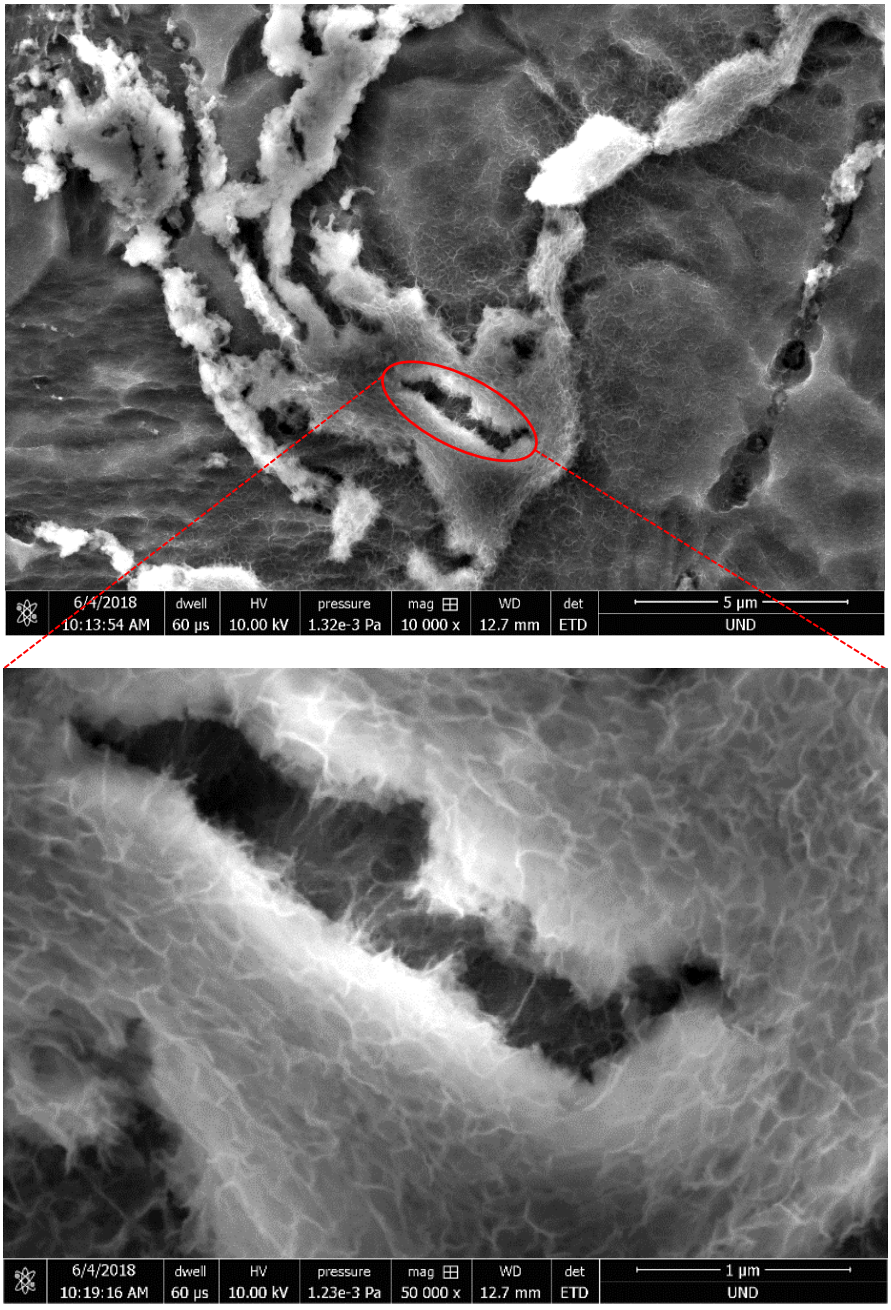

Figure 4.2. Scanning electron microscopy (SEM) images of Mg-0.5 vol.% CNT. A single CNT fiber is pointed out in the higher-magnification SEM inset, indicated with an arrow.

Due to the nature of the processing method used to fabricate these materials, i.e., powder metallurgy, the formation of magnesium oxide particles is unavoidable and expected (due to the contact between Mg and oxygen during powder preparation). To verify the presence of MgO in the samples, energy-dispersive spectroscopy (EDS) was used. Figure 4.3 shows the EDS analysis performed on Mg-0.5 vol.% CNT. Spectrum points 1,2, 3, and 6 were chosen as candidates to be MgO particles. The EDS spectra reveals that points 1 and 2 indeed consist of Mg and O, however points 3 and 6 have Mg, O, and some C, likely because points 3 and 6 included CNTs. Spectrum points 4 and 5 were control points made to ensure that the matrix material is indeed pure Mg, and the results of the EDS spectra confirm this.

A study by Ding et al. [2] also studied the effect of CNTs on a Mg matrix. The nanocomposites were produced by powder metallurgy and they contained 38 wt.% CNTs. They nickel-coated their CNTs before incorporation into the Mg matrix and still ended up with MgO in their samples. This confirms how completely natural it is to have MgO particles in the sample due to oxidation during the powder metallurgy process. Ding et al. also note that MgO likely had an influence on hardness and other mechanical properties during testing.

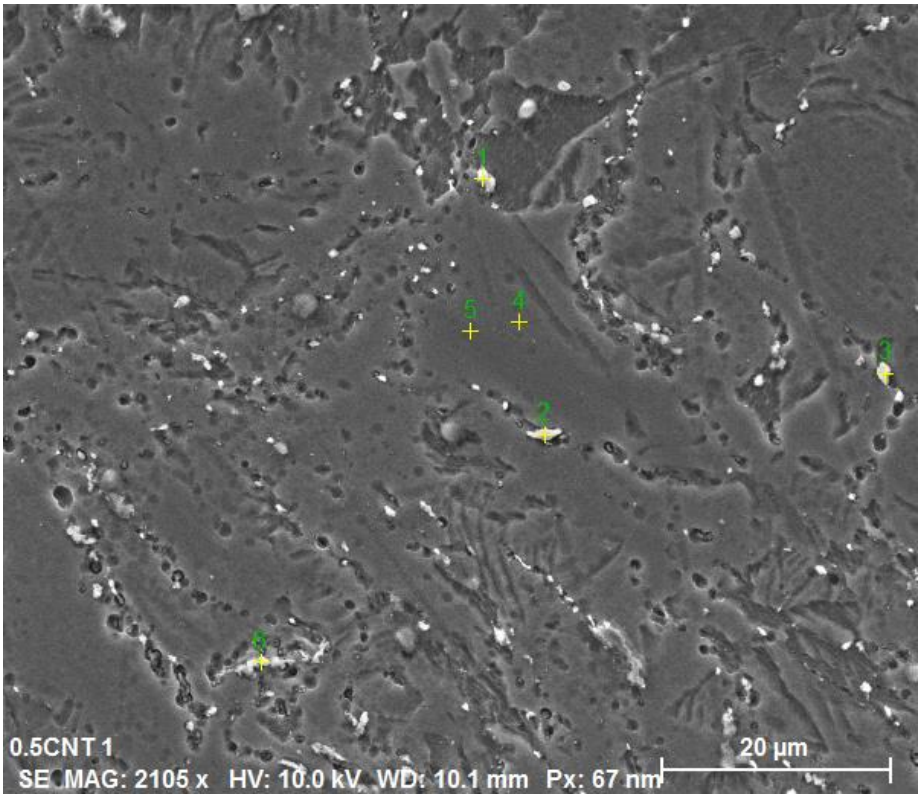

Norm. mass percent (%)

Spectrum	C	O	Mg
1	-	43.34	56.66
2	-	39.19	60.81
3	8.46	41.82	49.72
4	-	-	100.00
5	-	-	100.00
6	4.28	17.78	77.94

Figure 4.3. Energy Dispersive X-ray Spectroscopy (EDS) performed on Mg-0.5 vol.% CNT sample to verify the sample composition.

4.2. Ambient (Room) Temperature Results

4.2.1. Load-Displacement Curves

Figure 4.4 presents the load-displacement (*P*–*h*) curves for all Mg-CNT nanocomposites at room temperature. In all *P*-*h* curves, it can be seen that when strain rate increases, the required load to reach a constant depth increases. This is a work hardening effect. The rates of dislocation generation and dislocation multiplication are also enhanced as strain rates increase in the loading stage [3-5]. The grain boundaries or the CNTs in the matrix can block these newly formed dislocations. This is evidence to confirm that magnesium and its CNT-nanocomposites are rate-sensitive at room temperature. The trend becomes more pronounced at higher CNT loadings in Mg simply because there are more obstacles (CNTs) impeding dislocation motion.

It should also be borne in mind that additional geometrically necessary dislocations (GNDs) can be formed from thermal and physical processing due to the magnesium matrix and the CNTs having differing coefficients of thermal expansion (CTE) and elastic moduli, i.e., CTE mismatch and elastic modulus mismatch. GNDs formed through CTE and elastic modulus mismatch help to strengthen the material. Eqns. 2.3 and 2.4 from the previous chapter mathematically express the hardening effect due to CTE and elastic modulus mismatch, respectively.

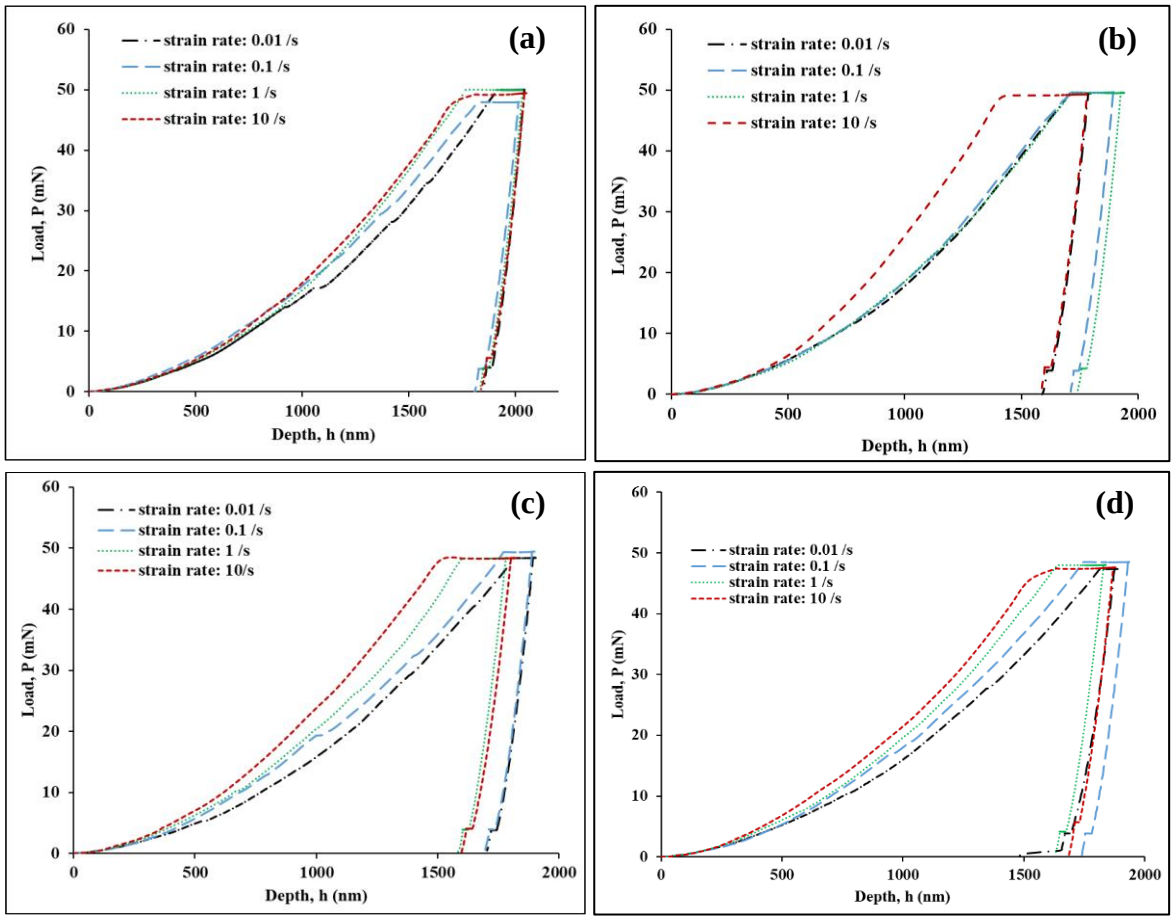

Figure 4.4. Load-displacement (or *P-h*) curves displaying loading, holding, and unloading measurements at all four strain rates tested (0.01–10 s^{-1}) for: **(a)** Pure Mg, **(b)** Mg-0.25 vol.% CNT, **(c)** Mg-0.5 vol.% CNT, and **(d)** Mg-0.75 vol.% CNT.

4.2.2. Indentation Stress versus Depth Behavior

From classical plasticity, or more specifically continuum mechanics, it is expected that a material's properties (e.g., hardness) are independent of scale. In other words, hardness should not change regardless of how shallow or deep an indent is, given that the tip is self-similar, e.g., conical or wedge-shaped tips, because hardness does depend on the angle of the cone or wedge. However, a large size-dependence is observed in indentation tests on metals with self-similar indenter tips [6-8] This large size-dependence is a phenomenon considered as a deviation from classical plasticity and it is well-known as the Indentation Size Effect (ISE).

Indentation stress for a Berkovich indenter as a function of indentation depth and indenter tip radius is expressed mathematically in Eqn. 3.5 in Chapter III. Figure 4.5 presents indentation stress (σ) as a function of indentation depth (h) for all strain rates and materials tested. Strong indentation size effects are observed in all four samples and over all strain rates tested.

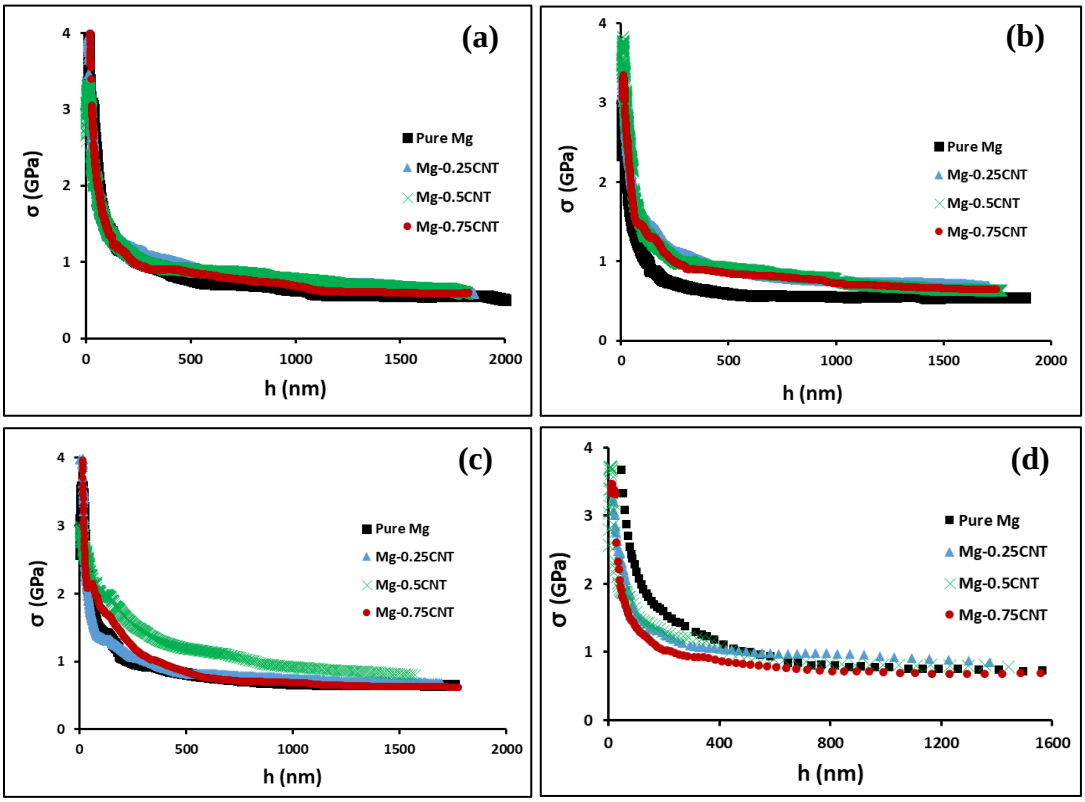

Figure 4.5. Indentation stress (σ_{ind}) versus displacement (h) curves for all materials over strain rates of: **(a)** 0.01 /s, **(b)** 0.1 /s, **(c)** 1.0 /s, and **(d)** 10 /s. The indentation size effect (ISE) is observed in all tests.

Indentation size effects can be understood through dislocation starved plasticity (DSP) and strain gradient plasticity (SGP) [9-11]. According to DSP, at the very beginning stage of the nanoindentation, the material volume beneath the indenter is quite small and can be considered as a dislocation-free structure [9]. This implies that the strength of the material can be as large as the theoretical strength. Naturally, as the indenter tip presses further into the sample, a larger volume beneath the indenter is available for dislocation generation. At this point, SGP can be used to explain the ISE. The material will generate geometrically necessary dislocations (GNDs) to accommodate

the shape of the indenter within the sample. However, there is only a limited volume for the GNDs to generate and interact. Normal, statistically stored dislocations (SSDs) from within the material are expected and do not contribute anything new to the strengthening mechanisms of the material. GNDs have different Burgers' vectors, slip systems, and mobility systems which allow them to directly contribute toward strengthening of the material in the shallow (near the surface) areas.

It is expected that Mg reinforced with CNTs will have more pronounced ISE effects. When the number of CNTs in the sample increases, the number of obstacles impeding dislocation motion, i.e., GNDs and SSDs, increases. As these obstacles impede dislocation motion, pile-ups form, and this is due to a stronger pinning effect of the obstacles, i.e., CNTs and/or grain boundaries. This creates a greater local work hardening effect through Orowan strengthening, discussed in the last chapter in Section 2.3.4.3.

This does not explain why ISE occurs, however. When the indenter is well-below the material's surface (at a large indentation depth), the mechanisms at play become more involved. There is a complex interplay among dislocation generation and multiplication, and dynamic recovery induced by dilation rearrangement and annihilation. This is what causes the plateaued trend in the indentation stress versus depth curves at deeper indentation depths.

4.2.3. Indentation Hardness as a Function of CNT Loading

Intuitively, one may think that adding higher and higher CNT loadings into a magnesium matrix yields a composite material with increasingly higher hardness. Figure 4.6 is evidence that this is indeed not the case. The figure shows indentation hardness as a function of CNT loading for all materials and all strain rates tested. There appears to be a parabolic trend in that hardness is low at pure Mg and is low again at 0.75 vol.% CNTs, however hardness reaches a maximum somewhere between 0.25 and 0.5 vol.% CNTs, depending on the strain rate. Intermolecular forces, namely van der Waals forces, are largely responsible for this observed parabolic behavior.

CNTs are strongly attracted to one another by van der Waals forces, and this can cause agglomerations to form. Agglomerations of CNTs lower the hardness of the overall composite because CNT clusters cause defects, higher stress concentrations, and ultimately result in hard spots and soft spots throughout the composite (worsened mechanical properties). Further, the less uniformly distributed the CNTs are in the processing steps, the more likely agglomerations are to form [12, 13]. Of course, proactive de-agglomeration and the most uniform dispersion of the nanoparticles are goals during processing, however, these tasks are not trivial for metal matrix composites.

Some ways to accomplish dispersion and de-aggregation are through shear stress by erosion, bulk rupture during high shear mixing in milling, and ultrasonic processing (ultra-sonication) [12]. However, with nanoparticles the issue is only exacerbated by the

fact that as agglomerations become smaller through de-agglomeration, surface forces will dominate mass forces. This implies that mechanical action can only go so far in helping to de-agglomerate and it has been suggested that nanoparticles smaller than 10-100 nm cannot be broken up by mechanical action [14, 15].

Despite how easy CNTs can agglomerate, and how difficult it is to achieve uniform CNT dispersion throughout a Mg matrix, CNTs do offer hardness improvement at low volume percentages in Mg, as shown in Fig. 4.6. The initially improved hardness at these lower CNT loadings can be attributed to: (i) the presence of hard CNT in the Mg matrix, (ii) CNTs strengthening the composite by hindering dislocation movement (suppressing the recrystallization and growth of crystal grains), (iii) effective load transfer from the soft Mg matrix onto the hard CNT reinforcements, and (iv) generation and multiplication of dislocations through CTE and elastic modulus mismatch between Mg and CNTs [16, 17].

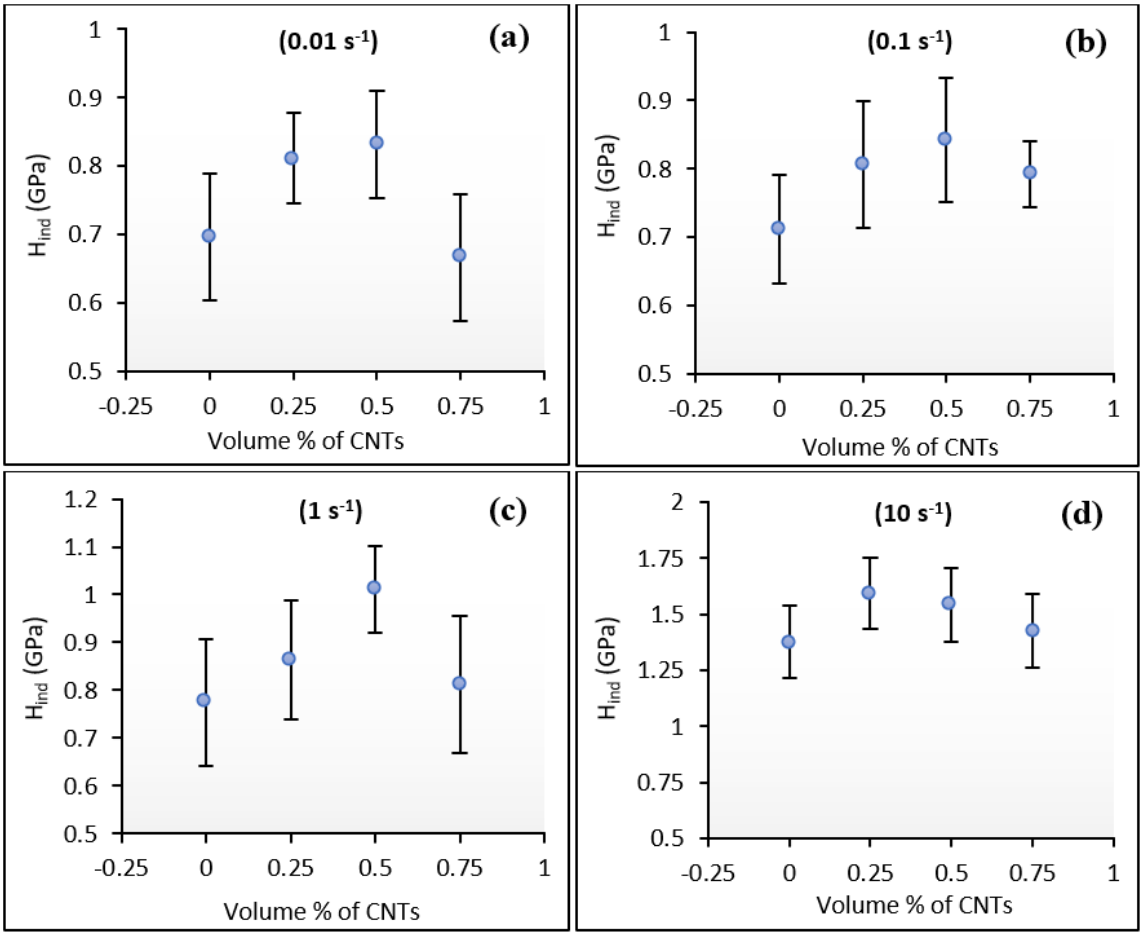

Figure 4.6. Indentation hardness (H_{ind}) as a function of CNT loading for all materials over four strain rates: **(a)** 0.01 /s, **(b)** 0.1 /s, **(c)** 1.0 /s, and **(d)** 10 /s.

4.2.4. Creep Rate and Displacement as a Function of Time

Figure 4.7 and 4.8 show the creep rate and creep displacement behavior over the 500 s dwell period, respectively. The dwell (or holding) period is where creep deformation is expected. As discussed in Chapter II, creep is a sensitive and complex phenomenon. Creep is dependent on temperature, time, and many other factors. From Fig. 4.7, it can be seen that creep rate is also a strain rate-dependent phenomenon. For

example, the highest recorded initial material creep rates increase from about 0.0013 s^{-1} to 0.035 s^{-1} going from the lowest strain rate (0.01 s^{-1}) to the largest one (10 s^{-1}).

A noteworthy consequence of the nanoindentation creep test itself being compressive also means there is no tertiary creep stage involved. In the absence of this tertiary stage, the steady-state stage provides a stable zone beneath the indenter. Fig. 4.8 illustrates the creep displacement as a function of dwell time, and the vertical red dashed line illustrates the creep stage transition from primary creep to steady-state creep (when displacement plateaus).

Perhaps it is still unclear as to why creep can even occur at room temperature since creep is often considered to be a high-temperature deformation. This quandary can be reasoned by considering how drastically different the stress distribution of an indentation creep test is as compared to a uniaxial tensile or compressive creep test. Consider, even at low displacements the maximum shear strength underneath the indenter far exceeds the yield stress of the specimen (large triaxial stresses in the magnitude of a few gigapascals). This is what permits creep to occur at room temperature, and over such a brief amount of time as compared to traditional testing methods.

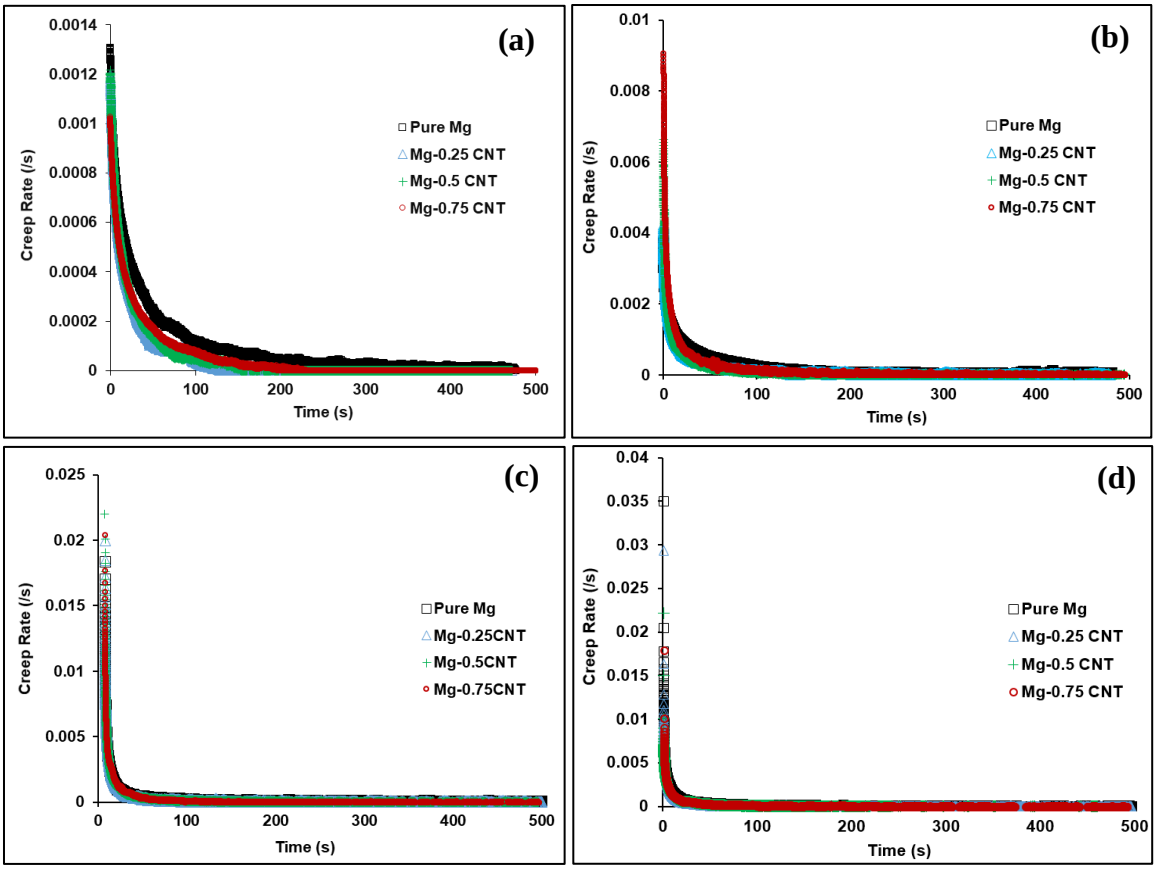

Figure 4.7. Creep rate (/s) as a function of time for all materials over the four strain rates of: **(a)** 0.01 /s, **(b)** 0.1 /s, **(c)** 1.0 /s, and **(d)** 10 /s.

Notice in Fig. 4.8 that pure Mg (black square series) has the largest creep displacement over all other nanocomposites in all strain rates tested. However, Mg-0.75 vol.% is just behind pure Mg in all strain rates tested too. This means that CNTs do provide magnesium creep resistance, but only at small volume fractions. Also from Figure 4.8, it appears that the Mg-0.25 vol.% CNT nanocomposite has the best creep resistance at room temperature as it has the lowest creep displacement over all tests conducted.

The CNTs provide this creep resistance either through pinning the grain boundaries or blocking the glide (or other motion) of dislocations. When CNTs block dislocation movement, they can begin to pile-up and these pile-up formations also create back-stresses that oppose the applied stress in a creep test, thereby providing creep resistance to the overall nanocomposite.

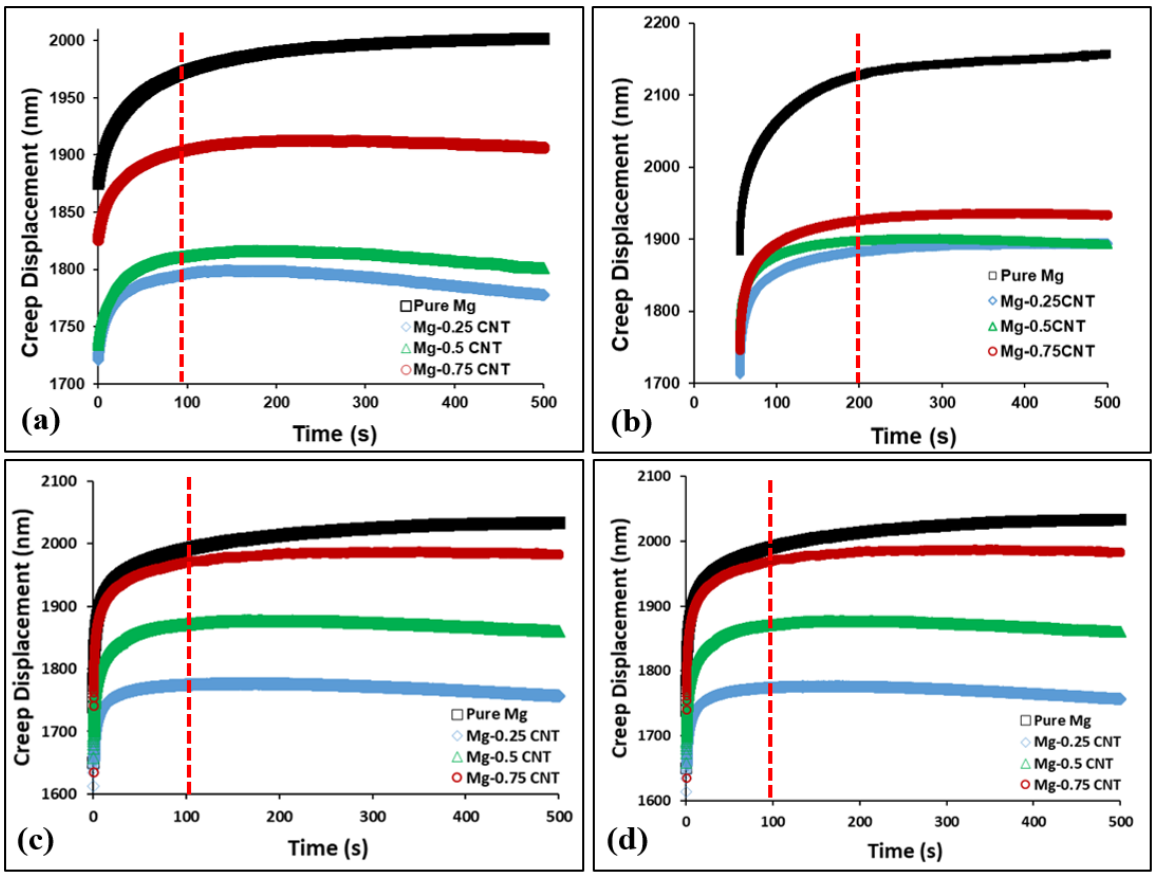

Figure 4.8. Creep displacement (nm) versus dwell time (500 s) for all materials over the four strain rates of: **(a)** 0.01 /s, **(b)** 0.1 /s, **(c)** 1.0 /s, and **(d)** 10 /s. The transition from transient to steady-state creep is observed in all tests (demarcated with a red dashed line).

4.2.5. Creep Power Exponent for Dominant Creep Mechanism at 298 K

The creep exponent (or power-law exponent), *n*, was calculated for each combination of material and strain rate at room temperature by obtaining the slope of the natural logarithm of creep rate versus the natural logarithm of indentation stress. This parameter *n* was introduced in Chapter III, and here this value is of paramount importance for shedding light on what creep deformation mechanism is dominant at room temperature. The *n*-values for all samples and strain rates are plotted in Fig. 4.9.

Values of *n* can be used to distinguish between several creep mechanisms. For example, literature [18-22] suggests that diffusion-creep is dominant (Coble creep and Nabarro-Herring Creep) when $n = 1$, grain boundary sliding (GBS) is dominant when $n = 2$, and dislocation movements (e.g., glide and climb) are dominant when *n* is 3 or greater. Dislocation creep can be further divided into Harper-Dorn creep ($n = 1$), solute-drag creep ($n = 2$), and climb-controlled creep (n = 5-7) [19-20].

From Fig. 4.9 it is clear that n is greater than three for all materials and strain rates tested. This result suggests that the dominant cold flow (room-temperature creep) deformation mechanism is dislocation motion (i.e., glide and climb).

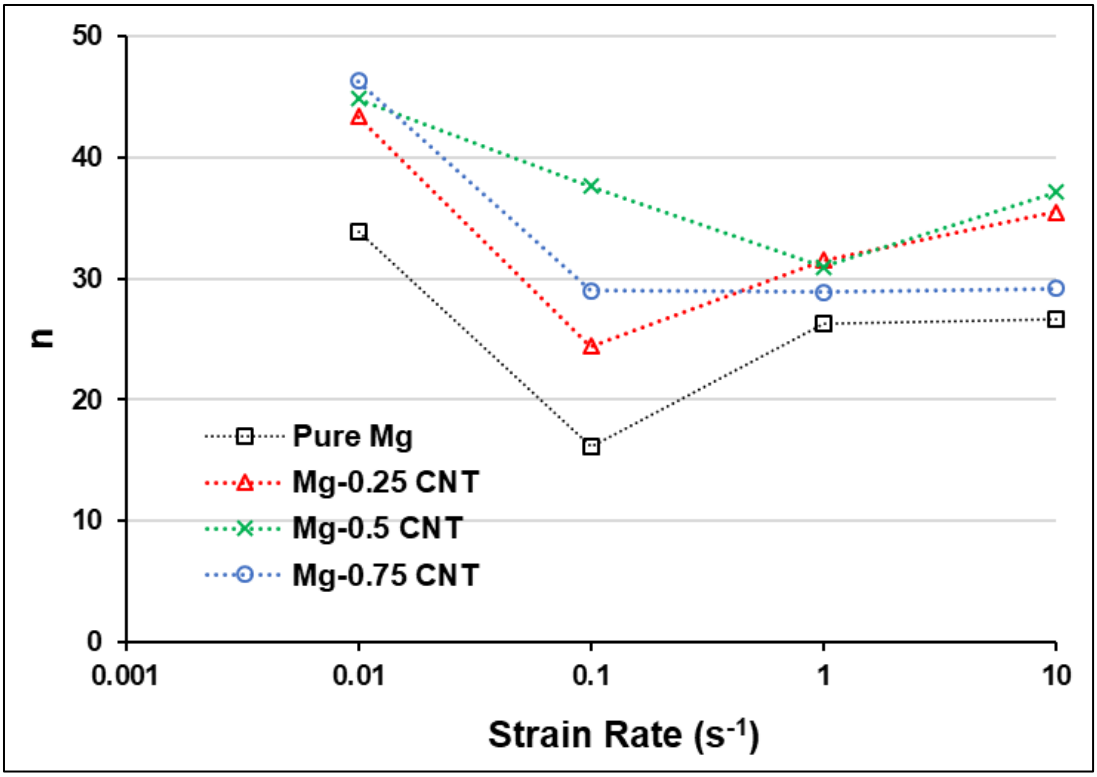

Figure 4.9. Power law exponent (*n*) values for all strain rates tested.

4.3. Elevated-Temperature Results

4.3.1. Berkovich Indentation Morphologies

The microstructures of some of the Berkovich indentations made in pure Mg and Mg-0.75 vol.% CNT are shown in Figs. 4.10 and 4.11, respectively. In pure Mg (Fig. 4.10) microcracks are visible around the indentations. Microcracks on pure Mg are demarcated with small red arrows in this Fig. 4.10. These microcracks in pure Mg are attributed to the limited plasticity (brittleness) of Mg due to the limited number of slip systems Mg has, i.e., the HCP crystal structure of Mg.

In contrast to pure Mg, the Mg-0.75 vol.% CNT nanocomposite had no visible microcracks near the Berkovich indentation sites. Studies [23-25] have already demonstrated that adding CNTs to Mg matrices does enhance ductility. These studies attribute the improved ductility from the CNTs to: (i) slip mode transition (activation of basal slip systems and the initiation of prismatic <a> slip), (ii) texture modification (change in crystallographic orientation), (iii) transition in stress state from plane strain to plane stress near the crack tip due to even dispersion of the nanoparticles in the matrix, and (iv) grain refinement (nanoparticles can cause grain boundaries to have a pinning effect).

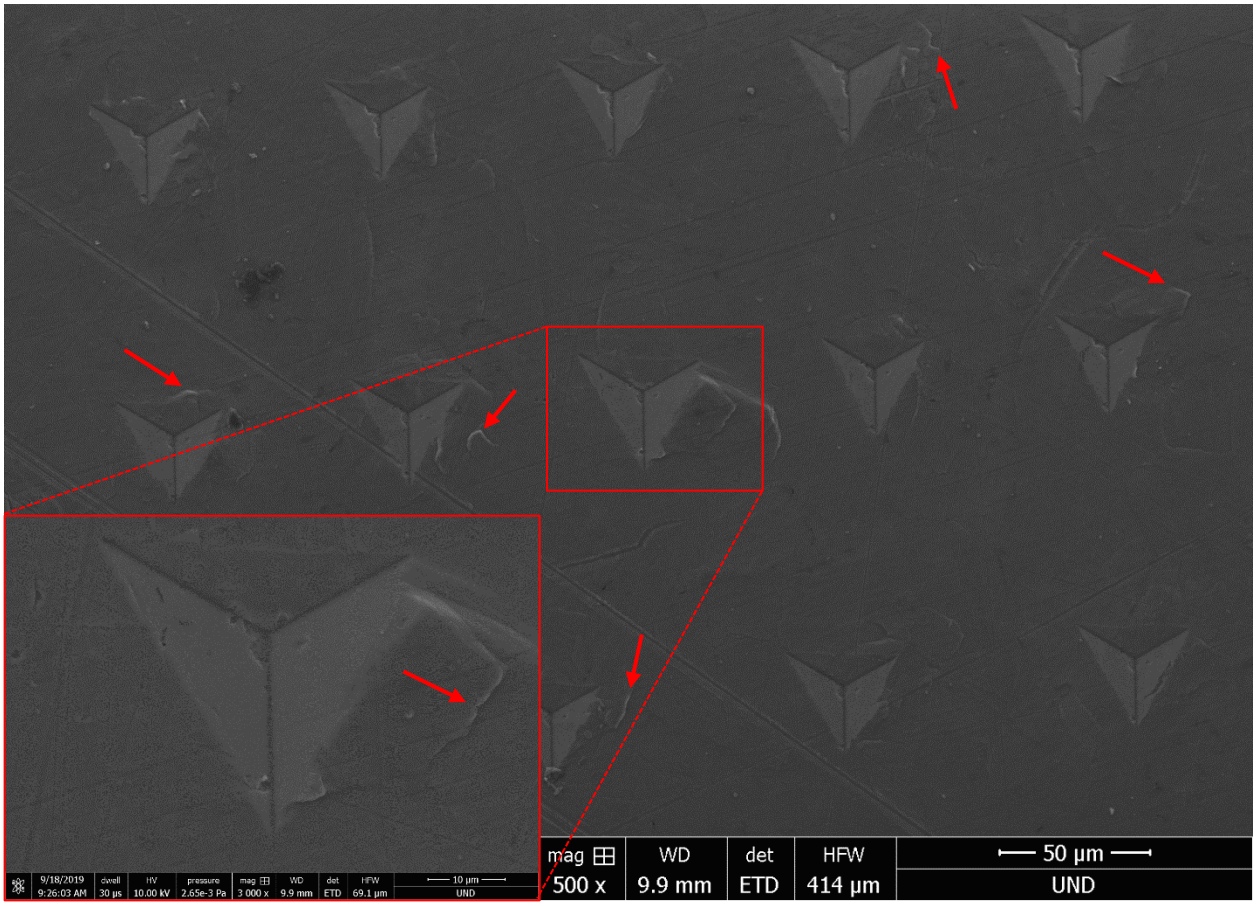

Figure 4.10. Scanning electron microscopy (SEM) image of Berkovich indentations made on pure Mg at 500x magnification and a close-up of a single indentation made at 3,000x magnification (inset). Red arrows point out microcracks near indentations.

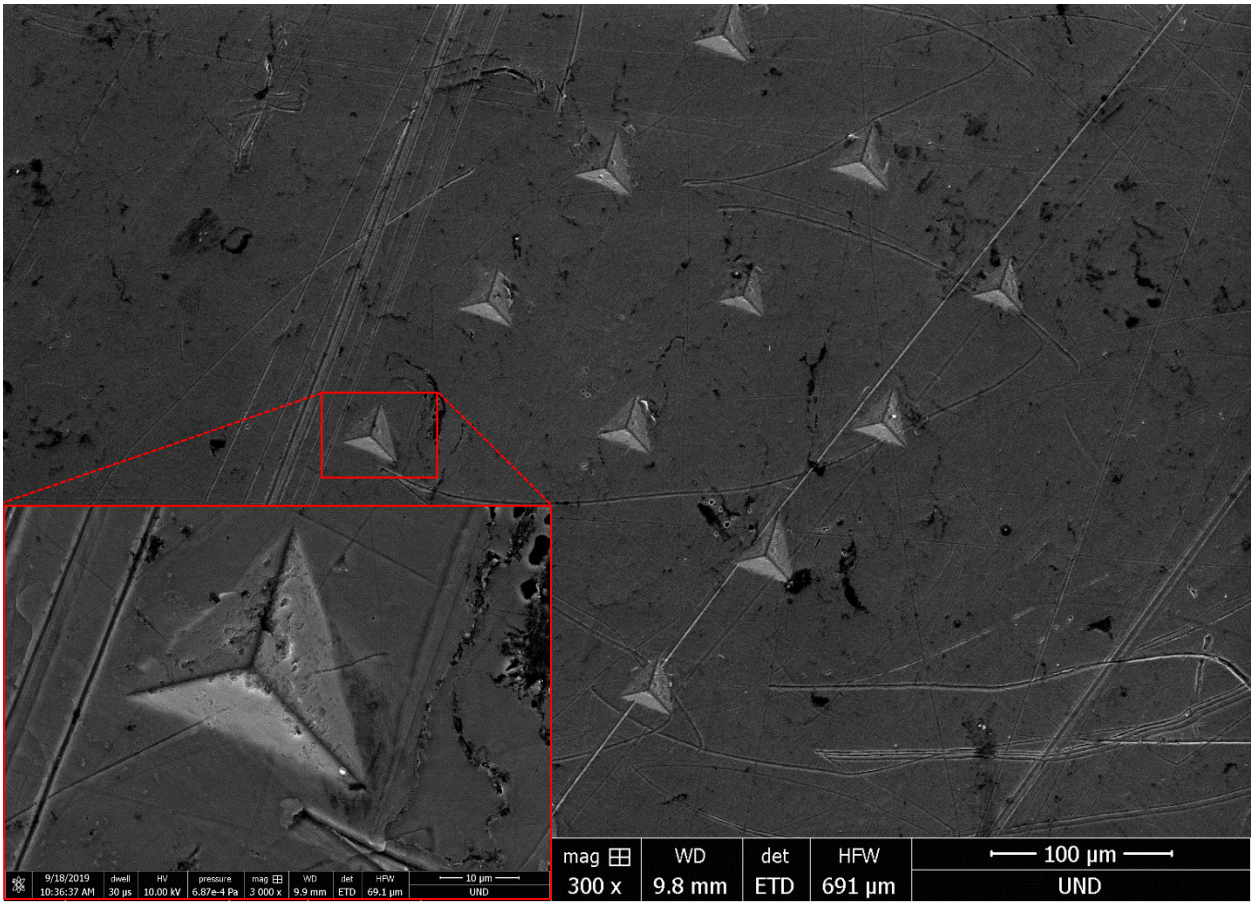

Figure 4.11. SEM image of indentations made on Mg-0.75 v/v% CNT at 300x magnification and a close-up of a single indentation made at 3,000x magnification (inset).

Additional Berkovich indentations made on Mg-0.75 vol.% CNT are shown in Fig. 4.12. Four large grouping of indentations (solid green ellipses) denote the different indentations made at four temperatures (298, 373, 473, 573 K). The indentations are identifiable by their depth, e.g., the smallest indents were made at room temperature (298 K) and the largest indents were made at 300°C (573 K). The group of indentations grouped by the dashed orange ellipse denotes five re-runs.

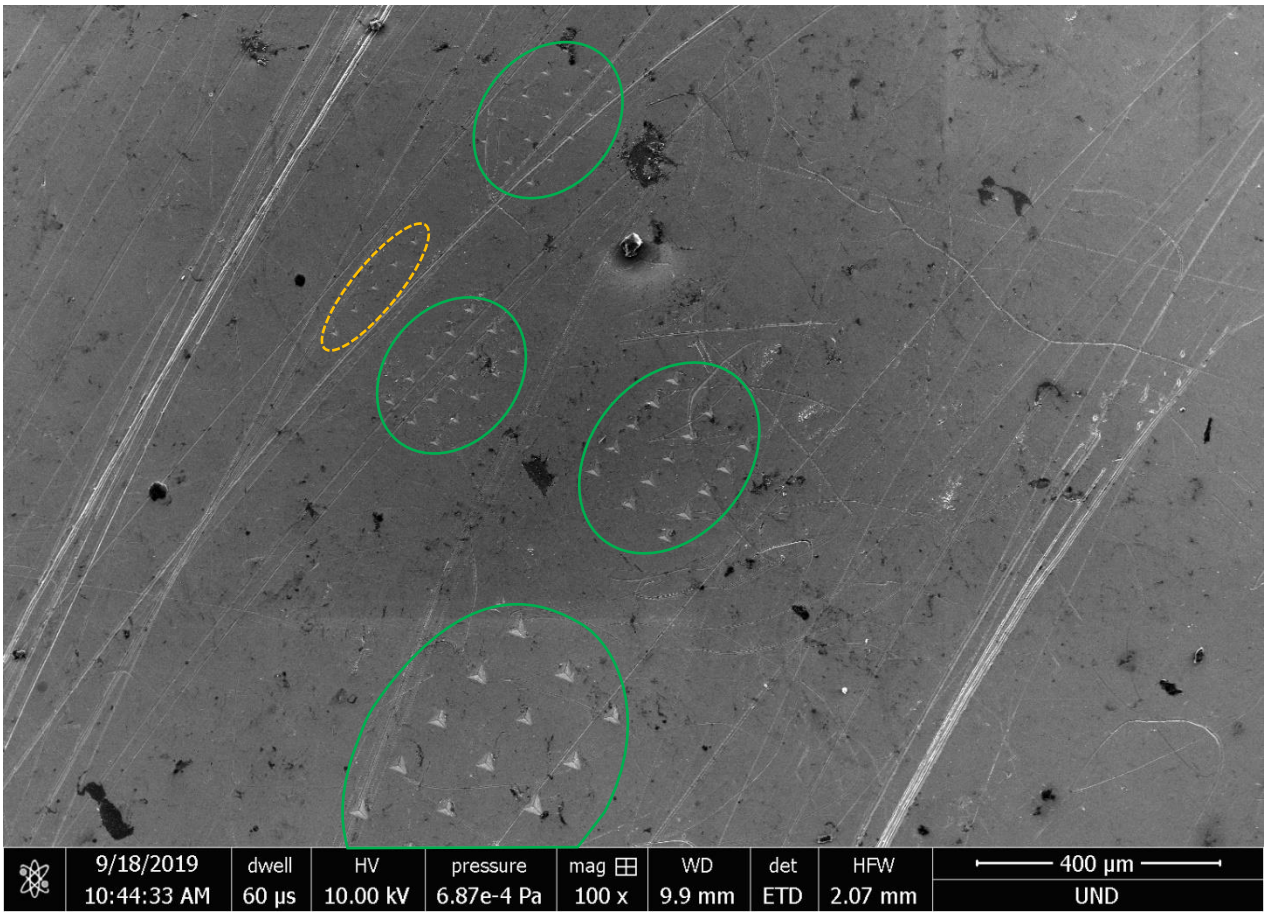

Figure 4.12. SEM image of Mg-0.75 v/v% CNT with distinct groups of indentations (circled). Largest indentations are made at 300°C, the smallest indentations at room temperature (25°C), etc. Indents in the dashed orange grouping were re-runs. Surfaces of pure Mg, Mg-0.25, and Mg-0.5 v/v% CNT are visually similar.

4.3.2. Load-Displacement (*P-h*) Curves

4.3.2.1. *P-h* Curves as a Function of Temperature

Load-displacement curves for all materials at a fixed load rate of 0.5 mN/s are shown in Figure 4.13. All test curves show loading, holding, and unloading segments. An expected and intuitive result arises from this figure. As temperature increases, the indenter depth increases at a fixed load (50 mN). In other words, the materials are more easily deformed (softened) at increasing temperatures when subject to the same load. *P-h* curves for the materials at the remaining load rates (5 and 50 mN/s) are visually similar and can be found in Appendix B.

It is also clear that the "width" of each holding segment for each creep test curve varies, i.e., depth of penetration under a constant load is dependent on temperature and material being tested. This confirms that larger creep displacement is occurring as temperature increases due to dynamic recovery (softening) of the material. Additionally, the widths of these dwell periods do differ from material to material, and also strain rate to strain rate, at a constant temperature. This is not readily seen in Fig. 4.13. These differences are better made with a deeper investigation of the creeping (dwell or holding) segment itself. The dwell periods for all creep tests conducted are discussed in isolation in sections to follow.

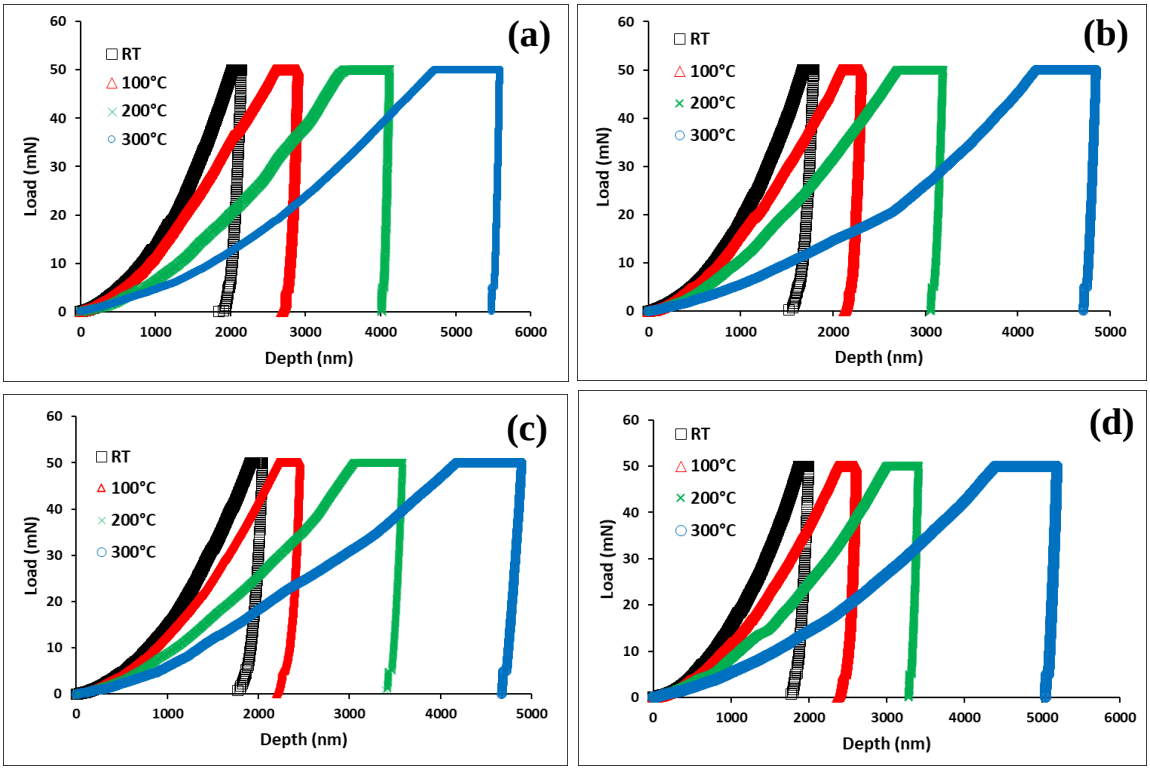

Figure 4.13. Load-displacement (*P-h*) curves as a function of temperature for a fixed load rate of 0.5 mN/s for: **(a)** Pure Mg, **(b)** Mg-0.25 vol.% CNT, **(c)** Mg-0.5 vol.% CNT, and **(d)** Mg-0.75 vol.% CNT. **RT**: room temperature (298 K).

4.3.2.2. *P-h* Curves as a Function of Load Rate

Another interesting trend is revealed when studying the *P-h* curves as a function of load rate, as opposed to temperature as in Fig. 4.13. Load-displacement curves are shown for all four materials at a constant temperature of 573 K (300°C), allowing load rate to vary, in Fig. 4.14. Not readily apparent from the previous figure, is now a feature in the loading segments of these creep tests. Notice how the tests conducted at low load rates reach the 50 mN load at a much shallower depth than those conducted at high load rates. This means with an increase in load rate, a natural increase in the required load to

reach constant depth follows (work hardening effect). Both softening (dynamic recovery) and work hardening effects are at play in these elevated-temperature creep tests.

Figure 4.14 only shows the *P-h* curves for a fixed temperature of 200°C so load rate trends can be observed. The rest of the *P-h* curves for the remaining temperatures for all materials as a function of load rate are available in Appendix B. These figures are visually similar to the ones presented in Fig. 4.14 and it is for this reason that only one representative set of figures is shown.

Another feature to appreciate regarding the test load rates is how fast the sample reaches a constant load of 50 mN. Load rates of 0.5, 5, and 50 mN/s take 100, 10, and 1 second(s), respectively, to reach this peak load. Further, for the fastest load rate (50 mN/s), the plastic deformation is "arrested" in the loading portion and then released in the dwell period. Conversely, for the slowest load rate (0.5 mN/s), the plastic deformation is "consumed" in the loading portion and then less plastic deformation is observed in the dwell period.

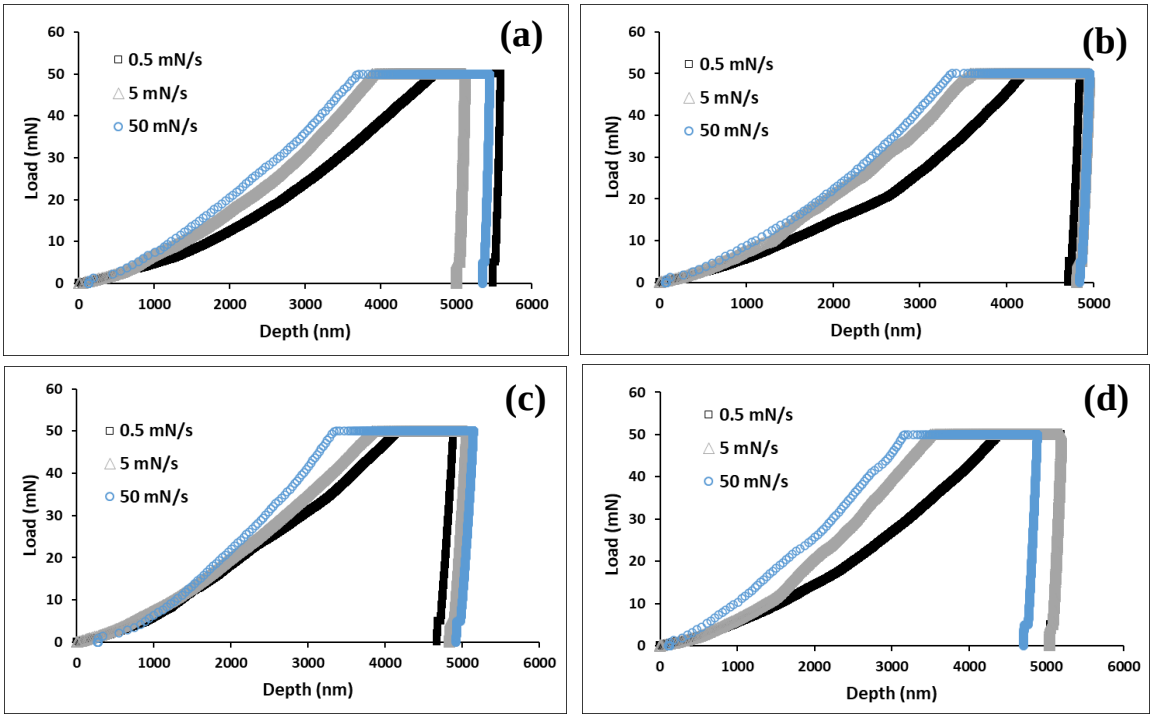

Figure 4.14. Load-displacement (*P-h*) curves as a function of load rate for a fixed temperature of 300°C for: **(a)** Pure Mg, **(b)** Mg-0.25 vol.% CNT, **(c)** Mg-0.5 vol.% CNT, and **(d)** Mg-0.75 vol.% CNT.

4.3.3. Indentation Stress vs. Depth Behavior: Indentation Size Effect

4.3.3.1. Indentation Size Effect (ISE) Curves as a Function of Temperature

The indentation size effect has been studied fairly extensively at room temperature. However, a limited number of studies have investigated ISE (in hardness) at elevated temperatures [26-29]. Franke et al. [26] studied single crystal copper, Prasitthipayong et al. [27] studied unirradiated and ion-irradiated 800H steel, Haghshenas et al. [28] studied Mg-Sm_2O_3 nanocomposites, and Beake et al. [29] studied polycrystalline tungsten.

The first three elevated ISE behavior studies [26-28] agree that ISE becomes less pronounced with increasing temperature due to the increase in the size of the plastic zone underneath the indenter. In contrast, Beake et al. [29] report an increase in ISE with an increase in temperature, however this study indicated that FCC metals tend to see reduced ISE and BCC metals (e.g., tungsten in Beake's study) see increased ISE in hardness at elevated temperatures. Magnesium is an HCP metal, and Haghshenas et al [28] reported a decrease in ISE with increasing temperature. This is the temperature dependence of the ISE effects expected in this project as well.

Figure 4.15 shows the temperature dependence of indentation size effects over all materials tested at a selected load rate of 0.5 mN/s. As seen, the most pronounced ISE behavior is observed at room temperature and the least pronounced ISE behavior is observed at 300°C. The remaining ISE plots for fixed load rates of 5 and 50 mN/s are in

Appendix C. These graphs are visually similar and suggest the same conclusions (ISE in hardness decreases with increasing temperature) as graphs presented in Fig. 4.15.

This trend can be understood more readily in Fig. 4.16. Prasitthipayong et al. [27] illustrate how as temperature increases, shear modulus and Peierls stress of dislocation decrease. This causes an increase in geometrically necessary dislocation (GND) storage volume. Also, these dislocations have increased (or activated) mobility with increasing temperature, and this causes softening in the plastically deformed volume underneath the indenter and softening of the overall metal. This explains why ISE in hardness at high temperatures is not as pronounced as the material is softer (not so many large hardness measurements at shallow indents).

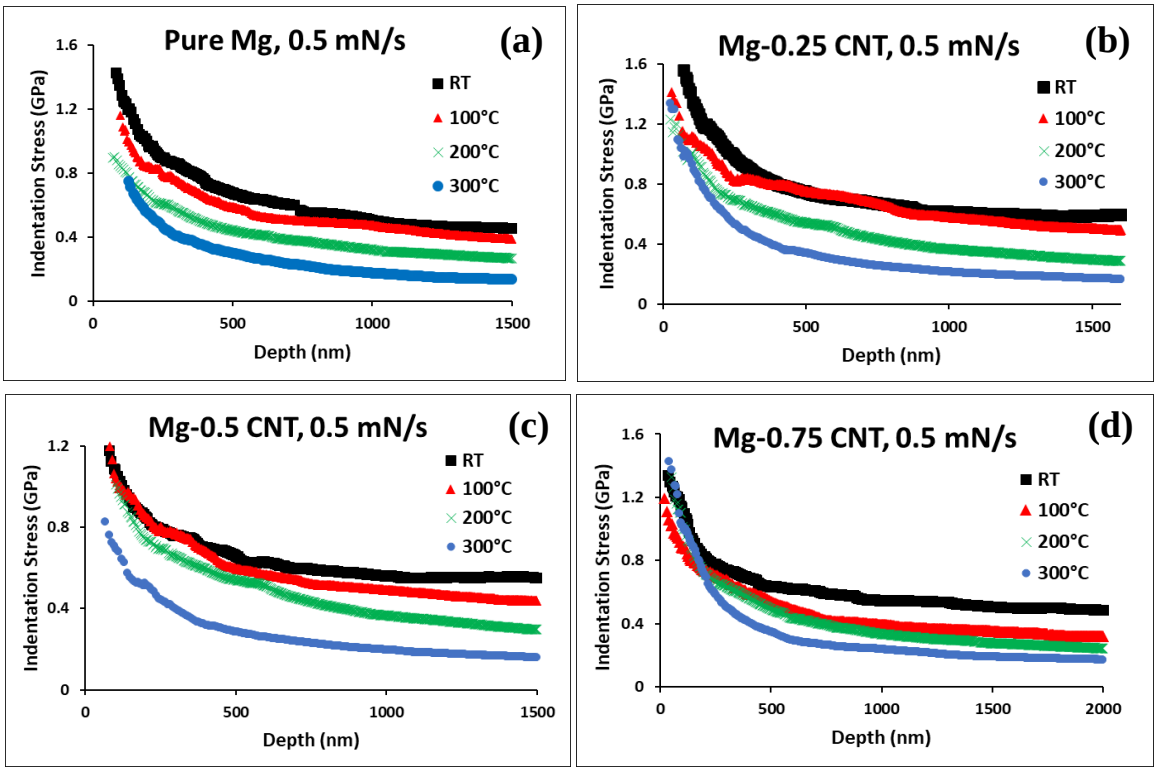

Figure 4.15. Indentation stress versus loading depth behavior (ISE behavior) as a function of temperature for a fixed load rate of 0.5 mN/s for: **(a)** Pure Mg, **(b)** Mg-0.25 vol.% CNT, **(c)** Mg-0.5 vol.% CNT, and **(d)** Mg-0.75 vol.% CNT. **RT**: room temperature (298 K).

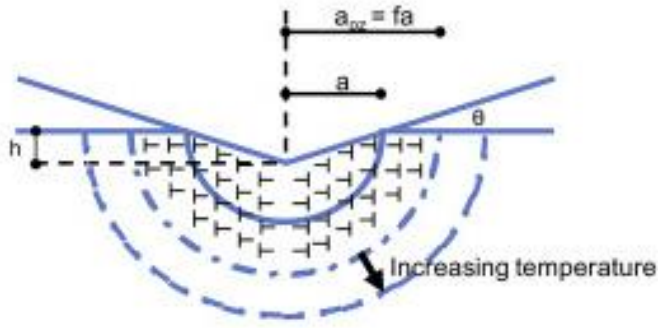

Figure 4.16. Schematic on the temperature dependence of ISE and GND storage volume [27].

4.3.3.2. ISE Curves as a Function of Load Rate

Indentation size effects in hardness can also be studied as a function of load rate. Figure 4.17 shows this trend in all samples over the varying load rates for a fixed temperature of 300°C. Again, ISE plots similar to the ones in this figure at the rest of the temperatures tested are visually similar and are available in Appendix C to show the representative trends without needless redundant information.

One trend immediately apparent from Fig. 4.17 is that ISE in hardness is more pronounced in higher load rates. In other words, hardness measurements made at low load rates are not as skewed (over-estimated) by the indentation size effect as those at higher load rates. Ma et al. [30] also observed a load- and strain rate-dependence on ISE behavior in a Ti-10V-2Fe-3Al alloy. They report a similar ISE behavior in hardness to the one in Fig. 4.17. Ma et al. attribute this to the increase in geometrically necessary dislocations (GNDs) and statistically stored dislocations (SSDs) beneath the indentation as load rate increases.

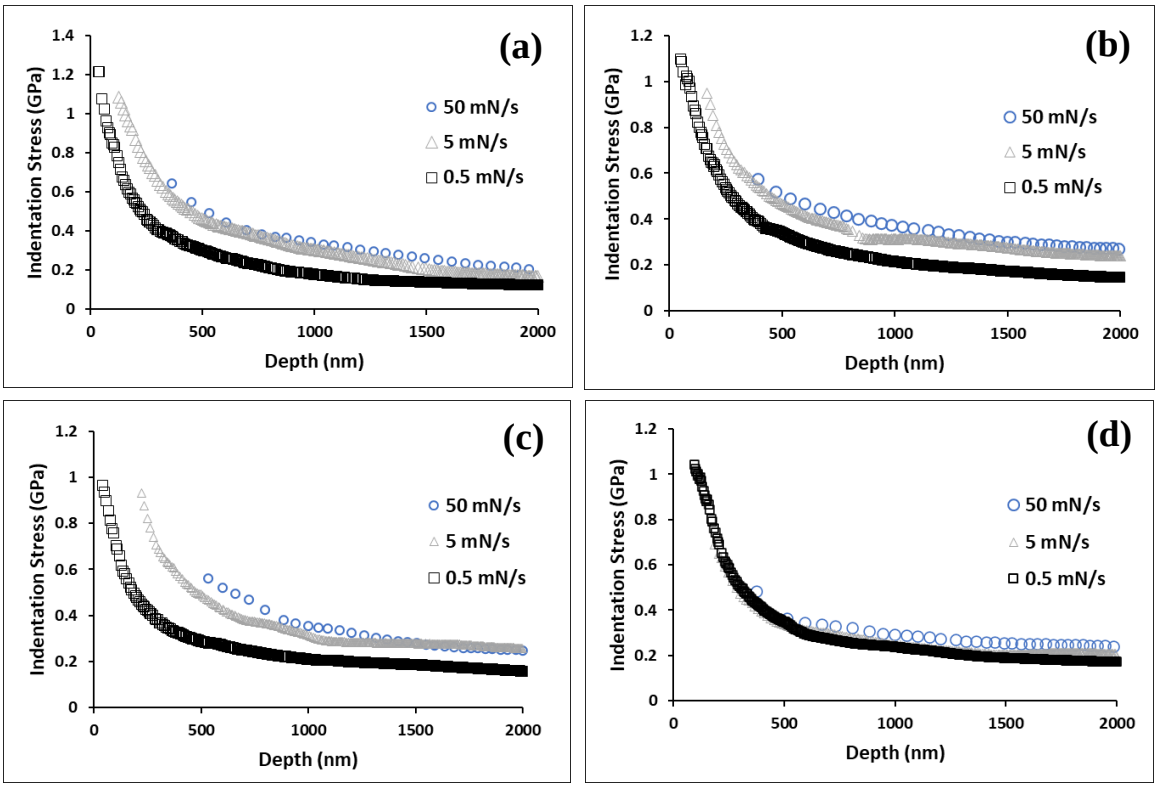

Figure 4.17. Indentation stress versus loading depth behavior (ISE behavior) as a function of load rate for a fixed temperature of 300°C for: **(a)** Pure Mg, **(b)** Mg-0.25 vol.% CNT, **(c)** Mg-0.5 vol.% CNT, and **(d)** Mg-0.75 vol.% CNT. **RT**: room temperature (298 K).

4.3.3.3. ISE Curves as a Function of CNT Content

Another hardness trend that is to be expected from room temperature trends previously observed is that CNTs should improve the hardness of the overall nanocomposite (but at low volume fractions of 0.25-0.5 vol.%). At high temperatures, CNTs (and many different nanoreinforcements) can be considered to be extra thermally stable obstacles to dislocation motion, thereby improving hardness especially at shallow indents [28]. This implies that ISE phenomena should be even more pronounced in nanocomposites as opposed to pure Mg.

Figure 4.18 is in fair agreement with this expected trend. This figure shows ISE behavior as a function of CNT content at a fixed temperature of 300ºC. In general, the pure Mg (black square series) are typically lower than the ISE plots for the Mg-nanocomposites, confirming that the ISE phenomena are more pronounced for the nanocomposites. This trend is also observed in ISE curves for the remaining combinations of material and load rate at 200°C, 100°C, and room temperature. These plots are available in Appendix C.

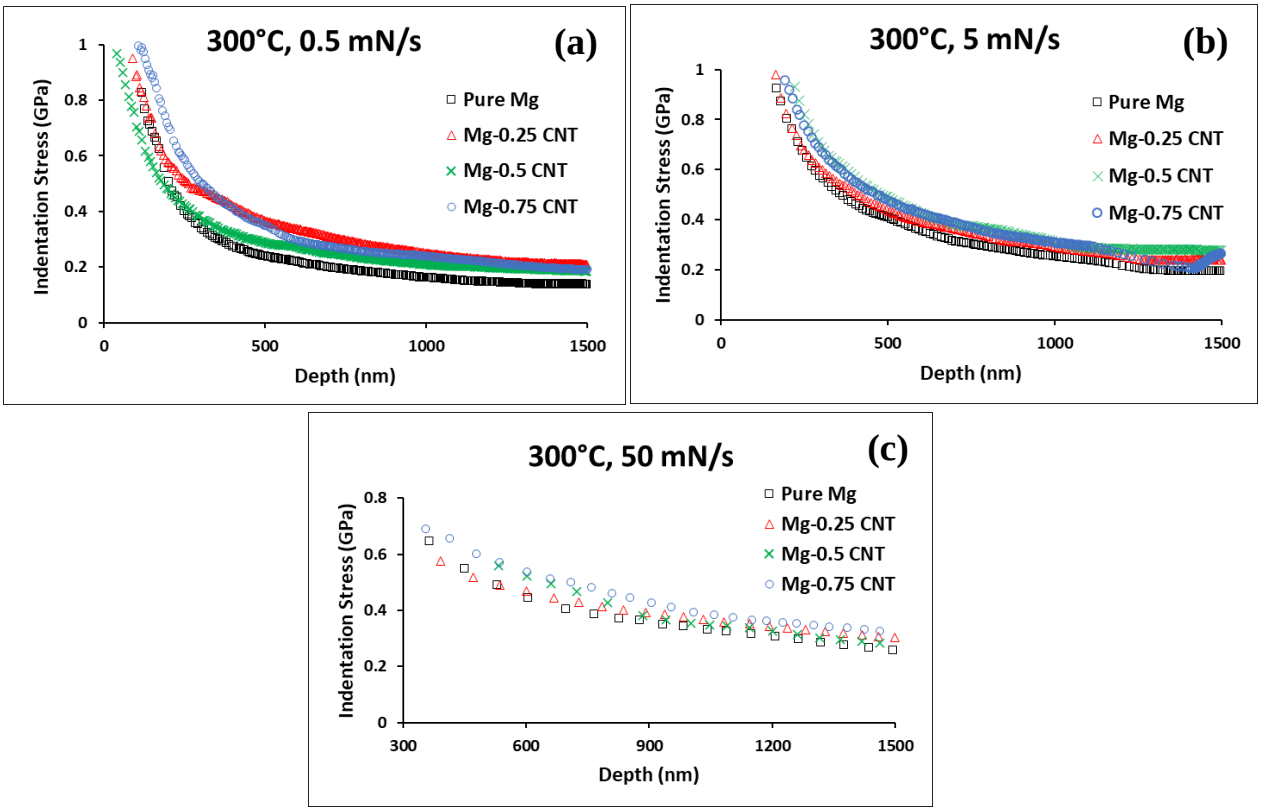

Figure 4.18. Indentation stress versus loading depth behavior (ISE behavior) as a function of CNT content at a fixed temperature of 300°C over all load rates tested: **(a)** 0.5 mN/s, **(b)** 5 mN/s, and **(c)** 50 mN/s.

4.3.4. Indentation Hardness Behavior

4.3.4.1. Hardness Behavior as a Function of Temperature and Load Rate

Figure 4.19 shows indentation hardness behavior as a function of temperature and CNT loading. This behavior is also presented for all load rates tested. There is a large amount of error bar overlap for each set of four samples at a constant temperature and load rate (each series of four data points with same color and marker for a single load rate). Considering the error bar overlap, hardness is not changed significantly with the addition of CNTs, however, the average hardness is improved, then decreased when CNT addition exceeds about 0.5 vol.%. This decrease in hardness occurs due to CNT agglomeration, as van der Waals forces are enhanced at larger CNT loadings. The CNT clusters tend to worsen mechanical properties like hardness, as observed in the room-temperature indentation hardness findings.

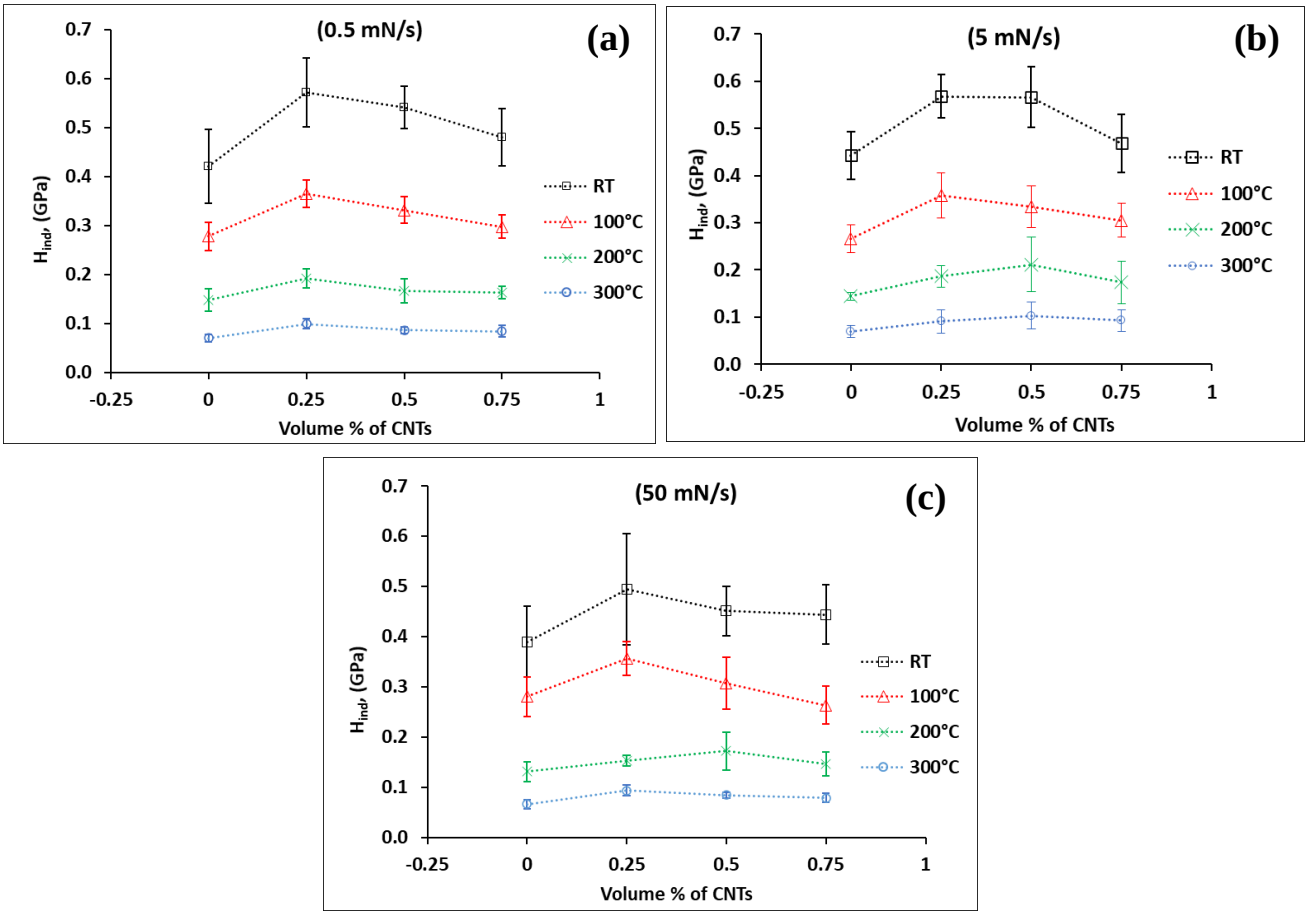

Figure 4.19. Variation of indentation hardness as a function of CNT loading and temperature over three load rates: **(a)** 0.5 mN/s, **(b)** 5 mN/s, and **(c)** 50 mN/s.

4.3.5. Young's (Elastic) Modulus Response

A display of Young's moduli obtained for all tests is shown in Fig. 4.20 as a function of temperature, CNT loading, and load rate. The trend in Young's modulus is temperature-dependent. At room temperature, a trend similar to indentation hardness seen in the last section is evident. Young's modulus increases until about 0.5 vol.% CNTs is reached, and then the modulus decreases beyond this CNT loading. Stiffness behavior for the materials at 100ºC is similar for the load rate of 0.5 mN/s, but Young's modulus does not change in a statistically significant way as error bars overlap for 5 and 50 mN/s loading rates. Finally, a statistically significant change in Young's modulus is observed at 200 and 300ºC. The modulus begins to decrease immediately and reaches a minimum at 0.5 vol% CNTs. This initial decrease in stiffness is likely due to the dynamic recovery (softening) of the matrix at these higher temperatures. Dynamic recovery is due to rearrangement and annihilation of the existing dislocations which contribute to the softening of the structure.

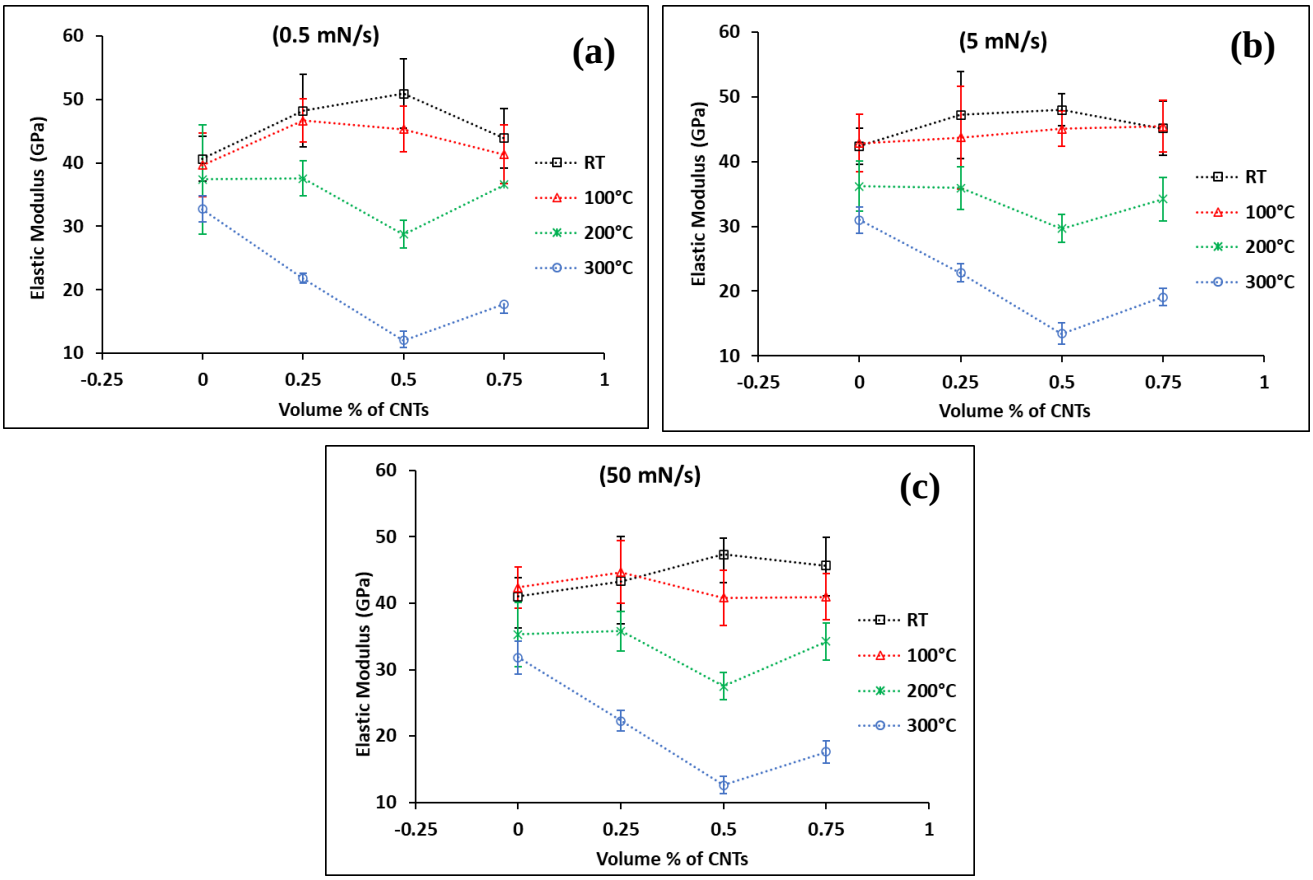

Figure 4.20. Variation of Young's modulus as a function of CNT loading and temperature over three load rates: **(a)** 0.5 mN/s, **(b)** 5 mN/s, and **(c)** 50 mN/s.

4.3.6. Creep Rate Curves

4.3.6.1. Creep Rate Curves as a Function of Temperature

At elevated temperatures, creep rates are expected to be higher because the dynamic recovery (softening) of the material assists in flowing (creep), especially near the material melting point, thereby reducing creep resistance. Haghshenas et al. [28] suggests that more than one creep mechanism may be at play for Mg-nanocomposites at elevated temperatures, also enhancing creep rate. Fig. 4.21 shows creep rates for all materials as a function of time at fixed load rates. It can be easily seen from this figure that the creep rate increases with temperature.

The rest of the creep rate versus dwell time plots for all materials for the remaining load rates (0.5 and 50 mN/s) are available in Appendix D. The figure shown is representative and the appended figures yield the same conclusions.

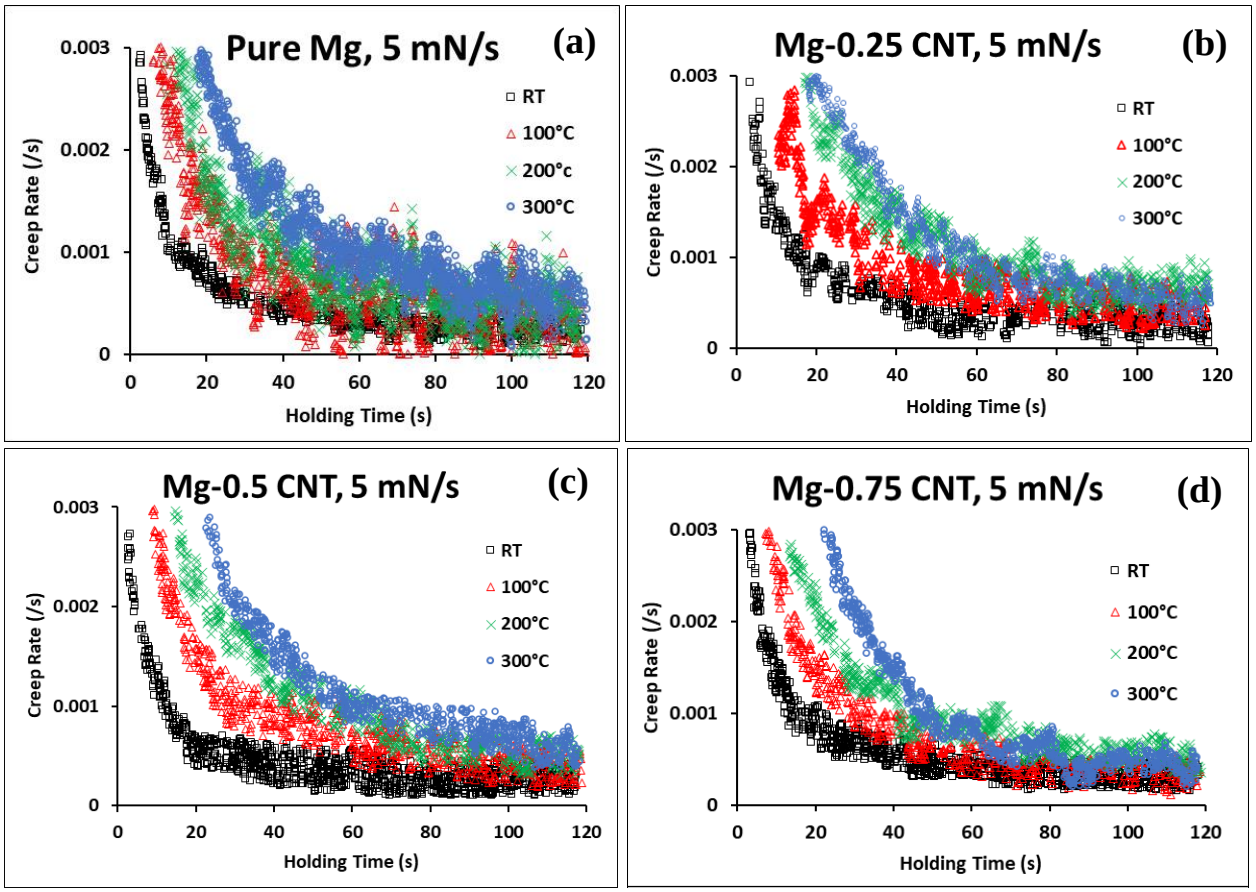

Figure 4.21. Creep rate versus holding time behavior as a function of temperature for a fixed load rate of 5 mN/s for: **(a)** Pure Mg, **(b)** Mg-0.25 vol.% CNT, **(c)** Mg-0.5 vol.% CNT, and **(d)** Mg-0.75 vol.% CNT. **RT**: room temperature (298 K).

4.3.6.2. Creep Rate Curves as a Function of Load Rate

Creep rate for these materials can also be studied as a function of load rate at fixed temperatures. This behavior is displayed in Fig. 4.22 for all materials at 300°C. The remaining plots of this nature are available in Appendix D. There is not a strong trend in Fig 4.22, however there is a fairly mild correlation that creep rate increases with load rate in approximately the first third of the holding time, then the creep rates become so close to one another that their differences become statistically insignificant.

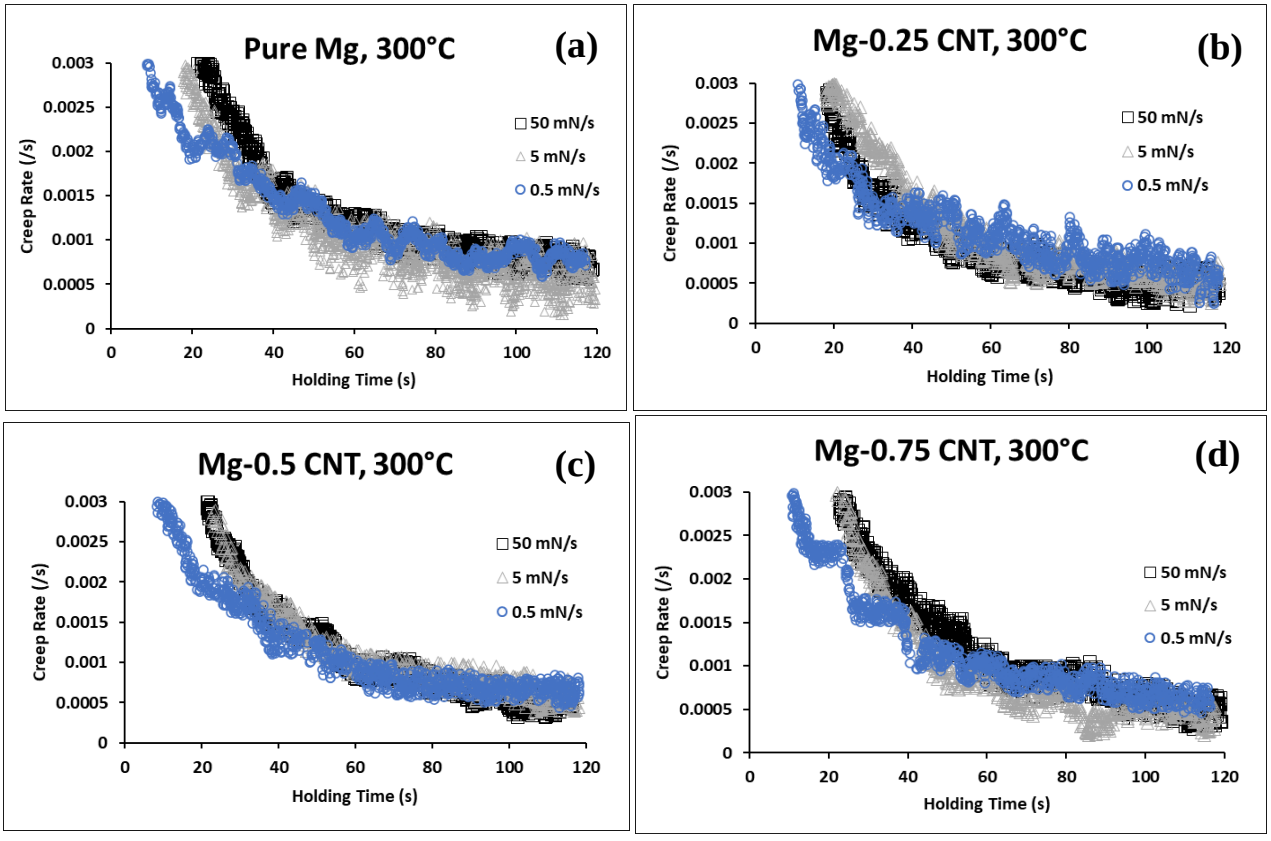

Figure 4.22. Creep rate versus holding time behavior as a function of load rate for a fixed temperature of 300°C for: **(a)** Pure Mg, **(b)** Mg-0.25 vol.% CNT, **(c)** Mg-0.5 vol.% CNT, and **(d)** Mg-0.75 vol.% CNT. **RT**: room temperature (298 K).

4.3.6.3. Creep Rate Curves as a Function of CNT Loading

The last variable to hold constant when examining creep rate behavior is load rate. Creep rate versus holding time behavior for all materials and all four temperatures at a constant load rate of 50 mN/s is shown in Fig. 4.23. This time, there is no readily apparent trend in the creep rate from this perspective. These graphs are shown for completion and to note how no statistically significant differences in creep rate were observed when the creep rate data is viewed as a function of CNT loading.

The remaining creep rate plots as a function of CNT loading at fixed load rates of 0.5 and 50 mN/s also do not have any readily apparent trends. These graphs are available in Appendix D.

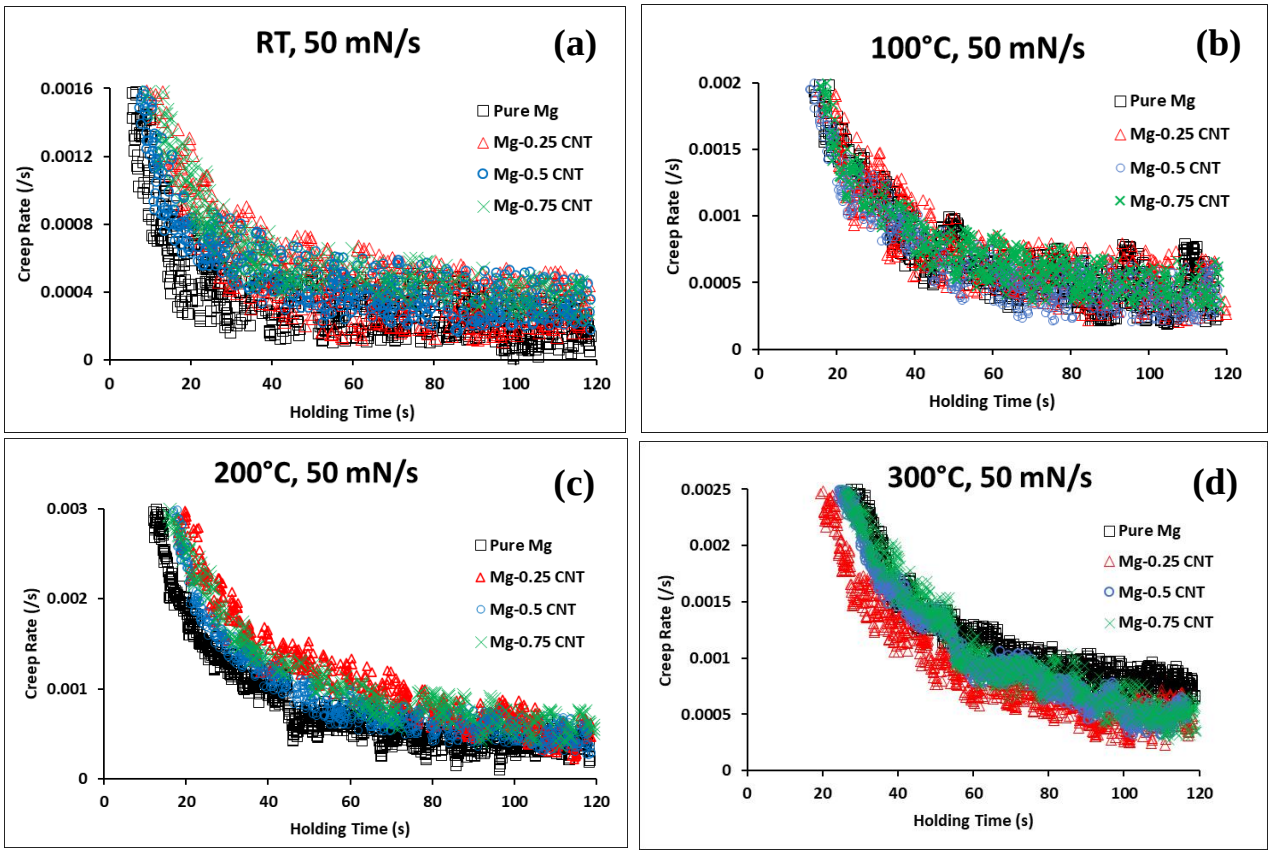

Figure 4.23. Creep rate versus holding time behavior as a function of material tested (CNT loading) at a fixed load rate of 50 mN/s, over all temperatures tested: **(a)** RT, **(b)** 100°C, **(c)** 200°C, and **(d)** 300°C. **RT**: room temperature (298 K).

4.3.7. Creep Displacement Behavior

4.3.7.1. Creep Displacement Behavior as a Function of Temperature

In addition to creep rate, creep displacement (or depth) is also a useful measure for a full assessment of a material's creep behavior. Fig. 4.24 shows creep displacement versus dwell time as a function of temperature for all materials at a fixed load rate of 50 mN/s. This figure shows an obvious and expected trend, that is that creep displacement increases with temperature. Similar to how it is expected that the creep rate should increase with temperature, creep displacement also increases with temperature.

The remaining combinations of CNT content and temperature at the fixed load rates of 0.5 and 5 mN/s for creep displacement versus time plots are available in Appendix E. These plots are visually similar, meaning they also exhibit the stated trend observed in Fig. 4.24.

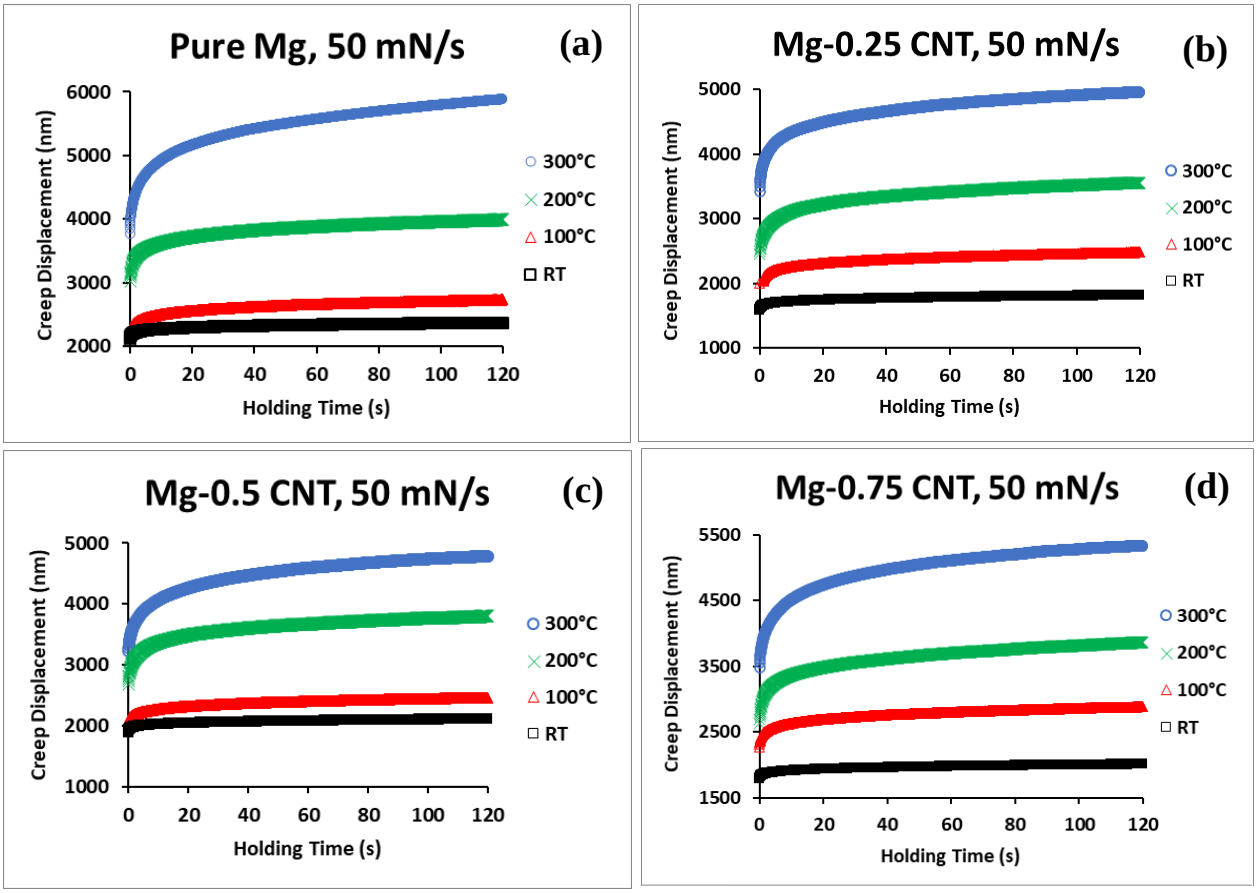

Figure 4.24. Creep displacement versus holding time behavior as a function of temperature for a fixed load rate of 50 mN/s for: **(a)** Pure Mg, **(b)** Mg-0.25 vol.% CNT, **(c)** Mg-0.5 vol.% CNT, and **(d)** Mg-0.75 vol.% CNT. **RT**: room temperature (298 K).

4.3.7.2. Creep Displacement Behavior as a Function of Load Rate

There is not a strong trend in creep displacement as a function of load rate. This observation is drawn from Fig. 4.25, which shows creep displacement for all materials as a function of load rate at a fixed temperature of 200°C. The remaining set of figures similar to those shown in Fig. 4.25 at room temperature, 100°C, and 200°C is available in Appendix E. No trends are readily apparent from these plots either, but these graphs are shown for completeness.

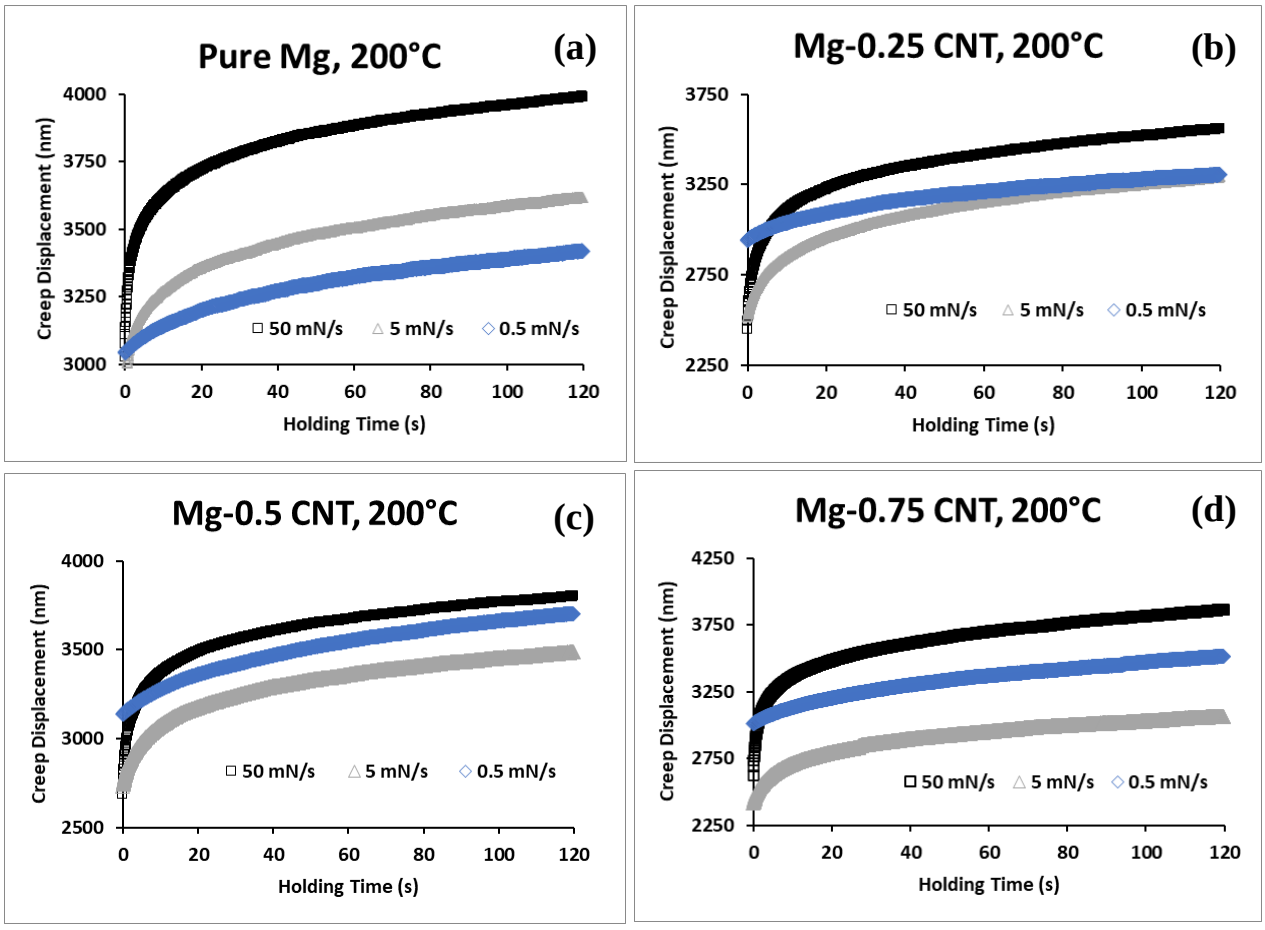

Figure 4.25. Creep displacement versus holding time behavior as a function of load rate at a fixed temperature of 200°C for: **(a)** Pure Mg, **(b)** Mg-0.25 vol.% CNT, **(c)** Mg-0.5 vol.% CNT, and **(d)** Mg-0.75 vol.% CNT. **RT**: room temperature (298 K).

4.3.7.3. Creep Displacement Behavior as a Function of CNT Loading

Creep displacement as a function of CNT content does exhibit a noteworthy and expected trend. Figure 4.26 shows creep displacement variation as a function of CNT loading over all temperatures at a fixed load rate of 50 mN/s. In all graphs, pure Mg (black square series) has the highest creep displacement and Mg-0.75 CNT (green *X* series) has the second-highest creep displacement. The Mg-CNT nanocomposites with low CNT loadings, i.e., 0.25 and 0.5 vol.% CNTs have the lowest creep displacements. Therefore, the creep resistance is best at these low CNT loadings. This trend also holds for the other combinations of temperature and material at fixed load rates of 0.5 and 5 mN/s, and these plots can be seen in Appendix E as only one representative set of figures is shown to convey the trend.

Similar to how indentation hardness exhibits a parabolic behavior when CNT content is increased from 0 to 0.75 vol.%, creep resistance also seems to have a parabolic dependence on this same CNT loading. Low loadings of CNTs, namely those between 0.25 and 0.5 vol.%, exhibit the best creep resistance. This can be explained through nanoparticle size. Pure Mg has no CNT reinforcements, so it cannot benefit from Orowan strengthening in the same way that a Mg-CNT nanocomposite can. However, adding too many CNTs, as in the nanocomposite with 0.75 vol% CNTs experiences agglomerations. It is at this point that the term “nanocomposite” hardly describes the material because the CNTs have likely clustered into “micron-size” agglomerations.

From Chapter II, it is clear that Orowan strengthening works best for small grains and coarse, agglomerated CNT clusters will not benefit from this mode of strengthening. It is for this reason that Mg reinforced with low CNT loadings (0.25-0.5 vol.% CNTs) exhibits the best creep resistance. The low CNT loadings can still effectively achieve uniform dispersion throughout the matrix so agglomerations are avoided and Orowan strengthening can greatly contribute to the nanocomposite.

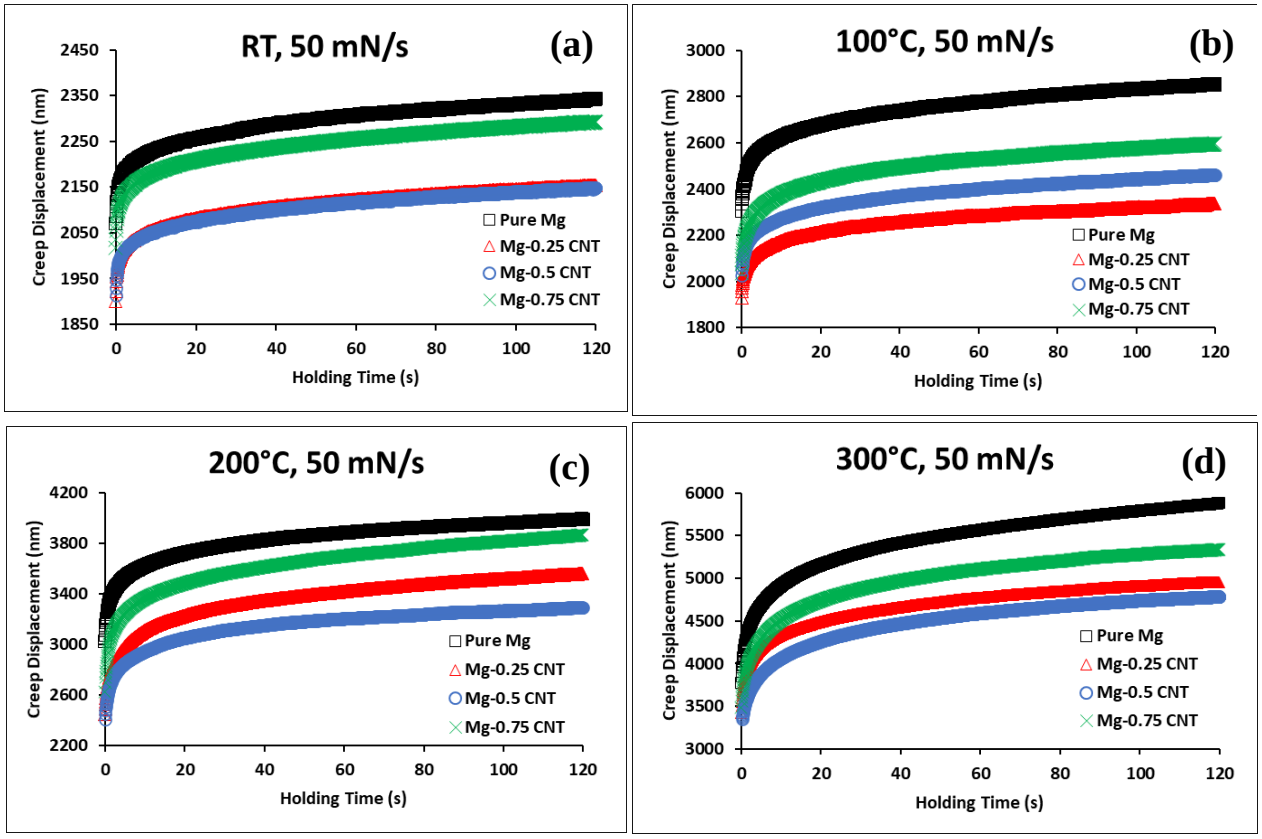

Figure 4.26. Creep displacement versus holding time behavior as a function of material tested (CNT loading) at a fixed load rate of 50 mN/s, over all temperatures tested: **(a)** RT, **(b)** 100°C, **(c)** 200°C, and **(d)** 300°C. **RT**: room temperature (298 K).

4.3.8. Creep Power Exponent for Dominant Creep Mechanism Determination

The procedure for determining dominant creep mechanisms is outlined in Chapter III through an approach using the creep power law (Eqn. 3.7 in Chapter III). At isothermal and steady-state creep conditions, the stress exponent, *n*, can be determined from the slope of a plot of $\ln \dot{\varepsilon}_{ind}$ versus $\ln \sigma_{ind}$. The slopes of these graphs are the *n*-values and the value of *n* is what determines the dominant creep mechanism.

Figure 4.27 shows all *n*-values obtained for all materials and temperatures over all three load rates. From room temperature to 200°C (473 K), *n*-values gradually decrease as temperature increases. Behavior at 300°C (573 K) is slightly different for the samples at the highest load rate of 50 mN/s because n-values increase at this temperature. However, for load rates of 0.5 and 5 mN/s at this temperature, *n*-value is only getting lower. This means that the general trend creep mechanism transitions from dislocation movements to diffusional creep as temperature increases.

For example, at room temperature, all materials across all load rates indicate an *n*-value greater than 3. From literature [18-22], this means that the dominant creep mechanism at room temperature is dislocation motion, and this is in good agreement with room temperature tests examined in Section 4.2.5. Increasing the temperature to 100°C (373 K), all *n*-values are greater than 3, which indicates that the dominant creep mechanism at this temperature for these materials is still dislocation motion.

However, at 200 and 300°C, evidence of diffusional creep mechanisms is seen in Fig. 4.27. At 200°C, the value of *n* varies from 2 to 3 or greater (but not unity quite yet). This implies dislocation motion is still playing a role in the creep deformation of the materials at 200°C, however grain boundary sliding (GBS) is also a co-dominant mechanism. Finally, at 300°C, every significant *n* value indicative of a dominant creep mechanism is present, i.e., *n* varies from one to three or greater. This means that dislocation movements, GBS, and diffusional creep mechanisms (e.g., Nabarro-Herring and Coble creep) are all present at 300°C.

In summary, dominant creep mechanisms at elevated temperature are tougher to identify, because multiple mechanisms are present. Also, the fairly simple analysis presented here only hints as to what mechanisms are involved and does not give any indication as to how representative each mechanism is, or how to distinguish between Nabarro-Herring and Coble creep if diffusional mechanisms are involved. The general trend for Mg-CNT nanocomposites regarding creep mechanisms is that as temperature increases from room temperature to elevated temperatures (100-300°C or 373-573 K), creep mechanisms shift from dislocation movements controlled by atoms moving from regions of compression to tension by the coordinated movement of "blocks" of material via glide or climb shifts to diffusion movements largely controlled by diffusion.

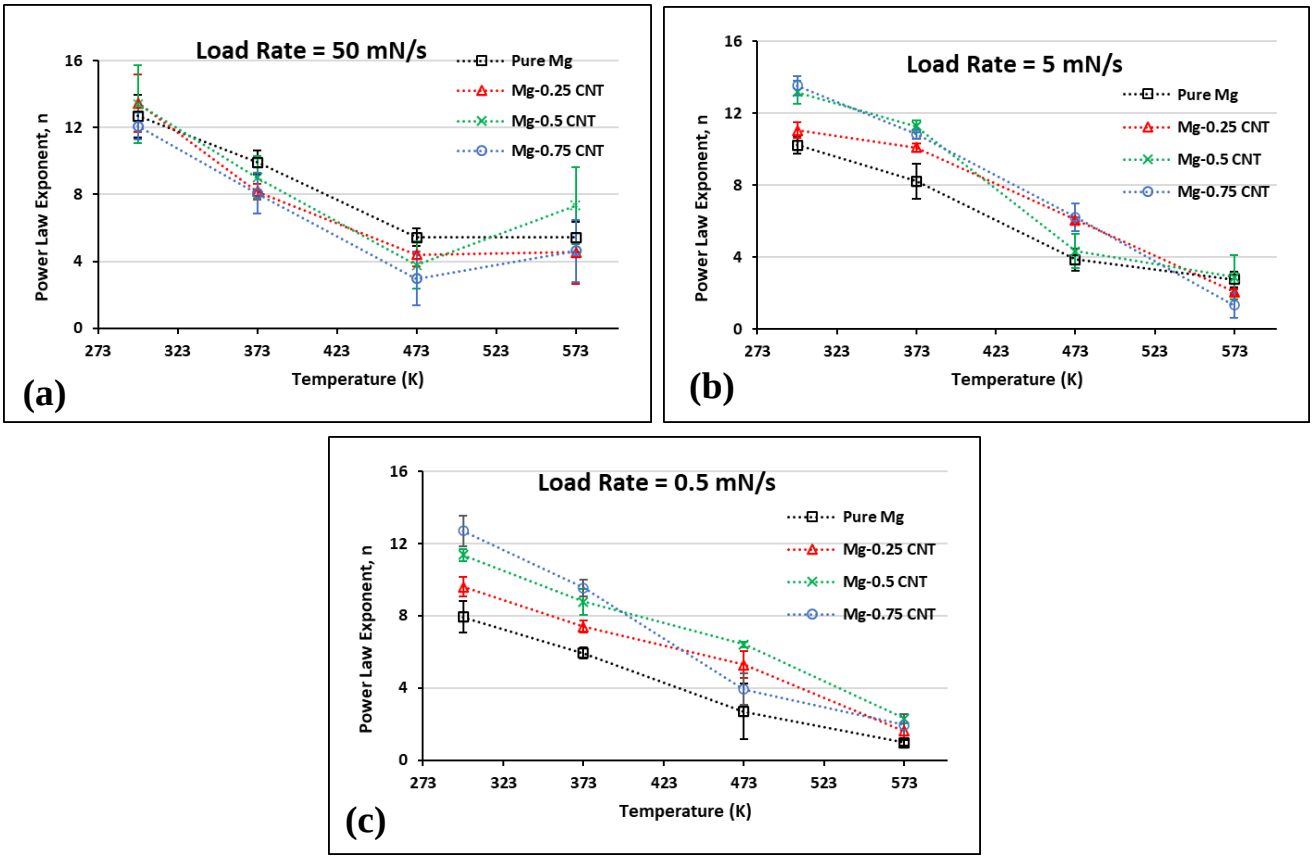

Figure 4.27. Creep power exponents (*n*-values) for all materials over all temperatures and for all load rates tested: **(a)** 0.5 mN/s, **(b)** 5 mN/s, and **(c)** 50 mN/s.

REFERENCES

CHAPTER IV – RESULTS AND DISCUSSION OF INDENTATION CREEP TESTS PERFORMED AT ROOM AND ELEVATED TEMPERATURE

[1] Kumar, M.A., et al. "Deformation twining and grain partitioning in a hexagonal close-packed magnesium alloy." *Nature Communications*, vol. 9, no. 4761, November 2018, pp. 1-8.

[2] Ding, Y., Xu, J., Hu, J., Gao, Q., Guo, X., Zhang, R., An, L. "High performance carbon nanotube-reinforced magnesium nanocomposite." *Materials Science and Engineering: A*, vol. 771, January 2020, article no. 138575. https://doi.org/10.1016/j.msea.2019.138575.

[3] Ganguly, S., Mondal, A.K. "Influence of SiC nanoparticles addition on microstructure and creep behavior of squeeze-cast AZ91-Ca-Sb magnesium alloy." *Materials Science and Engineering: A*, vol. 718, March 2018, pp. 377-389. https://doi.org/10.1016/j.msea.2018.01.131.

[4] Fernández, R., González-Doncel, G. "Threshold stress and load partitioning during creep of metal matrix composites." *Acta Materialia*, vol. 56, no. 11, June 2008, pp. 2549-2562. https://doi.org/10.1016/j.actamat.2008.01.037.

[5] Ma, Z.Y., Mishra, R.S., Tjong, S.C. "High-temperature creep behavior of TiC particulate reinforced Ti-6Al-4V alloy composite." *Acta Materialia*, vol. 50, no. 17, October 2002, pp. 4293-4302. https://doi.org/10.1016/S1359-6454(02)00261-6.

[6] Nix, W.D., Gao, H. "Indentation size effects in crystalline materials: A law for strain gradient plasticity." *Journal of the Mechanics and Physics of Solids*, vol. 46, no. 3, March 1998, pp. 411-425. https://doi.org/10.1016/S0022-5096(97)00086-0.

[7] Poole, W.J., Ashby, M.F., Fleck, N.A. "Micro-hardness of annealed and work-hardened copper polycrystals." *Scripta Materialia*, vol. 34, no. 4, February 1996, pp. 559-564. https://doi.org/10.1016/1359-6462(95)00524-2.

[8] Zong, Z., Lou, J., Adewoye, O.O., Elmustafa, A.A., Hammad, F., Soboyejo, W.O. "Indentation size effects in the nano- and micro-hardness of fcc single crystal metals." *Materials Science and Engineering: A*, vol. 424, no. 1-2, October 2006, pp. 178-187. https://doi.org/10.1016/j.msea.2006.06.137.

[9] Elmustafa, A.A., Stone, D.S. "Nanoindentation and the indentation size effect: Kinetics of deformation and strain gradient plasticity." *Journal of the Mechanics and Physics of Solids*, vol. 51, no. 2, February 2003, pp. 357-381. https://doi.org/10.1016/S0022-5096(02)00033-9.

[10] Zhao, M., Slaughter, W.S., Li, M., Mao, S.X. "Material-length-controlled nanoindentation size effects due to strain-gradient plasticity." *Acta Materialia*, vol. 51, no. 15, September 2003, pp. 4461-4469. https://doi.org/10.1016/S1359-6454(03)00281-7.

[11] Nix, W.D., Greer, J.R., Feng, G., Lilleodden, E.T. "Deformation at the nanometer and micrometer length scales: Effects of strain gradients and dislocation starvation." *Thin Solid Films*, vol. 515, no. 6, February 2007, pp. 3152-3157. https://doi.org/10.1016/j.tsf.2006.01.030.

[12] Xu, J. "Achieving Uniform Nanoparticle Dispersion in Metal Matrix Composites." *Dissertation*. University of California, Los Angeles, CA, 2015, p. 14.

[13] Ma, P., Jia, Y., Gokuldoss, P.K., Yu, Z., Yang, S., Zhao, J., Li, C. "Effect of Al2O3 nanoparticles are reinforcement on the tensile behavior of Al-12Si composites." *Metals*, vol. 7, no. 9, 2017, p. 359. https://doi.org/10.3390/met7090359.

[14] Kendall, K., Stainton, C. "Adhesion and aggregation of fine particles." *Powder Technology*, vol. 121, no. 2-3, November 2001, pp. 223-229. https://doi.org/10.1016/S0032-5910(01)00386-2.

[15] Mende, S., Stenger, F., Peukert, W., Schwedes, J. “Mechanical production and stabilization of submicron particles in stirred media mills.” *Powder Metallurgy*, vol. 132, no. 1, May 2003, pp. 64-73. https://doi.org/10.1016/S0032-5910(03)00042-1.

[16] Zhou, M., Qu, X., Ren, L., Fan, L., Zhang, Y., Guo, Y., Quan, G., Tang, Q., Liu, B., Sun, H. “The effects of carbon nanotubes on the mechanical and wear properties of AZ31 alloy.” *Materials*, vol. 10, no. 12, 2017, pp. 1-17. https://doi.org/10.3390/ma10121385.

[17] Li, F., Xie, Y., Song, M., Ni, S., Guo, S., Liao, X. “A detailed appraisal of the stress exponent used for characterizing creep behavior in metallic glasses.” *Materials Science and Engineering: A*, vol. 654, January 2016, pp. 53-59.

[18] Somekawa, H., Hirai, K., Watanabe, H., Takigawa, Y., Higashi, K. “Dislocation creep behavior in Mg-Al-Zn alloys.” *Materials Science and Engineering: A*, vol. 407, no. 1-2, October 2005, pp. 53-61. https://doi.org/10.1016/j.msea.2005.06.059.

[19] Kassner, M.E., Kumar, P., Blum, W. “Harper-Dorn creep.” *International Journal of Plasticity*, vol. 23, no. 6, June 2007, pp. 980-1000. https://doi.org/10.1016/j.ijplas.2006.10.006.

[20] Ganguly, S., Mondal, A.K. “Influence of SiC nanoparticles addition on microstructure and creep behavior of squeeze-cast AZ91-Ca-Sb magnesium alloy.” *Materials Science and Engineering: A*, vol. 718, March 2018, pp. 377-389. https://doi.org/10.1016/j.msea.2018.01.131.

[21] Mohamed, F.A., Park, K.T., Lavernia, E.J. “Creep behavior of discontinuous SiC-Al composites.” *Materials Science and Engineering: A*, vol. 150, no. 1, February 1992, pp. 21-35. https://doi.org/10.1016/0921-5093(90)90004-M.

[22] McEvily, A.J. “Characteristics of creep.” *Metal Failures: Mechanisms, Analysis, Prevention, 2nd ed.*, John Wiley & Songs, Hoboken, New Jersey, 2013, p. 219

[23] Goh, C.S., Wei, J., Lee, L.C., Gupta, M. “Ductility improvement and fatigue studies in Mg-CNT nanocomposites.” *Composites Science and Technology*, vol. 68, no. 6, May 2008, pp. 1432-1439. https://doi.org/10.1016/j.compscitech.2007.10.057.

[24] Goh, C.S., Wei, J., Lee, L.C., Gupta, M. “Simultaneous enhancement in strength and ductility by reinforcing magnesium with carbon nanotubes.” *Materials Science and Engineering: A*, vol. 423, no, 1-2, May 2006, pp. 153-156. https://doi.org/10.1016/j.msea.2005.10.071.

[25] Gupta, M., Wong, W.L.E. “Magnesium-based nanocomposites: Lightweight materials of the future.” *Materials Characterization*, vol. 105, July 2015, pp. 30-46. https://doi.org/10.1016/j.matchar.2015.04.015.

[26] Franke, O., Trenkle, J.C., Schuh, C.A. “Temperature dependence of the indentation size effect.” *Journal of Materials Research*, vol. 25, no. 7, July 2010, pp. 1225-1229. doi: 10.1557/JMR.2010.0159.

[27] Prasitthipayong, A., Vachhani, S.J., Tumey, S.J., Tumey, S.J., Minor, A.M., Hosemann, P. “Indentation size effect in unirradiated and ion-irradiated 800H steel at high temperatures.” *Acta Materialia*, vol. 144, February 2018, pp. 896-904. https://doi.org/10.1016/j.actamat.2017.11.001.

[28] Haghshenas, M., Muhammad, M., Hasannaeimi, V., Mukherjee, S., Gupta, M. “Ambient and non-ambient Mg-Sm_2O_3 nanocomposites.” *The International Journal of Advanced Manufacturing Technology*, vol. 105, no. 7-8, November 2019, pp. 2947-2956. DOI: 10.1007/s00170-019-04583-4.

[29] Beake, B.D., Harris, A.J., Moghal, J., Armstrong, D.E.J. “Temperature dependence of strain rate sensitivity, indentation size effects, and pile-up in polycrystalline tungsten from 25-950°C.” *Materials and Design*, vol. 156, October 2018, pp. 278-286. https://doi.org/10.1016/j.matdes.2018.06.063.

[30] Ma, X., Li, F., Sun, Z., Hou, J., Li, J., Fang, X. “Strain rate dependence of the indentation size effect in Ti-10V-2Fe-3Al alloy.” *Materials Science and Technology*, 2019. https://doi.org/10.1080/02670836.2019.1612596.

CHAPTER V
CONCLUSIONS AND FUTURE WORK

5.1. Project Conclusions

The objectives of this project were to investigate the ambient- and elevated-temperature creep response of Mg-CNT nanocomposites through instrumented indentation, determine if CNTs provide any creep resistance, and identify the dominant creep deformation mechanisms over every temperature tested. Optical microscopy (OM), scanning electron microscopy (SEM), and nanoindentation was used to gather the results necessary to address these objectives. The following sections present the main findings of these assessments.

5.1.1. Ambient-Temperature Conclusions

The following conclusions are drawn from the ambient-temperature (298 K) assessments made in the project:

1. OM indicates that marginal grain refinement is attained upon adding CNTs to the Mg matrix. SEM showed that the CNTs were in fair condition and were well-dispersed throughout the Mg matrix.
2. Indentation size effects are observed in hardness at ambient (room) temperature. Meaning, hardness is high at shallow indents and softer at deeper depths. This is observed over the loading portion of each nanoindentation test performed.
3. Hardness is improved for Mg-CNT nanocomposites at low CNT volume fractions, namely 0.25-0.5 vol.% CNT. This is due to the presence of hard CNT

nanoparticles in the matrix, CNTs hindering dislocation motion, load transfer from soft Mg matrix to hard CNTs, and generation and multiplication of dislocations through CTE and elastic modulus mismatch.

4. Pure Mg exhibited the highest creep displacement, and thus had the least creep resistance. Magnesium reinforced with 0.25 vol.% CNTs showed the lowest creep displacement, and thus had the best creep resistance. However, the Mg-0.5 vol.% CNT nanocomposite is a close runner-up for this title. Creep resistance is lost on Mg-0.75 vol.% CNT largely due to the formation of CNT agglomerations which cannot support the matrix as effectively as individual nanoparticles can.
5. Creep exponents indicate that dislocation motion (e.g., glide and climb) is the dominant cold flow (ambient-temperature creep) deformation mechanism.

5.1.2. Elevated-Temperature Conclusions

5.1.2.1. Conclusions Drawn from SEM Observations

SEM images of Berkovich indentations made on Pure Mg and Mg-0.75 vol.% CNT revealed the poor ductility of pure Mg. Several microcracks were observed near the indents made on pure magnesium. No microcracks were observed on the Mg-CNT nanocomposite. The ability of CNTs to better enhance ductility is attributed to texture modification, slip mode transition, stress state transition, and grain refinement.

5.1.2.2. Conclusions Drawn from Nanoindentation Tests

The following conclusions are drawn from the elevated-temperature (373, 473, and 573 K) assessments made in the project:

Conclusions involving the indentation size effect (ISE) in hardness:

1. Indentation size effects (ISEs) in hardness becomes less pronounced as temperature increases. This implies that a more accurate value of the true hardness of the material is recorded at shallow depths for elevated temperatures. This is attributed to increased geometrically necessary dislocation (GND) storage volume beneath the indenter at high temperatures.
2. The ISE phenomenon is a load rate and temperature-dependent concept. The ISE becomes more pronounced as load rate increases. This is due to the increased density of the induced GNDs formed beneath the indenter at increased load rates.

Conclusions regarding small-scale mechanical properties:

1. Mg-nanocomposites also experience stronger ISE behavior than pure Mg due to the ability of CNTs to improve hardness (over all temperatures) and act as extra thermally stable obstacles to hinder dislocation motion (at elevated temperatures).
2. There is no statistically significant difference in the measured hardness between pure Mg and Mg-CNT nanocomposites over all elevated temperatures due to error bar overlap.
3. Elastic modulus does not statistically vary between materials at 373 K. However, at 473 and 573 K, elastic modulus decreases as CNTs are added to Mg, until 0.5

vol.% CNTs. At 0.75 vol.% CNTs, elastic modulus increases again marginally. The initial decrease in modulus (stiffness) is attributed to the dynamic recovering (softening) of the material.

Conclusions regarding time-dependent plastic deformation (creep):

1. As temperature increases, creep displacement and creep rate both increase for all materials tested.
2. There is no observed trend in creep rate as a function of load rate when material and temperature are held constant. There is also no observed trend in creep rate as a function of CNT loading when temperature and load rate are held constant.
3. There is no observed trend in creep displacement as a function of load rate when material and temperature are held constant.
4. When creep displacement is varied as a function of CNT content, an optimum exists (or a close tie between two materials). For all high-temperature tests conducted, pure Mg exhibited the most creep displacement (least creep resistance) and the Mg-0.75 vol.% CNT nanocomposite always has the second-highest creep displacement. The best creep resistance belongs to magnesium reinforced with 0.25 or 0.5 vol.% CNTs, depending on temperature and load rate, over all tests.

Conclusions regarding the dominant creep deformation mechanism:

1. The dominant creep mechanism operative at 373 K (100°C) for all samples and load rates tested is dislocation movement (e.g., climb and glide). This is because the creep exponent, *n*, is greater than 3 for all samples.
2. At 473 K (200°C), the dominant creep mechanism is split between dislocation glide and grain boundary sliding (GBS) as *n*-values vary from 2 to 3 or greater (but not quite unity).
3. At 573 K (300°C), three creep mechanisms are "co-dominant" because *n*-values vary from unity to 3 and greater. Dislocation motion, GBS, and diffusional creep mechanisms (i.e., Nabarro-Herring and Coble creep) are all contributing to the creep of the materials at this temperature.

5.2. Recommendations for Future Work

Since this work has identified a range of CNTs, namely 0.25-0.5 vol.%, as being able to impart creep resistance to a Mg matrix, future work should include investigating if a lower volume fraction of 0.25 vol.% imparts any creep resistance to Mg. Since the samples in this project jumped from 0 vol.% CNTs (pure Mg) to Mg-0.25 vol.% CNTs, it is quite possible that an even lower volume fraction of CNTs may impart creep resistance. This would be a useful piece of information for someone who wishes to implement Mg-CNT nanocomposites into automotive, aerospace, or other applications as he or she can minimize costs associated with the addition of CNTs into the matrix (100 grams of SWCNTs are roughly 1000 USD at the time of this project). It is recommended that an

optimization project be carried out at 298, 373, 473, and 573 K to identify which volume fraction of CNTs has the best creep response at each temperature studied (or the targeted application's operating temperature if known). A design of experiments (DOE) statistical approach could be used to identify the optimum CNT loading for the best creep resistance.

The second future work recommendation is in regard to the dominant creep mechanisms. This project successfully assessed the creep response of Mg-CNT nanocomposites from ambient to elevated temperatures and identified which creep mechanisms are involved at each temperature tested. However, at elevated temperatures multiple mechanisms are at play. The simple analysis performed in this project did not sufficiently address which mechanism is the best represented (or truly dominant) at each temperature, or give any differentiation as to which diffusion mechanism is occurring at 573 K (300°C), i.e., whether Nabarro-Herring or Coble creep is occurring, or both, and quantitatively how much of each is present if both diffusional mechanisms are involved.

For future work, performing electron backscattered diffraction (EBSD) and also transmission electron microscopy (TEM) assessments could help differentiate which mechanisms are controlling at each test temperature. These analytical techniques could yield the microstructure evolution, so possibly a distinction between Nabarro-Herring creep and Coble creep could be made at 573 K.

A third recommendation for future work calls fatigue to mind. Since Mg-CNT nanocomposites are promising materials for engine components for aerospace and

automotive applications, it may be worthwhile to investigate the fatigue response of these materials in addition to the creep response. Engines are usually subjected to repeated, cyclic plastic and thermal strains. When a material is subject to repeated cycles of tensile and compressive loading, especially at high temperatures, fatigue can cause severe material weakening and result in abrupt and catastrophic failures. When assessing the lifetime of a service part, fatigue should not be ignored for this reason. Goh et al. [1] studied the fatigue behavior of a Mg-1.3 wt.% CNT nanocomposite, but only at room temperature (298 K). Fatigue response of these materials is more useful at elevated temperatures, or at least temperatures closer to the operating temperature of the intended application.

The last recommendation for future work is *interrupted* creep testing. This method compensates for a flaw in continuous creep testing, makes creep responses more credible, and perhaps brings materials one step closer to wider industrial application. A majority of powertrain components in vehicles experience discontinuous stresses, both thermal and mechanical. Mondal et al. [2] performed interrupted creep tests on Mg alloys to give more industrially-relevant information for powertrain manufacturing. This study makes a compelling argument for the investigation of interrupted creep behavior because real engine parts are not in continuous stress, but rather in interrupted chunks. These interrupted tests also gave rise to a primary creep appearing at the beginning of each testing cycle, which resulted in higher average strain rates than those in continuous creep tests. Testing Mg-CNT nanocomposites for creep behavior in an interrupted test mode may be bringing these materials one step closer to actual application in powertrain components.

REFERENCES

CHAPTER V – CONCLUSIONS AND FUTURE WORK

[1] Goh, C.S., Wei, J., Lee, L.C., Gupta, M. "Ductility improvement and fatigue studies in Mg-CNT nanocomposites." *Composites Science and Technology*, vol. 68, no. 6, May 2008, pp. 1432-1439. https://doi.org/10.1016/j.compscitech.2007.10.057.

[2] Mondal, A.K., Fechner, D., Kumar, S., Dieringa, H., Maier, P., Kainer, K.U. "Interrupted creep behavior of Mg alloys developed for powertrain applications." *Materials Science and Engineering: A*, vol. 527, no. 9, April 2010, pp. 2289-2296. https://doi.org/10.1016/j.msea.2009.12.010.

Appendix A: Intermediate Results Supporting Magnesium Trend Price

A.1. Magnesium Price

The trend price for magnesium metal was used to illustrate how expensive the metal is at this time. This commodity price was determined for China, the EU, and the US over 10 years of historical data, as shown below in Figure A-1.

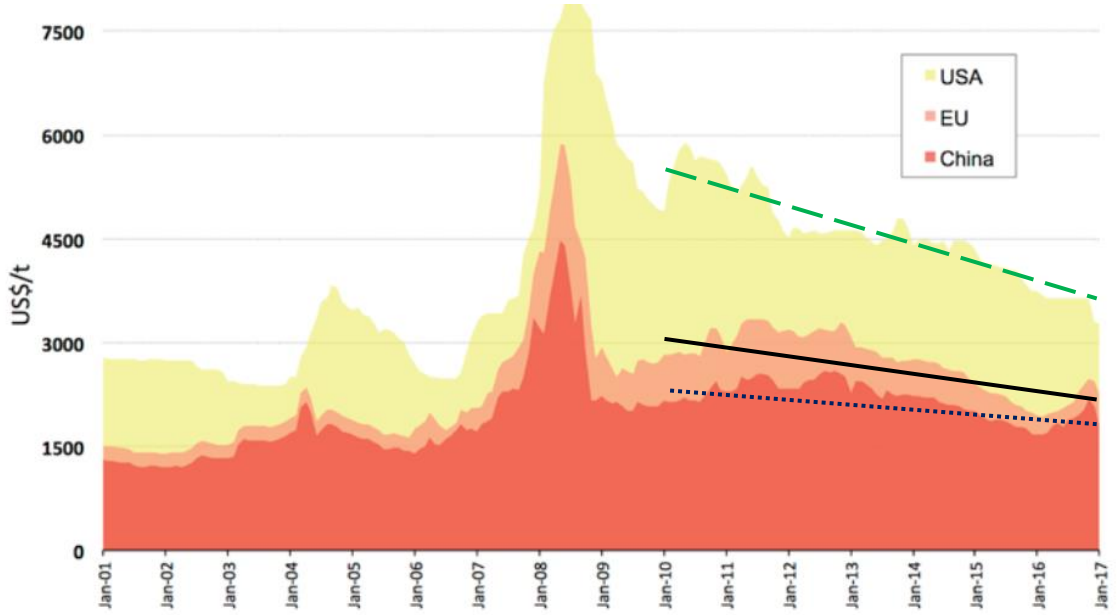

Figure A-1. Historical wholesale price of magnesium metal[1].

At a basis date of 2020, the trend wholesale price for magnesium is 1.41 USD/lb (3.11 USD/kg) in the USA (green trendline with long dashes), 0.90 USD/lb (1.98 USD/kg) in the EU (solid black trendline), and 0.77 USD/lb in China (square dot dark blue trendline).

[1] Li, L., Grandfield, J., Sun S., and Wang, C. Global Primary Magnesium Supply and Demand Balance 2016. IMA International Conference, May 2017. Web reference. Retrieved from: < www.intlmag.org> Date accessed: 15 March 2020.

Appendix B: Supplementary *P-h* curves

B.1. *P-h* curves obtained at 5 and 50 mN/s to supplement Chapter IV-Section 4.3.2.1.

A series of *P-h* curves were shown in Chapter IV, Section 4.3.2.1 for constant material and load rate, as a function of temperature. Below are the remaining figures at constant load rates of 5 and 50 mN/s for completion.

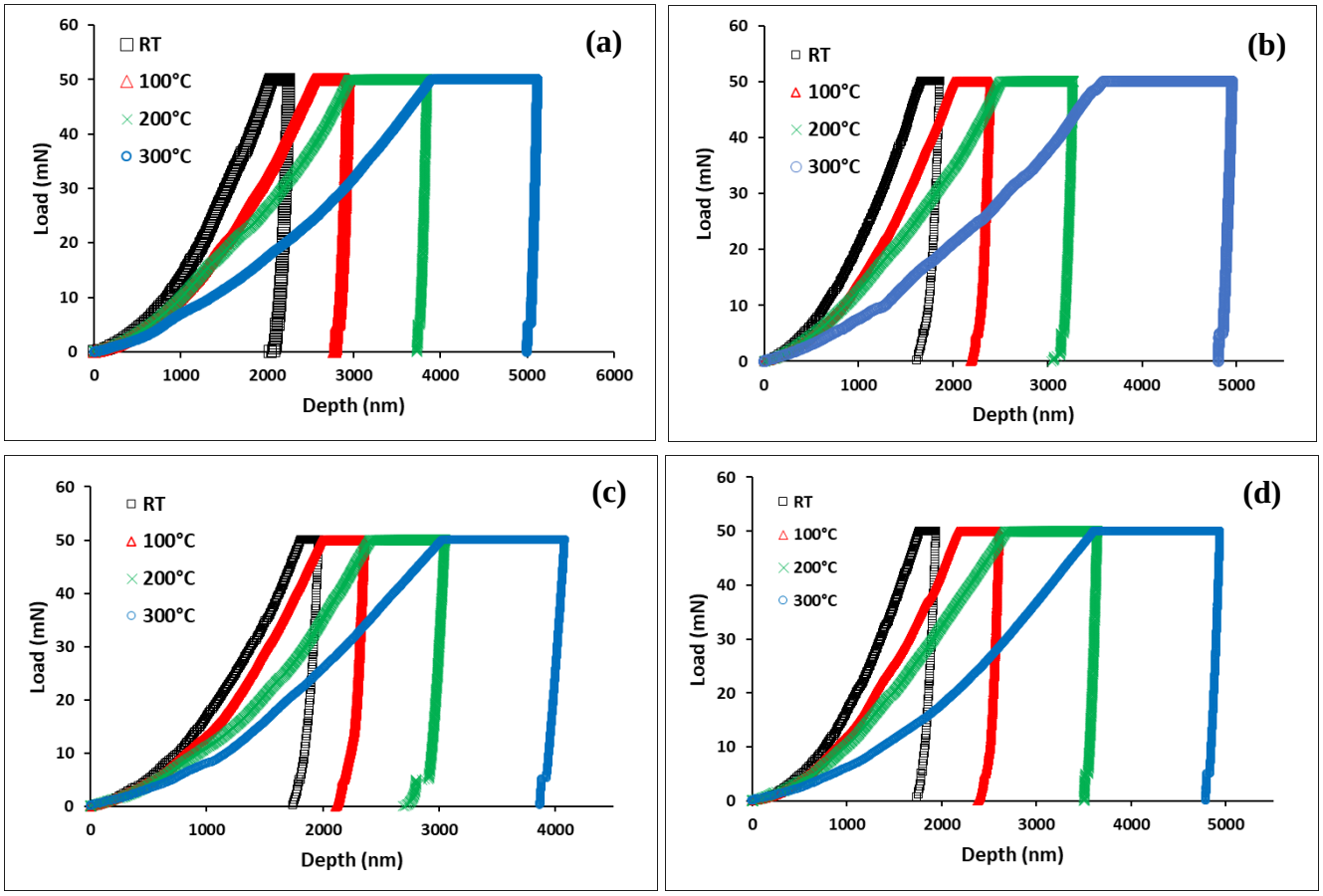

Figure B-1. Load-displacement (*P-h*) curves as a function of temperature for a fixed load rate of 5 mN/s for: **(a)** Pure Mg, **(b)** Mg-0.25 vol.% CNT, **(c)** Mg-0.5 vol.% CNT, and **(d)** Mg-0.75 vol.% CNT. **RT**: room temperature (298 K).

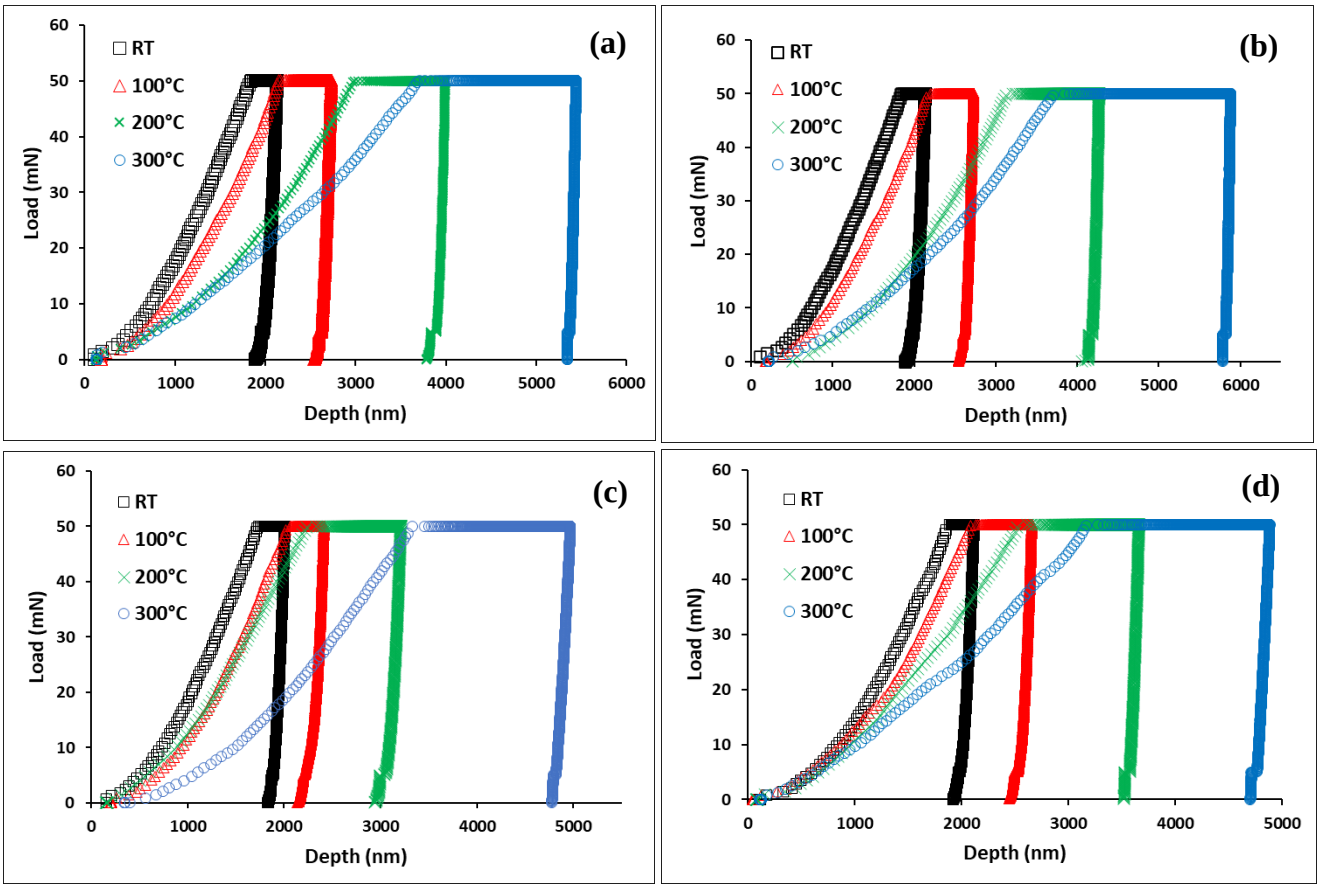

Figure B-2. Load-displacement (*P-h*) curves as a function of temperature for a fixed load rate of 50 mN/s for: **(a)** Pure Mg, **(b)** Mg-0.25 vol.% CNT, **(c)** Mg-0.5 vol.% CNT, and **(d)** Mg-0.75 vol.% CNT. **RT**: room temperature (298 K).

B.2. *P-h* curves obtained at room temperature, 100, and 200°C to supplement Chapter IV-Section 4.3.2.2.

A series of *P-h* curves were shown in Chapter IV, Section 4.3.2.2 for constant material and temperature, as a function of load rate. Below are the remaining figures at a constant temperature of room temperature, 100, and 200°C for completion.

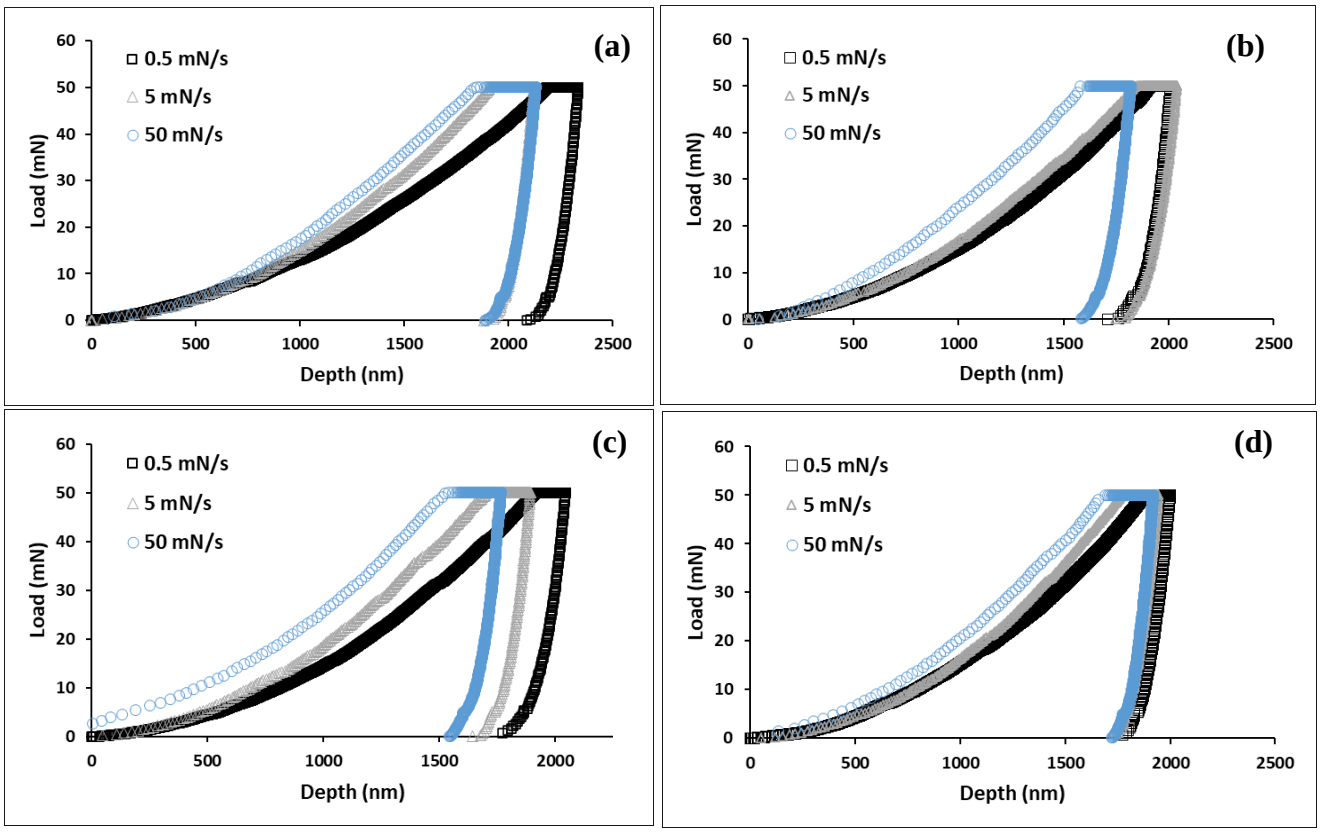

Figure B-3. Load-displacement (*P-h*) curves as a function of load rate for a fixed temperature of room temperature (298 K) for: **(a)** Pure Mg, **(b)** Mg-0.25 vol.% CNT, **(c)** Mg-0.5 vol.% CNT, and **(d)** Mg-0.75 vol.% CNT.

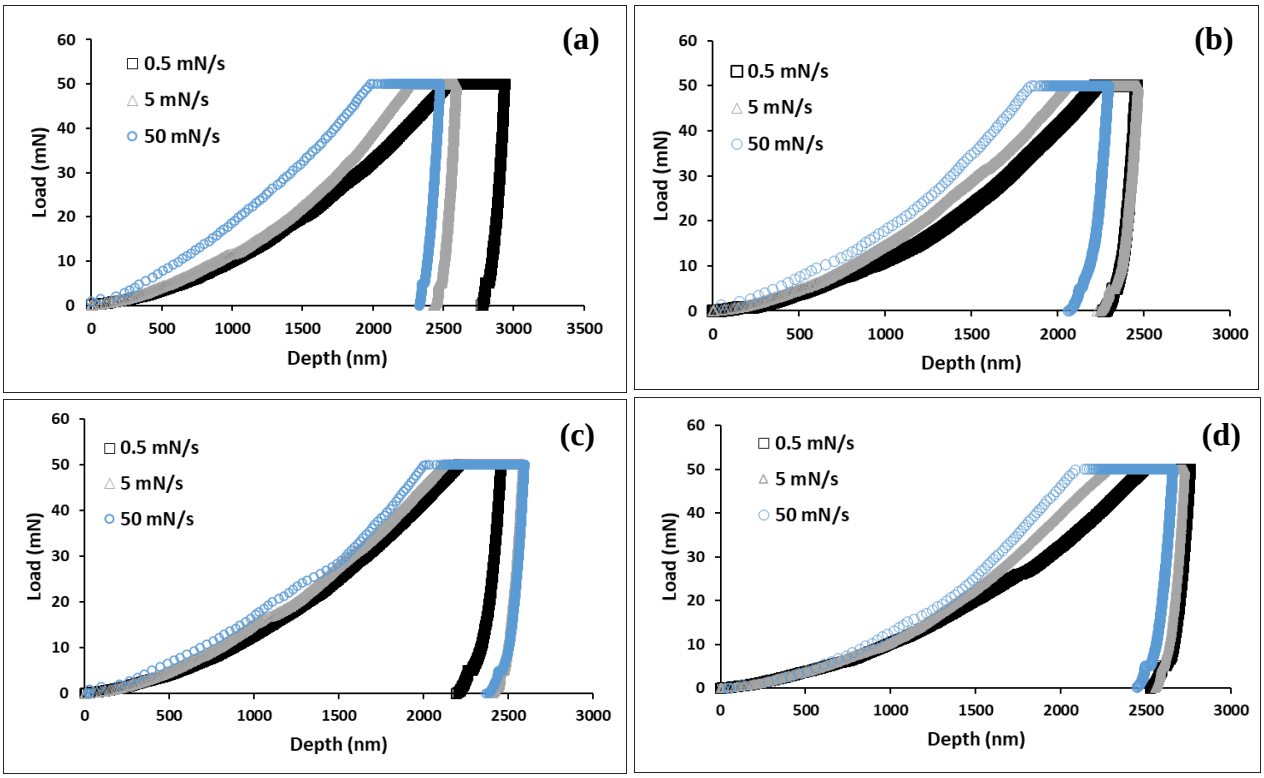

Figure B-4. Load-displacement (*P-h*) curves as a function of load rate for a fixed temperature of 100°C for: (a) Pure Mg, (b) Mg-0.25 vol.% CNT, (c) Mg-0.5 vol.% CNT, and (d) Mg-0.75 vol.% CNT.

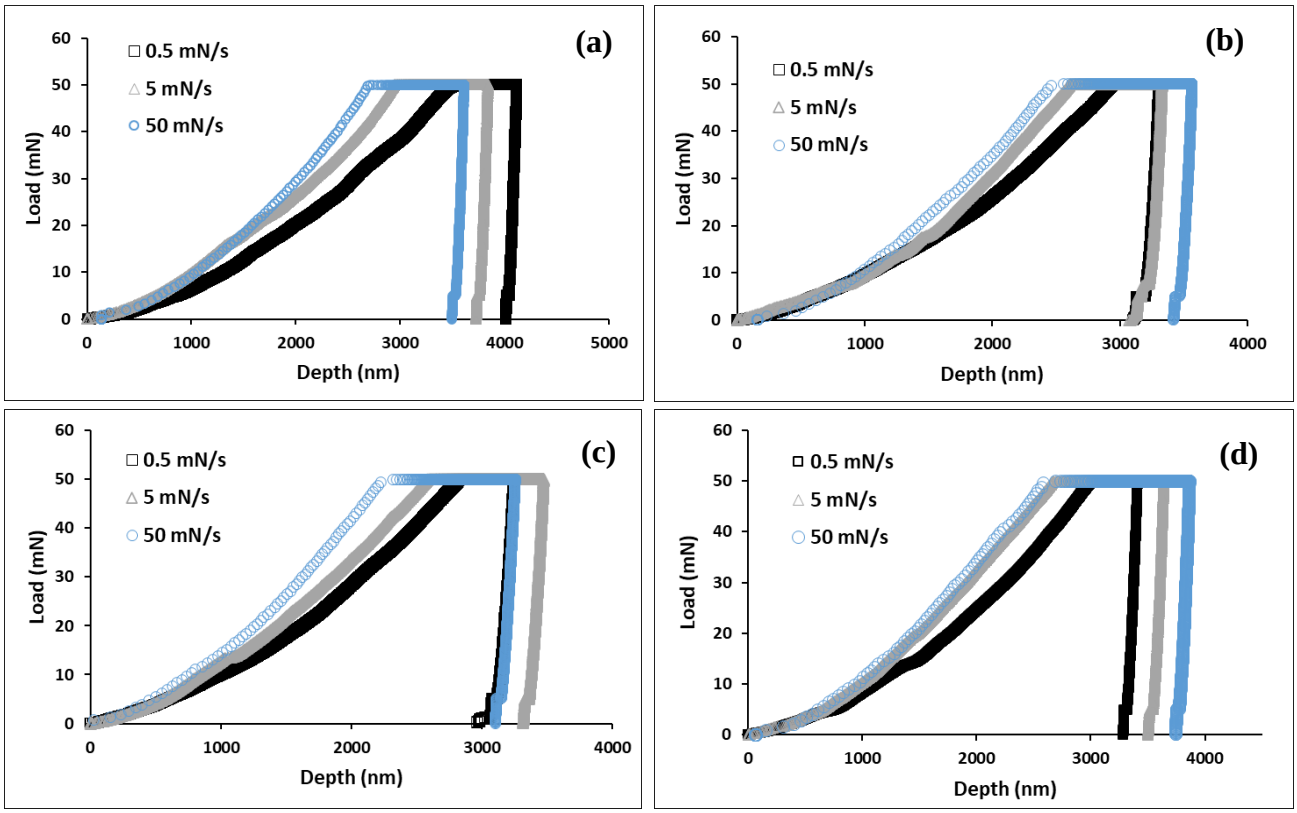

Figure B-5. Load-displacement (*P-h*) curves as a function of load rate for a fixed temperature of 200°C for: (a) Pure Mg, (b) Mg-0.25 vol.% CNT, (c) Mg-0.5 vol.% CNT, and (d) Mg-0.75 vol.% CNT.

Appendix C: Supplementary Indentation Size Effect (ISE) Curves

C.1. ISE curves obtained at 5 and 50 mN/s to supplement Chapter IV-Section 4.3.3.1.

A series of ISE curves were shown in Chapter IV, Section 4.3.3.1 for constant material and load rate, as a function of temperature. Below are the remaining figures at constant load rates of 5 and 50 mN/s for completion.

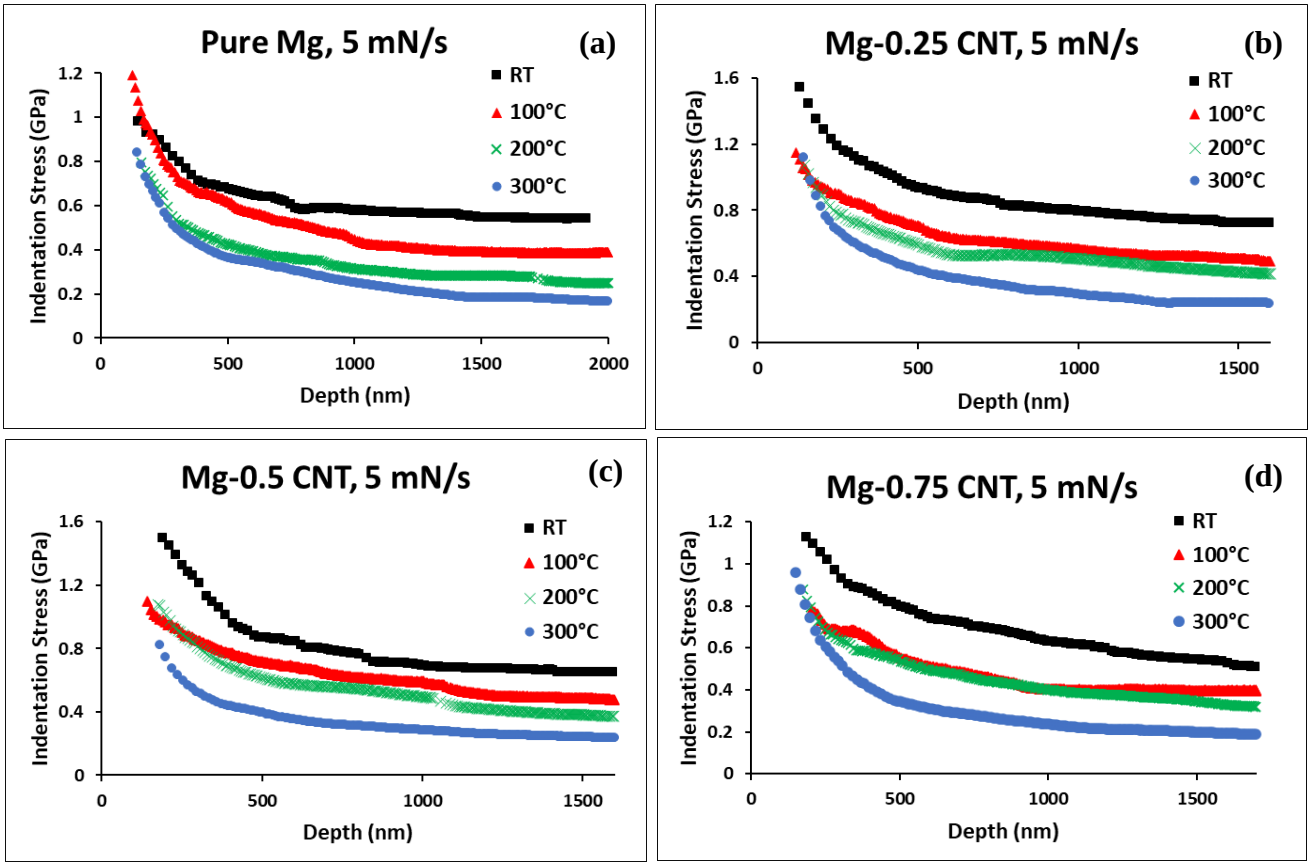

Figure C-1. Indentation stress versus loading depth behavior (ISE behavior) as a function of temperature for a fixed load rate of 5 mN/s for: **(a)** Pure Mg, **(b)** Mg-0.25 vol.% CNT, **(c)** Mg-0.5 vol.% CNT, and **(d)** Mg-0.75 vol.% CNT. **RT**: room temperature (298 K).

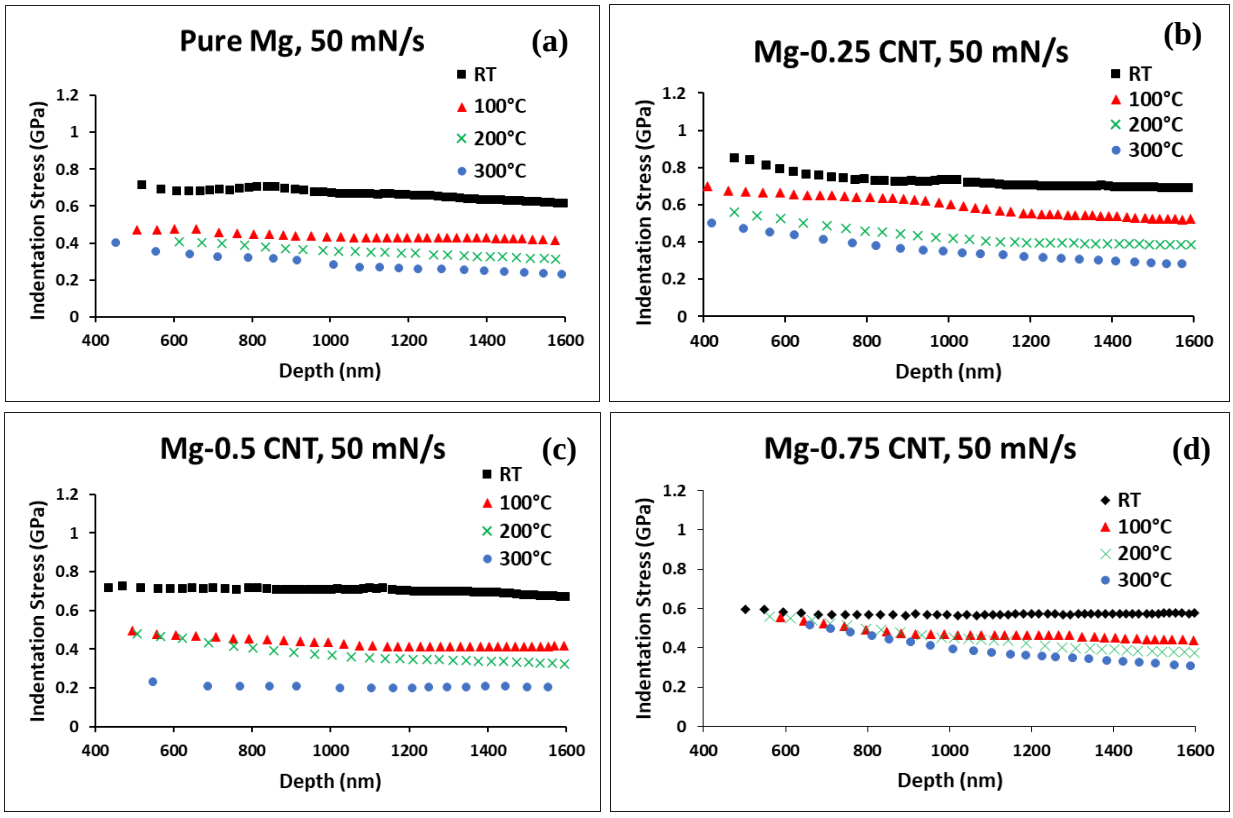

Figure C-2. Indentation stress versus loading depth behavior (ISE behavior) as a function of temperature for a fixed load rate of 50 mN/s for: **(a)** Pure Mg, **(b)** Mg-0.25 vol.% CNT, **(c)** Mg-0.5 vol.% CNT, and **(d)** Mg-0.75 vol.% CNT. **RT**: room temperature (298 K).

C.2. ISE curves obtained at 200°C, 100°C, and room temperature to supplement Chapter IV-Section 4.3.3.2.

A series of ISE curves were shown in Chapter IV, Section 4.3.3.2 for constant material and temperature, as a function of load rate. Below are the remaining figures at 200°C, 100°C, and room temperature for completion.

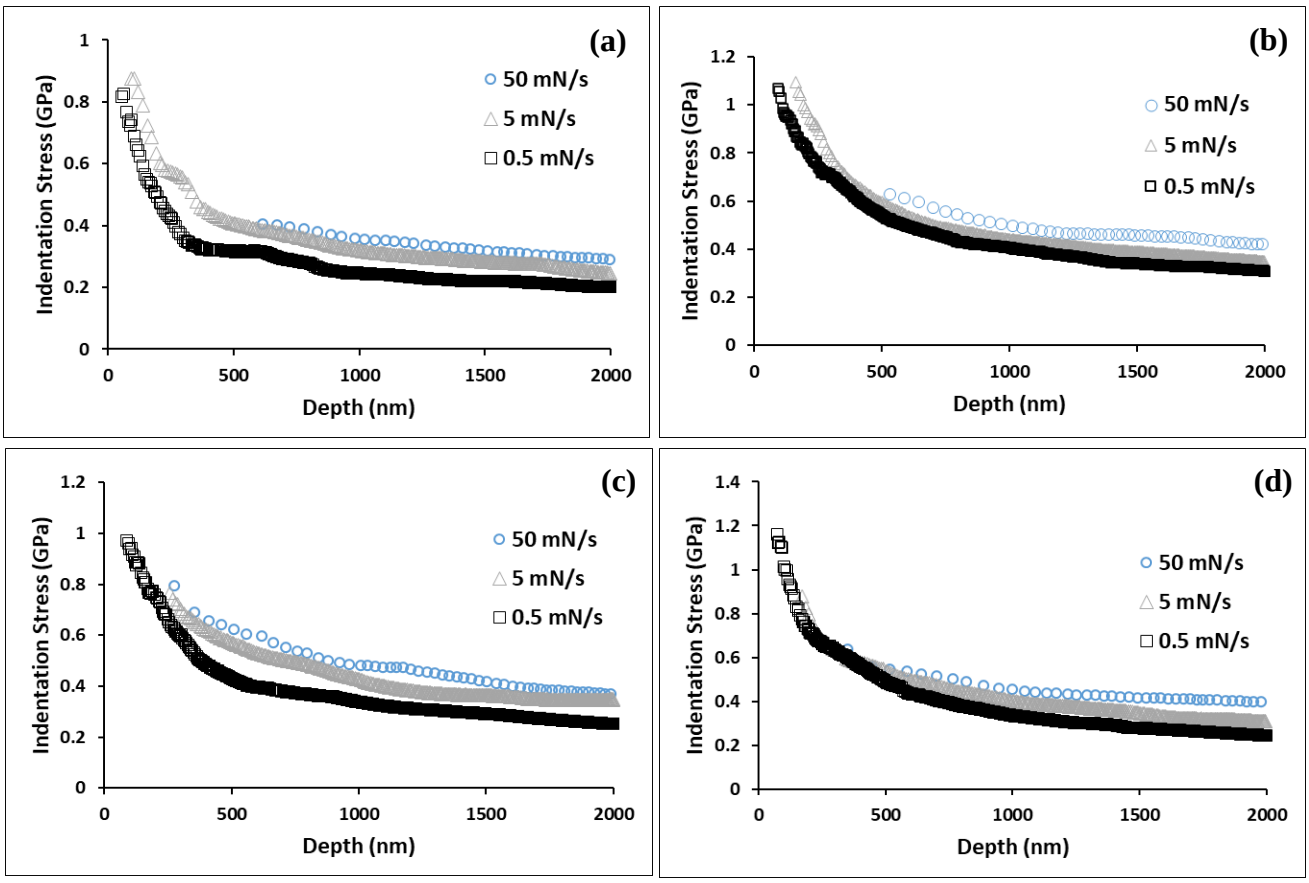

Figure C-3. ISE curves as a function of load rate for a fixed temperature of 200°C for: **(a)** Pure Mg, **(b)** Mg-0.25 vol.% CNT, **(c)** Mg-0.5 vol.% CNT, and **(d)** Mg-0.75 vol.% CNT.

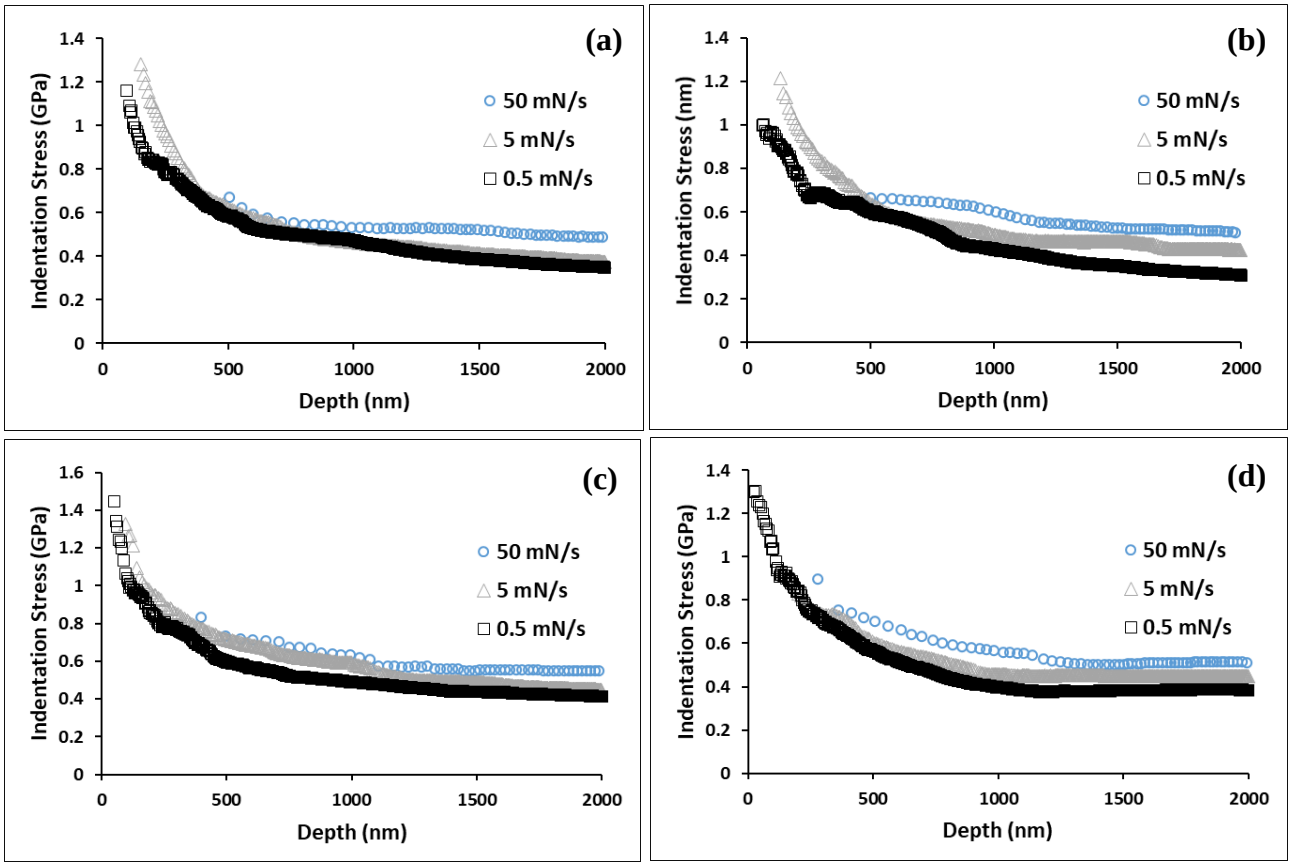

Figure C-4. ISE curves as a function of load rate for a fixed temperature of 100°C for: **(a)** Pure Mg, **(b)** Mg-0.25 vol.% CNT, **(c)** Mg-0.5 vol.% CNT, and **(d)** Mg-0.75 vol.% CNT.

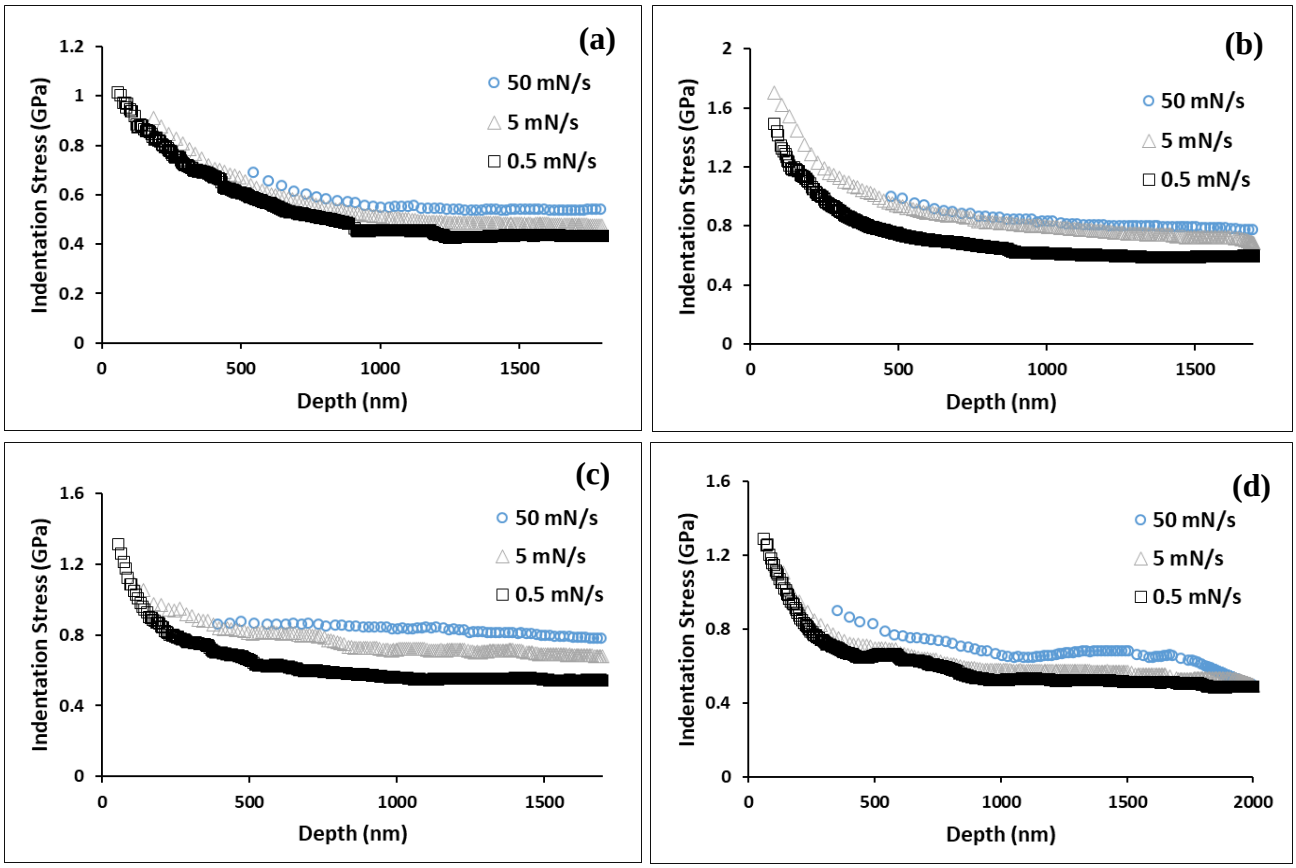

Figure C-5. ISE curves as a function of load rate fixed at room temperature (298 K) for: **(a)** Pure Mg, **(b)** Mg-0.25 vol.% CNT, **(c)** Mg-0.5 vol.% CNT, and **(d)** Mg-0.75 vol.% CNT.

C.3. ISE curves obtained at 200°C, 100°C, and room temperature to supplement Chapter IV-Section 4.3.3.3.

A series of ISE curves were shown in Chapter IV, Section 4.3.3.3 for a fixed load rate and temperature, as a function of CNT content. Below are the remaining figures at 200°C, 100°C, and room temperature for completion.

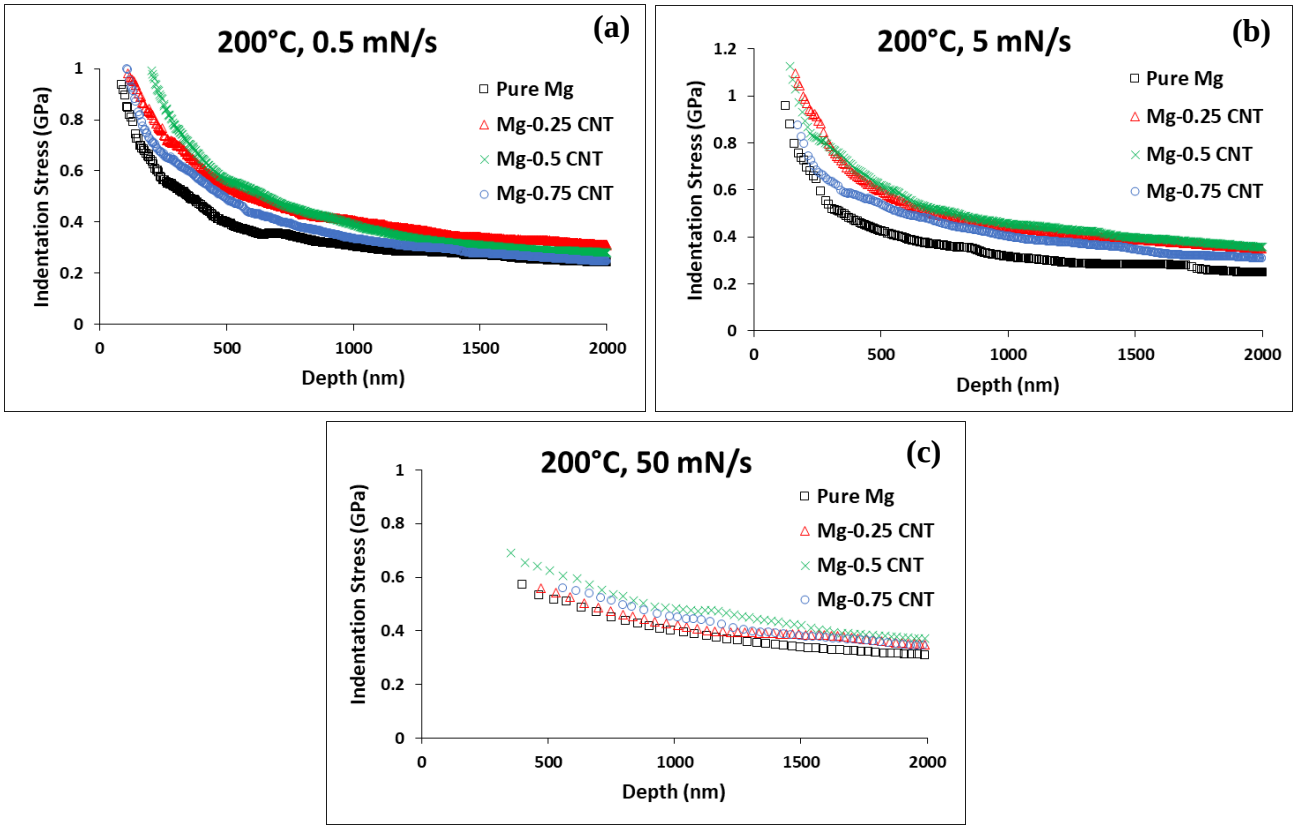

Figure C-6. Indentation stress versus loading depth behavior (ISE behavior) as a function of CNT content at a fixed temperature of 200°C over all load rates tested: **(a)** 0.5 mN/s, **(b)** 5 mN/s, and **(c)** 50 mN/s.

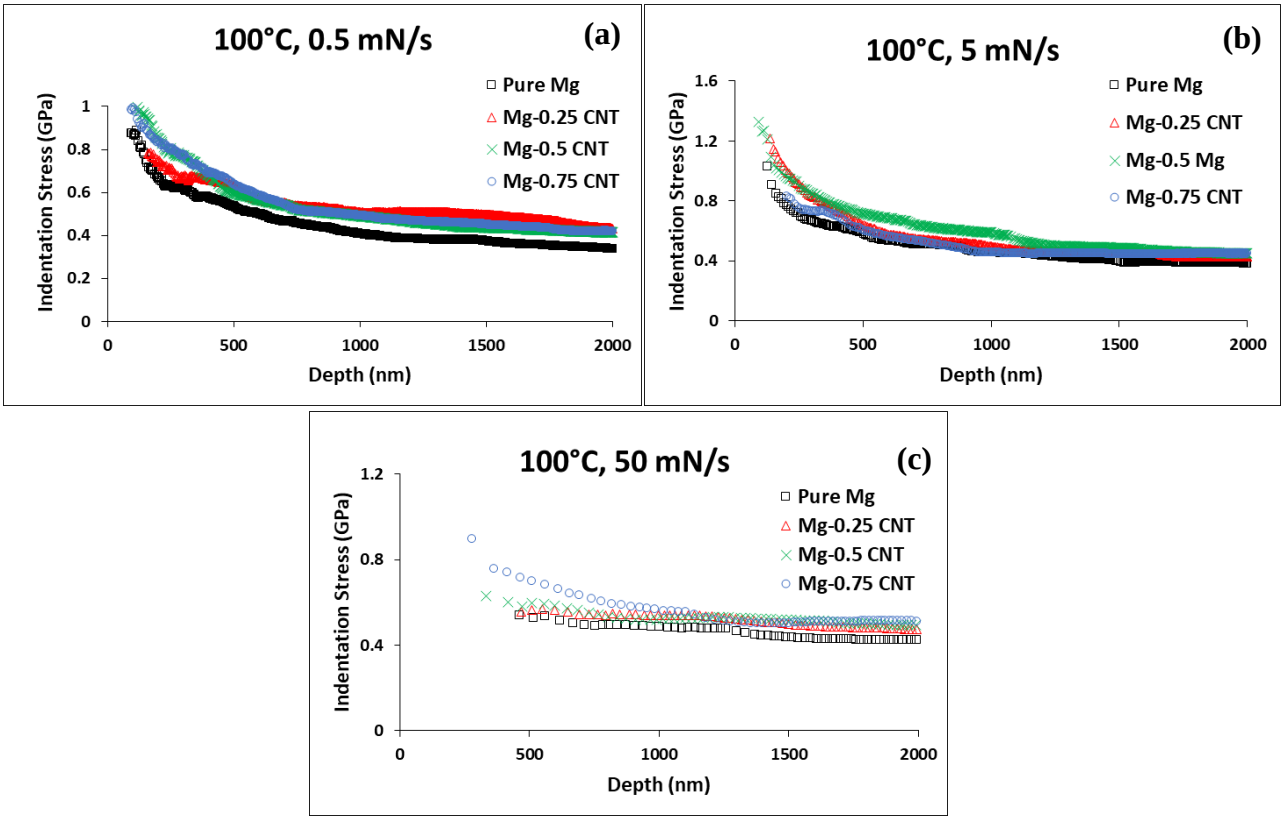

Figure C-7. Indentation stress versus loading depth behavior (ISE behavior) as a function of CNT content at a fixed temperature of 100°C over all load rates tested: **(a)** 0.5 mN/s, **(b)** 5 mN/s, and **(c)** 50 mN/s.

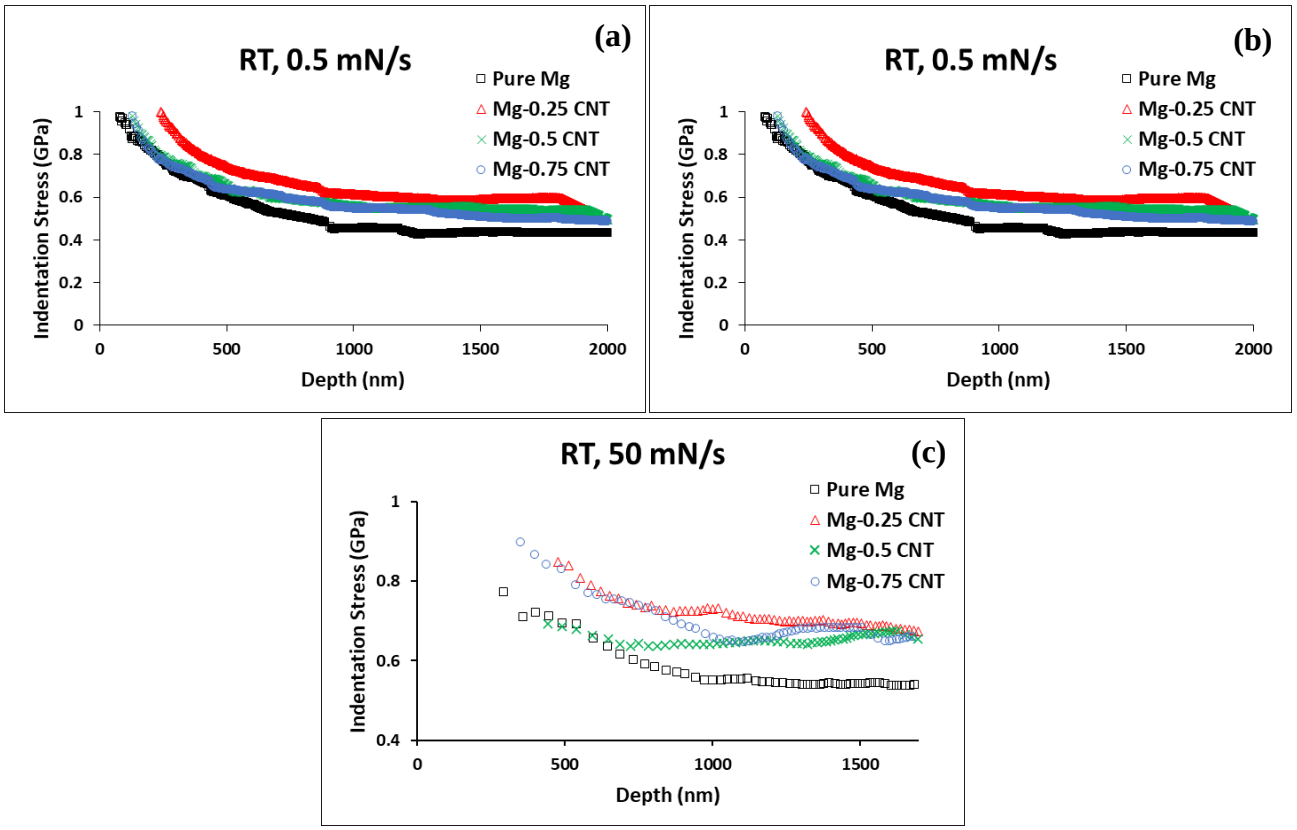

Figure C-8. Indentation stress versus loading depth behavior (ISE behavior) as a function of CNT content fixed at room temperature (298 K) over all load rates tested: **(a)** 0.5 mN/s, **(b)** 5 mN/s, and **(c)** 50 mN/s.

Appendix D: Supplementary Creep Rate Curves

D.1. Creep rate curves obtained at 5 and 50 mN/s to supplement Chapter IV-Section 4.3.6.1.

A series of creep rate curves were shown in Chapter IV, Section 4.3.6.1 for a fixed material and load rate, as a function of temperature. Below are the remaining figures at fixed load rates of 5 and 50 mN/s for completion.

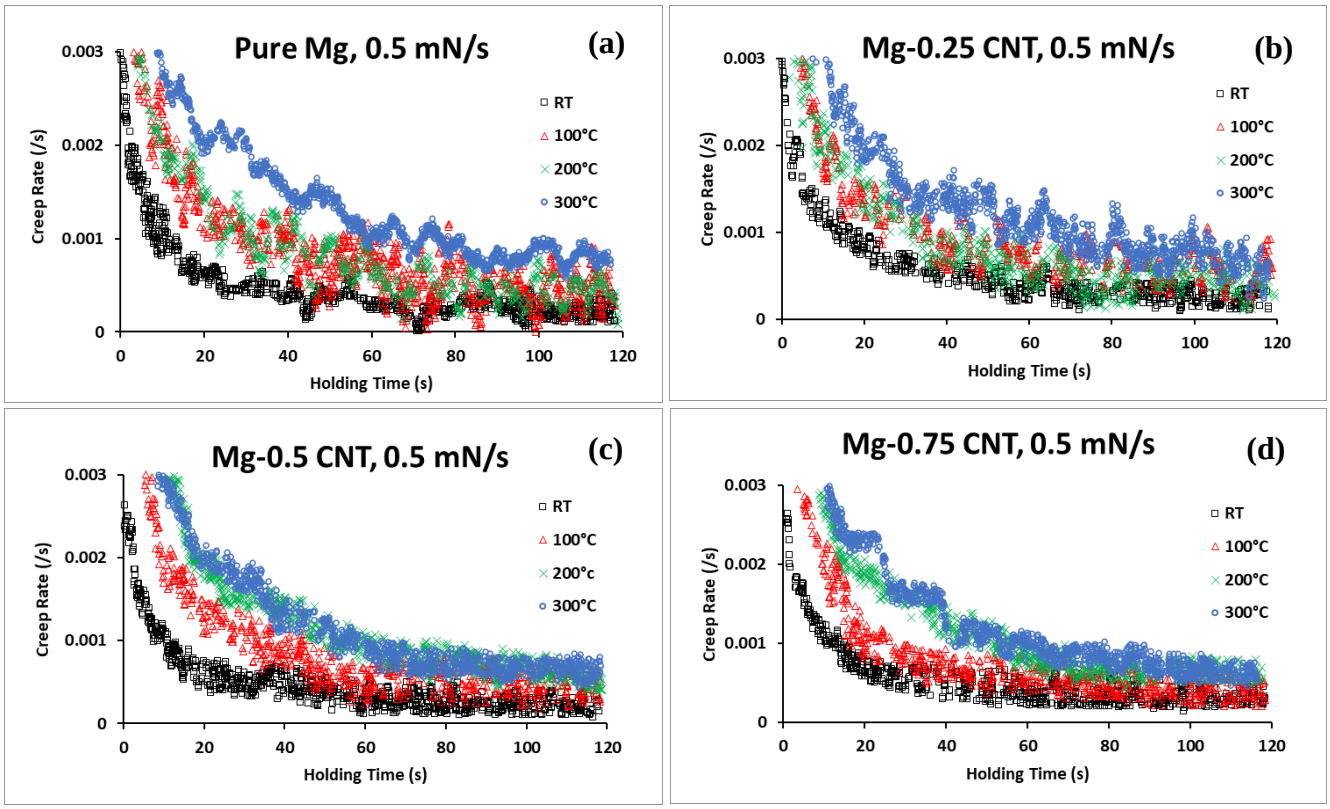

Figure D-1. Creep rate versus holding time behavior as a function of temperature for a fixed load rate of 0.5 mN/s for: **(a)** Pure Mg, **(b)** Mg-0.25 vol.% CNT, **(c)** Mg-0.5 vol.% CNT, and **(d)** Mg-0.75 vol.% CNT. **RT**: room temperature (298 K).

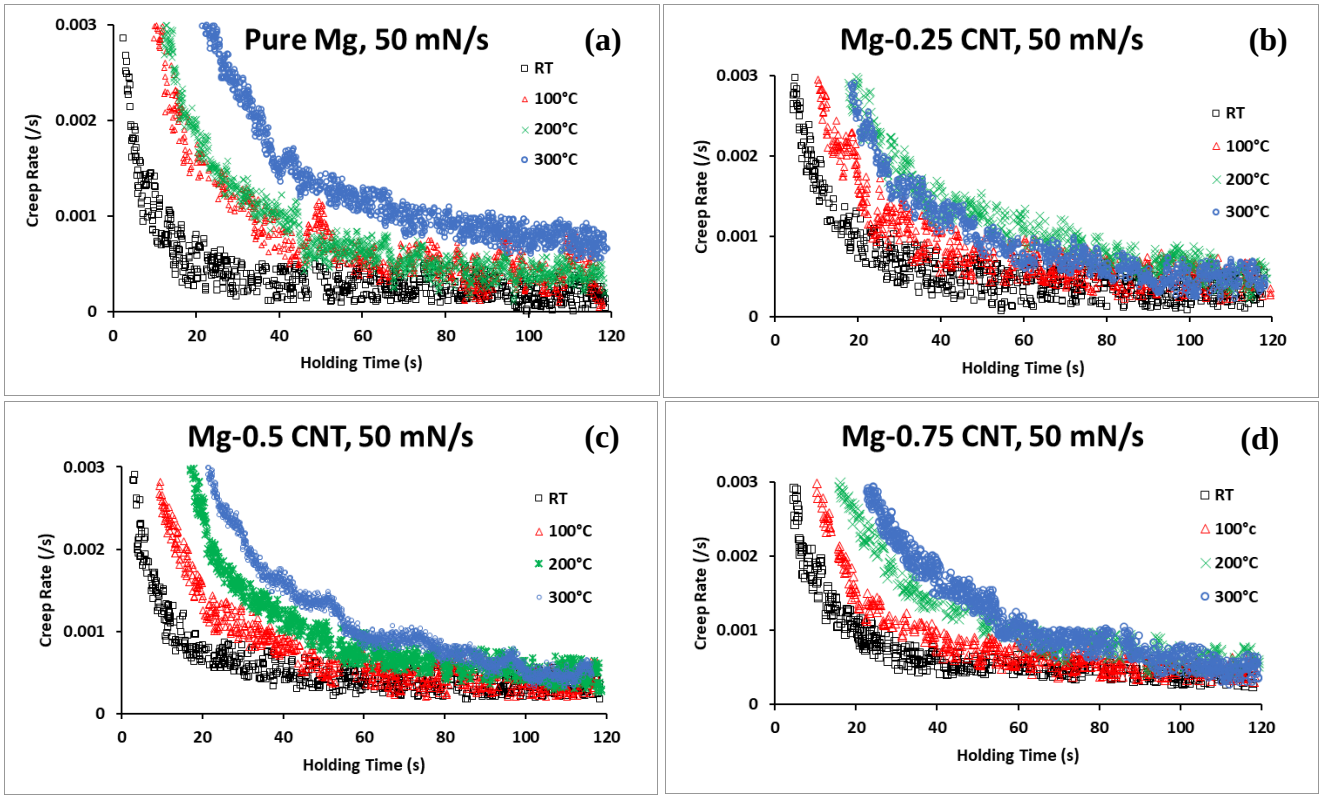

Figure D-2. Creep rate versus holding time behavior as a function of temperature for a fixed load rate of 50 mN/s for: **(a)** Pure Mg, **(b)** Mg-0.25 vol.% CNT, **(c)** Mg-0.5 vol.% CNT, and **(d)** Mg-0.75 vol.% CNT. **RT**: room temperature (298 K).

D.2. Creep rate curves obtained at 5 and 50 mN/s to supplement Chapter IV-Section 4.3.6.2.

A series of creep rate curves were shown in Chapter IV, Section 4.3.6.2 for a fixed material and temperature, as a function of load rate. Below are the remaining figures at fixed temperatures of 200°C, 100°C, and room temperature for completion.

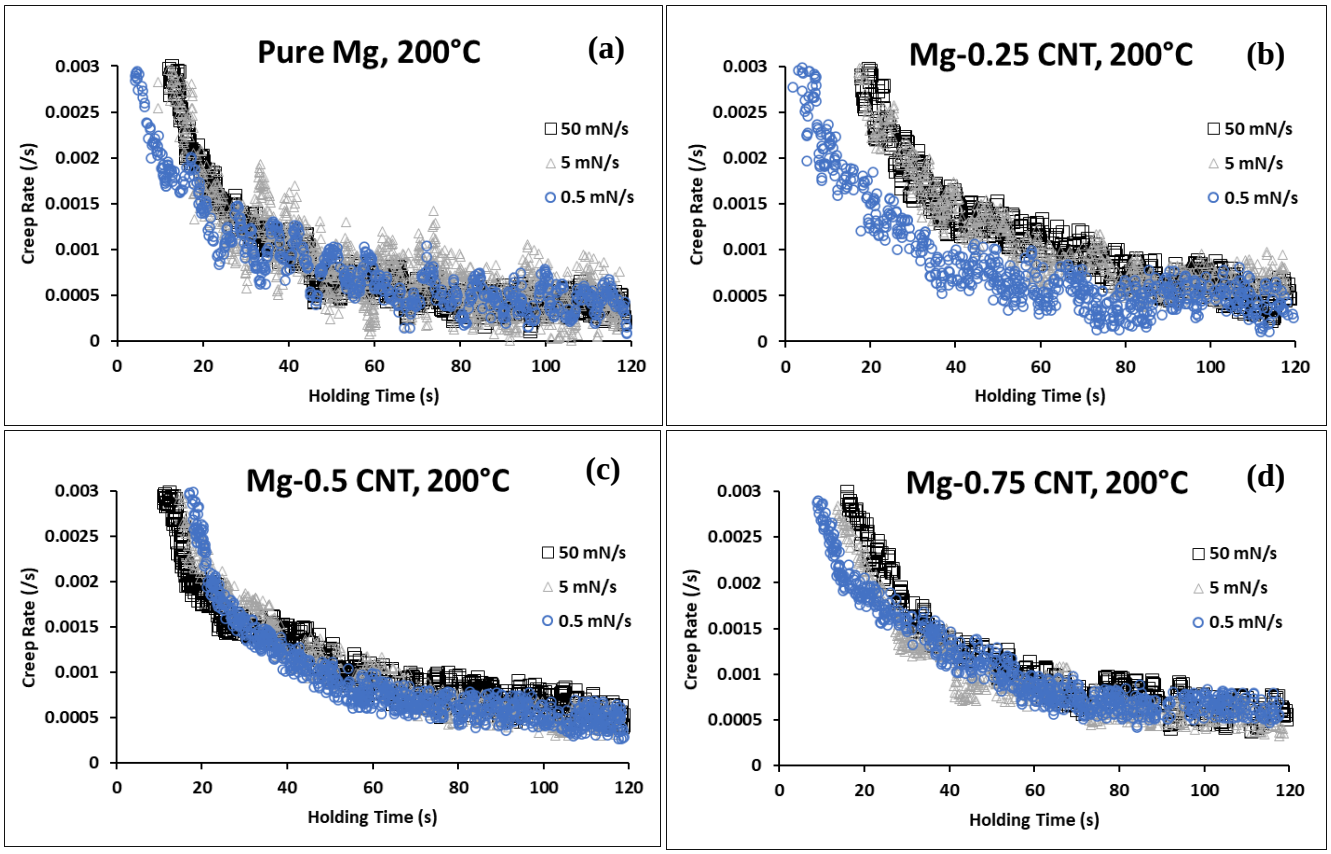

Figure D-3. Creep rate versus holding time behavior as a function of load rate for a fixed temperature of 200°C for: **(a)** Pure Mg, **(b)** Mg-0.25 vol.% CNT, **(c)** Mg-0.5 vol.% CNT, and **(d)** Mg-0.75 vol.% CNT. **RT**: room temperature (298 K).

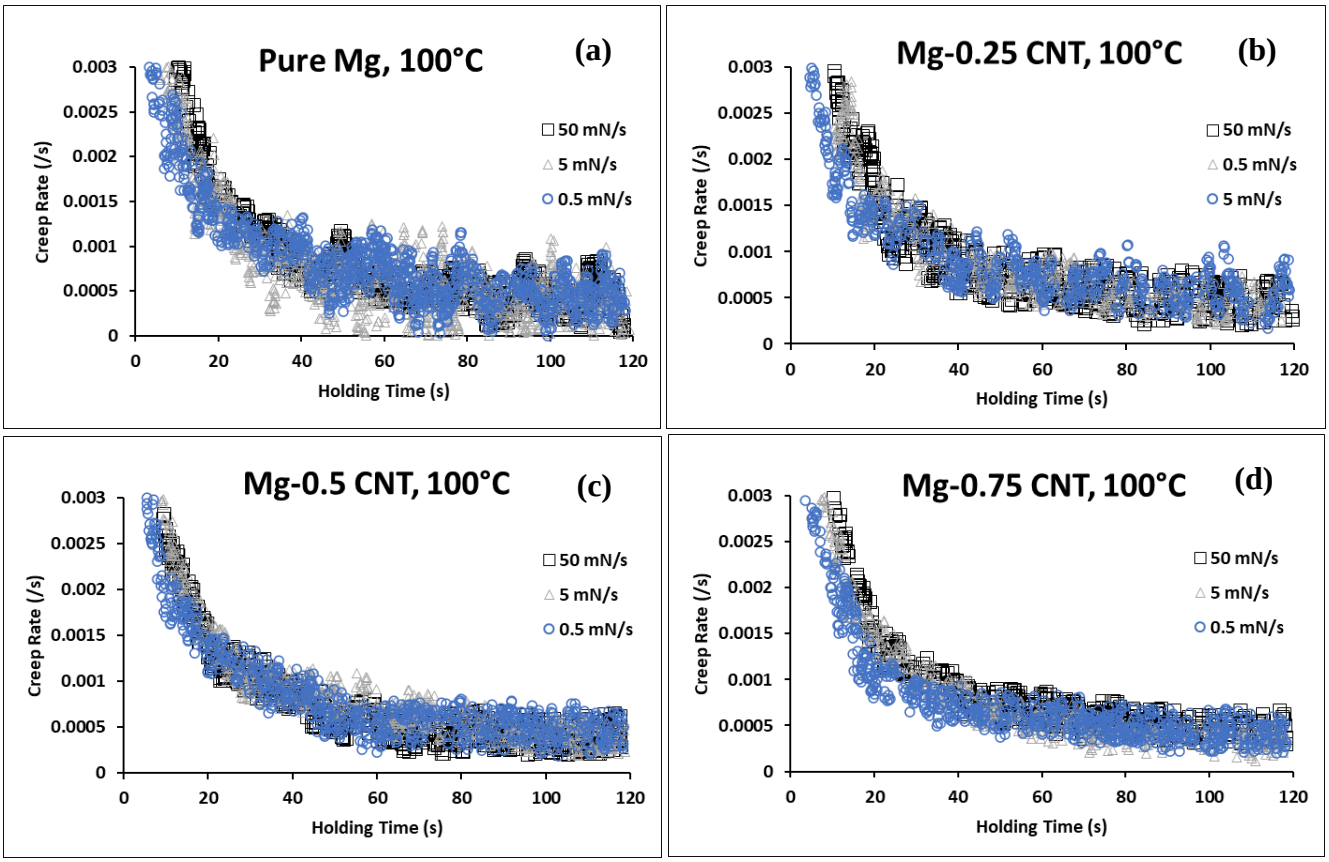

Figure D-4. Creep rate versus holding time behavior as a function of load rate for a fixed temperature of 100°C for: **(a)** Pure Mg, **(b)** Mg-0.25 vol.% CNT, **(c)** Mg-0.5 vol.% CNT, and **(d)** Mg-0.75 vol.% CNT. **RT**: room temperature (298 K).

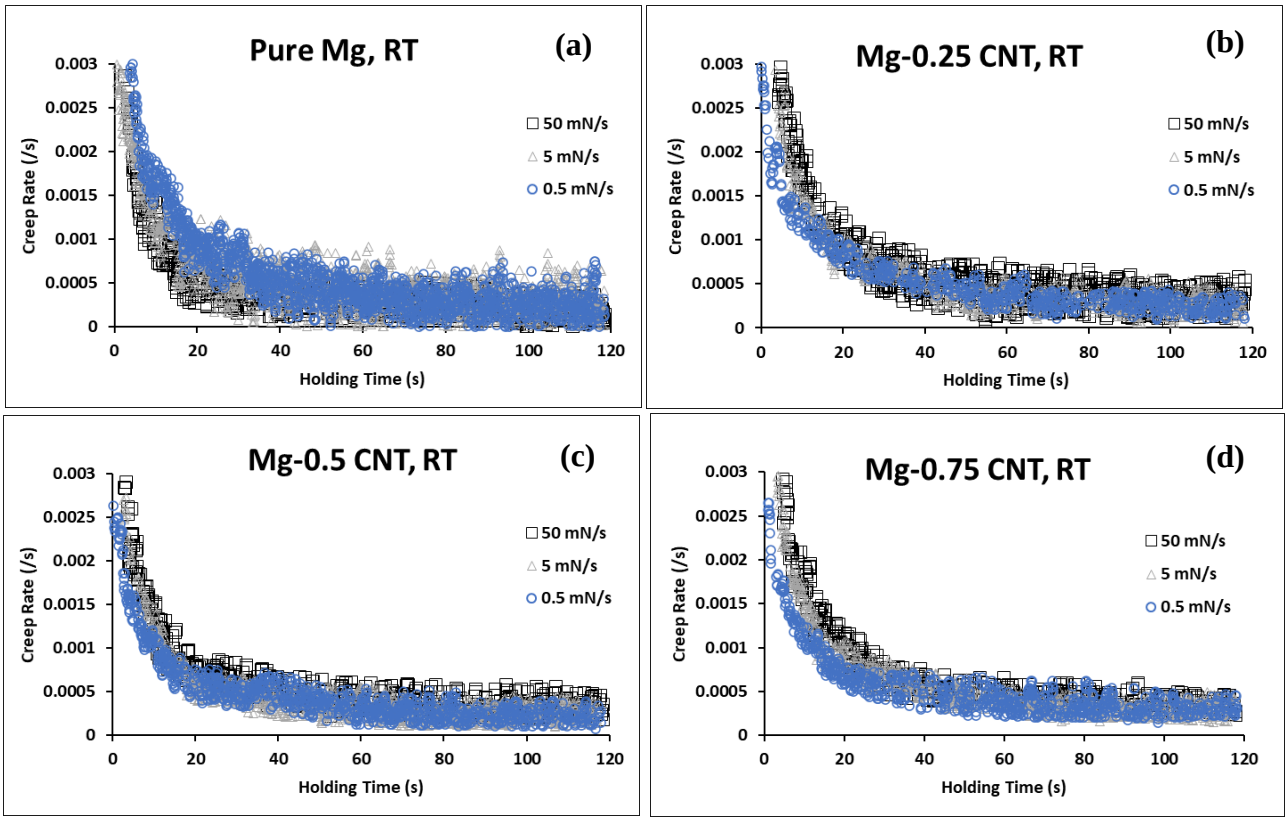

Figure D-5. Creep rate versus holding time behavior as a function of load rate fixed at room temperature (298 K) for: **(a)** Pure Mg, **(b)** Mg-0.25 vol.% CNT, **(c)** Mg-0.5 vol.% CNT, and **(d)** Mg-0.75 vol.% CNT. **RT**: room temperature (298 K).

D.3. Creep rate curves obtained at 5 and 50 mN/s to supplement Chapter IV-Section 4.3.6.3.

A series of creep rate curves were shown in Chapter IV, Section 4.3.6.3 for a temperature and load rate, as a function of CNT volume percentage. Below are the remaining figures at fixed temperatures of 200°C, 100°C, and room temperature for completion.

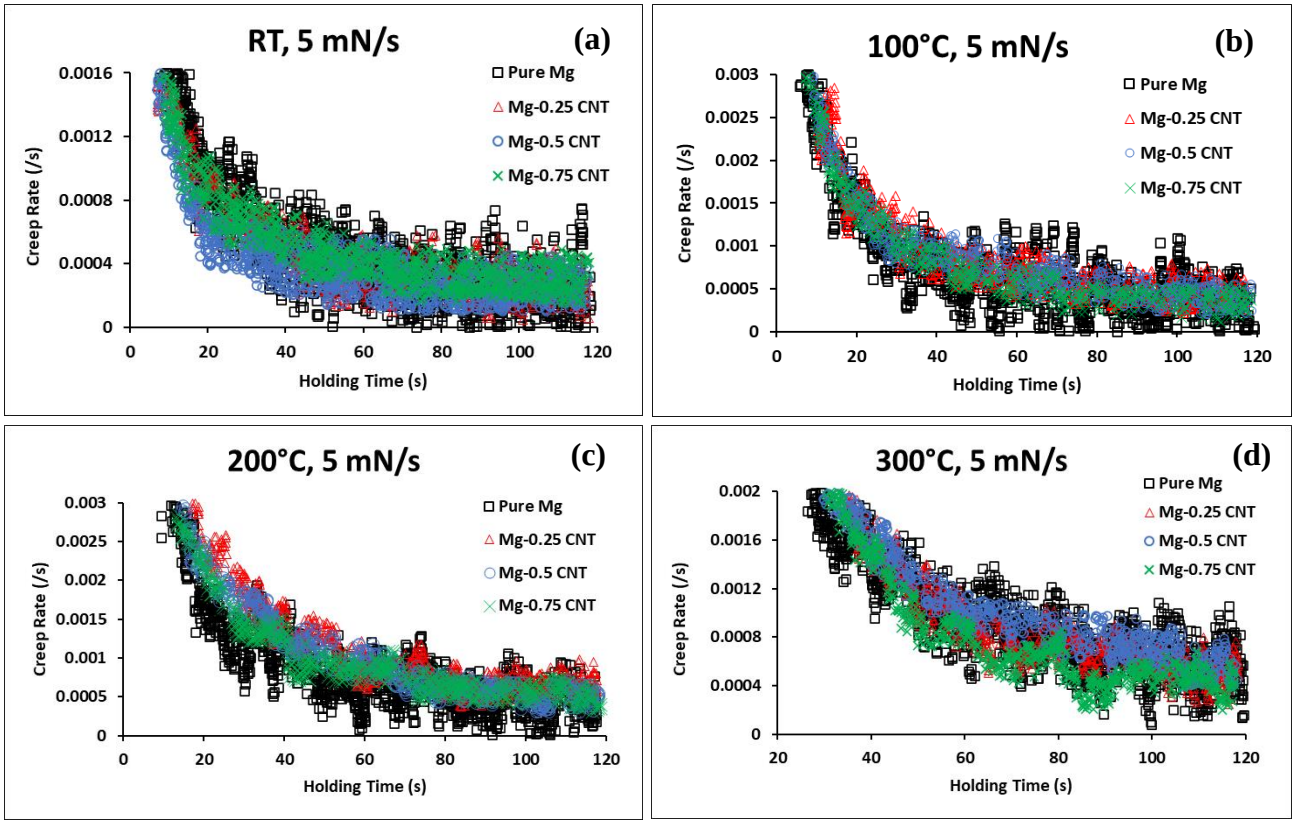

Figure D-6. Creep rate versus holding time behavior as a function of material tested (CNT loading) at a fixed load rate of 5 mN/s, over all temperatures tested: **(a)** RT, **(b)** 100°C, **(c)** 200°C, and **(d)** 300°C. **RT**: room temperature (298 K).

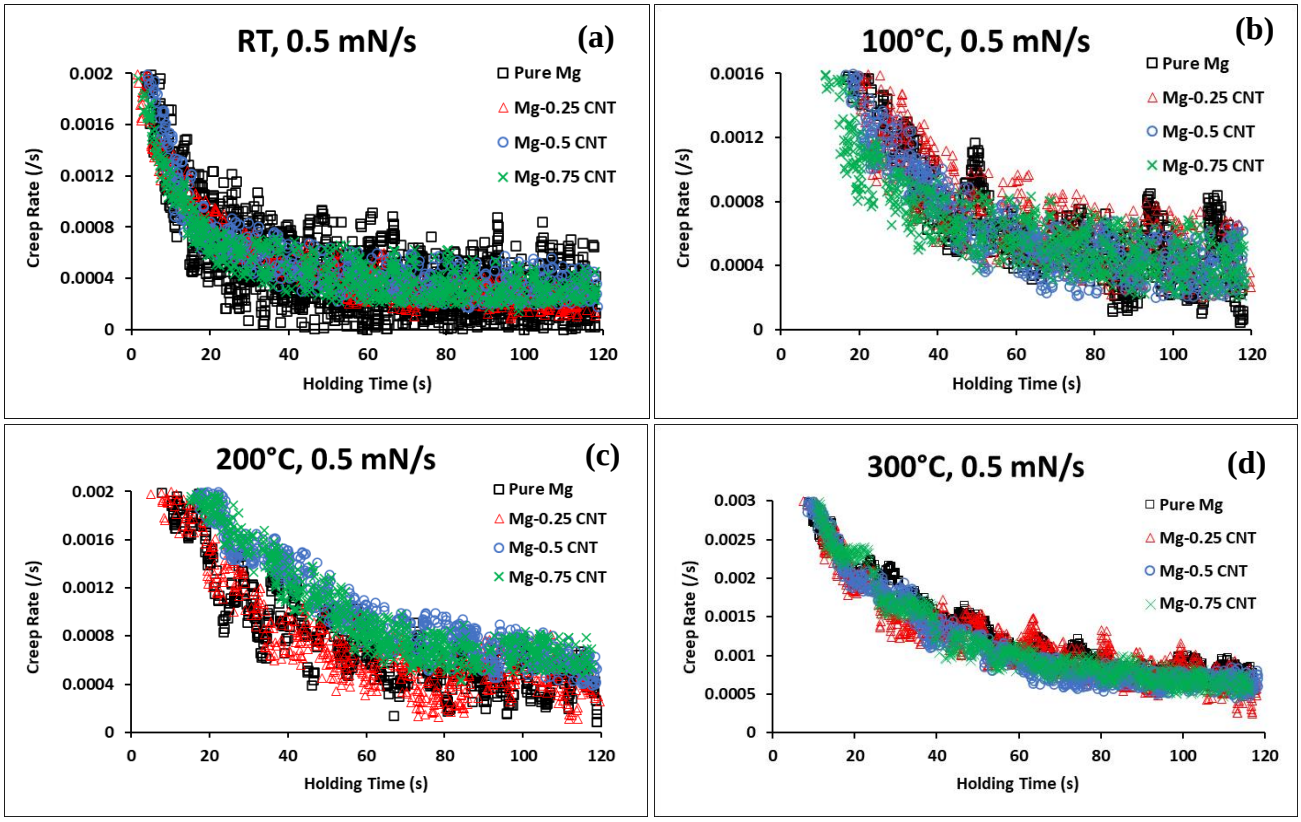

Figure D-7. Creep rate versus holding time behavior as a function of material tested (CNT loading) at a fixed load rate of 0.5 mN/s, over all temperatures tested: **(a)** RT, **(b)** 100°C, **(c)** 200°C, and **(d)** 300°C. **RT**: room temperature (298 K).

Appendix E: Supplementary Creep Displacement Curves

E.1. Creep displacement curves obtained at 0.5 and 5 mN/s to supplement Chapter IV-Section 4.3.7.1.

A series of creep displacement curves were shown in Chapter IV, Section 4.3.7.1 for a fixed material and load rate, as a function of temperature. Below are the remaining figures at fixed load rates of 0.5 and 5 mN/s for completion.

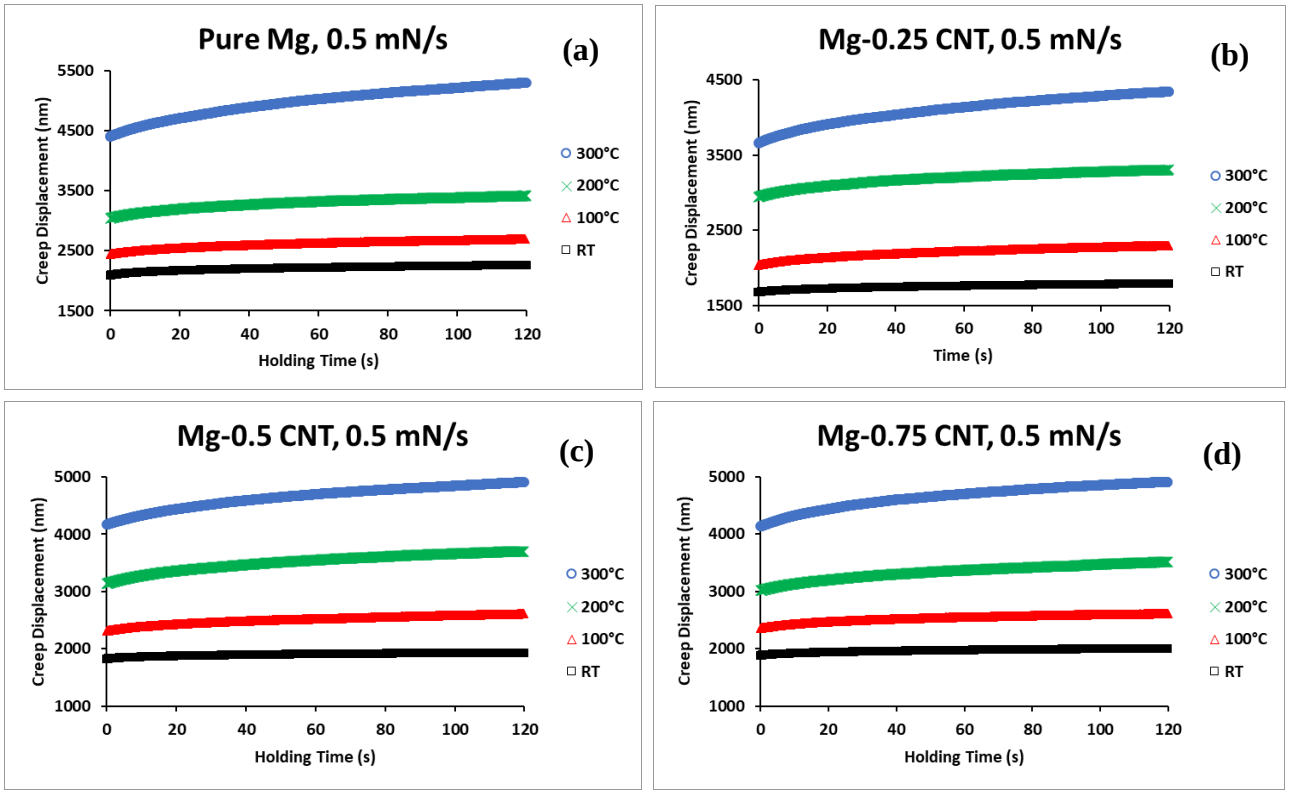

Figure E-1. Creep displacement versus holding time behavior as a function of temperature for a fixed load rate of 0.5 mN/s for: **(a)** Pure Mg, **(b)** Mg-0.25 vol.% CNT, **(c)** Mg-0.5 vol.% CNT, and **(d)** Mg-0.75 vol.% CNT. **RT**: room temperature (298 K).

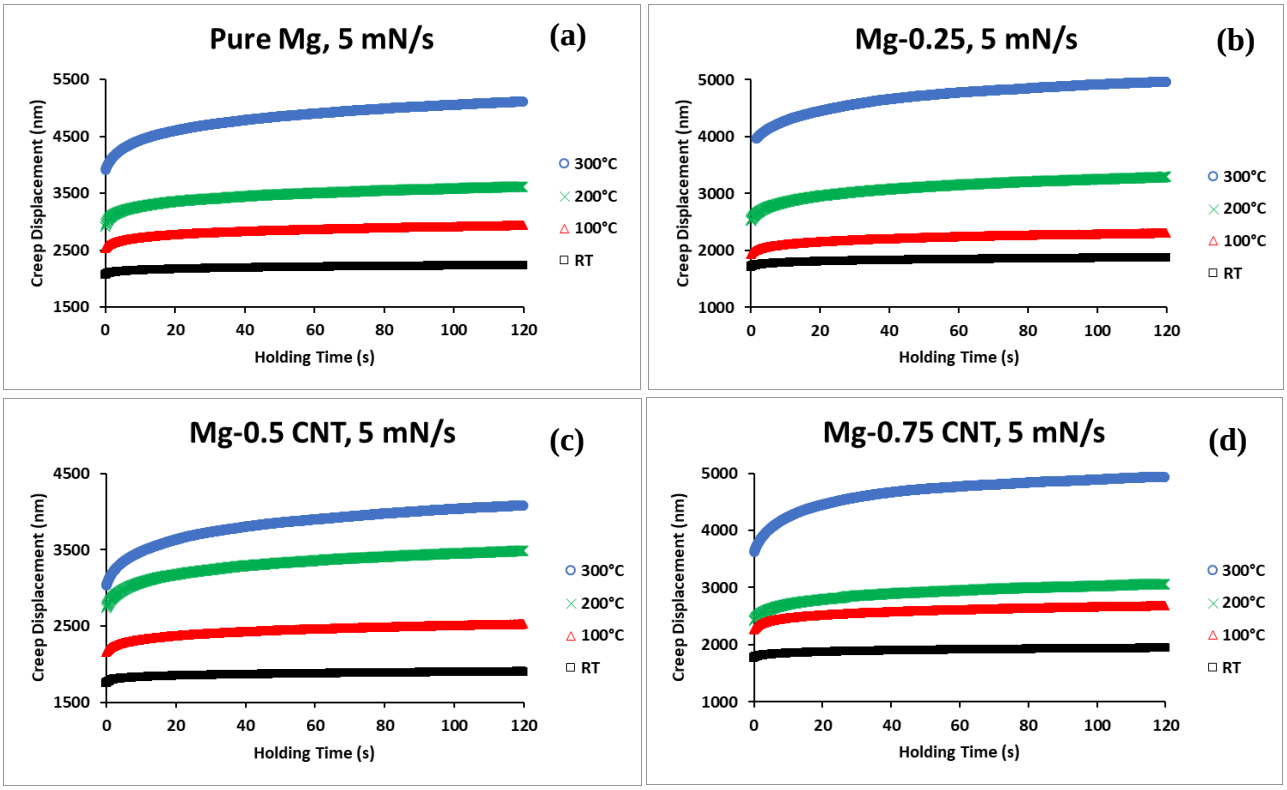

Figure E-2. Creep displacement versus holding time behavior as a function of temperature for a fixed load rate of 5 mN/s for: **(a)** Pure Mg, **(b)** Mg-0.25 vol.% CNT, **(c)** Mg-0.5 vol.% CNT, and **(d)** Mg-0.75 vol.% CNT. **RT**: room temperature (298 K).

E.2. Creep displacement curves obtained at room temperature, 100°C, and 300°C to supplement Chapter IV-Section 4.3.7.2.

A series of creep displacement curves were shown in Chapter IV, Section 4.3.7.2 for a fixed temperature and CNT volume percentage, as a function of load rate. Below are the remaining figures at fixed temperatures of ambient (298 K), 100°C, and 300°C for completion.

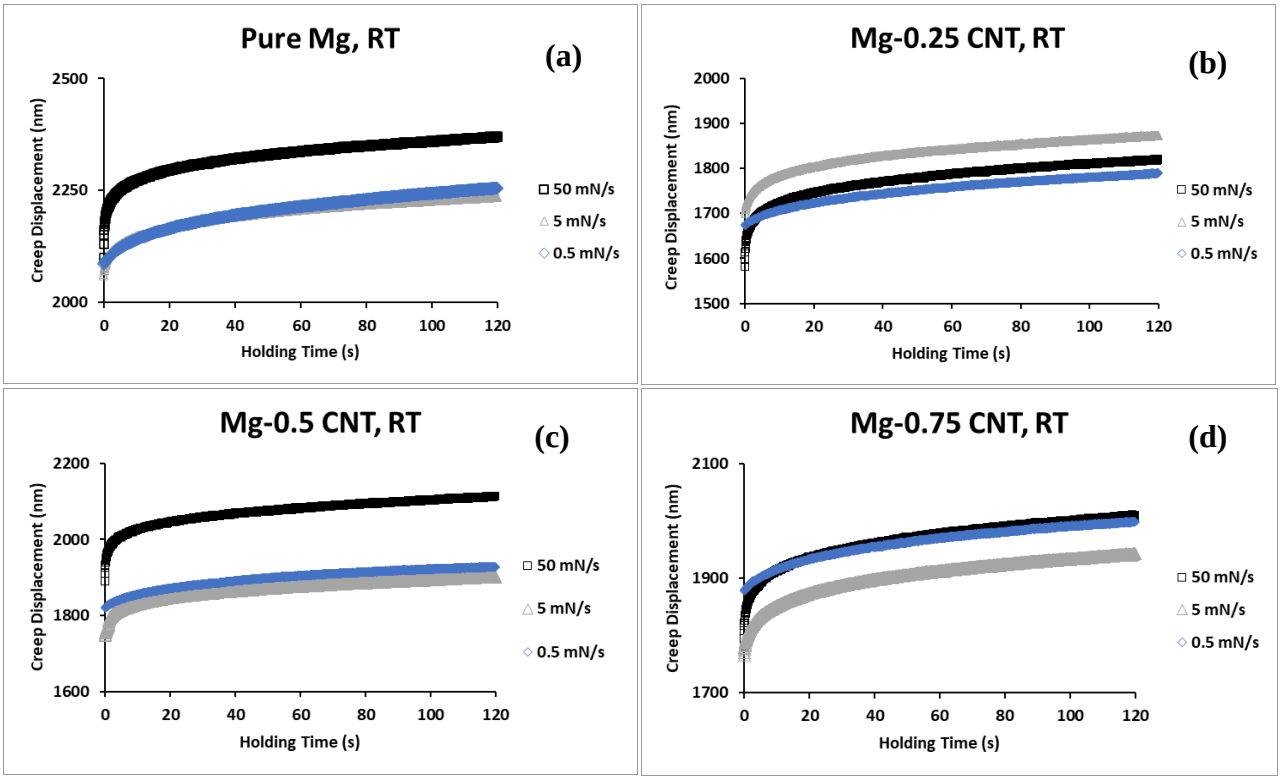

Figure E-3. Creep displacement versus holding time behavior as a function of load rate at a fixed temperature of 298 K (room temperature) for: **(a)** Pure Mg, **(b)** Mg-0.25 vol.% CNT, **(c)** Mg-0.5 vol.% CNT, and **(d)** Mg-0.75 vol.% CNT. **RT**: room temperature (298 K).

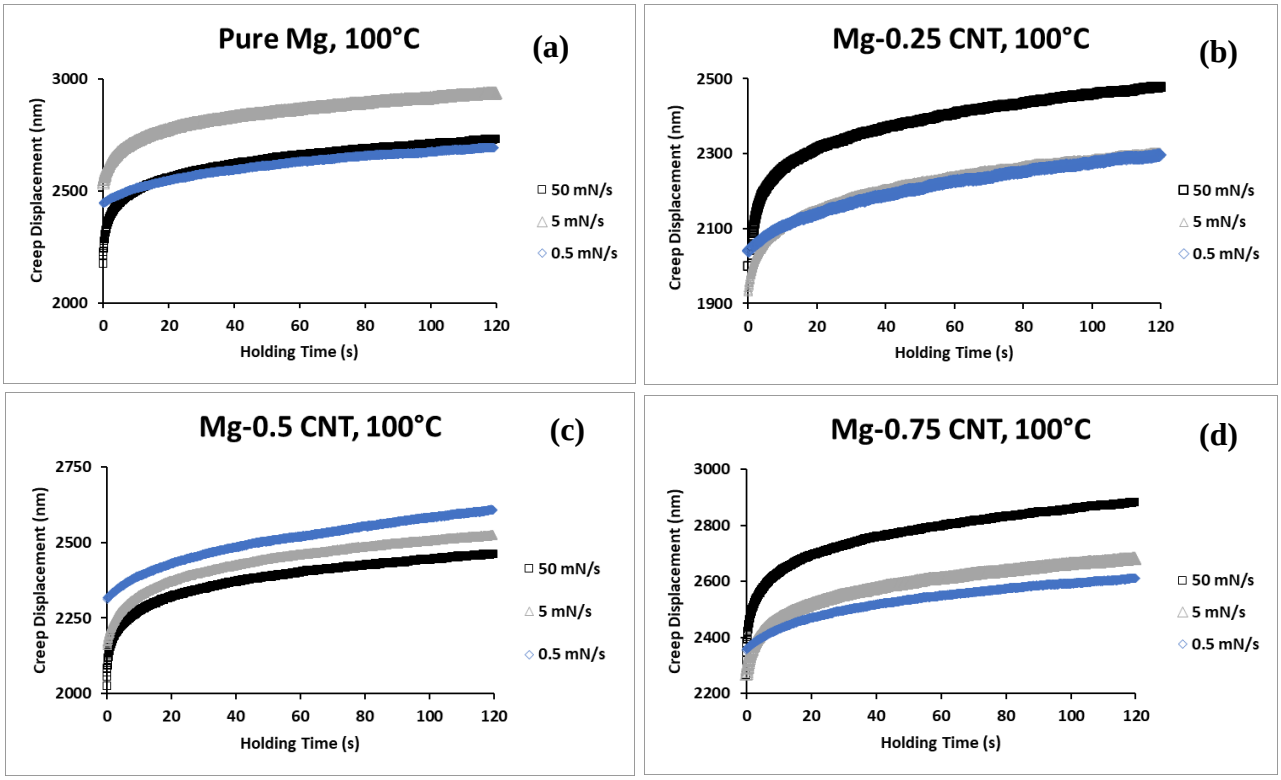

Figure E-4. Creep displacement versus holding time behavior as a function of load rate at a fixed temperature of 100°C for: **(a)** Pure Mg, **(b)** Mg-0.25 vol.% CNT, **(c)** Mg-0.5 vol.% CNT, and **(d)** Mg-0.75 vol.% CNT. **RT**: room temperature (298 K).

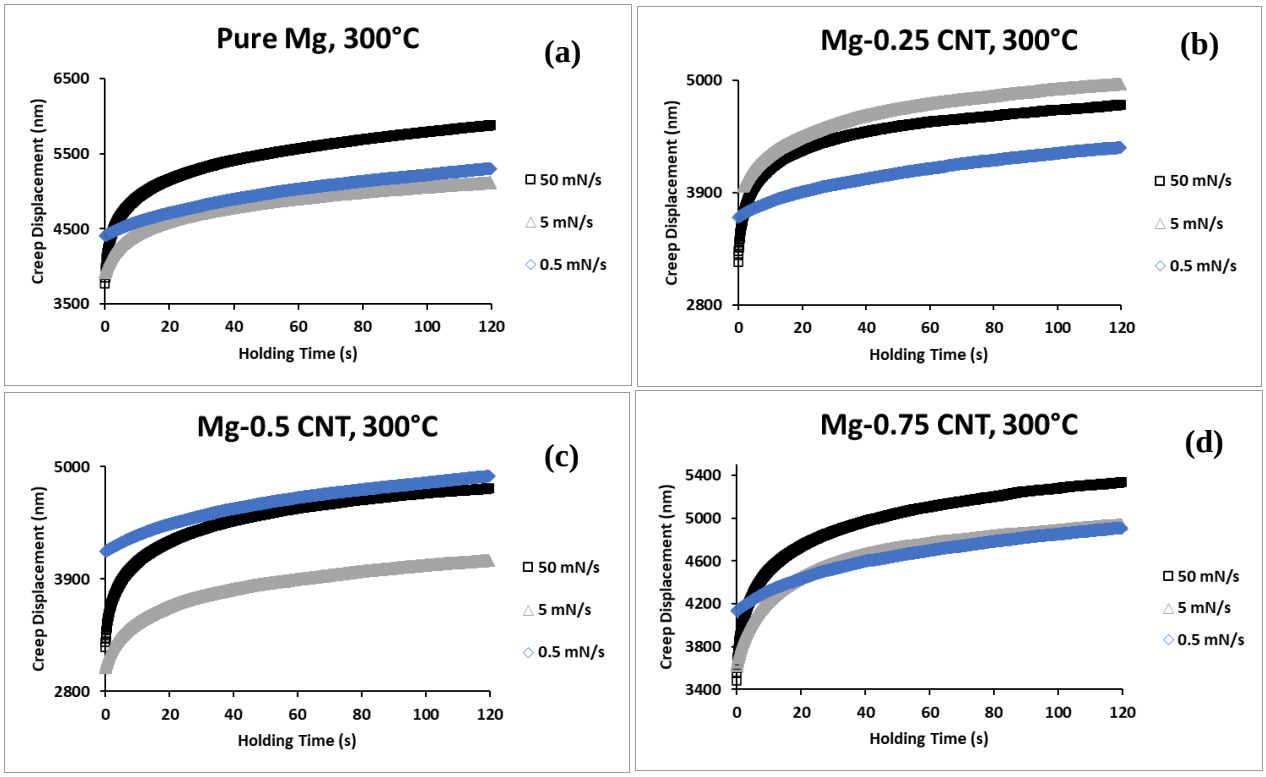

Figure E-5. Creep displacement versus holding time behavior as a function of load rate at a fixed temperature of 300°C for: **(a)** Pure Mg, **(b)** Mg-0.25 vol.% CNT, **(c)** Mg-0.5 vol.% CNT, and **(d)** Mg-0.75 vol.% CNT. **RT**: room temperature (298 K).

E.3. Creep displacement curves obtained at 0.5 and 5 mN/s to supplement Chapter IV-Section 4.3.7.3.

A series of creep displacement curves were shown in Chapter IV, Section 4.3.7.3 for a fixed temperature and load rate, as a CNT volume percentage. Below are the remaining figures at fixed load rates of 0.5 and 5 mN/s for completion.

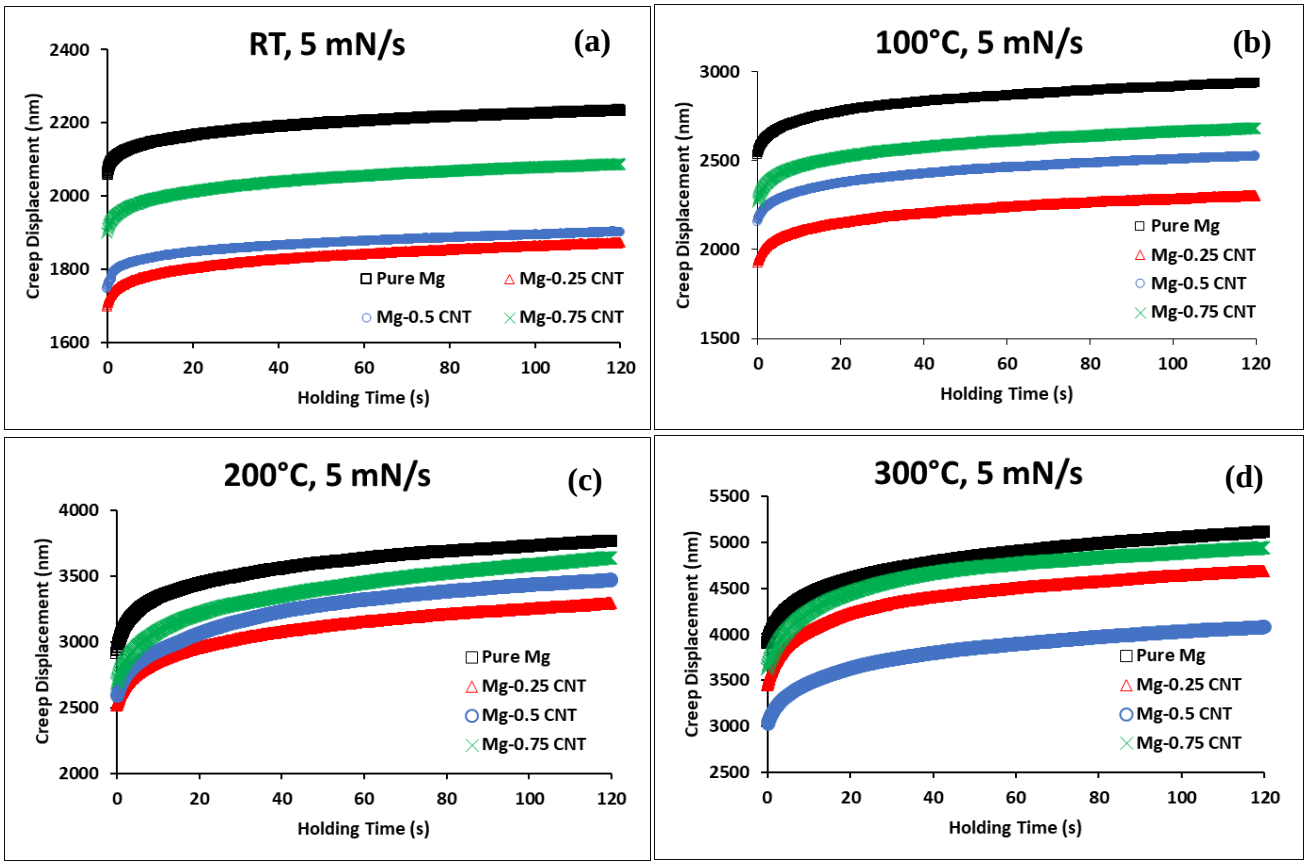

Figure E-6. Creep displacement versus holding time behavior as a function of material tested (CNT loading) at a fixed load rate of 5 mN/s, over all temperatures tested: **(a)** RT, **(b)** 100°C, **(c)** 200°C, and **(d)** 300°C. **RT**: room temperature (298 K).

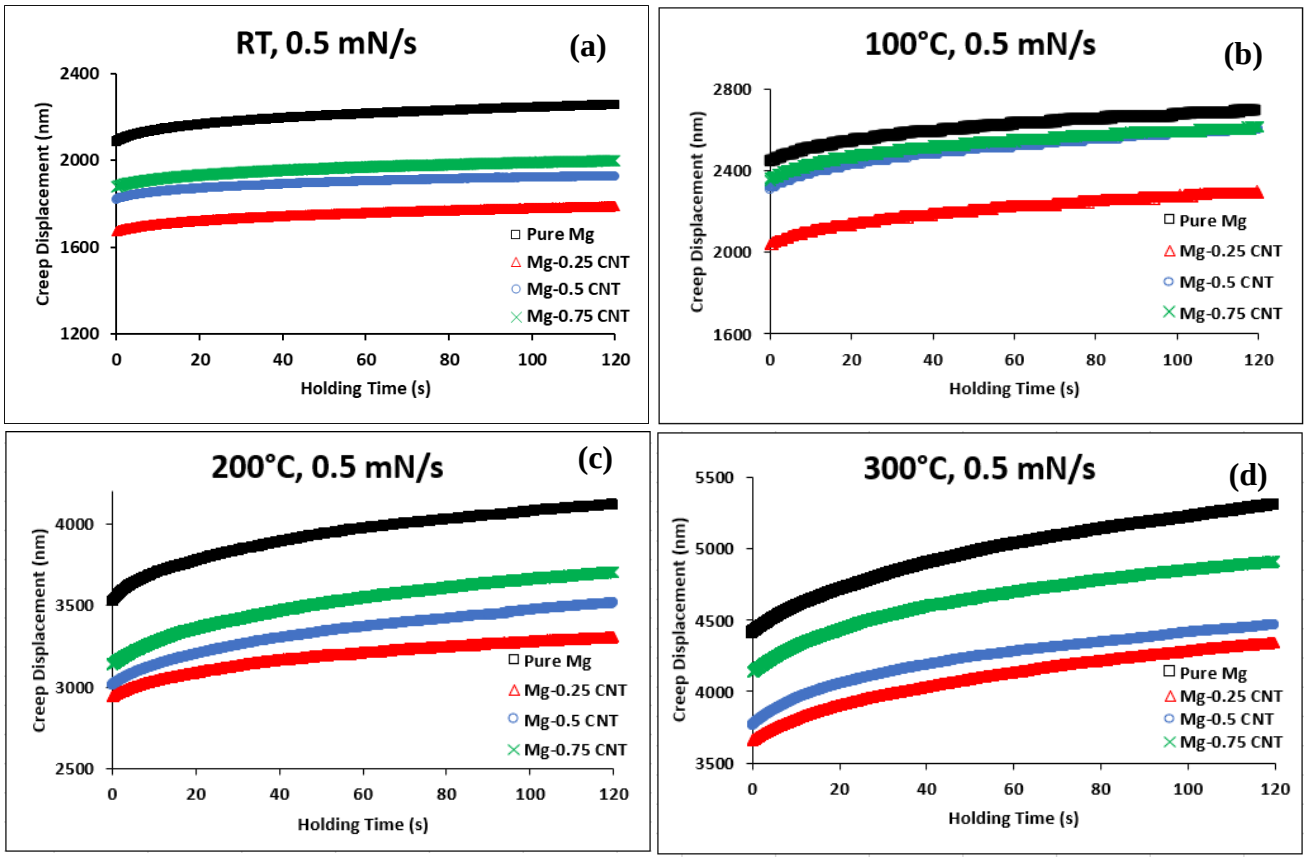

Figure E-7. Creep displacement versus holding time behavior as a function of material tested (CNT loading) at a fixed load rate of 0.5 mN/s, over all temperatures tested: **(a)** RT, **(b)** 100°C, **(c)** 200°C, and **(d)** 300°C. **RT**: room temperature (298 K).